



**UNDERSTANDING AND OPTIMISING
PARAMETERS FOR LIGHTNING
STRIKE TESTING OF CFRP
MATERIALS**

**A thesis submitted in fulfilment of the requirement for the
degree of Doctor of Philosophy**

By

Giuseppe Mastrolembo

B.Sc., M.Sc.

School of Engineering - Cardiff University

UK

2017

Abstract

In this thesis experimental tests and numerical simulations were carried out on the effects of the grounding system on CFRP test samples for the aerospace industry. The grounding system was assessed as one of the parts that can contribute to increasing the cost effectiveness of the sample and the relative test campaign.

A numerical investigation was performed to understand the current distribution within anisotropic CFRP laminates. The influence of the grounding system and the interlaminar impedance on the current distribution were studied using parametric simulations and the results were compared. It was found that the side grounding system produces the best performance between the arrangements investigated. It allows for the best current spreading within the sample and for the lowest voltage drop between the injection and grounding points. Furthermore, it allows for the manufacturing of more cost effective test samples. However, a real implementation of the side grounding system introduces the contact pressure variable between the sample and the grounding electrode which influences the contact resistance.

To implement the side grounding system, a test rig was designed and manufactured. This made it possible to control the compression force. A low current DC test campaign was carried out on five test samples with the same number of grounding systems. It was found that the contact resistance for the three side grounding systems is dependent on the compression force applied between the grounding electrode and the side of the sample. The influence was more pronounced for the sample without any metal coating on the side in contact with the electrode. Furthermore, the resistances measured for the two side grounding systems with metalized sides were comparable with the resistances measured for the fastener grounding systems.

It was found in the literature that the variation of contact resistance due to compression force, for the side grounding cases, is related to variations in the topography of the surfaces in contact, specifically, the variations in the real contact area. Therefore, an investigation on the effects of the compression force on the surfaces in contact was carried out. It was found that the increase in compression force contributes to the decrease in the roughness mean; the increase in the material ratio curve which is a parameter related to the load bearing area; and the modification of the distribution of the height of the surfaces with the appearance of a negative tail.

Further to the low current tests and the characterization of the surfaces of the side grounding samples a high current test campaign was performed. Through the use of typical lightning current waveforms, the thermal and electrical limits of the five grounding systems were investigated. The side grounding systems were tested at the maximum compression force to improve the contact area between the sample and the return electrode and therefore, decrease the risk of the sparking phenomena. The side grounding system paired with the sample with the metal sputtered side showed the best performance in terms of sustaining the highest current peak without appreciably increasing the risk of sparking phenomena at the contact interface between the sample and the

return electrode. Conversely, the sample without any metal coating on its side showed the poorest performance, showing the sparking phenomena at the lowest current peak. The results of the thermal investigation were used for a visual validation of the numerical model created in the first part of the thesis.

A comparison between a numerical model and an analytical model was performed. The dynamics of the temperature when a carbon fibres tow is subjected to a lightning current and thus to Joule effects were studied. The analytical model had the advantage of offering a simpler solution compared to the numerical model and a limited amount of data to input into the problem. The two models were found to produce similar results for the first transient of the temperature. However, the analytical model did not take into account the heat dissipation effects of the carbon fibres in the surrounding environment therefore, after the first transient the analytical model was found not to be as accurate as the numerical model.

If you fall down, as long as you can get up, you have to, you have to fly again.

Nothing of this manuscript would have been written without the infinite love of Maria, Salvina, Ana and Melo.

Acknowledgements

I would like to offer special thanks to two people in particular for their help and support, but above that, for their unconditional moral support, namely, Manu Haddad and Simon Evans. I will be forever grateful for their support during the difficult period of this project. I am also grateful to Matthew Cole for his precious inputs and for letting me spend several months working in the Airbus offices. I would also like to thank David Clark and Chris Stone for their technical support.

Publications and Awards

1. G. Mastrolembo, C. Stone, D. Clark, H. Griffiths, “ Morgan Botti Lightning Laboratory”, UHVnet Colloquium, Guilford, UK, 2014.
2. Giuseppe Mastrolembo, A. Manu Haddad, Matthew Cole, Simon Evans, “UNDERSTANDING VOLTAGE AND CURRENT DISTRIBUTION OF COST EFFECTIVE CARBON COMPOSITE TEST SAMPLES FOR AIRCRAFT LIGHTNING STRIKE TESTS”, 20th International Conference on Composite Materials, Copenhagen, Denmark, 2015.
3. Giuseppe Mastrolembo, A. Manu Haddad, Matthew Cole, Simon Evans, “UNDERSTANDING VOLTAGE AND CURRENT DISTRIBUTION OF COST EFFECTIVE CARBON COMPOSITE TEST SAMPLES FOR AIRCRAFT LIGHTNING STRIKE TESTS”, UHVnet Colloquium, Cardiff, UK, 2016.
4. Giuseppe Mastrolembo, A. Manu Haddad, David Clark, Matthew Cole, Simon Evans, “Modelling the effect of ground return fasteners on current distribution and power dissipation in carbon composite test samples subjected to lightning strikes”, UPEC 2016, Coimbra, Portugal.
5. Best Poster Awards Certificate, UHVnet 2016, Universities High Voltage Network Colloquium, Cardiff, 2016, for the poster entitled “UNDERSTANDING VOLTAGE AND CURRENT DISTRIBUTION OF COST EFFECTIVE CARBON COMPOSITE TEST SAMPLES FOR AIRCRAFT LIGHTNING STRIKE TESTS”.
6. Best Poster Awards, MEDOW Open Day and Energy Exhibition, Cardiff School of Engineering, Cardiff, 2016, for the poster entitled

“UNDERSTANDING VOLTAGE AND CURRENT DISTRIBUTION OF
COST EFFECTIVE CARBON COMPOSITE TEST SAMPLES FOR
AIRCRAFT LIGHTNING STRIKE TESTS”.

List of figures

Figure 1-1. Evolution of the use of composite materials in Airbus over the past 40 years [4].	2
Figure 1-2. a) Boeing 787 Dreamliner made by 50% of composite materials. b) Airbus A350 XWB made by 52% of composite materials [3] [5].	3
Figure 2-1. Examples of human bones [12].	12
Figure 2-2. Composite mud and straw bricks [13].	12
Figure 2-3. Types of composite materials [14].	14
Figure 2-4 Temperature dependence curve of resistivity of 12 artificial graphite products [15].	14
Figure 2-5: Temperature dependence curve of resistivity of 12 artificial graphite products [17].	15
Figure 2-6. Representation of a section of a carbon fibre [16].	16
Figure 2-7. Pre-preg plies rolls. Unidirectional ply on the left and woven ply on the right [22].	18
Figure 2-8. Orientation of unidirectional plies in a stack, according with the reference system of the laminate [22].	19
Figure 2-9. Microscopic picture of cross section of laminate. It is possible to notice the interlaminar layer between the plies oriented in different directions [23].	21
Figure 2-10: Voltage-Current characteristic of cold gases subjected to electric potential [34].	27
Figure 2-11. Grounding configurations that represent two different boundary conditions [37].	30

Figure 2-12. Grounding of test sample along two sides using metal electrode clamped on the surface of the sample [38].	31
Figure 2-13. Lightning zones [40].	33
Figure 2-14. EUROCAE ED-84 current waveforms for lightning direct effects test (figure not to scale). [41]	34
Figure 2-15. A component.	35
Figure 2-16. B component.	36
Figure 2-17. C component.	37
Figure 2-18. D component.	38
Figure 2-19. Experiment setup of Anway [46].	44
Figure 3-1 Simplified scenario of the current flow within a Unidirectional CFRP ply [48].	50
Figure 3-2. Current density magnitude normalized for cross sections A and B (not to scale). The values are purely indicatives [48].	50
Figure 3-3. Schematic of a pre prepreg unidirectional ply. The blue core represents the fibres uniformly distributed whereas the two red parts represent the two layers rich in resin.	51
Figure 3-4. SEM picture of cross section of a unidirectional ply. Inside the core, the current spreads uniformly in both transverse and through thickness direction.	51
Figure 3-5. Grounding systems geometry: a) 2-fasteners, b) 4-fasteners, c) 8-fasteners, d) 8-fasteners rotated, e) side.	54
Figure 3-6. Comparison between two meshing method: row a) quadrilateral base prism, 2D plot, 1D plot; row b) triangular base prism, 2D plot, 1D plot.	59

Figure 3-7. Current density distribution within ply 0° for five grounding scenarios: A) 0.01 S/m ; B) 100 S/m interlaminar conductivity.	61
Figure 3-8. Current density distribution within ply 45° for five grounding scenarios and 0.01 S/m interlaminar conductivity [48].	62
Figure 3-9. Circular cross section (red lines) for circular CFRP sample made by a stack of four plies [50].	63
Figure 3-10. Current density evaluation on cross section at 5 mm radius for all the four plies of the sample, for a side grounding system with 2.4 S/m interlaminar conductivity [50].	64
Figure 3-11. Current density evaluation for seven concentric cross sections in ply 45° for <i>side</i> grounding arrangement and 2.4 S/m interlaminar conductivity [50].	65
Figure 3-12. Current density evaluation for seven concentric cross sections in ply 45° for <i>8f</i> grounding arrangement and 2.4 S/m interlaminar conductivity.	65
Figure 3-13. Highest current density squared in the four plies at 2.4 S/m interlaminar conductivity, for grounding.	67
Figure 3-14. Comparison of normalized peak current density squared for the five grounding systems in the four plies of the sample at 2.4 S/m interlaminar conductivity.	69
Figure 3-15. Voltage drop between the samples terminal for five grounding systems and four interlaminar conductivities.	72
Figure 3-16. Power dissipation for different grounding arrangements at 2.4 S/m interlaminar conductivity [50].	73

Figure 4-1. Test rig for lightning strike test: square CFRP sample screwed to the metal frame of the rig. The fasteners at the perimeter of the sample act as electrical grounding as well as mechanical fixing with the rig.	76
Figure 4-2. Contact surface (not to scale).....	79
Figure 4-3. Constriction resistance [52].	79
Figure 4-4: Relative contact resistance for: a) Elastic contacts and b) Plastic contacts [52].....	82
Figure 4-5: Experimental contact resistance data and calculation results (dashed line) for silver specimen. Numerals on the curves correspond to specimens reported in Table 4-2 [52].....	84
Figure 4-6. Contact between homogenous metal material and laminate composite material: a) ply oriented orthogonally to the contact surface, b) ply oriented parallel to the contact surface, c) ply oriented with a specified angle to the contact surface.....	86
Figure 4-7. 3D draft of the test rig included the CFRP sample.....	87
Figure 4-8. Component of surface profile. (1) error in form, (2) waviness, (3) roughness, (4) subroughness, S_w , R_w , waviness spacing and height; S , R_{max} , roughness spacing and height [52].	89
Figure 4-9. Rough surface profile [52].....	89
Figure 4-10. Electrical equivalent for DC current excitation of the grounding system: a) fastener grounding system, b) side grounding system, c) side grounding system with a high conductive film between the sample and the electrode.	91
Figure 4-11. a) Return current path of the sample provided with three fasteners, b) return current path with one fastener.	93

Figure 4-12. Contact sides of the samples: a) sample with no coating, b) sample with silver paint coating, c) sample with metal sputter coating.	94
Figure 4-13: Test rig for side grounding arrangements.	96
Figure 4-14. Injection fastener set: a) nut, b) fastener, c) nylon washer, d) metal washers, e) crimp ring terminal	97
Figure 4-15. a) Load cell, b) % of reading error over the load levels applied during the test campaign.....	98
Figure 4-16. Aluminium electrode: the two screws and nuts are required to connect the electrode with the circuit through copper wires.....	99
Figure 4-17. Load spreading plate with insulator and return metal plate.....	99
Figure 4-18. Schematic of the electric circuit and measurement system.	100
Figure 4-19. Resistance vs load for <i>metal sputter</i> grounding system for three values of current and Holm's law trend line normalised to the maximum value of 1000 mA.	105
Figure 4-20. Resistance vs load for silver paint grounding system for three levels of current.....	106
Figure 4-21. Resistance vs load for no-layer grounding system for three levels of current.....	107
Figure 4-22. Fastener grounding systems. Cross for the three fasteners grounding system; circle for one fastener grounding system.	108
Figure 4-23. Comparison of the grounding systems resistances at 500 mA; it must be noted that the <i>3 fast</i> (blue dashed line) and <i>1 fast</i> (yellow dashed line) values are not related to any load values, but they have been added to the plot to aid comparison.....	109

Figure 4-24. Geometry of the numerical models: a) geometry of the sample with the side grounding systems, b) geometry of the sample with 1-fastener grounding system, c) geometry of the sample with 3-fasteners grounding system, d) meshing refinement around the fastener region.....	112
Figure 4-25. Comparison between numerical model and high current test: a) current distribution within ply -45° (135°).b) thermal capture at current peak. c) current distribution in ply 45° . d) thermal capture 44 ms after the current peak.	115
Figure 5-1. Zeiss Axiovision 7 materials optical inverted microscope.	122
Figure 5-2. Schematic of different depths of field (DOF) [55].	124
Figure 5-3. Schematic representation of the DOF of a microscope objective when used for surface analysis (Not to scale). The top left picture shows the upper part of the surface in focus whereas the top right picture shows the bottom part of the same surface is in focus. The bottom picture represents the processing of the two main pictures with the results of a new picture where all the surface is in focus.	125
Figure 5-4. Mosaic and z-stack method: a) portion of surface under investigation, b) mosaic made by 6X13 tiles, c) z-stack composition for each tile of the mosaic.....	127
Figure 5-5. Typical raw TIFF image of the topography of the surface.....	128
Figure 5-6. Planes for profiles acquisitions : a) Normal surface profile, b) oblique surface profile, c) parallel surface profile [57]......	129
Figure 5-7. Primary profile and its composition as superimposition of roughness, waviness, and form [57].	130

Figure 5-8. Gaussian filters used to isolate the roughness and the waviness from the primary profile [57].	131
Figure 5-9. Mean line of the profile [57].	133
Figure 5-10. Arithmetic mean of a profile refers to the mean line [57]......	133
Figure 5-11. Illustration of the main amplitude parameters that referred to the profile.	134
Figure 5-12. Load bearing area.....	134
Figure 5-13. Surface of the sample under investigation: a) No-layer surface, b) silver paint surface, c) metal sputtering surface.	135
Figure 5-14. Profile inclined in respect of the horizontal line.	137
Figure 5-15. Areal and profiles acquisitions from no-layer/no-pressure surface: a) primary areal image, b) areal image filtered from noise and sub-roughness, c) waviness areal image. The red line shows the position of the normal plane where the waviness and roughness profiles have been traced, d) roughness areal image, e) waviness profile. The red circle shows the section where the roughness profile has been evaluated, and f) roughness profile.....	139
Figure 5-16. a) primary material ratio curve, b) primary magnitude density distribution.....	140
Figure 5-17. Areal and profiles acquisitions from no-layer/pressure surface: a) primary areal image, b) areal image filtered from noise and sub-roughness, c) waviness areal image, d) roughness areal image, e) waviness profile, f) roughness profile.	142
Figure 5-18. a) primary material ratio curve, b) primary magnitude density distribution.....	143

Figure 5-19. Areal and profiles acquisitions from metal sputter/no-pressure surface: a) primary areal image, b) areal image filtered from noise and sub-roughness, c) waviness areal image, d) roughness areal image, e) waviness profile, f) roughness profile.	147
Figure 5-20. a) primary material ratio curve, b) primary magnitude density distribution.....	148
Figure 5-21. Areal and profiles acquisitions from metal sputter/pressure surface: a) primary areal image, b) areal image filtered from noise and sub-roughness, c) waviness areal image, d) roughness areal image, e) waviness profile, f) roughness profile.	150
Figure 5-22. a) primary material ratio curve. b) primary magnitude density distribution.....	152
Figure 5-23. Areal and profiles acquisitions from silver paint/pressure surface: a) primary areal image, b) areal image filtered from noise and sub-roughness, c) waviness areal image, d) roughness areal image, e) waviness profile, f) roughness profile.	155
Figure 5-24. a) primary material ratio curve, b) primary magnitude density distribution.....	157
Figure 6-1. Schematic diagram of the A/D components generator.	162
Figure 6-2. Simplified cross section of a T joint and the outgassing phenomenon at the interface between the fastener and the CFRP skin, spar/rib.	164
Figure 6-3. Outgassing phenomena at the interface between the CFRP sample and the grounding system.....	165

Figure 6-4. a) Still picture of the test sample before the test, b) still picture of the sample during the test. The red dots guarantee the correct record of the framing.	167
Figure 6-5. Rogowski coil placed around [64].	168
Figure 6-6. Voltage probe placed between the injection fastener and the return plate.	169
Figure 6-7. Normalized current and voltage superimposed.	172
Figure 6-8. Typical voltage and current acquisitions.	172
Figure 6-9. a) Still picture before the current injection, b) still picture during the current injection at 7 kA peak. Inside the red rectangle, sparking is visible located at the interface between the metal electrode and sample side.	175
Figure 6-10. Zooming of the sparking location at 7 kA peak (rotated).	175
Figure 6-11. Acquisitions of thermal camera: a) before the current injection, b) during the current injection, 7 kA peak. An increase in temperature is noticeable in the correspondence to the interface between the sample and the return electrode.	176
Figure 6-12. Image of the sample side painted with silver paint after three consecutive high current tests at 5, 6 and 7 kA peak.	176
Figure 6-13. a) Still picture before the current injection, b) still picture during the current injection at 5 kA peak. Inside the red square visible sparking are located at the interface between the metal electrode and sample side.	177
Figure 6-14. Details shot of the sparking location at 5 kA peak (rotated).	177
Figure 6-15. Acquisitions of thermal camera: a) before the current injection, b) during the current injection, 5 kA peak. An increase of temperature is noticeable	

in correspondence with the interface between the sample and the return electrode.....	178
Figure 6-16. Resistance vs peak current.	179
Figure 6-17. Still pictures of the metal sputter grounding arrangement: a) before the test, b) during the test.	180
Figure 6-18. Details of the sparks at the contact interface between the sample and the return electrode.....	180
Figure 6-19. Acquisitions of thermal camera: a) before the current injection, b) during the current injection, 60 kA peak. An increase in temperature is noticeable at the interface between the sample and the return electrode.	180
Figure 6-20. Thermal camera acquisition at 25 kA current peak. The frame shows some hot spots at the contact interface.	181
Figure 6-21. a) Thermal acquisition 44 ms after the current injection, b) thermal acquisition 1119 ms after the current injection.....	182
Figure 6-22. Still picture after the test. The picture shows the corners of the sample where sparks appeared (1 and 5). Furthermore, locations 2, 3 and 4 show potential contact areas where thermal sparking had occurred. The area at location 6 reveals deep damage of the metal sputter layer.....	182
Figure 6-23. Still pictures of the 3-fasteners grounding arrangement: a) before the test, b) during the test.	183
Figure 6-24. Acquisitions of thermal camera: a) before the current injection, b) at 40 kA peak. The red arrows highlight the sputtering of hot particles from the interface between the grounding fasteners and the sample.....	184
Figure 6-25. Still pictures of the 1-fastener grounding arrangement: a) before the test, b) during the test.	185

Figure 6-26. Acquisitions of thermal camera: a) before the current injection, b) during the current injection, 25 kA peak.....	186
Figure 6-27. Comparison of the resistances calculated for the different grounding systems.....	187
Figure 6-28. a) Square CFRP sample with one injection fastener at its centre and four pairs of grounding fasteners located at 0° , 45° , 90° and 135° . Voltage sensor location for test set 1 in 0° direction and test set 2 in 90° direction; b) picture of the sample connected to the rig of the MBL. The red wires connect the grounding fasteners to the ground of the circuit, whereas the black wire connects the central fastener to the injection point.	189
Figure 6-29. Grounding configurations of each test set and location of the current sensor (black circle).....	191
Figure 7-1. Trend of the temperature of the yarn and of the current impulse for 250 μ s gap time.	202
Figure 7-2. 3D rendering of the geometry of the numerical model. The sphere represents the air or the epoxy inside the sphere, the carbon yarn is visible. The scales are in millimetres.....	204
Figure 7-3. Carbon fibre in air. It is possible to note the yarn is composed of thousands of carbon filaments, some of which are broken.	205
Figure 7-4 Rendering of the modelled carbon yarn.....	205
Figure 7-5. a) The light blue represents the sphere surrounding the carbon filament whereas the dark blue disk represents the cross section at which the maximum temperature has been calculated, b) zoom shot of the cross section around the carbon filament. The image shows the temperature at 60 μ s.	208

Figure 7-6. Comparison between the analytical model the air sphere numerical model and epoxy sphere numerical model.	210
Figure 7-7. Geometry of the array of carbon filaments embedded in epoxy matrix.	212
Figure 7-8. Refining of the mesh around the carbon filaments.	213
Figure 7-9. Section of the geometry used to solve the model. The top and left borders have been considered as symmetric surfaces.	214
Figure 7-10. Position of the temperature evaluation points within the cross section of the geometry.	215
Figure 7-11. Temperature trend at the four locations specified in Figure 7-10.	217
Figure 7-12. Comparison of temperature trend results from the analytical model and numerical models.	218
Figure 0-1: Representation of a single ply (not to scale) and its electric equivalent circuit.	230

List of tables

Table 2-1. Electric conductivity of typical materials used in aerospace applications [24].	22
Table 2-2. Electrical conductivity measured along the three main directions of CFRP unidirectional sample [27].	23
Table 2-3. Electrical conductivity measured along the three main directions of CFRP unidirectional sample [29].	24
Table 2-4 Description of the lightning zones	33

Table 2-5. Resistances measured across CFRP test samples for three different bonding techniques and two compression weights. Each value is the result of the mean of twelve measurements [45].	42
Table 4-1: Surface-Roughness Parameters and mechanical Characteristics of Silver Specimens [52]	82
Table 4-2: power factor d in the function approximating the calculated and test data. [52]	84
Table 4-3. Voltage drop for different load and current.	102
Table 4-4. Comparison between resistances evaluated with the numerical model and the real measurements.	116
Table 5-1 Roughness cut-off wavelength ratio (DIN EN ISO 4287).	131
Table 5-2. Left section, roughness amplitude parameters. Central section, waviness mean. Right section, statistical parameters of the roughness. All for the no-layer/no-pressure surface.	140
Table 5-3. Left section, roughness amplitude parameters. Central section, waviness mean. Right section, statistical parameters of the roughness. All for the no-layer/pressure surface.	143
Table 5-4. Comparison between no-pressure and pressure of the <i>no-layer</i> surfaces: a) data referred to the no-pressure case, b) data referred to the pressure case.	144
Table 5-5. left section, roughness amplitude parameters; central section, waviness mean; right section, statistical parameters of the roughness. All for the metal sputter/no-pressure surface.	148

Table 5-6. Left section, roughness amplitude parameters; central section, waviness mean; right section, statistical parameters of the roughness. All for metal sputter/pressure surface.....	151
Table 5-7. Comparison between no-pressure and pressure of the metal sputter surfaces: a) data referred to the no-pressure case, b) data referred to the pressure case.	153
Table 5-8. Comparison between silver paint (a), no-layer (b), metal sputter (c) cases after the application of the compression force.	156
Table 6-1. Voltage, current, resistance and action integral at 5, 6 and 7 kA peak for <i>silver paint</i> sample.	174
Table 6-2 Voltage, current, resistance and action integral at 5 kA peak for <i>no-layer</i> sample.....	177
Table 6-3. Voltage, current, resistance and action integral in the range 5-60 kA peak for metal sputter sample.....	178
Table 6-4 Voltage, current, resistance and action integral in the range 5-40 kA peak for the 3-fasteners system.....	183
Table 6-5 Voltage, current, resistance and action integral in the range 5-25 kA peak.....	185
Table 6-6 Resistances calculated from low and high current test. (*) The force is referred only to the grounding systems that require the compression test rig.	188
Table 6-7 Resistances in (Ω) calculated in the two test sets. Variation in percentage between the resistances calculated at the 0° and the 90° direction.	191
Table 7-1. Temperature of the yarn with air sphere and epoxy sphere at specific time steps.	209

Table 7-2. Temperatures evaluated at the four positions shown in Figure 7-10.

.....215

Table of Contents

DECLARATION AND STATEMENTS	II
Abstract	III
Acknowledgements	VI
Publications and Awards	VII
List of figures	IX
List of tables	XX
1 Introduction	1
1.1 Aircraft construction materials.....	1
1.2 Economic aspects of use of composite materials	3
1.3 Lightning strike hazards	4
1.4 Research motivations	5
1.5 Contribution of this thesis.....	8
1.6 Thesis outline.....	9
2 Lightning strike experiments on aircraft components: A literature review	11
2.1 Composite materials	11
2.2 CFRP materials	13
2.2.1 Carbon fibres.....	14
2.2.2 Matrices.....	16
2.2.3 CFRP Laminates	17
2.2.4 Electrical characteristics of CFRP laminates	21
2.3 Lightning strike tests	25
2.3.1 Review of electrical sparks principles.....	25
2.3.2 Lightning strike test environment.....	27
2.4 Numerical test environment	39
2.5 Grounding system techniques	41
2.6 Conclusion	46
3 Effect of grounding system on current distribution in CFRP panels ..	48
3.1 Introduction	48
3.2 Mechanism of current conduction within unidirectional CFRP plies	49
3.3 Numerical modelling of CFRP sample	52
3.3.1 Geometry of the sample	52
3.3.2 Electrical properties of the sample and model excitations	55

3.3.3	Software	58
3.3.4	Meshing technique	58
3.4	Effects of grounding arrangement on current distribution: Simulation results.....	60
3.4.1	Current density distribution in plane	60
3.4.2	Current distribution along circular cross sections	62
3.4.3	Peak of the current density squared.....	65
3.4.4	Voltage drop	70
3.4.5	Power dissipation	72
3.5	Conclusion	73
4	Effect of pressure on CFRP-Metal contact resistance.....	76
4.1	Introduction	76
4.2	The contact resistance.....	77
4.2.1	Contact resistance and surface topography	77
4.2.2	Contact resistance for metal to metal contact in large parts.....	80
4.2.3	Simplified scenario of a metal - CFRP contact surface	84
4.2.4	Factors which influence the contact resistance R_c	86
4.2.5	Electrical equivalent of a grounding system under DC excitation..	90
4.3	The Grounding systems.....	91
4.3.1	Fastener grounding systems	92
4.3.2	Side grounding systems	93
4.4	Experimental set up and equipment	95
4.4.1	Test rig	95
4.4.2	Electric circuit and measurement equipment.....	100
4.5	Measurement method.....	101
4.6	Resistance measurement results.....	102
4.6.1	Metal sputter grounding system	103
4.6.2	Silver paint grounding system	105
4.6.3	No-layer grounding system	106
4.6.4	Fastener grounding systems	107
4.6.5	Comparison of grounding systems	108
4.7	Numerical simulation and model validation.....	110
4.7.1	Geometry of the sample	111
4.7.2	Electrical parameters.....	112
4.7.3	Current distribution simulation results	113
4.8	Conclusion	116

5 CFRP surface roughness characterization using microscopic techniques.....	120
5.1 Introduction	120
5.2 Surface characterization technique and equipment	121
5.2.1 Images acquisition.....	122
5.2.2 Data processing	123
5.2.3 Data acquisition.....	127
5.3 Profile and areal surface characterization.....	128
5.3.1 Profile definition.....	129
5.3.2 Profile filtering	129
5.3.3 Roughness parameters	132
5.4 Surfaces under investigation.....	135
5.5 Surface analysis method.....	135
5.6 Surface visualization results	136
5.6.1 no-layer/no-pressure surface	137
5.6.2 no-layer/pressure surface.....	141
5.6.3 Comparison pre- and post- compression	143
5.6.4 Metal sputter/no-pressure surface.....	146
5.6.5 Metal sputter/pressure surface	149
5.6.6 Comparison no-pressure/pressure surfaces	152
5.6.7 Silver paint/pressure.....	154
5.7 Conclusion	157
6 High current test: experimental results on thermal and electrical variables measured under lightning current excitation	161
6.1 Introduction	161
6.2 Lightning current generator	162
6.3 Damage threshold assessment and outgassing phenomenon	163
6.4 Test procedure.....	166
6.5 Equipment.....	167
6.6 Test samples and relative grounding systems	169
6.7 High current test results	170
6.7.1 <i>No-layer</i> grounding system	176
6.7.2 <i>Metal sputter</i> grounding system	178
6.7.3 <i>3-fasteners</i> grounding system	182
6.7.4 <i>1-fastener</i> grounding system	184
6.7.5 Resistance comparison for the various grounding systems	186
6.7.6 Assessment of the location of the grounding fasteners	188

6.8	Conclusion	192
7	Heat proposed analytical model for temperature rise in CFRP under lightning strikes and validation using numerical modelling	196
7.1	Introduction	196
7.2	Energy associated with electric current.....	197
7.3	Temperature threshold.....	198
7.4	Proposed analysis approach.....	199
7.4.1	Solution of proposed analytical model.....	200
7.4.2	Results	202
7.5	Numerical simulation of the heating process in CFRP materials	203
7.5.1	Geometry, input, equations and boundary conditions of the numerical model	204
7.5.2	Numerical model simulation results.....	208
7.6	Comparison between analytical and numerical models	210
7.7	Numerical simulation of an array of carbon fibres embedded in epoxy matrix.....	211
7.7.1	Geometry of the model.....	211
7.7.2	Computation results for the refined numerical model of CFRP material.....	214
7.8	Comparison with the analytical model.....	217
7.9	Conclusion	218
8	General conclusions and future work.....	221
8.1	Research contribution	221
8.2	Future work.....	227
Appendix A		229
	Analytical calculation of the interlaminar conductivity.....	229
Appendix B		232
	Data required for the analytical model	232
References.....		234

Chapter 1

Introduction

It is more than 100 years since the first aircraft properly speaking took to the skies in North Carolina, USA. Since then, aircraft have evolved remarkably. In the first stage, the development had sportive aims, that is, to reach new records in terms of speed or altitude. Scientific development of aircraft took place during the First World War for military purposes. After the war, aircraft were subjected to development for civil purposes, mainly for transportation, but it was during the Second World War that aircraft technology underwent drastic development, with the shift from biplane aircraft to single plane aircraft. Again, the evolution was for military reasons. The end of the Second World War brought another revolution in the development of aircraft, when the reaction engine was created to replace the conventional propeller that had been used up until that moment. Nowadays, most commercial aircraft are powered by jet engines; however, conventional propeller aircraft can be found in specific sectors, such as the military sector or for sportive purposes, or in small aircraft for civil transportation. [1]

1.1 Aircraft construction materials

The evolution of aircraft has involved many aspects of flight technology and science, for example, engine development, civil transportation capabilities, military capabilities, and the type of electrical and electronic equipment on board. However, the development of the materials can be considered to be as important as the other factors in the long evolution sequence that started with

the Wright brothers, and it is more pertinent than ever with the use of composite materials. Although wood is a natural composite material made by cellulose fibres embedded in a matrix of lignin with high specific strength and stiffness, the wooden structures of the first biplane aircraft have been gradually substituted with metal materials, such as steel and aluminium alloys both for the structure and for the covering of aircraft [2]. Industrial composite materials began to be used in the civil sector of aerospace applications in the 1950s in the Boeing 707, where 2% of its weight was due to fibre glass composite material [3]. Since then, the biggest aircraft manufacturers have gradually increased the use of composite materials in the aircraft structure. Figure 1-1 shows the evolution in the use of composite materials in aircraft structures over the past 40 years by Airbus Company.

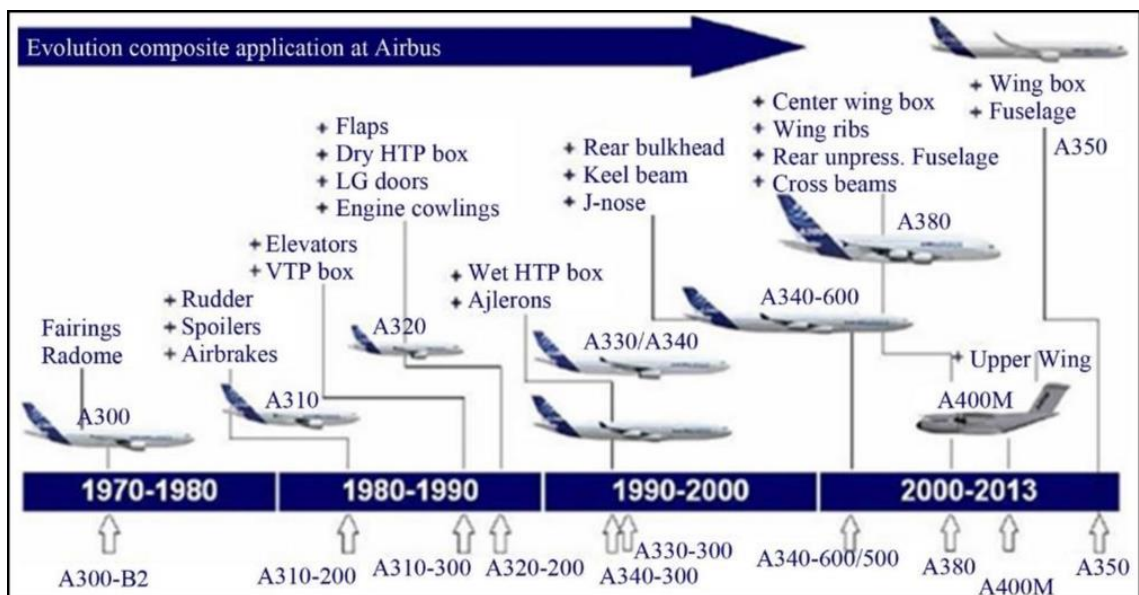


Figure 1-1. Evolution of the use of composite materials in Airbus over the past 40 years [4].

Although the first use of composite materials was for non-structural purposes, nowadays, companies such as Airbus and Boeing claim to produce aircrafts of

which at least 50% of the weight comprises composite materials, which means that the composite materials are widely used in structures as well (Figure 1-2).

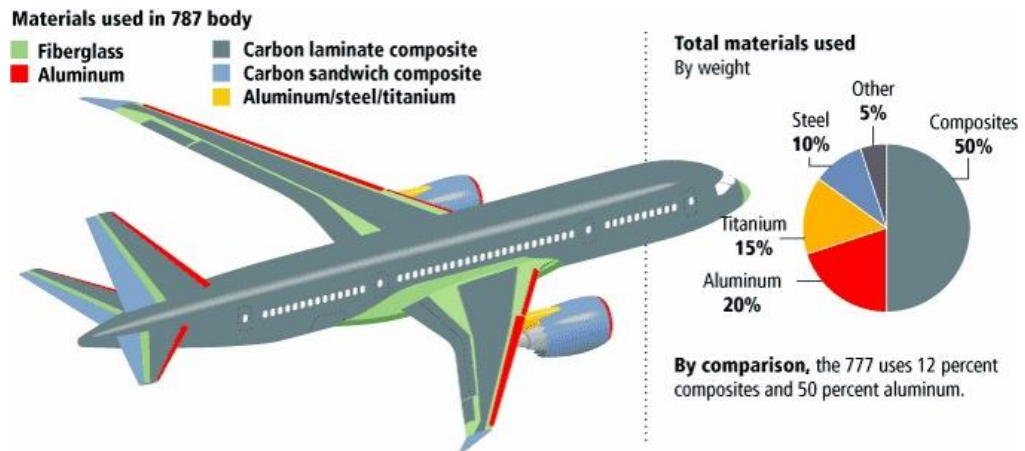


Figure 1-2. a) Boeing 787 Dreamliner made by 50% of composite materials. b) Airbus A350 XWB made by 52% of composite materials [3] [5].

1.2 Economic aspects of use of composite materials

The reason for the gradual substitution of the conventional metal alloys by composite materials is the weight of the aircraft. Composite materials have a higher strength-to-weight ratio compared to conventional aerospace materials; therefore, the same mechanical characteristics can be achieved with a lighter structure. In turn, the desire for weight reduction depends on two main factors:

fuel consumption and emissions. It has been calculated that in a typical transatlantic route such as London – New York, the Boeing 787 Dreamliner consumes 2.26 L/100 km of fuel per seat. On the same route, the Boeing 767-200ER, which had its first flight in 1984, consumes 3.34 L/100 km per seat, that is, 32% more [6]. This can be a significant benefit for the airline companies considering that the price of crude oil, and thus of jet fuel, has dramatically increased in the last decades [7].

The reduction in emissions is one of the great challenges of the 21st century for developed countries. Several agreements have been signed to reduce the emission of GHG (greenhouse gases), and the aviation sector must also contribute to meeting this challenge. According to the Stern Review [8], the amount of CO₂ emissions contributed by the aviation sector can be estimated to be 1.6% of the total GHG emissions; however, it has been predicted that, by 2050, it might be as high as 2.5% [8]. Again, from this perspective, the weight of the aircraft is one factor, together with factors such as the aerodynamic efficiency and the engine efficiency, which can contribute to a reduction in total emissions.

1.3 Lightning strike hazards

Aircraft are subjected to different hazards during flight, such as bird strike, turbulence, etc. The lightning strike hazard is a definite hazard, as it is a relatively common event for an aircraft. Rupke [9] stated that each commercial aircraft can be hit by lightning every 3,000 hours of flight whereas, the French Office National d'Etudes et Recherches Aérospatiales [10] instead cites 1000 hours of flight as the statistical interval between lightning strikes. Although the

frequency of occurrence depends on several factors, such as the zone in the world where the aircraft operates or the number of landings and take offs, of primary importance is the protection of the aircraft against the potential hazards the lightning strike can produce. In general, the effects of a lightning strike on an aircraft are divided into two main groups: lightning direct effects (LDE) and lightning indirect effects (LIE). The first encompasses all the effects caused by the lightning and its current, such as burning, melting, and puncturing at the attachment spot of the lightning on the aircraft. Damage due to the lightning shock wave can be considered a direct effect. Furthermore, the lightning current that flows within the structures of the aircraft can be a threat because it can overheat the structures, and so can be responsible for the phenomenon known as outgassing that occurs at the interface between different materials of the aircraft. In some specific environments, the effect of the outgassing phenomenon can be fatal for the safe flight of the aircraft.

The lightning current creates electromagnetic interferences, which can couple with the electronic and electrical systems of the aircraft, such as avionic systems and radar and communication systems. If these apparatus are not protected, they can suffer dysfunctions, which again, can influence flight safety. These hazards belong to the lightning indirect effects category.

1.4 Research motivations

The continued development of aircraft design, together with efforts to maintain the highest level of protection of the aircraft during its lifetime, has led to the development of new LDE test strategies not only to prove the safety of the structures, but also to predict new potential lightning strike hazards due to the

use of new materials and/or new designs or to test the effectiveness of new solutions. From this perspective, the test campaigns can be extremely expensive because they can require test samples that are particularly costly to manufacture, such as an entire wing tail or an entire fuel tank. Furthermore, other test campaigns can require a large number of test samples in order to analyse statistical results for a specific experiment.

Thus, aircraft companies would like to make the test campaign more efficient from an economic point of view, which means understanding if some of the factors related to the cost of the test campaign can be modified in order to increase the cost effectiveness but maintain the reliability of the experiments.

The aim of this project is to investigate new, more cost-effective solutions for lightning strike tests. A lightning strike is a complex event, which involves several physical mechanisms; however, the focus of this project was on the following factors:

- to understand the distribution of the electrical quantities within CFRP materials when subjected to a lightning current, through numerical simulations and understand the influence of specific parameters which have not been considered in previous works.
- based on the knowledge acquired through the numerical simulation, to develop a test strategy on real test sample which takes into account cost effectiveness factors, leading to the development of more complex numerical models to predict the results of the physical test. The attention of the test campaign and the development of the numerical model have

focused on the grounding system of the sample, which is one of the main factors that influence the cost effectiveness of the sample.

- To analyse the results of the test campaign in order to compare the different designs adopted for the test samples and validate the results of the numerical models, comparing them against the experimental results.
- To understand the impact of the surface characteristics of the sample, such as the roughness of the CFRP surface and the impact of the load force on contact interfaces on the electrical quantities under investigation.

One way to increase the cost effectiveness of an experiment is to use a numerical approach. This allows the researcher freedom in designing the geometry and offers a selection from among countless types of excitations and a number of outputs for analysis, which frequently, are not accessible in a real experiment. An advantage of the numerical approach over the physical experiment is the possibility of investigating the variation of single parameters through parametric simulations. This allows for the analysis of the influence of a specific parameter on the output of the model.

The other approach used in this work was physical. The physical approach allows for real measurement of the quantities under investigation and for validation of the numerical model that has been developed.

The development of a new design made possible the individuation of new variables that had to be considered during the test campaign, such as the load force between the grounding system and the sample that are in contact, the

roughness of the CFRP surfaces, and the influence of the surface characteristics on the electrical quantities under investigation.

1.5 Contribution of this thesis

This work contributes to expand the knowledge of several aspects of the electric current distribution within the CFRP test sample; these are listed below:

- Distribution of the electric current within laminate highly anisotropic materials: The influence of the interlaminar interface on the electric current distribution and on the electrical resistivity of the test sample was investigated using a homogenization technique in the numerical design of the CFRP materials.
- Quantification of the impact of the grounding system of a CFRP sample on the current distribution, and therefore, on the reliability of the experiment.
- Quantification of the impact of the grounding system on the thermal response of the sample under lightning current tests. The comparison between several grounding arrangements has established the thermal limits of each system.
- Quantification of the influence of the surface characteristics and load force applied to contact surfaces on the electrical quantities investigated for non-homogenous laminate materials, such as CFRP.
- An analytical approach to study the thermal evolution of CFRP materials subjected to a fast transient current, such as a lightning current.

1.6 Thesis outline

The thesis is divided into eight main chapters as well as the bibliography, the abstract, and the appendix.

Chapter 2 includes a review of CFRP materials characteristics, a description of lightning strike environment and an analysis of previous work carried out on the effects of the grounding system of CFRP sample for lightning strike test.

Chapter 3 shows the methodology used to create a first numerical model to investigate the electrical quantities inside laminate anisotropic materials. The current distribution and the influence of the grounding systems on the current distribution are investigated. Furthermore, a parametric simulation was carried out in order to underline the influence of the interlaminar impedance on the electrical quantities under investigation. The results are discussed and conclusions drawn.

Chapter 4 includes the development of a low current test campaign on CFRP test samples. The chapter shows the design of several grounding systems for the CFRP test samples. For some of these, it was necessary to design and manufacture a specific test rig that would be able to control the force applied to the grounding electrode in contact. The results of the experiment are shown and discussed. Furthermore, the results are compared with the numerical simulation in order to validate the model.

Chapter 5 shows the method and the results of the surface characterization carried out on some of the test samples used for the physical experiment. The chapter describes the characterization technique and the equipment. The results are reported and discussed.

Chapter 6 sums up the results of the high current test carried out on the same test sample as was presented in Chapter 4. After a brief description of the high current generator used to carry out the experiment, the results of the test campaign are shown. In this campaign, the thermal effects of the electric current have been investigated together with the electrical quantities. A comparison with the results of the low current test is shown and discussed.

Chapter 7 describes a comparison between an analytical and a numerical model for investigating the dynamics of the temperature of carbon fibres embedded either in air or in epoxy. The chapter shows both the analytical and numerical methods. Moreover, the results of both methods are discussed and compared.

Chapter 8 sums up the overall achievements of the work, discussing improvements that could be made to the experiments. Furthermore, the possible directions of future research are discussed.

Chapter 2

Lightning strike experiments on aircraft

components: A literature review

To understand how the design of the test sample can affect the electrical response of a lightning strike test on CFRP laminates, a survey of related works was undertaken. This first section shows some useful fundamentals of CFRP materials, including the advantages and disadvantages of CFRP laminates. A review of the reason for lightning strike tests and the importance of the grounding system is given in the second part. The lightning strike test environment, including the description of typical current excitations for lightning direct effects tests, is described in the third section. A review of the numerical simulation approach and the contributions of the literature to the thesis is provided in the fourth section. The last section reports the review of some previous works that were useful for the development of the test campaign of this project.

2.1 Composite materials

Composites are multiphase compounds obtained by combining different materials in order to achieve properties that the single materials do not have [11]. Examples of composite materials can be found in nature, such as human bones, wood, etc. The longest bone of the human body is made up of an outer part, which is porous and very hard, which surrounds a narrow cavity filled with softer bone, thus creating a multiphase material.

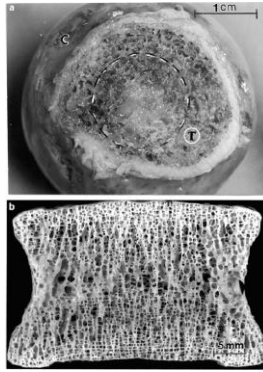


Figure 2-1.Examples of human bones [12].

Wood, which is one of the most used materials for building in human history, is mainly composed of fibres of cellulose embedded in a matrix of lignin, which acts as a stiffener for the cellulose [12].

Humans have created composite materials since the Mesopotamian era, such as building bricks made of straw fibres embedded in a mud matrix. Traces of composite mud bricks have been found in the geographical area of the ancient Egyptians.



Figure 2-2. Composite mud and straw bricks [13].

Although mud bricks are still in use in some parts of the world, such as Mexico, Romania, and sub Saharan Africa, nowadays, manufactured composite materials are present in a countless number of production sectors. The following list, which is by no means exhaustive, gives examples of applications of composite materials:

- sport: bike frames, ski equipment, masts for sailing boats
- automotive: honeycomb chassis of Formula 1 car, lightweight parts for commercial vehicles
- constructions: concrete, reinforced concrete, laminate wood, asphalt
- biomedical: prosthesis
- energy: wind turbines
- aerospace: civil and military aircraft, satellites

The reasons why a composite material can frequently be more desirable than a non-composite material is due mainly to the higher structural properties or higher functional properties, the tailorability of its characteristics, and its lower weight compared to conventional metal materials [11].

2.2 CFRP materials

CFRP usually refers to composite materials obtained by binding a reinforcement of carbon fibres and a polymeric matrix. The fibres can be short and embedded randomly within the matrix, or they can be in the form of long filaments which all lie in the same direction, thus creating very thin sheets of what are called unidirectional plies. By stacking several layers of unidirectional plies, it is possible to obtain CFRP laminates with tailored properties. Another common use of long carbon filaments is in woven plies where the filaments lie to form fabric sheets similar to clothing fabrics [14].

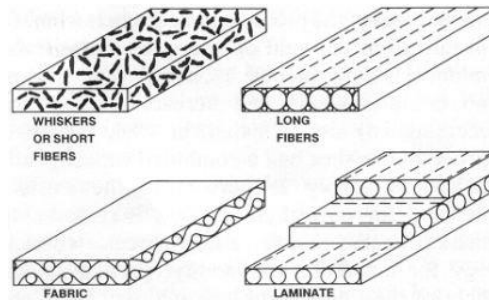


Figure 2-3. Types of composite materials [14].

2.2.1 Carbon fibres

Carbon fibres consist of crystals of graphite, as shown in Figure 2-4. The carbon atoms are arranged in a two dimensional structure, creating planes in the x-y direction. The atoms are bonded together by a strong covalent bond and a metallic bond while the planes are held together by a weaker Van Der Waals force.

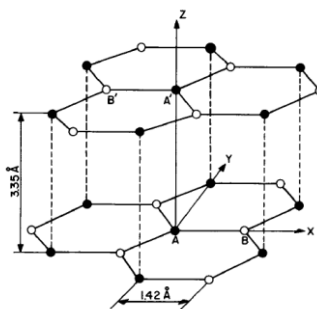


Figure 2-4 Temperature dependence curve of resistivity of 12 artificial graphite products [15].

Therefore, the graphite is a good electrical and thermal conductor in the x-y direction; furthermore, it shows better mechanical characteristics in the plane direction [11]. According to Hull [16], the graphite crystal shows a Young modulus in the plane direction of 1000 GPa in front of 35 GPa perpendicular to the plane. Chung [15] claimed the electrical resistivity of carbon fibres to be in the range between 3 and $12 \mu\Omega m$ varying with temperature. Experiments on the

effects of the temperature on the electrical resistivity of carbon materials, with bulk density similar to that used in aerospace applications, were carried out by Iwashita et al. [17]. In a temperature range between ambient temperature and 1200 °C the electrical resistivity varies as shown in Figure 2-5. In the range up to 600 °C the electrical resistivity shows a negative trend that means the total resistance of the material decreases. Conversely above 600 °C the trend is positive with the results of an increase of the electrical resistance of the material

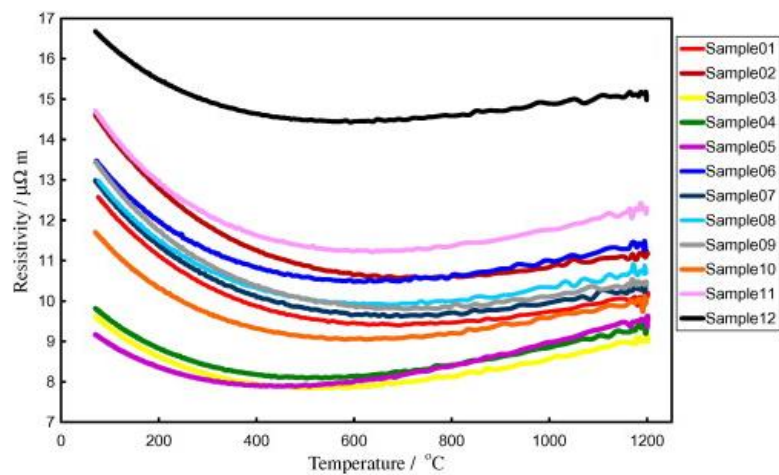


Table 1 - Bulk density of graphite products.

Sample	Bulk density (M kg/m ³)
1	1.73
2	1.68
3	1.71
4	1.71
5	1.67
6	1.64
7	1.67
8	1.71
9	1.71
10	1.75
11	1.65
12	1.65

Figure 2-5: Temperature dependence curve of resistivity of 12 artificial graphite products [17].

In the datasheet of a common carbon fibre used for aerospace applications, Hexcel [18] showed the electrical resistivity to be $1.5 \cdot 10^{-5} \Omega m$.

To achieve good mechanical characteristics along the axis of the filament, the layers of the crystals should achieve a good alignment with the fibre axis;

ideally, they should lie in parallel with the axis. A typical structure of a carbon fibre is shown in Figure 2-6, and it is possible to identify two different patterns. In the outer part, close to the skin of the fibres, the crystal planes are distributed in an ordinated parallel distribution, whereas, in the inner part, the core of filament, the crystal planes are distributed more randomly. The thickness of a carbon fibre can vary between 4 and 8 μm , however, thousands of them are gathered together, thus obtaining tows of carbon fibres.

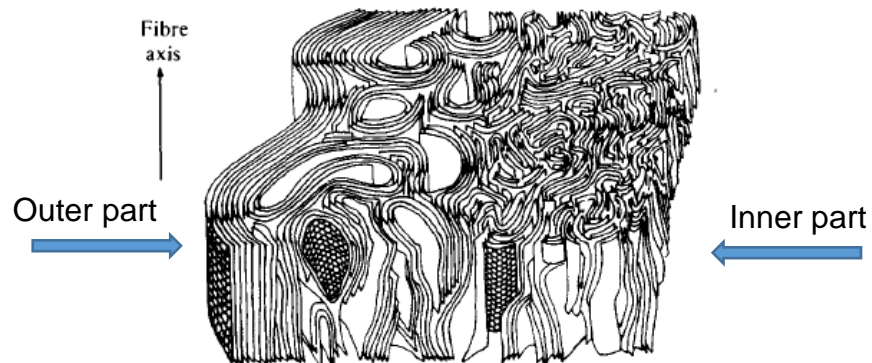


Figure 2-6. Representation of a section of a carbon fibre [16].

2.2.2 Matrices

There is a vast choice of polymeric matrices that can be paired with carbon fibres. However, the polymeric matrices can be divided into two main families: thermoset and thermoplastic. One of the main properties which marks the difference between the two families is that the thermoset resins, such as epoxy, unsaturated polyester or vinyl ester, after the conversion from the liquid phase to the solid phase through a curing process, which heats the material at a temperature between 100 and 200 °C [19], cannot be returned to the liquid form because the chemical reaction to produce them is not a reversible process. Conversely, for the thermoplastic matrices, such as nylon or polypropylene, the

curing process is a completely reversible process, thus giving the material the possibility of being remoulded. In his work, Chippendale [19] stated that polymeric materials are widely used as matrices for composite materials because of their relatively easier fabrication process compared to other matrices, such as metallic, ceramic, or carbon matrices. Sonnenfeld et al. [20] remarked upon the increasing use of polymer matrices in civil and military aircraft, focusing their attention on the mechanical differences between thermoset and thermoplastic matrices. Although the thermoset materials, the most used, show higher strength and stiffness properties compared to the thermoplastic counterparts, they reveal poorer characteristics in terms of toughness [21] [20]. Other disadvantages of the thermoset materials, and which are generally true of the polymeric matrices, for aerospace applications can be found in their poor thermal and electrical conductivity (0.35 W/m °K for the thermal conductivity). Later in this chapter, the reasons why poor electrical and thermal conductivity are not recommendable characteristics for aircraft structures are explained.

2.2.3 CFRP Laminates

CFRP laminates consist of stacks of CFRP plies. The two most common ways of producing plies are either by laying long carbon fibres all in the same direction or in the form of a fabric, both embedded in a polymeric matrix. The thickness of each ply is in the order of an eighth of a millimetre. There are several processes to produce laminates; however, one of the most used in the aerospace industry is first to create a pre-preg ply, which means a ply of fibres pre impregnated with the polymeric matrix.

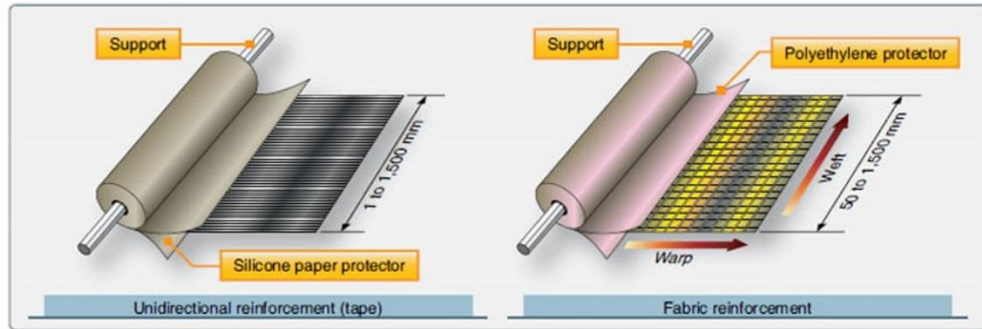


Figure 2-7. Pre-preg plies rolls. Unidirectional ply on the left and woven ply on the right [22].

In a second stage, by stacking a number of pre-preg plies and curing them in an autoclave at a specific temperature and pressure, it is possible to create laminates with specific properties. Several parameters are necessary to identify and characterize the laminate. The most common are as follows:

- the two or more constituents of the composite
- ply lay-up: The laminate which is composed of unidirectional plies has a reference system to which all the plies refer. Inside each ply, it is possible to identify a direction along the fibres, a direction that is perpendicular to the fibres but in the plane, which is called the transverse direction, and a direction perpendicular to the fibres but out of plane, which is called the through-thickness direction. Usually, the orientations described in the ply lay-up refer to the direction along the fibres of each ply of the laminate.

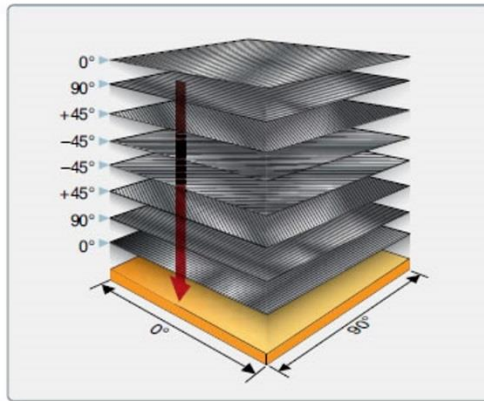


Figure 2-8. Orientation of unidirectional plies in a stack, according with the reference system of the laminate [22].

- fibre volume fraction: this refers to the volume occupied by the fibres in reference to the total volume of the composite; it can be calculated through the following equation:

$$V_f = \frac{v_f}{v_c} \quad (2.1)$$

where:

V_f is the fibre volume fraction

v_f is the volume of the fibre

v_c is the volume of the composite

A similar assumption can be made for the matrix volume fraction.

As highlighted previously, one of the main advantages of CFRP materials over metallic materials is their tailorability, which means that the plies can be oriented in order to meet specific characteristics in a specific direction. The fact that the CFRP laminates are made by stacking unidirectional plies, and each ply can be oriented in a different direction, means the CFRP laminates are anisotropic materials. This means that the properties of the laminate are

dependent on the direction in which they are evaluated. Common metallic materials are defined as isotropic because their properties do not change with the direction. However, a special class of laminates can be defined as “quasi-isotropic” if they show in-plane isotropic characteristics.

The unidirectional ply can be considered an anisotropic material as well, because its properties depend on the direction considered. For instance, the electrical conductivity of a unidirectional ply can vary noticeably if measured along the direction of the fibres, in the transverse direction, or in the through-thickness direction. In this work, the evaluation of the electrical conductivity of the CFRP laminate has been of primary importance in the development of the numerical models.

During the manufacturing process of some types of laminates made of pre prep unidirectional plies, what is called the interlaminar layer appears between the plies. According to Chung [11] and Okabe [23], the interlaminar layer represents the weaker mechanical part of the laminate. Several studies have been carried out in order to characterize the mechanical properties of the interlaminar layer. However, few studies have been carried out to characterize and understand its influence on the distribution of the electric current within the sample. Figure 2-9 shows a microscopic image of a section of a CFRP sample. It can be seen that between plies oriented in different directions, there is an interlaminar layer that is rich in resin. The resin is an electrical insulator; thus, it contributes to reducing the through thickness conductivity of the laminate. Nevertheless, a number of contact spots between fibres of adjacent plies allow for the flow of the current through the interlaminar layer.

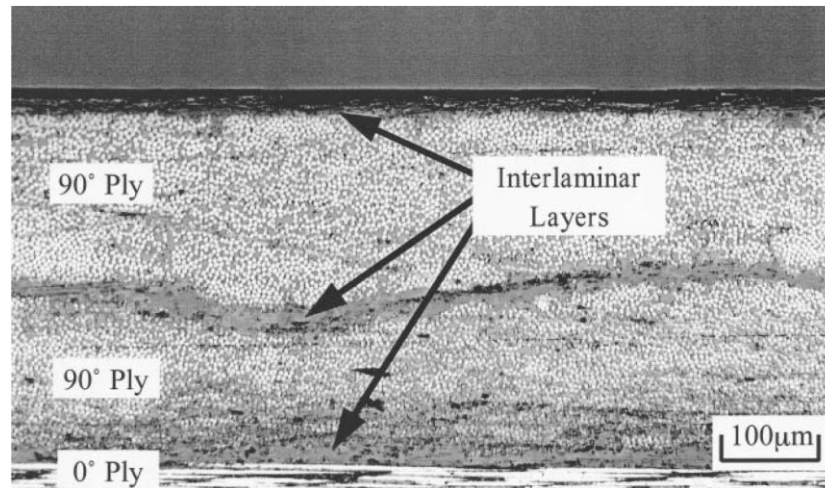


Figure 2-9. Microscopic picture of cross section of laminate. It is possible to notice the interlaminar layer between the plies oriented in different directions [23].

2.2.4 Electrical characteristics of CFRP laminates

In a lightning scenario, the electrical characteristics of CFRP laminates can be considered as one of their disadvantages when compared with conventional metal materials. The main reason is that the conductivity of CFRP materials can be significantly lower compared to metal. This has the consequence of a higher energy dissipation through the Joule effect and, consequently, a higher risk of damage due to resistive heating of the material. Table 2-1 shows the electrical conductivity of typical metal materials and the electrical conductivity measured for a unidirectional laminate used in aerospace industry. The table shows that the highest conductivity of the laminate, which is along the fibres direction, is four orders of magnitude lower than the common metal materials.

Table 2-1. Electric conductivity of typical materials used in aerospace applications [24].

Material	Electrical conductivity (S/m)
CFRP laminate fibres direction	$16 \cdot 10^3$
CFRP laminate transverse direction	10^2
CFRP laminate through thickness dir	1
Aluminium	$3.5 \cdot 10^7$
Copper	$5.96 \cdot 10^7$
Titanium	$2.38 \cdot 10^6$

Hyrano et al. [25], in their research on the characterization of the electrical conductivity of CFRP laminates, performed a measurement using a frequency current source to understand the behaviour of the through-thickness conductivity, and they discovered that for cured CFRP laminate, the current and voltage are in phase for a frequency of *1 KHz*, thus demonstrating that the sample can be considered as a pure resistor up to that frequency. Further studies on the electrical characterization were carried out by Habid [26], and in agreement with Hyrano, the results show that in the frequency range of *20 Hz – 100 KHz*, the CFRP laminate under investigation shows pure resistive behaviour.

The results of the experiments mentioned above were useful because they allowed for the exclusion of frequency sources in favour of measurement with DC sources for the low current test carried out in this project. Furthermore, to reduce the complexity of the model, the numerical model developed to investigate the current distribution within the laminate took into account only DC

excitation. However, the inductive and/or capacitive behaviour of a laminate depends on its geometry and dimension. The experiments mentioned above consider a test sample with a size of approximately a few tenths of millimetres. Increasing the dimensions of the sample to approximately several hundreds of millimetres means the inductive effects are no longer negligible.

The electrical conductivity of CFRP laminates is highly variable depending on the characteristics of the sample. Factors that influence the conductivity are the volume fraction of the fibres, the type of fibres and matrix, and the interlaminar layer thickness. Most of the measurements are focused on the measure of the electrical conductivity along the three main directions. For the quasi-isotropic sample, similar electrical conductivity in plane directions and a lower conductivity in the through-thickness direction are expected. For unidirectional samples instead, the conductivity is usually highest along the fibres direction and lowest in the through-thickness direction with an intermediate value for the transverse direction; the difference between them can be of several orders of magnitude. Ogasawara et al. [27] performed electrical conductivity measurements on unidirectional CFRP laminates with the carbon volume fraction $V_f=0.47$ [28], as reported in Table 2-2.

Table 2-2. Electrical conductivity measured along the three main directions of CFRP unidirectional sample [27].

Direction	Electrical conductivity (S/m)
Longitudinal	29.3
Transverse	7.78×10^{-4}
Through thickness	7.94×10^{-7}

The results show clearly how the unidirectional plies are strongly anisotropic. The transverse conductivity is three orders of magnitude lower than the longitudinal, and the through-thickness conductivity is three orders of magnitude lower than the transverse. However, the absolute values appear to be considerably lower compared to other measurements. The suspect is that the effects of the contact resistance was not taken into account accurately, therefore its impact on the computation of the resistances was not negligible.

Todoroki et al. [29] carried out conductivity measurements on unidirectional laminates using an accurate technique which aims to reduce the effect of the contact resistance on the measurements. Furthermore, they related the conductivity values with the carbon volume fraction of the laminate and found the following conductivity values of Table 2-3 for a carbon volume fraction $V_f = 0.47$:

Table 2-3. Electrical conductivity measured along the three main directions of CFRP unidirectional sample [29].

Direction	Electrical conductivity (S/m)
Longitudinal	5×10^3
Transverse	5
Through thickness	5×10^{-1}

The results show again high variation between the main directions of the laminate, confirming the anisotropy of the material. However, the absolute values appear appreciably higher compared to the measurements of Hyrano. Similar values of conductivity were found by Habid [30] using a measurement technique similar to that used by Todoroki [29].

2.3 Lightning strike tests

Lightning strike tests in industry are necessary to meet the rigorous lightning protection standards required by the certification process. For some part of the aircraft, such as the fuel tank, the requirements are particularly strict [31]. Over the past 40 years, the Federal Aviation Administration (FAA) has updated the regulations regarding the lightning protection in accordance with the developments of new structure design; new materials, such as carbon composites; and new electrical and electronic equipment in the aircraft [31]. However, Kostogorova-Beller et al. [32] reported that, in order to achieve the requirements of the regulatory bodies, the industry has to undertake huge investment. One part of such investment is related to the campaign to test the capability of the specific design, which is usually tested in the worst case scenario. Sometimes, specific requirements of the regulation, such as fault tolerance, have been found “impractical” by the aircraft manufacturers, as Martin [33] stated.

Another reason for conducting lightning tests on aircraft structures is to create a background of knowledge, which can be useful to produce future, more cost effective test campaigns. Kostogorova-Beller et al. [32] presented a large test project on the parameters that influence the fastener sparking thresholds at the fuel tank level with the aim of collecting a range of results which can be used by other aircraft manufacturers to achieve more efficient test campaigns.

2.3.1 Review of electrical sparks principles

Part of the project was focused on the analysis of the electrical phenomena at the interface between carbon composite materials and metal materials. It was

supposed that due to the roughness of the surfaces in contact a number of voids filled with air could very likely appear between the surfaces in contact. The high magnitude of current involved in the lightning test may establish an electric potential between the surfaces high enough to ignite electrical arcs in the voids (in this section the word arc is used with the same meaning of spark). The formation of thermal sparks in several locations of the contact surface may influence the total electrical resistance of the contact surface. Furthermore, the formation of electrical arcs could increase the risk of damage of the contact surfaces.

The thermal sparks in gas make part of a larger spectrum of electrical discharge phenomena in gases. The main physical phenomenon that drives the conduction of current in gases is the ionization process of the gas atoms. Although it is not the aim of this project the description of the entire process of discharges in gases, it is worth to mention that the discharge in gases can be divided in three main steps as shown in Figure 2-10.

In the glow discharge region, after the breakdown point there is a drop of voltage that leads to a drop of electrical resistance of the gas column. Between the point *F* and *G* the increase of current is related to a very small increase of voltage with the results of a very small increase of electrical resistance. Furthermore, in the arc region, that is the region where the gas emits visible light, after the *H* point, there is another fast drop of voltage with the consequence of the electrical resistance decrease to the lowest value, point *J*. After point *J* the voltage, again, is almost independent from the current.

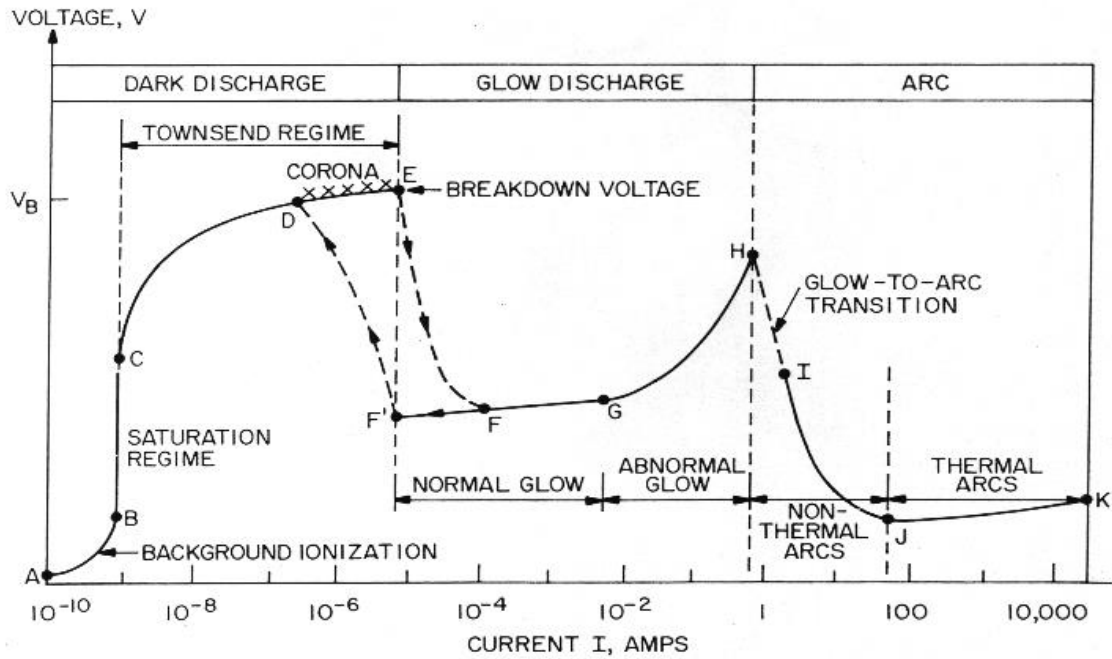


Figure 2-10: Voltage-Current characteristic of cold gases subjected to electric potential [34].

Therefore, when the gas is in the thermal arc region it produces the lowest electrical resistance. It can be supposed that when the lightning current pass the contact interface it can produce a potential high enough to bring the gas trapped within the voids in the thermal arc region with the consequence of a drastic drop of the electrical resistance of the gas. This in turn can influence the total electrical resistance of the contact interface.

2.3.2 Lightning strike test environment

To achieve a specific result from a lightning test, such as the lightning threat at the interface between a fastener and a panel, two factors must be chosen: the test object and the method of excitation of the sample which is related to the test equipment.

The Policy Guidance for Lightning Protection of Fuel Tank Structure and System [35] reported that while the “test sample pyramid” can be valid, it is not

the only possible strategy for compliance demonstration of aircraft parts. The test object complexity is closely related to the cost effectiveness of a test campaign. A typical test sample pyramid for a lightning strike test on aircraft components includes:

- aircraft production standards components
- large scale demonstrators (e.g. wing box)
- sub assembly components (e.g. rib bay demonstrator)
- T-joints
- multi fastener lap joints
- individual fastener joints

The choice of the pyramid level depends on the type of compliance that needs to be demonstrated. Lightning threat at the interface between fasteners and the sample can be studied through multi-fastener lap joints or even individual fastener joints. Conversely, if what is required is the study of the temperature inside a fuel tank when the structure is passed by lightning current, a large scale demonstrator can be a more suitable choice. The cost effectiveness of the test object is highly dependent on its complexity; therefore, an aircraft production standard component can prove more expensive to produce compared to an individual fastener joint. On the other hand, the individual fastener joint can be selected for a statistical study; therefore, a large number of specimens can be required, which contributes to increasing the cost of the experiment. In any case, the grounding system has an impact on the cost of the sample which can be a relevant part of the entire sample.

The EUROCAE ED-105 [36] reports that

“the grounding system must be a part of the test object which ensures a proper bonding with the current generator so that the test current can flow along representative paths and so that the test part mounting is consistent with actual installation of the part. This is of particular importance on smaller test objects where edge effects and surrounding structure may influence test object current distributions and affect test results”.

This statement highlights the importance of the grounding system for a lightning strike test; furthermore, it can be interpreted as saying that the grounding system is required not only for collecting the current injected within the test object, but also for creating a boundary condition which replicates a real scenario.

The ED-105 guideline provides test techniques for simulated lightning strike to aircraft. However, it does not consider designing criteria specifically for the grounding system associated with the test object.

Martinez [37], in his experiments of lightning effects on lightweight sandwich panels, reported a comparison between two different grounding systems, emphasizing the important function of the grounding system to create a boundary condition. He highlighted how the grounding system is required not only to collect the injection current, but also to be reproduced in laboratory specific scenarios which can be encountered in the aircraft structure. He defines a side grounding system as a boundary condition that can reproduce a scenario where the sample is a small representation of a bigger panel. Conversely, a grounding system that comprises a CFRP frame and metal fasteners at the

corners of the sample has been associated with a boundary condition where the panel is the real representation of the scenario, and the grounding system reproduces the real connection of the sample with the rest of the aircraft structure.

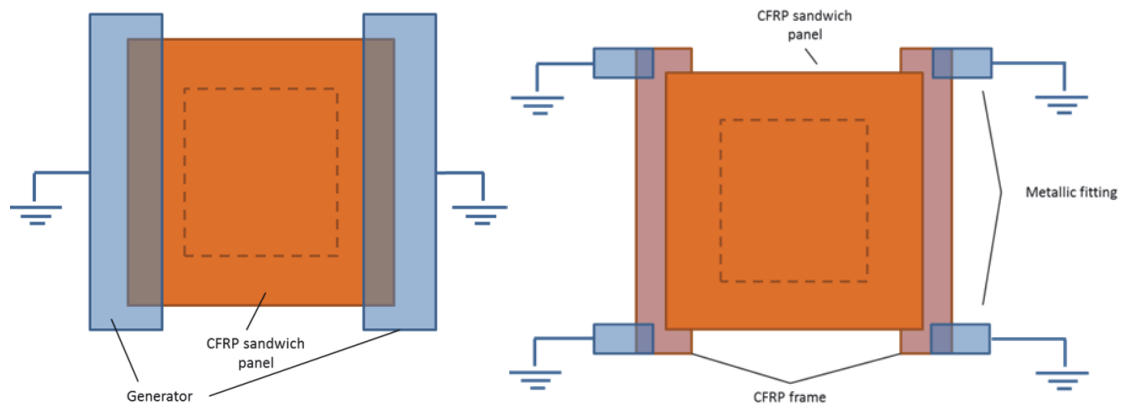


Figure 2-11. Grounding configurations that represent two different boundary conditions [37].

Gibson et al. [38] reported a comparison between several techniques to increase the electrical conductivity of CFRP panels. They used nano and macro conductive materials applied to the surface of laminates to improve the current conduction ability of the sample. The samples were tested in a high current environment using a full D-component to characterize the damage produced by the injected current. Each of the test samples required a proper grounding system to collect the current flowing within the laminate. Gibson reported that the grounding system was made from two metal electrodes placed on the surface of the sample and clamped to the test rig, as Figure 2-12 shows.

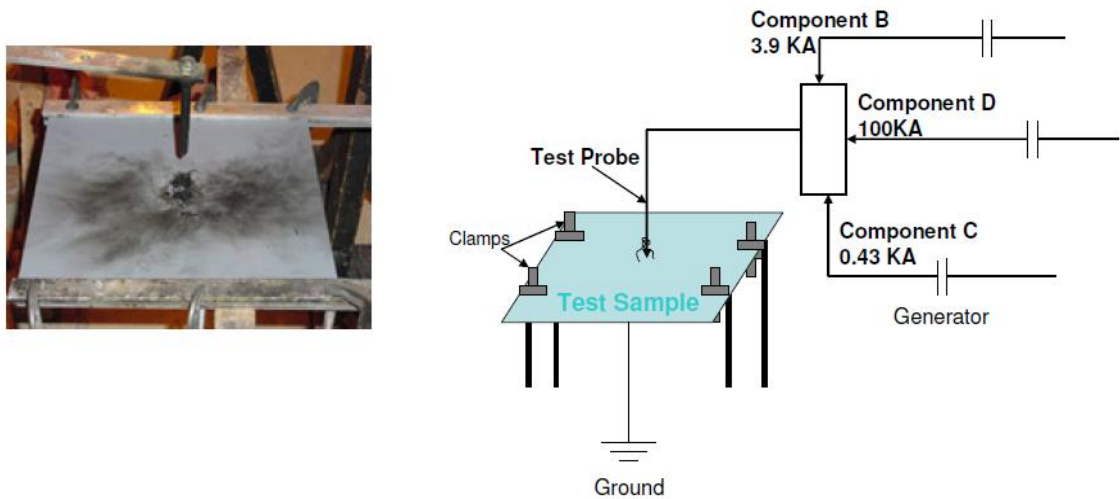


Figure 2-12. Grounding of test sample along two sides using metal electrode clamped on the surface of the sample [38].

Although the grounding system keeps the sample free from the use of grounding fasteners, the arrangement considers the grounding of only two sides of the sample, which means that the current is constricted to flow in a specific direction dictated by the location of the grounding, thus affecting the boundary conditions of the current distribution. The author does not mention, specifically, the reason for that choice; however, it can be supposed that the arrangement is required to replicate a specific scenario where the current is able to flow only along two directions because the other two sides are in contact with insulating materials or are the boundary of a structure.

The excitation of the test object is another essential aspect of a lightning test scenario. Investigations have been carried out to identify the proper type of excitation to apply to a specific test object. The conclusions are that the type of excitation depends on the part of the aircraft that needs to be tested. This implies that, not all the parts of the aircraft are subjected to the same lightning current excitation or to the same lightning threat. Therefore, the regulation bodies have required investigations on the lightning zones of the aircraft in

order to provide specifications on the appropriate protection of each part and location.

According to the EUROCAE ED-91 guide [39], the surface of the aircraft can be divided into regions called lightning strike zones:

“These zones represent the areas likely to experience the various types of lightning current. There are three major divisions representing:

- *Regions likely to experience initial lightning attachment and first return strokes (zones 1 of Figure 2-13).*
- *Regions which are unlikely to experience first return stroke but which are likely to experience subsequent return strokes. This will happen where the aircraft is in motion relative to a lightning channel causing sweeping of the channel backwards from a forward initial attachment point (zones 2 of Figure 2-13)*
- *Regions which are unlikely to experience any arc attachment but which are likely to have to conduct lightning current between attachment points.” [39] (zones 3 of Figure 2-13)*

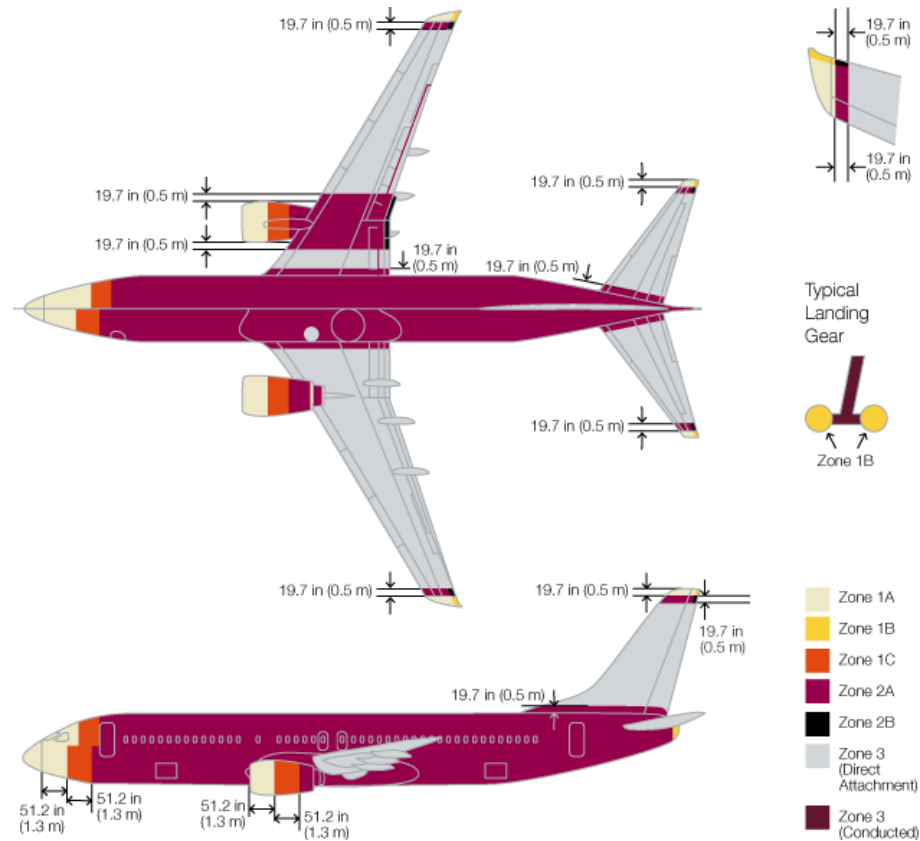


Figure 2-13. Lightning zones [40].

A table which describes the zone designation of an aircraft can be found in [40] and resumed hereafter.

Table 2-4 Description of the lightning zones

Zone designation	Description	Definition
1A	First return stroke zone	All areas of the airplane surfaces where a first return is likely during lightning channel attachment with a low expectation of flash hang on
1B	First return stroke zone with a long hang on	All areas of the airplane surfaces where a first return is likely during lightning channel attachment with a high expectation of flash hang on.
1C	Transition zone for first return stroke	All areas of the airplane surfaces where a first return stroke of reduced amplitude is likely during lightning channel attachment with a low expectation of flash hang on.
2A	Swept stroke zone	All areas of the airplane surfaces where a first return of reduced amplitude is likely during lightning channel attachment with a low expectation of flash hang on.
2B	Swept stroke zone with long hang on	All areas of the airplane surfaces into which a lightning channel carry subsequent return stroke is likely to be swept with a high expectation of flash hang on.
3	Strike locations other than Zone 1 and Zone 2	Those surfaces not in Zone 1A, 1B, 1C, 2A, or 2B, where any attachment of the lightning channel is unlikely, and those portions of the airplane that lie beneath or between the other zones and/or conduct a substantial amount of electrical current between direct or swept stroke attachment points.

The EUROCAE and SAE International (Society of Automotive Engineers) also have developed a guide that defines four main current waveforms to apply to a test object for a lightning direct effects test. The guide provides descriptions on how to associate the waveforms with the test object in accordance with the lightning zones described in the ED-91 guide. The guide shows the four typical lightning current waveforms that can be reproduced in a laboratory for lightning direct effects. The four waveforms are a statistical representation of the real lightning event, as a lightning stroke is a natural event that is subjected to high variability depending on numerous environmental factors, which are hard to predict. The waveforms are intended to reproduce the worst case scenario of the lightning attachment on the skin of the aircraft.

The Morgan Botti Lightning Laboratory (MBLL) is a Cardiff University laboratory. It has been designed to replicate the A, B, C, and D current waveforms shown in the ED-84 guide and replicated in the Figure 2-14 below:

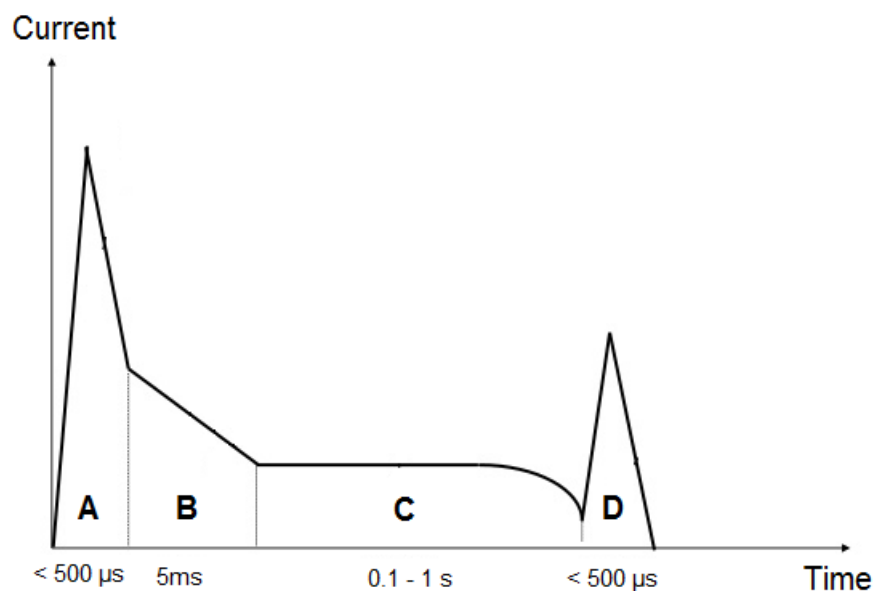


Figure 2-14. EUROCAE ED-84 current waveforms for lightning direct effects test (figure not to scale). [41]

A component

The A component (Figure 2-15) represents the first return stroke, and it includes the most severe parameters of both the negative and the positive return strokes. It is characterized by

- peak amplitude: 200 kA ($\pm 10\%$)
- action integral: $2 \cdot 10^6 \text{ A}^2\text{s}$ ($\pm 20\%$) (in $500 \mu\text{s}$)
- time duration: $\leq 500 \mu\text{s}$

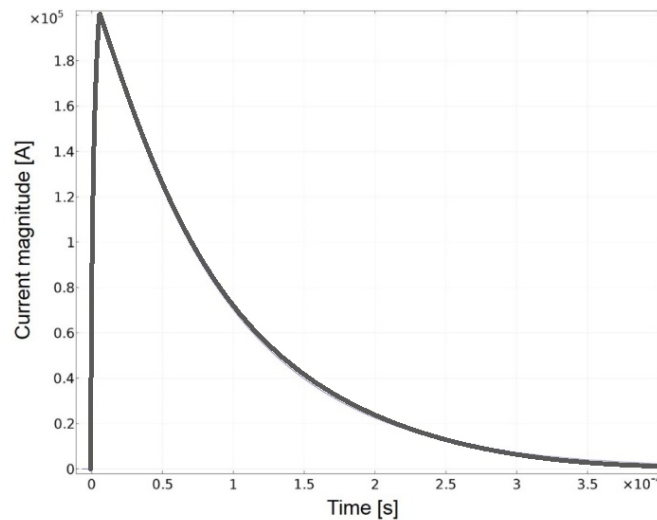


Figure 2-15. A component.

The waveform can be represented analytically through a double exponential equation:

$$i(t) = I_0(e^{-\alpha t} - e^{-\beta t}) \quad (2.2)$$

where

- $I_0 = 218,810 \text{ A}$
- $\alpha = 11,354 \text{ s}^{-1}$

- $\beta=647,265 \text{ s}^{-1}$

B component

The B component, Figure 2-16, represents the intermediate current following the initial return strokes and/or restrikes.

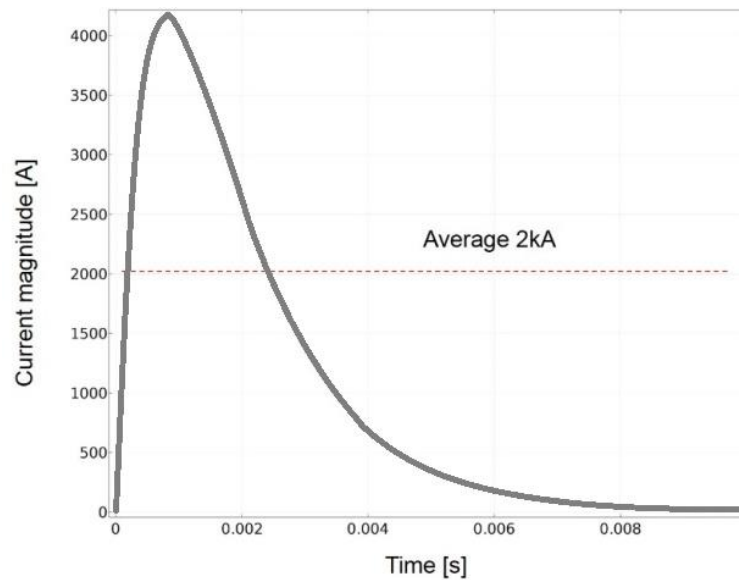


Figure 2-16. B component.

From the analytical point of view, the waveform is described by the following double exponential equation:

$$i(t) = I_0(e^{-\alpha t} - e^{-\beta t}) \quad (2.3)$$

where

- $I_0=11,300$
- $\alpha=700 \text{ s}^{-1}$
- $\beta=2,000 \text{ s}^{-1}$

For direct effect testing, the waveform should be unidirectional or linearly decaying. The average amplitude must be 2 kA ($\pm 20\%$) for a duration of 5 ms . The charge transfer must be 10 coulombs ($\pm 10\%$).

C component

The C component (Figure 2-17) represents the lightning environment that might be caused by the long duration currents that may follow some restrikes of the negative cloud-to-ground lightning strikes and the return stroke of the positive cloud-to-ground lightning flashes. For direct effects testing, the C component should have a current amplitude between 200 and 800 A , a time duration between 0.25 and 1.0 s , and a transfer charge of 200 coulombs ($\pm 20\%$). This waveform should be unidirectional, e.g., rectangular, exponential, or linearly decaying.

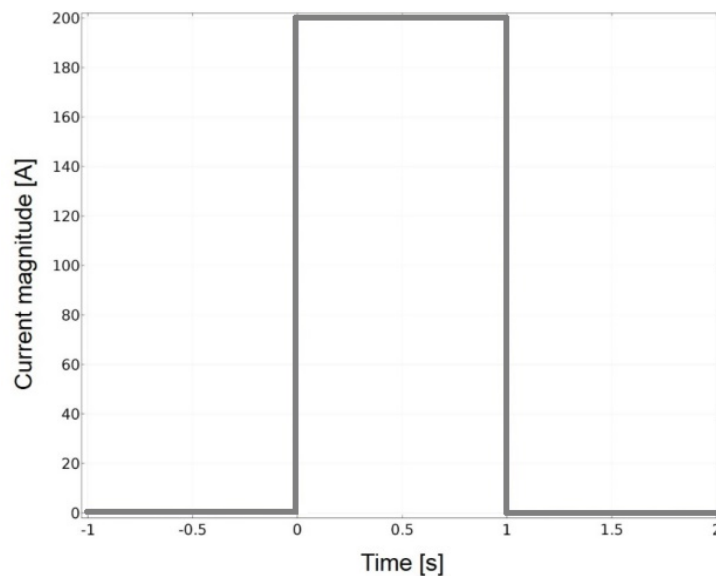


Figure 2-17. C component.

D component

The D component represents a subsequent stroke in a negative cloud-to-ground lightning flash. It is characterized by

- peak amplitude: $100 \text{ kA } (\pm 10\%)$
- action integral: $0.25 \cdot 10^6 \text{ A}^2\text{s } (\pm 20\%)$ (in $500 \mu\text{s}$)
- time duration: $\leq 500 \mu\text{s}$

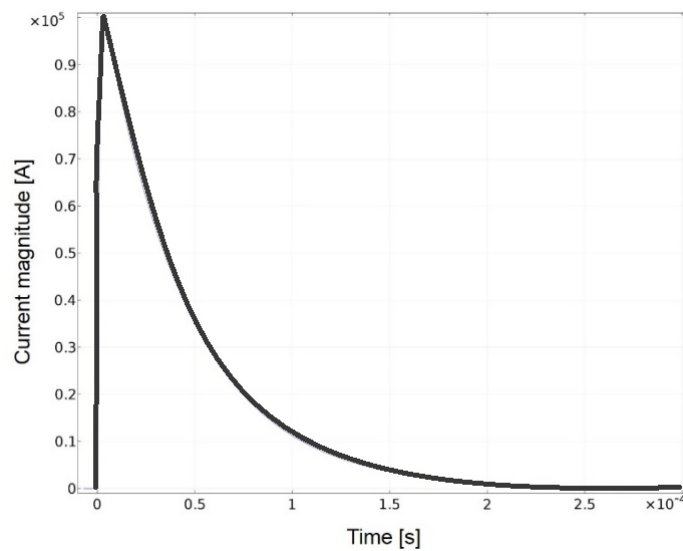


Figure 2-18. D component.

The waveform can be described mathematically by a double exponential equation:

$$i(t) = I_0(e^{-\alpha t} - e^{-\beta t}) \quad (2.4)$$

where

- $I_0 = 109,405 \text{ A}$
- $\alpha = 22,708 \text{ s}^{-1}$

- $\beta=1,294,530 \text{ s}^{-1}$

2.4 Numerical test environment

In recent decades, several studies have been carried out to understand if numerical simulations can reproduce reliably results obtained with lightning tests. The numerical test has the great advantage of reducing drastically the cost of a test campaign because the manufacturing of test samples is not required. Due to significant developments in the field, the simulation technique can predict with a high level of reliability real lightning tests or support them providing results that a physical test is not able to provide.

Evans et al. [42] presented a comparison between two commercial simulation software programs for a coupled electro-thermal simulation on CFRP anisotropic material. The two software were COMSOL Multiphysics® and Ansys Multiphysics®. They highlighted how a reliable numerical method for this type of simulations must be able to

- reproduce the anisotropic characteristics of the materials
- produce transient simulations of current density
- produce transient simulations of temperature distribution
- allow coupling of the electromagnetic and the thermal simulation

The results of the study show that the two software programs under investigation produce comparable results and take into account the anisotropic characteristics of the materials. However, they report that the reliability of the numerical simulation is closely related with the properties of the material under investigation. Furthermore, the authors offer some useful suggestions on the

grounding systems. These suggestions have been useful for the development of the test campaign of this thesis. Evans et al. [42], in their simulation, created a CFRP sample with a fastener grounding system, asserting that the location of the grounding fasteners may influence the current distribution within the anisotropic plies of the sample.

Similar statements can be found in the work of Greigor et al. [43] where a numerical simulation was carried out and compared with experimental results. The investigation was conducted in order to assess the edge glow phenomenon on CFRP laminates used for fuel tank structures. A coupled electro-thermal simulation was carried out on a rectangular 16-ply laminate sample with one side used as injection and the opposite side as grounding. The results show that there is an increase in temperature due to an increase in current density within the plies, which puts the injection side directly in contact with the grounding side, in this case, the plies in the 0° direction. The authors recognised the effect of the grounding system on the current distribution within the sample.

In this thesis, the aspects of the interaction between the grounding fasteners' locations and the ply lay-up of the sample either with a numerical simulation or with a real test are investigated further.

Chippendale et al. [44] also carried out a numerical study on the electro thermal effects of the lightning current on aerospace materials, providing a comparison between the conventional aluminium alloys and the modern carbon fibre composites. What is of interest in their numerical model is an approximation of the model geometry, which was also considered for the simulation campaign carried out in this thesis. They report that the CFRP sample has been designed

as a stack of unidirectional plies with different orientations. Furthermore, each ply has been considered as a homogenous anisotropic ply instead of a proper geometry being made of millions of fibres embedded in the matrix. This has an important consequence in the development of numerical models because it reduces drastically the computational cost of the simulation. Nevertheless, due to the development of the FEM methods, the results of the simulation are kept at a high level of reliability. In the simulation campaign carried out in this thesis, the concept of a homogenous anisotropic ply has been claimed, but with the addition of the control of the interlaminar layer conductivity.

2.5 Grounding system techniques

The idea of the development of a new grounding system that abandons the use of fasteners for a more cost-effective CFRP sample with a side grounding led to a review of the literature regarding previous works which could give some guidelines and an up-to-date view of the topic for this research programme. Several works were noted and adopted to give important inputs for the design of the test campaigns, both numerical and physical.

Robb [45] carried out experiments on the grounding method for CFRP test specimens. He assumed that if the current is injected and collected by fasteners that are aligned with the direction of the fibres, the result is a reduction in the spreading of the current within the specimen with a consequence of a higher resistance. That is because few fibres are in contact with both fasteners, and most of the current flows only within those fibres. This can affect the results if the sample is used to perform measurements such as the electrical resistance of the material. However, he did not perform any test on fastener-bonded

samples to confirm his theory. He proposed a low cost method of bonding the sample using the electroplating technique where the side of the sample is coated with a layer of copper. The deposition of a conductive layer at the sides of the samples acts as a short circuit between all the fibres on the surface; thus, it helps in spreading the current more homogenously along the side surface. He carried out a resistance measurement between the injection and collecting electrodes, which are metal braids in contact with the sides of the samples. The braids ensure a uniform distribution of contact spots with the side. Furthermore, he took into account the effects of the contact pressure, between the electrodes and the sample, using two values of contact force. Robb also performed a comparison between the electroplated samples, the no-coated samples, and the no-coated sample with aluminium foil as a replacement for the braid electrodes. The results of the experiment reveal that the electroplated samples show the lowest resistance compared with the other two configurations, with the conclusion that the metal coating helps to distribute the current more homogenously.

Table 2-5. Resistances measured across CFRP test samples for three different bonding techniques and two compression weights. Each value is the result of the mean of twelve measurements [45].

	Compression weight	Compression weight 0.5
	1.5 Kg	Kg
Electroplated sample	80.4 (mΩ)	81.8 (mΩ)
Bare sample – braid electrode	676 (mΩ)	1145.9 (mΩ)
Bare sample – Al foil electrode	206 (mΩ)	222.3 (mΩ)

Moreover, the higher contact force helps in reducing the resistance. The results from Robb's research contributed to the development of the specimen configurations used in this work; however, he did not perform any comparison between side grounding specimens and fastener grounding specimens, and this is addressed in this thesis. Furthermore, the use of only two values of compression force makes this aspect of Robb's investigation less exhaustive compared to the work carried out in this investigation.

A more detailed investigation regarding the effects of pressure on the contact resistance between a CFRP material and a metal was carried out by Anway et al. [46]. The work reinforced the idea of the author that the contact force plays a fundamental role in the contact resistance between CFRP and metal, and so it contributed to the development of the test campaign that has investigated the effects of the compression force for different grounding solutions for CFRP sample. Conceptually, in her work, Anway considered the CFRP material and the metal material as a contact between CFRP materials and metal fasteners, which is a common scenario in the design of new aircraft. However, the experiment carried out fits perfectly the scenario of a CFRP sample in contact with a metal electrode, which works as a return current electrode, and, for this reason, some of the experimental set-up ideas have been used in this work to perform the low current measurement described in Chapter 4.

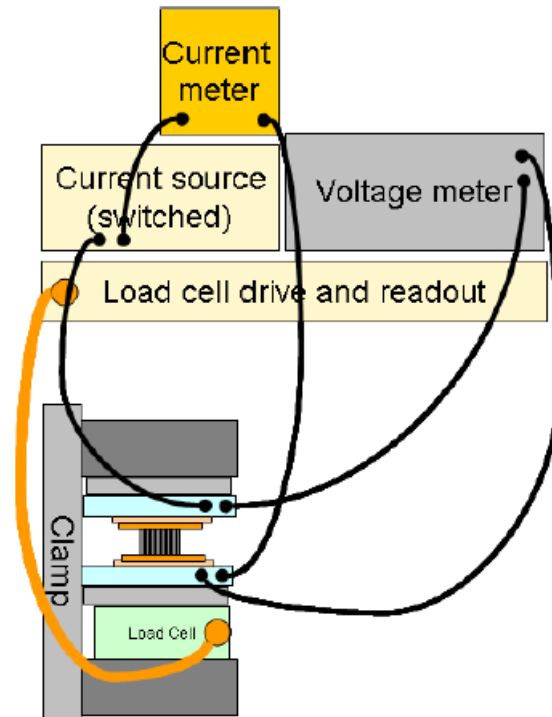


Figure 2-19. Experiment setup of Anway [46].

A similar configuration, which includes the use of a clamp to control the contact force, and a four-wires measurement technique for the calculation of the resistance have been used in the low current measurement of Chapter 4.

The purpose of the experiment was to understand if Holm's law regarding the contact resistance between two metals was reliable even for metal-CFRP contacts. The classical relation between contact resistance and force has been described by Holm [47]:

$$R_c = \alpha \frac{1}{\sqrt{F}} \quad (2.5)$$

where

α is a coefficient related with the characteristics of the materials

and

F is the force applied at contact interface

The experiment carried out by Anway revealed that the equation above is no longer accurate for metal–CFRP contacts. However, the article describes two new equations that fit the behaviour of the metal-CFRP contact under pressure variation. The new equations take into account two different scenarios: the first is when the CFRP sample has a metal coated surface in touch with a metal electrode used to inject the current and the opposite surface with no-coating in contact with another metal electrode used as a grounding. The metal-coated surface is used to short circuit all the fibres, in agreement with [45]. This scenario is known as bare-silver. The second scenario, in contrast, considers both sides of the samples with no metal coating in contact with the respective injection and grounding metal electrodes. This second scenario is known as bare-bare. For both scenarios, the contact force was varied in the range $100 - 1000\text{ N}$, and the resistance was calculated. The results reveal that the resistance calculated for the bare-silver samples follows:

$$R = \beta \frac{1}{F} \quad (2.6)$$

whereas for the bare–bare case, the trend of the resistance follows the second equation:

$$R = \beta^2 \frac{1}{F^2} \quad (2.7)$$

where β for both eq. (2.6) and (2.7) is a coefficient that includes the hardness of the materials and the virtual potential area in contact between the metal electrode and the fibres.

The experiments carried out in this thesis involved CFRP samples with the characteristics that the injection of the current has been always through metal

fasteners, differing in this way from the Anway experiment. Although the two experiments differed in the current injection section, the results of the low current measurements in Chapter 4 are compared with the equations of Anway to verify if an agreement of results can occur.

2.6 Conclusion

The literature review has reviewed the main findings regarding the electrical characteristics of CFRP materials and the role of the grounding system on a test sample. Although the CFRP materials have huge advantages in terms of mechanical performance and weight, it has been found that the electrical resistivity of CFRP materials can be considerably lower compare to metal materials and this is a disadvantage compare to conventional metal materials, when the composite is passed by a lightning current. The studies highlighted that the electrical characteristics of the CFRP materials are strongly dependent on the direction that is a consequence of the anisotropy of the material. Moreover, the electrical characteristic of the CFRP depends on its fiber volume fraction, number of plies, ply lay-up, type of fibres and matrix. It was found that the electrical measurement can be affected by errors which are not negligible. Therefore, some of the electrical measurement techniques require a further development in order to achieve reliability. Nevertheless, there is a desire to improve the electrical characteristics of CFRP materials and researches in this field are being carried out.

The lightning test campaigns are an essential part of the aircraft qualification/certification process and the manufacturers have to afford huge investments to demonstrate compliance with the regulations. From this

perspective there is a desire to reduce the costs of that test campaigns. It was seen that a huge part of those investments are related to the production of tests samples. Their complexity and dimension are directly related to the cost. A full CFRP T- joint that include top panel, rib/spar and grounding fasteners can cost up to several thousands of pounds depending on the sample specifications. Furthermore, it was seen that the grounding system of the sample has to meet the specifications of EUROCAE in order to produce safe and reliable tests and from this perspective further investigations are being carried out on how to create reliable grounding systems for CFRP materials subjected to lightning current. Moreover, the grounding system can impact consistently on the cost of the sample.

The use of CFRP materials led to the investigation on new grounding systems for electrical tests. Each study investigates some aspect of the use of CFRP materials and the relative grounding system. It was analysed the effects of the alignment of the grounding fasteners with the direction of the CFRP fibres and the results suggest that the location of the grounding fasteners in a CFRP sample must be carefully chosen. The literature reports studies that investigate the effects of the compression force at the contact interface between CFRP and metal materials. These studies were useful for the development of grounding systems that do not use fasteners to drain the current injected within the sample. Specifically, the researches were used for the development of more cost-effective grounding system made of a metal electrode in contact with the side of the CFRP test samples.

Chapter 3

Effect of grounding system on current distribution in CFRP panels

3.1 Introduction

The first step of the project was to develop a numerical model able to calculate the current distribution within laminated anisotropic materials, such as CFRP materials. An understanding of the current distribution was necessary in order to design reliable grounding systems for the experimental test.

The numerical simulation method has the advantage of a high level of freedom in terms of designing the test sample, the grounding systems, and the parametric simulations. The other advantage of the numerical simulation is that it allows for the study of test scenarios and configurations that might require big investments or that simply cannot be achieved with physical experiments.

The analysis of the current distribution within a CFRP panel is useful to understand the current behaviour, and so is able to predict threats due to Joule heating or to localise specific zones within the panel where phenomena such as sparking or outgassing can occur.

The investigation was focused on the influence of different grounding systems on the current distribution. For various quantities and positions of fasteners, parametric simulations were carried out varying the grounding arrangement to investigate the current density, the current path within the laminate, the voltage drop at the terminals and the power dissipation. Moreover, a parametric

simulation was carried out in order to understand the influence of the interlaminar impedance on the current distribution. The interlaminar impedance is a parameter not investigated in most of the numerical simulations regarding the current distribution within multilayer materials, but it is thought that it plays a main role.

3.2 Mechanism of current conduction within unidirectional CFRP plies

To understand the basics of current distribution and flow within a ply, Figure 3-1 illustrates a simple case of current injection into a single unidirectional ply. The carbon fibres are represented by the red lines, and they are embedded in a polymer matrix. During the manufacturing process, the fibres bend and touch each other or even cross, creating a type of net. Considering an ideal and simplified case, the current is injected into the ply from an isolated spot; in this case, it is injected within a single fibre, as indicated by the arrow on the left-hand side of the figure, and it is collected through the entire surface opposite to the injection point. The current spreads into adjacent fibres through the contact spots between fibres; however, it flows mostly inside the fibres because their electrical conductivity is considerably higher than the plastic matrix. This allows the current to spread in a transverse direction to the fibres. If the fibres were not in touch, the current would flow only in the fibre into which it had been injected. The most important consequence of the current spreading is a reduction in the current density.

In cross section A, close to the injection point, the current path does not cover the entire cross section of the test sample, resulting in a current density shape

similar to that shown in Figure 3-2a. Conversely, in cross section B, close to the ground side, the same current flows over a wider section of the test sample, giving a current density distribution similar to that shown in Figure 3-2b.

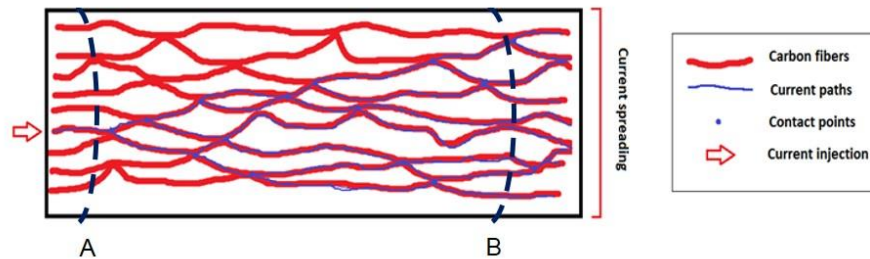


Figure 3-1 Simplified scenario of the current flow within a Unidirectional CFRP ply [48].

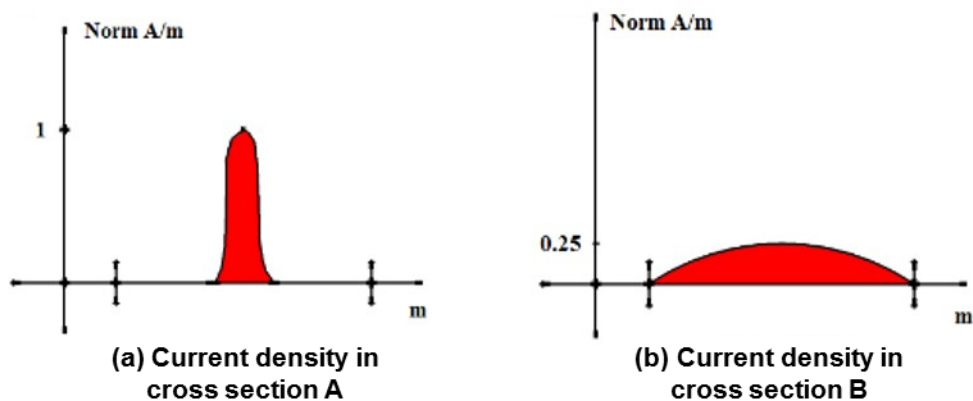


Figure 3-2. Current density magnitude normalized for cross sections A and B (not to scale). The values are purely indicative [48].

A pre prep unidirectional ply essentially comprises three parts: a core, where all the carbon fibres are uniformly embedded in the matrix, and two layers, one on top and one at the bottom of the core, which are rich in resin. Figure 3-3 shows the structure of a single ply. The two outer layers of the ply are responsible for the formation of the interlaminar layer, rich in resin, of the CFRP laminates under investigation.

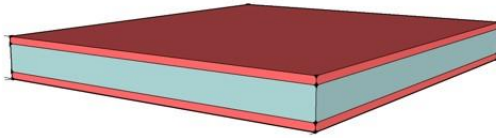


Figure 3-3. Schematic of a pre prep unidirectional ply. The blue core represents the fibres uniformly distributed whereas the two red parts represent the two layers rich in resin.

Within the core of the ply, the current spreads as uniformly in the transverse direction as in the through thickness direction. Figure 3-4 shows a cross section of a unidirectional carbon ply, which indicates the uniform distribution of the fibres. In a scenario such as the one described in Figure 3-1, the current injected within a single fibre will spread in both transverse and through-thickness directions.

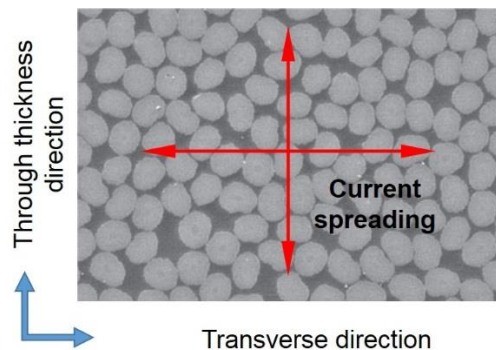


Figure 3-4. SEM picture of cross section of a unidirectional ply. Inside the core, the current spreads uniformly in both transverse and through thickness direction.

The assumption of the uniform distribution of the fibres within the core of the ply indicates that within the ply core, the electrical conductivity in the transverse direction is equal to the through thickness direction. In this way, it is possible to apply a value of conductivity to the ply core and a different value of conductivity

to the two outer layers of the ply. This assumption made it possible to perform the parametric simulations with the variation of the interlaminar conductivity.

3.3 Numerical modelling of CFRP sample

As already mentioned in the introduction, the model involves the design of a CFRP laminate sample, which is made by the stack of unidirectional plies. Due to the microscopic nature of the fibres, whose diameter is in the order of few microns, the numerical model does not consider the design of single fibres. Instead, it adopts a homogenisation technique which considers the core of the ply as a homogenous material but with anisotropic characteristics. This has the advantage of reducing considerably the computational cost of the model while maintaining a high degree of accuracy at the macroscopic level. Conversely, the disadvantage is that it is not possible to investigate the electrical characteristics on a microscopic scale, such as current distribution at the fibre level or interaction between fibres.

However, the thin resin-rich layers between each ply have been modelled as homogenous resistive layers.

3.3.1 Geometry of the sample

For all of the parametric investigations that were carried out, the CFRP sample had the same geometry of a circular panel with a radius of *50 mm* made by a stack of four unidirectional plies, with ply lay-up [45/135/90/0]. The sample is quasi isotropic, and each ply has a thickness of *0.25 mm*, whereas a thickness of *35 μ s* was attributed to the interlaminar layer according to a measurement on a microscopic picture [49]. A metal fastener was placed at the centre of the sample to replicate one of the typical lightning test scenarios where the current

is injected through the fastener head and flows within the sample. The radius of the fastener is 3.15 mm , which is one of the typical fastener sizes used in aerospace applications.

The grounding system was one of the two parameters that were varied in order to understand their effects on the current distribution; therefore, five different grounding systems were considered, and they can be divided into two main groups [50]:

- Grounding with fasteners:
 - *Grounding with one pair of diametrically opposed side fasteners (Scenario 2f) (Figure 3-5a):* This involves a pair of fasteners located on the sample perimeter on opposite sides of the central fastener. This is used to establish a symmetrical distribution of the potential/current near the central fastener. It forces the current to flow to specific ground sinks (the grounding fasteners), thus modifying the distribution of the potential/current within the panel compared with the side grounding scenario. This scenario also modifies the geometry of the test sample, as the grounding fasteners are fitted in the holes, thus excluding parts of the CFRP panel during the conduction process.
 - *Grounding with multiple pairs of diametrically opposed side fasteners:* Each pair of fasteners is positioned on the sample circumference diametrically opposed at 10 mm from the border of the panel. In addition to the one-pair scenario described above, where the pair of fasteners were aligned with ply 0° , four other scenarios

were studied using multiple pairs: two pairs of fasteners (Scenario 4f) (Figure 3-5b) aligned with 0° and 90° plies, and four pairs of fasteners (Scenario 8f) (Figure 3-5c) aligned with 0° , 45° , 90° and 135° plies sequentially and then rotated by 22.5° , which means the fasteners were not aligned with any of the plies (Scenario 8f)(Figure 3-5d).

- Side grounding (*scenario side*): This consists of grounding the entire panel perimeter edge. It creates a continuous grounding boundary around the panel, which then allows the current to be distributed within the panel according to the available conduction paths. However, it should be noted that it does not modify the geometry of the panel (Figure 3-5e).

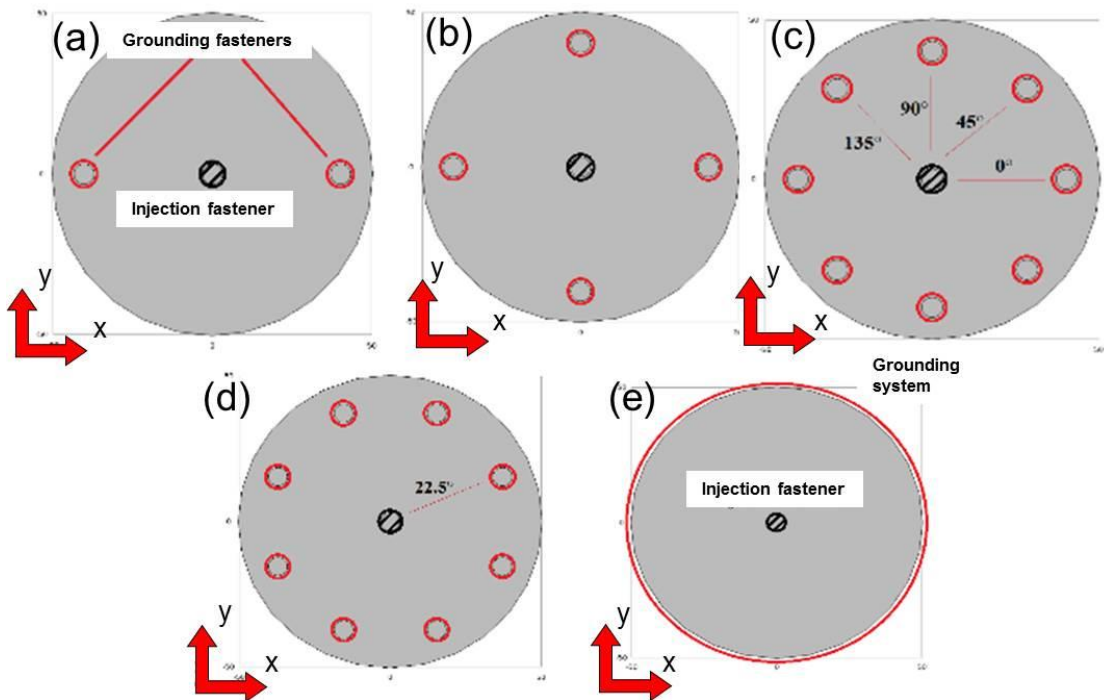


Figure 3-5. Grounding systems geometry: a) 2-fasteners, b) 4-fasteners, c) 8-fasteners, d) 8-fasteners rotated, e) side.

It was thought that the alignment between the direction of the ply and the pairs of fasteners facilitates, under specific conditions, the flow of the current through a highly conductive path between the injection fastener and the grounding fasteners within the ply. This reduces the current density uniformity in the panel and, at the same time, increases the current density along the high conductive path, thus increasing the risk of overheating due to the Joule effect. Therefore, to improve the uniformity of the current distribution in the test panel, another configuration with eight grounding fasteners was used. The rotation of these by 22.5° maintains the symmetry of the current/potential distribution within the panel.

3.3.2 Electrical properties of the sample and model excitations

The numerical simulation requires the knowledge of the electrical conductivity of the plies, of the interlaminar layer, and of the metal fastener. For the core of each ply, the following orthotropic conductivity matrix was used [51]:

$$\begin{bmatrix} \sigma_f & 0 & 0 \\ 0 & \sigma_t & 0 \\ 0 & 0 & \sigma_{tt} \end{bmatrix} = \begin{bmatrix} 16000 & 0 & 0 \\ 0 & 100 & 0 \\ 0 & 0 & 100 \end{bmatrix} S/m \quad (3.1)$$

where:

σ_f is the conductivity along the fibres

σ_t is the conductivity transverse the fibres

σ_{tt} is the conductivity in through-thickness direction

The conductivity in the transverse direction was considered equal to the conductivity in the through-thickness direction because in the ply core, the fibres are equally distributed in both directions, as already explained in section 3.2.

The orthotropic conductivity values belong to previous works carried out by AIRBUS on CFRP laminates similar to those used in this project. A very similar method of measurement of the conductivity can be found in the work of Todoroki [29].

As described previously, the interlaminar layer is rich in resin; however, it is recognised that contact spots between the fibres of the two adjacent plies can be present at this interface. Such contact acts like a uniformly distributed impedance, thus, allowing the through-thickness conduction of the current within the laminate. For this reason, the interlaminar layer was considered to have an isotropic resistive layer. The value of conductivity applied to it was 2.4 S/m .

The value was calculated analytically using the orthotropic conductivity matrix and the geometric characteristics of the ply. A description of the calculation can be found in Appendix A.

The interlaminar layer conductivity was the second parameter that was varied in the simulation; therefore, three other values were considered for the parametric simulation: 100 , 0.1 , and 0.01 S/m .

The conductivity of the fasteners was set to $2 \cdot 10^6 \text{ S/m}$, that is, equal to the titanium conductivity.

Furthermore, the contact surface between the fastener and the sample was considered ideal. This means that the apparent contact surface was equal to the load bearing area (for a general description of the contact surface characteristics please refer to section 4.2.1). The electrical conductivity at the interface was set to 10^6 S/m .

The model was excited using a DC current of 200 A, injected in the head of the central fastener for each test sample which represents the magnitude of the C-component extrapolated from the EUROCAE ED-84 guide [41]. Furthermore, the potential $V=0$ V was considered as boundary conditions for the electrical current on the base of each grounding fastener.

The set of equations solved by the software are reported hereafter:

Ohm's law,

$$\mathbf{J} = \sigma \mathbf{E} + \mathbf{J}_e$$

Equation of continuity,

$$\nabla \cdot \mathbf{J} = -\nabla \cdot (\sigma \nabla V - \mathbf{J}_e) = 0$$

Where,

\mathbf{J} is the current density

σ is the electrical conductivity

\mathbf{E} is the electric field

V is the potential (dependent variable)

\mathbf{J}_e is the external current density

The equations were solved in steady state in order to reduce the computational strength. The solution of the steady state model allows for the visualization of the current density distribution for any current magnitude applied. If the model is solved using a different current magnitude than the 200 A used, this would not modify the current distribution but only the scale. At this stage of the investigation were more relevant the results related to the current distribution compared to the current magnitude applied. According to this, it would be

possible to apply this method for other waveforms of the ED-84 such as the D or A waveforms.

3.3.3 Software

The software used to develop the model is COMSOL Multiphysics®. It is based on the Finite Element Method of solution of the differential equations of the problem. It has the advantage of combining several environments, called in the software “physics”, such as electrical, thermal and mechanical environments. Furthermore, it allows access to a very efficient support centre, which helps to improve the model in every aspect, from the geometry to the choice of the most appropriate set of equations for the meshing technique.

3.3.4 Meshing technique

The meshing step of the model design required special attention. Most of the simulation software allows for an automatic meshing of the geometry or a user-defined meshing method, while most of automatic meshing methods produce meshing elements with a tetrahedral shape because of the simplicity of meshing even very complex geometry. Other meshing methods divide the geometry into cubes. For the very thin plies, it was seen that the tetrahedral meshing method did not make it possible to get accurate results for 1D graphs. Therefore, it was necessary to create a more accurate mesh of the geometry. The prism elements were tried with two types of prism: one with a quadrilateral base and one with a triangular base. Figure 3-6 shows a comparison between the two meshing techniques: row “a” shows a meshing of the sample using quadrilateral prism elements, a 2D extrapolation of the current distribution within a ply of the

sample, and a 1D plot of the current density along circular paths inside the ply. In contrast, row “b” shows the meshing technique using triangular base prism elements and, again, a 2D plot and a 1D plot extrapolated from the results. It can be seen how the meshing technique with quadrilateral base prisms leads to a non-homogenous distribution of the elements on the surface. There is a refined mesh around the injection fastener, but this is not homogenously distributed. Away from the fasteners, the meshing size is not homogenous with zones of fewer refinements. Instead, the meshing with the triangular base elements shows a refined mesh around all the fasteners and a more homogenous distribution away from them. Although a comparison between the two 2D plots suggests that the results are very similar, a comparison between the 1D plots shows how the lack of mesh refinements influences the results. The 1D plot shows a more irregular trend compared to the second. The consequence of using the triangular base elements was a 30% increase in the *degrees of freedom* (DOF) of the model.

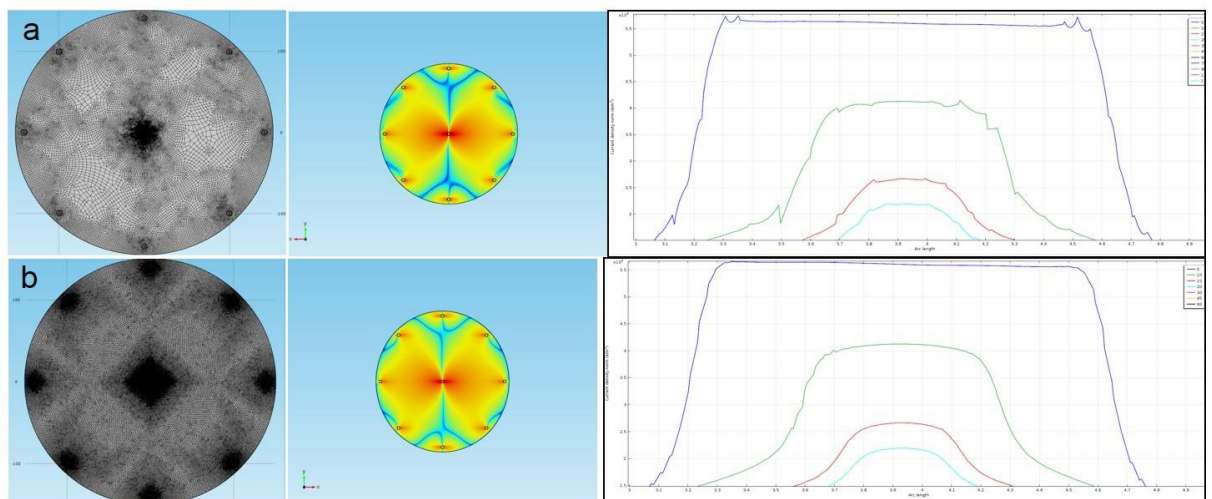


Figure 3-6. Comparison between two meshing method: row a) quadrilateral base prism, 2D plot, 1D plot; row b) triangular base prism, 2D plot, 1D plot.

3.4 Effects of grounding arrangement on current distribution:

Simulation results

Several aspects of the simulation were investigated in this work. Due to the parametric simulations on two variables of the model, the grounding system and the interlaminar conductivity, a huge amount of data was acquired; therefore, in this thesis, only the most relevant results and comparisons have been reported.

3.4.1 Current density distribution in plane

The current distribution was analysed for each of the four plies of the sample, for each of the grounding systems, and for each of the four values of interlaminar conductivity. Figure 3-7 shows the results for ply 0° for all the grounding systems and for two interlaminar conductivity values: 0.01 S/m in Row A and 100 S/m in Row B.

The highest and the lowest values are shown in order to emphasise how the interlaminar layer influences the current distribution. Considering Row A, it can be clearly seen that the current flows along the direction of the fibres for all the grounding arrangements. The presence of a symmetry line of the current distribution that is in the opposite direction of the fibres can confirm the symmetry of the distribution. For the $2f - 4f - 8f$ scenarios, the current flow is enhanced in a strip between the injection fastener and the fastener pair aligned with the 0° oriented ply. Most of the current within the ply is, thus, collected by that fastener pair. This effect is attributed to two main reasons: (a) the lowest resistivity of the ply is in the 0° direction, and the current does not need to flow in a transverse direction to reach the ground, and (b) the high electrical insulation between plies does not allow the current to flow between them.

Scenario *8f rotated* was investigated to restrict current flow, thus avoiding the low conductivity path along the fibre direction in all plies. The aim was to obtain a more homogenous distribution of the current, but a comparatively highly resistive path. From the computed pattern, it can be seen that the high current density strip is still present, but the magnitude is reduced. The current tends to spread to reach the ground, and all the grounding fasteners are involved in sharing the current flow. The side grounding scenario provides a smoother current distribution compared with other scenarios.

Row B shows the case of the interlaminar conductivity being equal to the transverse conductivity (100 S/m). In this case, the current still flows in the direction of the fibres, thus maintaining the symmetry, but it can also flow through the thickness direction more than in case of Row A. This leads to an improvement in the current distribution within each ply for all the grounding configurations.

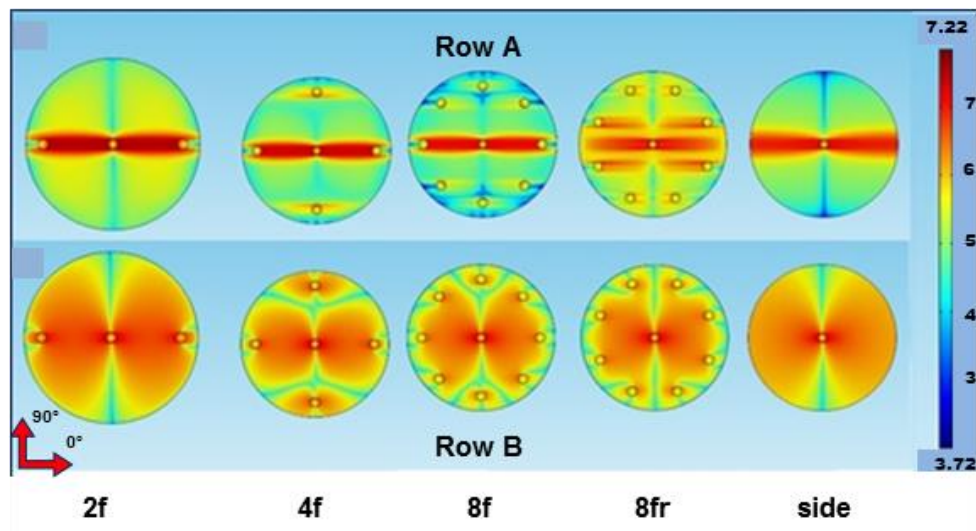


Figure 3-7. Current density distribution within ply 0° for five grounding scenarios: A) 0.01 S/m ; B) 100 S/m interlaminar conductivity.

The analysis of the other three plies of the test panel brought to light the following: in scenarios *8f*, *8f rotated* and *side* grounding, the current density distributions within plies 90° , 135° and 45° are similar to those of ply 0° but are rotated with the equivalent angles of the plies (Figure 3-8). In scenario *2f*, the other three plies did not have a pair of grounding fasteners aligned with them, which means that the grounding system is not matched with the entire panel, but just with one ply. In this case, the current of those plies flows in the transverse directions to reach the ground fasteners. For the scenario *4f*, the grounding system is matched with both ply 0° and ply 90° . The current distribution is similar, but is rotated just for those two plies exhibiting similar patterns as in the previous case.

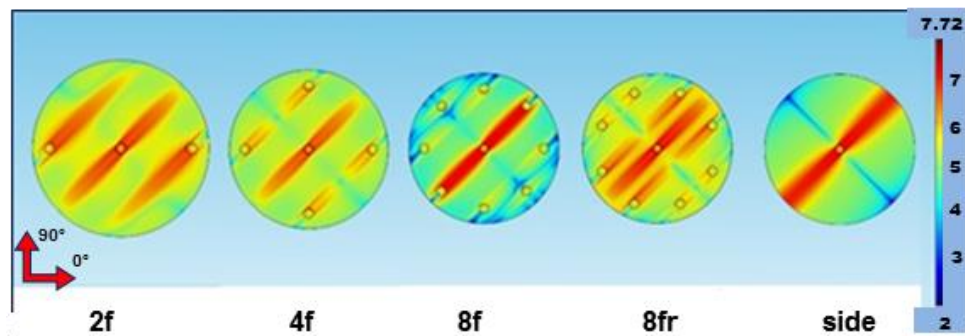


Figure 3-8. Current density distribution within ply 45° for five grounding scenarios and 0.01 S/m interlaminar conductivity [48].

3.4.2 Current distribution along circular cross sections

In addition to a visual qualitative analysis of the current distribution, a quantitative analysis was carried out in accordance with the results. In order to perform these analyses, it was necessary to design a virtual cross section within the sample to evaluate the results in a quantitative manner.

A set of seven virtual circular concentric cross sections were used to evaluate the current distribution at different distances from the injection fastener. Each

cross section comprises all four plies of the sample; Figure 3-9 shows one of them. The circular cross sections have radii of 5, 10, 15, 20, 25, 35, and 45 mm.

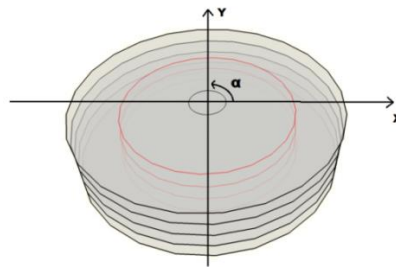


Figure 3-9. Circular cross section (red lines) for circular CFRP sample made by a stack of four plies [50].

The results of the current density evaluation for the side grounding case, for the circular cross section located at a 5 mm radius from the central fastener, are shown in Figure 3-10. As mentioned previously, the cross section comprises all four plies, which means it is made by a stack of four circular lines. The current density was evaluated along each line. As can be seen, the four waveforms have a periodic trend, and this is due to the symmetry of the current distribution. The current density reaches a magnitude of the order of $10^7 A/m^2$ along the direction of the fibres, and the trapezoidal shape of the plots is a reflection of the higher conductivity along the fibres within each ply. Conversely, in the opposite direction, a decrease of two orders of magnitude is noticeable.

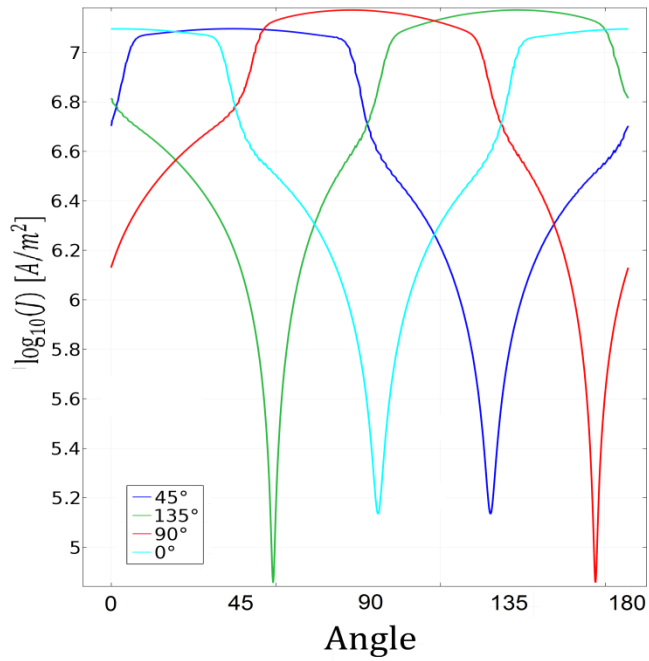


Figure 3-10. Current density evaluation on cross section at 5 mm radius for all the four plies of the sample, for a side grounding system with 2.4 S/m interlaminar conductivity [50].

Analysing the current density on the circular cross sections with larger radii of ply 45°, in Figure 3-11, the periodic behaviour is still present, but the amplitude of the waveforms is reduced, as the current spreads and disperses over a larger volume, hence, decreasing the average current density.

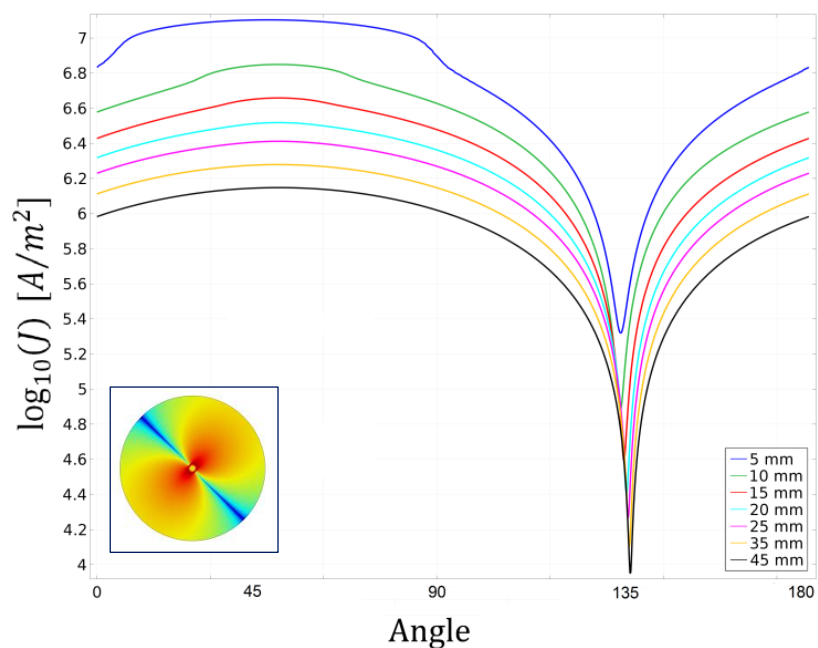


Figure 3-11. Current density evaluation for seven concentric cross sections in ply 45° for side grounding arrangement and 2.4 S/m interlaminar conductivity [50].

The same results for the 8-fasteners ($8f$) grounding system are shown in Figure 3-12. The yellow line represents the current density at a radius of 35 mm , which means it is very close to the grounding fasteners. It is clear that very close to the grounding fasteners, the current density is enhanced.

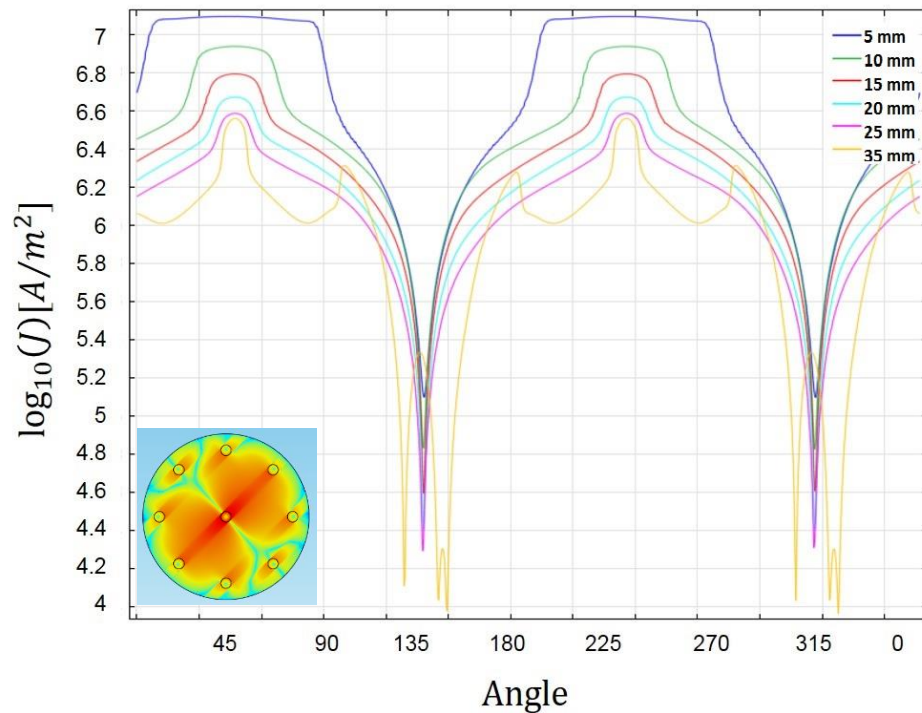


Figure 3-12. Current density evaluation for seven concentric cross sections in ply 45° for $8f$ grounding arrangement and 2.4 S/m interlaminar conductivity.

3.4.3 Peak of the current density squared

Another quantity extrapolated from the results of the simulations was the square of the current density, J^2 . The energy dissipation through the Joule effect is related with the square of the current density. This means that the increase in current density results in the quadratic increment of the dissipated energy. Excessive heating can lead to hazards, especially at the interface between the fasteners and the panel. Phenomena like overpressure, melting, and sparking,

are the main but not the only effects due to the high level of heating caused by the Joule effect. These kinds of threat must be avoided or, if they not avoidable, must be controlled during the flow of the current. Therefore, the peak of square current density was analysed for each grounding system. Furthermore, a comparison between the five cases was reported as well.

Figure 3-13 shows the peak of the current density squared, ply by ply, for all the grounding systems for interlaminar impedance of $2.4 S/m$. The *side* grounding system, Figure 3-13a, reveals that the most critical zones of the sample are in the two middle plies, 135° and 90° , close to the injection fastener. Moving from the centre, the current is distributed equally within the four plies, and the magnitude of the peak decreases exponentially in all four plies.

The *8-fasteners (8f)*, Figure 3-13b and *8-fasteners rotated (8f r)* case, Figure 3-13c, show a similar trend to the *side grounding* case except for the magnitude of the peak close to the grounding fasteners, which is respectively 80% and 50% higher than the *side* case.

The *4-fasteners* case, Figure 3-13d, also shows a similar trend to the first three cases close to the injection fastener. However, close to the grounding fasteners, there is an increase in the peak magnitude in the 0° and 90° plies. In this sample, the two fastener pairs are aligned with the 0° and 90° directions, creating the higher conductivity paths along ply 0° and ply 90° , as explained previously. Part of the current in ply 45° and ply 135° moves to the other two plies because of the lower resistive path resulting in greater peak magnitude. The magnitude of the peak is higher than the first three cases for all the plies because the number of collecting fasteners is reduced from eight to four.

In the 2-fasteners (2f) case, Figure 3-13e, there is just one pair of fasteners, aligned with the 0° direction. It means that there is a highly conductive path, between the injection point and the grounding, just in ply 0° . Again, close to the injection point, the higher peaks are within the two middle plies, whereas, very close to the grounding fasteners, the peak rises critically within ply 0° because it is the only ply with a grounding fastener pair aligned. Conversely, the 90° ply shows the lowest current peak.

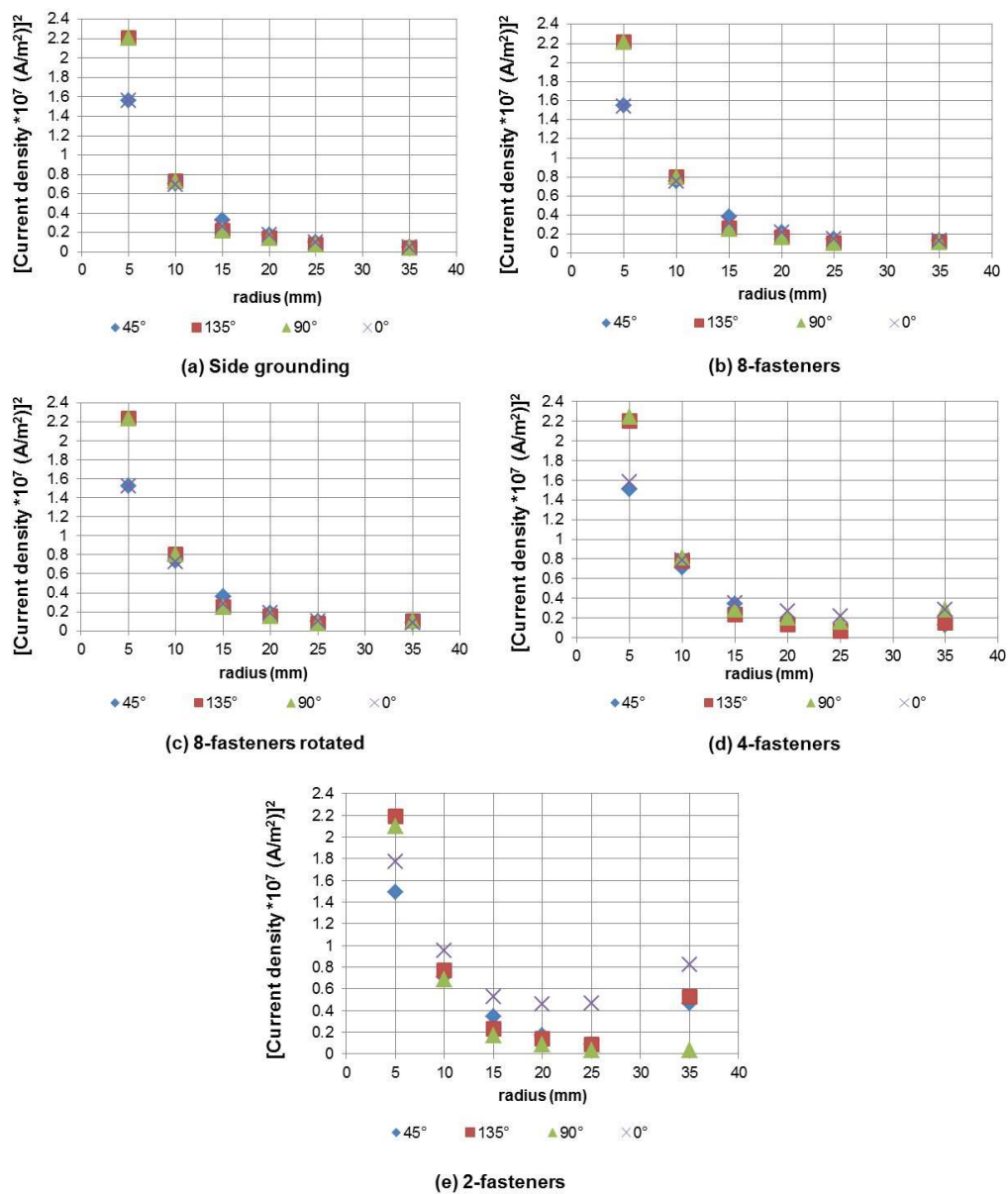


Figure 3-13. Highest current density squared in the four plies at 2.4 S/m interlaminar conductivity, for grounding.

In order to compare the performance of the different grounding systems, the *side* grounding was considered as the reference, and the peak values were normalized accordingly.

Figure 3-14 shows the normalized peak current density squared in the four plies of the sample for the interlaminar impedance of 2.4 S/m . Close to the injection point, all grounding arrangements show similar performances. Close to the edge of the sample, all fastener grounding systems produce an increase in the peak current density. The *8-fasteners rotated (8f r)* case shows the closest performance to the *side* case. That is because the rotation of the eight fasteners avoids the creation of low resistive paths where the current can flow with the consequence of the increase of the magnitude. The *2-fasteners (2f)* case performs the worst because the peak current density squared near the grounding system is nearly ten times that of the *side* case.

The peak magnitudes of ply 135° and ply 45° are comparable except for the magnitude at the radius of 35 mm .

In ply 90° , the current magnitude for the *2-fasteners (2f)* case is lower than for the *side* case. As described previously, in the *2-fasteners (2f)* configuration, the current has to flow along the 0° direction to reach the ground. In ply 90° , the 0° direction is the direction with the highest resistance; therefore, the current flows in the through thickness to the underneath ply 0° , where it finds the direct low resistive path between injection and collecting points. Furthermore, the ply 90° is subjected to the highest magnitude when a *4-fasteners (4f)* system is used due to the presence of a fastener pair aligned with it.

Confirmation of what was observed with the *2-fasteners (2f)* configuration can be seen in the graphs of ply 0° where the peak of the *2-fasteners (2f)* case is the highest.

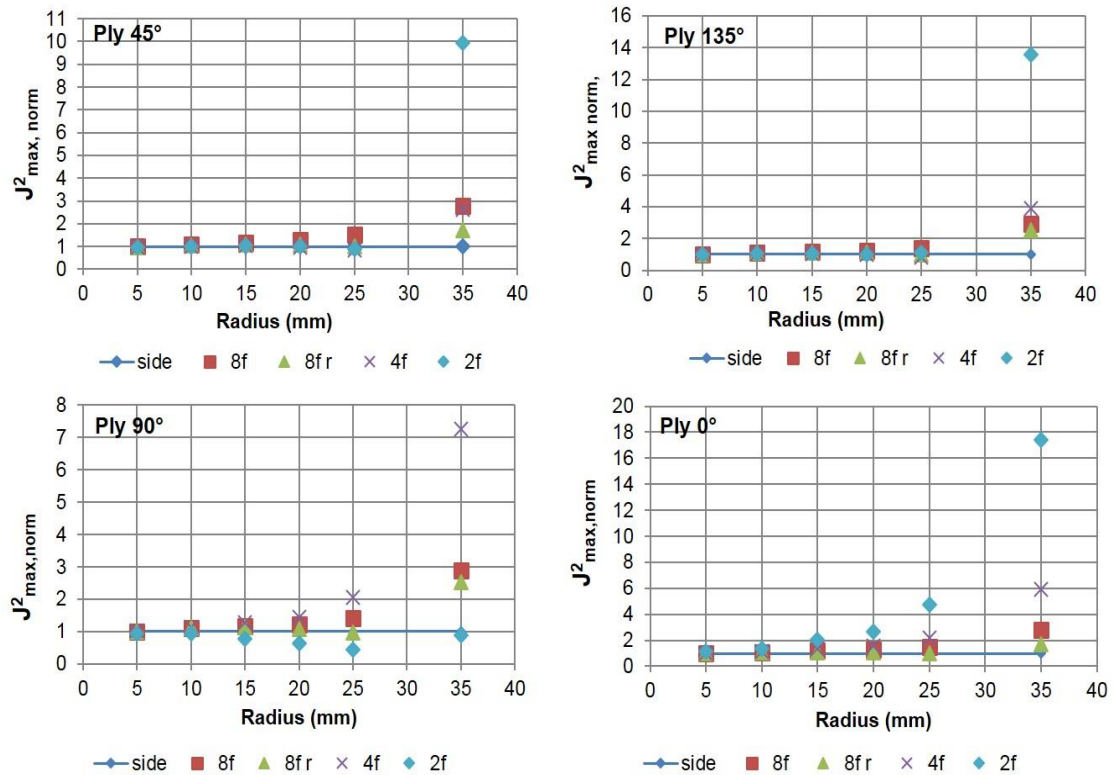


Figure 3-14. Comparison of normalized peak current density squared for the five grounding systems in the four plies of the sample at $2.4 S/m$ interlaminar conductivity.

Although ply 0° with the *2-fasteners (2f)* grounding arrangement has the worst performance, it is worth noting that close to the grounding system, the current density and, consequently, the dissipated energy are considerably reduced compared with the injection fastener (see Figure 3-13). Hence, the risk of damage is reduced as well.

Considering all four plies, the best overall performance in terms of keeping the peak of current density as low as possible is obtained by the *side grounding* system.

3.4.4 Voltage drop

The voltage drop is an indication of the terminal resistance of the sample. It was calculated between the injection fastener and the grounding system, which was considered to be always at 0 V .

Figure 3-15 shows the results of the voltage drops for the five different grounding systems and for the four different levels of interlaminar conductivity. All the grounding configurations show an increase in the voltage drop with the decrease in the interlaminar conductivity. It is thought that the interlaminar conductivity influences the voltage drop in two ways: it modifies the material properties of the sample because of the higher average material resistivity, and it forces the current to flow in highly resistive paths within the panel to reach the ground if no fastener pairs are aligned with the fibres. For higher conductivities ($100 - 2.4\text{ S/m}$), the voltage drop is independent from all the grounding arrangements, except for the *2-fasteners* case. Higher interlaminar conductivities allow the current to move freely across plies and flow through high conductivity paths within the sample. In this scenario, the grounding system does not influence appreciably the current path, and the voltage drop appears lower.

The cases *2f*, *4f*, *8f* show a decrease in voltage drop for lower conductivities ($0.1 - 0.01\text{ S/m}$) and with an increase in the number of fasteners. In these first three cases, each fastener pair is aligned with the main directions of the plies, which corresponds to highly conductive paths between the injection fastener and the grounding fasteners. In the *2-fasteners* case, the high conductivity path is in ply 0° , and the current injected in that ply flows through a low resistance path. However, in the other three plies, the current must spread in the

transverse direction of the fibres to reach the grounding point, which results in a higher voltage drop. In the *4-fasteners* case, there are two HCPs (Highly Conductive Path), that is, one in ply 0° and the other in ply 90° , and this leads to a reduction in the voltage drop. In the *8-fasteners* case, there is an HCP in each ply allowing the current in each ply to flow through a low resistance path resulting in the lowest voltage drop between the three cases being compared. Increasing the number of grounding fasteners, aligned with the plies, means the injected current flows in a greater number of low resistance paths, and this contributes to a decrease in the total voltage drop.

The *side* grounding scenario shows a voltage drop magnitude that is close to that of the *8-fasteners* case except for the 0.01 S/m conductivity case where the voltage drop of the *side* grounding is slightly higher (13% higher). For both cases, the current can flow through low resistance paths within all plies, but the difference in voltage drop can be found by analysing the length of the current paths. In the *8f* grounding case, the gap between the injection and the grounding fasteners is less than 40 mm , whereas in the *side* grounding arrangement, it is 50 mm from the central fastener to the side. The increase of 35% of that length can be related to the increase of the voltage drop for the *side* grounding system. The *8f-rotated* case was designed to avoid high conductivity paths and enhance the spreading of the current in the transverse direction of the fibres. In this case, the 0.01 S/m conductivity shows the highest voltage drop, as the current cannot move just in the direction of the fibres, and it cannot flow between plies. To reach the grounding fasteners, the current must flow in the transverse direction where it encounters higher resistivity paths, thus resulting in a higher voltage drop.

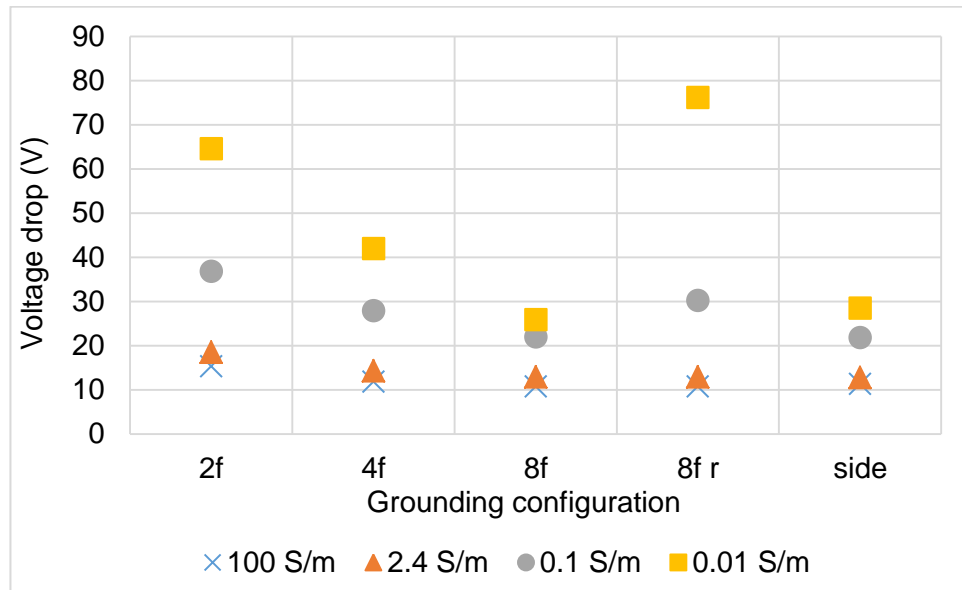


Figure 3-15. Voltage drop between the samples terminal for five grounding systems and four interlaminar conductivities.

The validation of the numerical results reported in this section can be found in section 6.7.6

3.4.5 Power dissipation

The grounding configuration had an impact on the power dissipated by resistive heating within the sample. The losses depend on the resistance of the laminate, and as has been already described, the resistance of the sample depends on both the current path and the electrical conductivity of the material. As can be seen in Figure 3-16, the grounding arrangements drive the current to move through paths with different levels of conductivity, which leads to different degrees of power dissipation. The graph in Figure 3-16 shows the power dissipation for all five grounding systems considering the interlaminar conductivity of 2.4 S/m. The samples with *side*, *8-fasteners* and *8-fasteners rotated* grounding systems dissipate approximately the same power. The

slightly lower power dissipation for the *8-fasteners* and *8-fasteners rotated* is due to the fact that part of the CFRP, the 17.2%, was removed to make room for the metal fasteners, which are less resistive compared to the CFRP. The *2-fasteners* system gives the highest power dissipation.

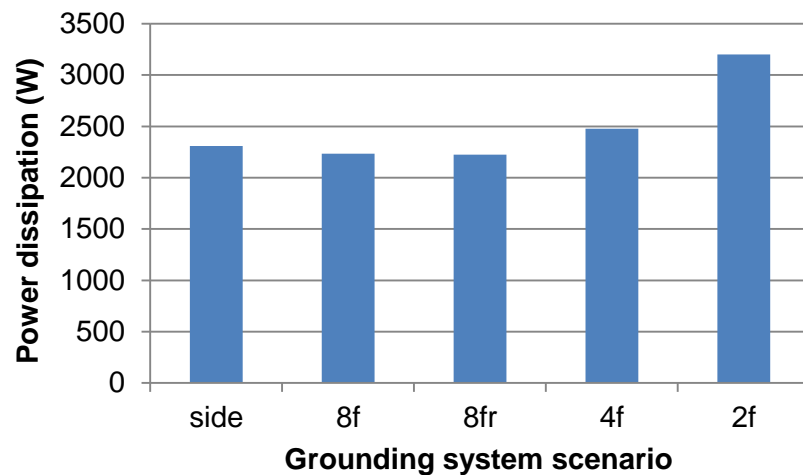


Figure 3-16. Power dissipation for different grounding arrangements at 2.4 S/m interlaminar conductivity [50].

3.5 Conclusion

The simulations carried out in the first step of this project have analysed the effects of the interlaminar conductivity and the grounding system on the electrical parameters of a CFRP panel.

It can be seen that the interlaminar conductivity plays a basic role in the current distribution within the laminate sample. Lower values of conductivity contribute to the decrease in the overall conductivity of the laminate. Furthermore, they prevent the current from flowing through low resistive paths within the sample and in the through-thickness direction. The consequence of this is a higher voltage drop between the sample terminal and a higher power dissipation.

Five different grounding systems were analysed, and according to the results, the side grounding arrangement can be considered the 'ideal' grounding because it allows the current to flow through the sample freely, similar to a larger sample, and there is no influence from fasteners. Conversely, it could be seen that the fastener arrangements influence the current distribution within the plies of the sample. The results have revealed that the increase of the fastener pairs improves the current distribution with the advantage of showing a similar performance to that of the side grounding. In addition, the position of the fastener pairs has a strong influence. Aligning the fasteners with the fibres reduces the current distribution by introducing low resistance paths. The fastener grounding arrangements require that each sample is drilled in order to install the grounding fasteners.

It has been shown that the influence of the grounding system depends on the interlaminar conductivity of the CFRP. The simulations have shown that higher interlaminar conductivity values allow a better current flow through the thickness of the panel, improving the current distribution within the test panel. Higher values of interlaminar conductivity have contributed to reducing the average resistance of the panel, leading to a lower voltage drop between the injection fastener and the grounding system. In addition, higher interlaminar conductivities were shown to help the current flow in lower resistivity paths, leading to a further reduction in the voltage drop. For higher interlaminar conductivity values, the change in grounding scenarios does not appreciably affect the current distribution.

The results of the numerical simulation campaign have been useful for predicting the current distribution within the CFRP samples that were used for

the experimental campaigns. The applications of the model are not only related to this project, but also, they can be used as background for future investigations on specific subjects, such as the high conductivity path within laminates. In this case, the *8-fasteners* grounding system can be the best choice. Conversely, if the high current paths are to be avoided during experiments, the *side* grounding or the *8-fasteners rotated* systems can be a valid alternative. The *4-fasteners* and *2-fasteners* arrangements can be considered to offer a more cost effective solution with the disadvantage of less current spreading within the ply and a higher voltage drop, which can lead to a higher power dissipation through the Joule effect.

Chapter 4

Effect of pressure on CFRP-Metal contact resistance

4.1 Introduction

The purpose of this investigation is to analyse and compare the effects of the grounding arrangement on the electrical resistance measured over the grounding system in a CFRP test sample. The results can be used to identify alternative grounding arrangements that allow for the manufacturing of more cost effective test samples. The grounding system is a part of the circuit which ensures the electrical connection of the sample with the return current part of the circuit. It allows for the drain of the current that is injected within the sample, and it must be able to sustain the quantity of energy delivered to the sample without damaging itself, the test sample or the current generator. For some experimental set ups, the grounding system also acts like a mechanical structure that keeps the sample firm on the test rig, so it has a double use as shown in Figure 4-1.

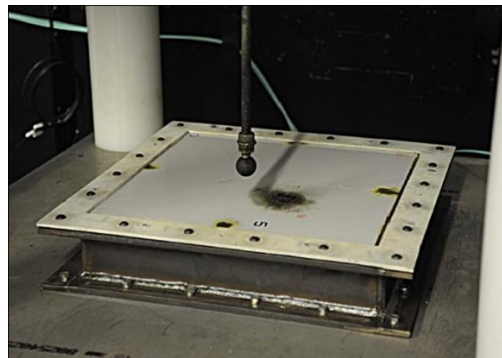


Figure 4-1. Test rig for lightning strike test: square CFRP sample screwed to the metal frame of the rig. The fasteners at the perimeter of the sample act as electrical grounding as well as mechanical fixing with the rig.

4.2 The contact resistance

In order to compare the performances of the different grounding systems, a comparison was made between the electrical resistance measured between the injection point of the sample and the grounding system. Taking into account that all the CFRP samples are made of the same materials and have the same geometry, it is possible to assume that they have the same resistance. Thus, variations in the measured electrical resistance are due to variations in the electrical resistance associated with the grounding arrangement. Low values of resistance are associated with good mechanical contact between the sample and the grounding with the advantage of low energy dissipation in the form of Joule heating and a decreased probability of damage. Conversely, higher values of resistance mean poorer mechanical contact, more energy dissipated due to the Joule effect, and therefore, a higher risk of damaging the ground system and/or the sample.

4.2.1 Contact resistance and surface topography

According to Holm [47], the contact resistance depends on the topographic characteristics of the area that is between the two elements of the contact which are defined as contact members. In turn, the contact area depends on the force that presses the two contact members together. Furthermore, Holm [47] found a relation that links the pressure with the contact resistance. Although the studies carried out by Holm mostly refer to the contact between homogenous metal materials, they have been a useful guide to understanding the mechanism of the creation of the contact resistance. In this work, the effect of the contact force on the electrical resistance in the case of the side grounding system was

analysed. A brief summary of some of Holm's outcomes is given in the next paragraph to provide a clearer understanding of the link between the contact resistance and the applied load.

According to Holm [47], when two homogenous metal materials are in contact, they form a contact surface, which is called *apparent contact surface* A_a because not all the area of one metal is in contact with the second. Ideally, if the two metals are infinitely hard, any pressure applied to the contact surface will bring the two metals in touch at no more than three points. In reality, every material is deformable, with the consequence that increasing the applied force causes the contact spots to become small areas and, simultaneously, new contact points may set in. The sum of all of these contact areas and spots is defined as the *load bearing area* A_b . Those load bearing areas can be created by elastic deformations, but most of the time, they develop from plastic deformations (Figure 4-2).

From the electrical point of view, the *load bearing area* can be divided into three main zones: a zone which is not conductive because it is covered by *thick films* of oxides or sulphides, and which in Figure 4-2 is represented by the white dots area; a second zone, which is electrically conductive, that is, a metallic contact which does not create a perceptible contact resistance, and which in Figure 4-2 is represented by the plain area; and the last zone, which can be defined as a quasi-metallic contact because it is covered by films that are thin enough for an electron current to pass through by means of the tunnel effect, and which in Figure 4-2 is represented by the hatched area.

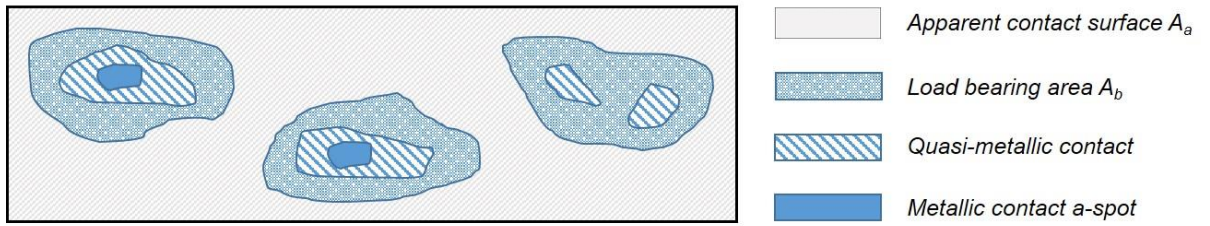


Figure 4-2. Contact surface (not to scale).

The relation between the applied load and the *load bearing area* A_b is described by the following equation:

$$P = \xi H A_b \quad (4.1)$$

where $0.2 < \xi < 1$ the pressure factor, and H is the “contact hardness”.

The current that passes across the contact surface is constricted to flow through the conductive areas creating a resistance, which is called *constriction resistance*. In Figure 4-3, the current flow is represented by parallel lines inside the materials, which have resistance R_m . Due to the conductive spots, the lines are deviated, which results in the formation of the constriction resistance R_s .

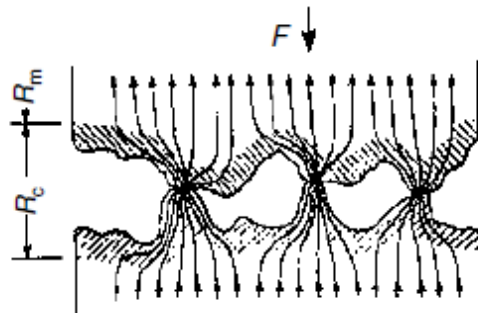


Figure 4-3. Constriction resistance [52].

In reference [47], the constriction resistance for a single a-spot is expressed as

$$R_s = (\rho_1 + \rho_2)/4a \quad (4.2)$$

where ρ_x is the electrical resistivity of the two materials in contact whereas a is the radius of the a-spots, which are supposedly circular. In the case that the current passes through thin films of oxide, sulphide, or other inorganic films, this resistance must be considered as well as in the final results.

$$R_c = R_s + R_f \quad (4.3)$$

$$R_f = \sigma / \pi a^2 \quad (4.4)$$

where σ is the resistance per unit area of the film.

As said previously, the applied load contributes to the expansion of the load bearing area, which leads to a decrease in the contact resistance R_c . The resistance is linked with the applied load in the range $0.1 < P < 100 \text{ N}$ through the Eq. (4.5) [47],

$$R_c = \frac{\rho_1 + \rho_2}{2} \sqrt{\frac{H}{P}} \quad (4.5)$$

which underlines that the contact resistance R_c is proportional to $1/\sqrt{P}$.

4.2.2 Contact resistance for metal to metal contact in large parts.

When large parts of metals are in contact, where for large parts are intended parts whose dimensions are several orders of magnitude greater than the contact spot dimensions, it is of interest the evaluation of the contact resistance variation in respect of the applied load in comparison to the previous situation where the study was carried out on a single spot. One of the issues related to the determination of the contact resistance for large surfaces in contact is the determination of the real contact area. Such a study can be carried out starting

from the measurement of the contact conductivity. One of the methods proposed in the literature to estimate the contact resistance, in analytical way, for large parts in contact is based on the random fields approach [52]. Braunovic et al. report a comparison between the calculated curve and a set values measured in an experiment. The first results showed that the contact resistance trend is dependent from the type of deformation of the material: elastic deformation or plastic deformation. Figure 4-4 shows the calculation, using the random field approach, of the contact resistance for the case of elastic contact and plastic contact of two silver specimens (the use of silver, that is a noble metal, derives from the desire to reduce at the minimum the deposition of oxidation films on the contact surfaces with a cylindrical shape that are in contact through the bases that have a diameter of 3 mm . The length of the cylinder was of 10 mm . Each trend refers to a different specimen whose characteristics are reported in Table 4-1. The relative contact resistance refers to the ratio between the resistance of the contacting cylinders R_{0+R} and the resistance of the solid cylinder R_0

$$R^* = \frac{R_0 + R}{R_0} \quad (4.6)$$

The results show how the elastic contacts are more affected by variation of roughness compare to the plastic contacts. Indeed for the elastic contacts trends are more dispersed compare to the plastic contacts trends.

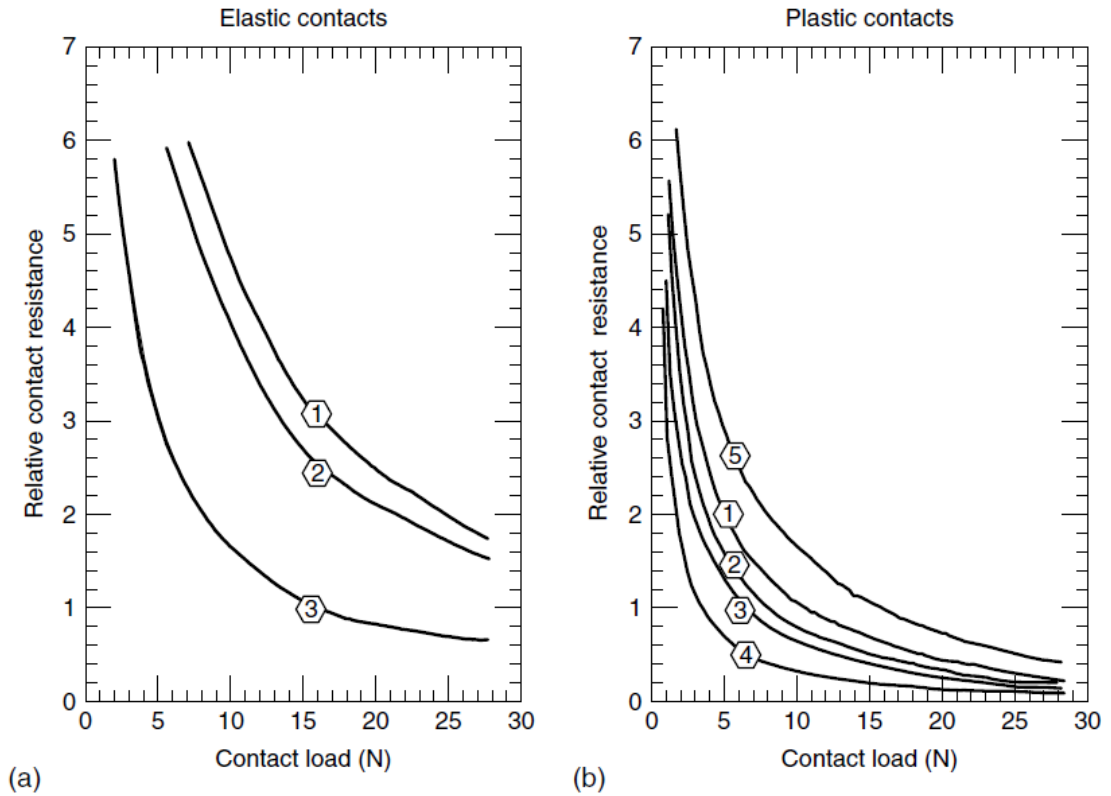


Figure 4-4: Relative contact resistance for: a) Elastic contacts and b) Plastic contacts [52]

Table 4-1: Surface-Roughness Parameters and mechanical Characteristics of Silver Specimens [52]

Specimen Number	R_a (μm)	R_z (μm)	m_0 (μm^2)	m_2	m_4 (μm^{-4})	α	q_m (MPa)	Specimen Preparation
1	1.5	6.7	3.7	0.023	9.7×10^{-4}	6.8	800	Polishing with abrasive paper
2	1.3	5.9	2.7	0.023	9.2×10^{-4}	4.7	800	The same
3	0.4	2.0	0.29	0.0013	6.1×10^{-5}	10.5	500	Annealing at 973 K in vacuum, polishing with felt and one loading cycle
4	1.5	6.7	3.7	0.023	9.7×10^{-4}	6.8	250	—*
5	1.5	6.7	3.7	0.023	9.7×10^{-4}	6.8	1000	—*
6	1.3	5.9	2.7	0.023	9.2×10^{-4}	4.7	1000	Polishing with abrasive paper and 10 loading cycles

*Note: For specimens 4 and 5 the calculation was made only for the smallest and largest hardness values.

A further comparison was performed between the results of the experiment carried out on the silver cylinder and the results of the analytical model are reported in Figure 4-5. In this case a least square method was used to conduct a qualitative analysis of both calculated and experimental results.

For this comparison the resistance trend was approximated to the following equation:

$$R^* = cN^{-d} \quad (4.7)$$

The results show that for the cases elastic contact where both the contact spot area and the number of spots are increasing with the increase of load it is common to accept values of d near to $2/3$. Instead, in the case of plastic deformation where the number of contact spots practically does not increase but it is only the contact area that grows, the value of d is supposed to be close to 0.5 . This results is similar to the one found by Holm where the load applied P is powered to -0.5 .

The specimen 6 represents the case where several cycles of compression and decompression (15-20 cycle) and in this case the values of d does not fit the either the elastic nor the plastic deformation trend and it is far from the calculated trend. Therefore, for this specific trend it can be concluded that the work cycle affects both the plastic and elastic behaviour of the surfaces in contact.

Conversely, for the specimen number where work cycles were less than specimen 6 it is possible to notice a good agreement between the calculation and the experiment for the value d .

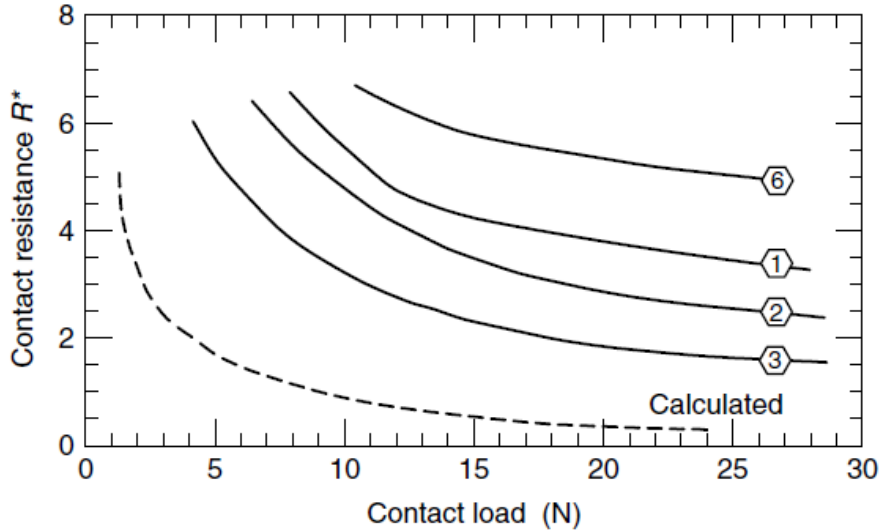


Figure 4-5: Experimental contact resistance data and calculation results (dashed line) for silver specimen. Numerals on the curves correspond to specimens reported in Table 4-2 [52]

Table 4-2: power factor d in the function approximating the calculated and test data. [52]

1–30 N, Correlation Coefficients > 0.95)

Specimen Number	d		Contact Mode in Calculation Scheme
	Calculation	Experiment	
1	0.50	0.53	Plastic
2	0.46	0.43	Plastic
3	0.46	0.46	Plastic
6	0.72	0.59	Elastic
	0.46		Plastic

It can be concluded that for large metal to metal contacts, the contact resistance trend for contacts that exhibit plastic deformation has a similar behaviour compare to the Holm's law for the single contact spot.

4.2.3 Simplified scenario of a metal - CFRP contact surface

Section 4.2.1 has been included in the chapter to give the reader a basic understanding of contact resistance and its relation to the applied pressure. When referring to this experiment, the metal electrode of the side grounding arrangement in touch with the edge of the sample creates a contact resistance.

However, it must be clarified that when the metal electrode is directly in touch with the CFRP sample side, it is not possible to apply Holm's equations because the second member of the contact is a composite non-homogenous material in contrast with Holm's statement.

Instead, when a CFRP is in contact with a homogenous material, considering a simplified scenario, the following may occur: the CFRP member comprises two materials, namely, matrix and fibres, which can be in touch with the metal member. The matrix is almost non-conductive whereas the carbon fibres, having larger electrical conductivity compared to the matrix, carry the current flowing through the interface. Usually, the fibres within a CFRP are distributed in plies, and within a ply, all fibres run in the same direction. In turn, that direction might be equal for all the plies of the stack or might not be, depending on the mechanical requirement of the laminate. Therefore, the *load bearing area*, A_b , in those situations can be formed by the following:

- matrix - metal contact
- fibres - metal contact
- both matrix and fibres in contact with the metal

Only the last two scenarios allow for the conduction of the current. Regarding the fibres, they might be oriented so that they are perpendicular, parallel or incident with a specific angle to the contact surface (Figure 4-6).

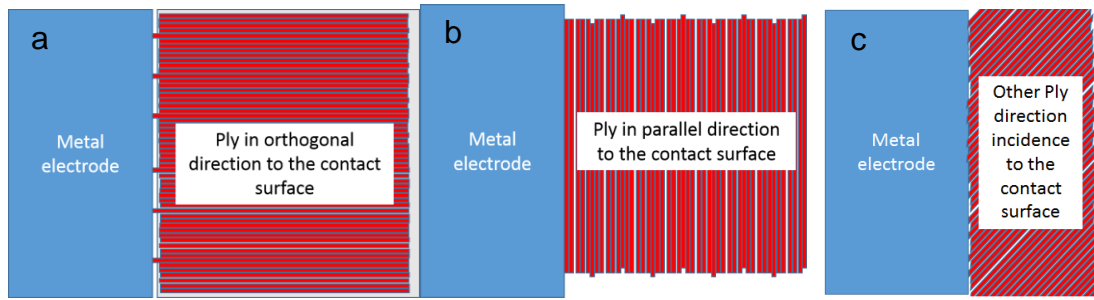


Figure 4-6. Contact between homogenous metal material and laminate composite material: a) ply oriented orthogonally to the contact surface, b) ply oriented parallel to the contact surface, c) ply oriented with a specified angle to the contact surface.

Commonly, in laminates for aerospace applications, the plies within the laminate are oriented to achieve a quasi-isotropic panel. Thus, the plies approach the contact surface at a different angle, usually 0° , 90° , 45° , 135° .

4.2.4 Factors which influence the contact resistance R_c

Due to Joule effects the current that flows through the contact surface releases an amount of energy equal to the following:

$$E = \int Ri^2(t)dt \quad (4.8)$$

which contributes to increasing the temperature at the contact surface. The temperature can rise to the level at which the grounding system and/or the sample can be damaged due to burning or melting of the surfaces. Moreover, the roughness of the surfaces in contact creates voids; this increases the probability of sparking between the surfaces due to the high voltage gradient with the consequence of overpressure and the expulsion of molten debris, a phenomenon identifiable as *outgassing* (a more exhaustive description of the *outgassing* phenomenon is given in section 6.3).

Equation (4.7) shows that the energy dissipated is also proportional to the contact resistance. Thus, by controlling the contact resistance, it is possible to

control the energy dissipated into the contact, for a given current waveform. In this work, the contact resistance was varied using three different approaches:

- the load pressure approach
- the materials approach
- the contact surface topography approach

The test campaign was designed to take into account variations of all the three factors.

The load pressure was controlled using a test rig that is able to vary the load in the range *600* to *3900 N*. At the same time, the test rig ensures the flow of the current within the sample (Figure 4-7). For a more detailed description of the test rig, please refer to the section 4.3.

The test rig is not required when the samples with the fasteners grounding arrangement are tested.

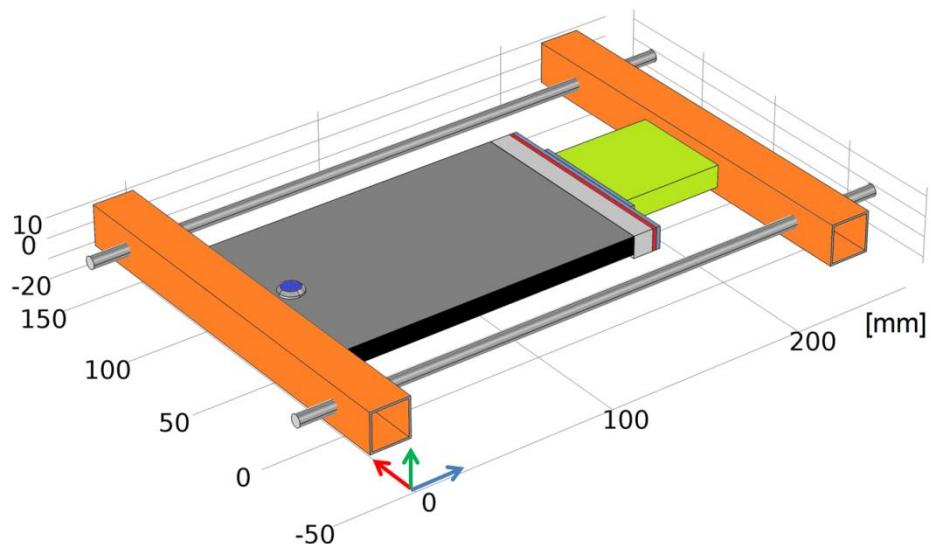


Figure 4-7. 3D draft of the test rig included the CFRP sample.

The second factor taken into account is the materials that create the contact surface. For all the experiments, the electrode used to collect the current flowing within the sample was made of aluminium (Figure 4-16) while the second member of the contact was varied. Specifically, the following contact scenarios were considered:

- CFRP – aluminium
- silver paint layer – aluminium
- metal sputtered layer – aluminium

The third factor taken into account for the study of the contact resistance is the topography of the surfaces that create the contact. According to [47], when real contact surfaces are investigated, it must be considered that a real surface deviates from an ideal totally flat surface because during the manufacturing and subsequent use of the surface, asperities appear, and those depend on several factors, which can be attributable to manufacture, operation, and structure.

The asperities can vary in height (amplitude) from a nanometre scale to a millimetre scale. Furthermore, the asperities are distributed along the contact surface, and the spacing parameter can have an even wider range than that of the amplitude. Nevertheless, a good method to investigate the topography of the surface is to divide the asperities into four main groups (Figure 4-8):

- *Errors in form*, which are defined as deviation of the real surface from the original geometry with spacing in the range of $S = 1-5,000 \text{ mm}$ and height in the range of $\Delta = 1-50 \text{ }\mu\text{m}$. As a general rule, it can be considered that $\Delta/S \leq 0.001$.

- *Waviness*, which refers to asperities with spacing in the range of $S_w = 0.810 \text{ mm}$ and height in the range of $R_w = 0.01\text{-}500 \mu\text{m}$.
- *Roughness*, which is defined as surface microrelief. It is usually measured using the assessment length l (Figure 4-9).
- *Sub-roughness*, which is related to the physical structure of the surface. It takes into account the imperfections of the crystallographic planes.

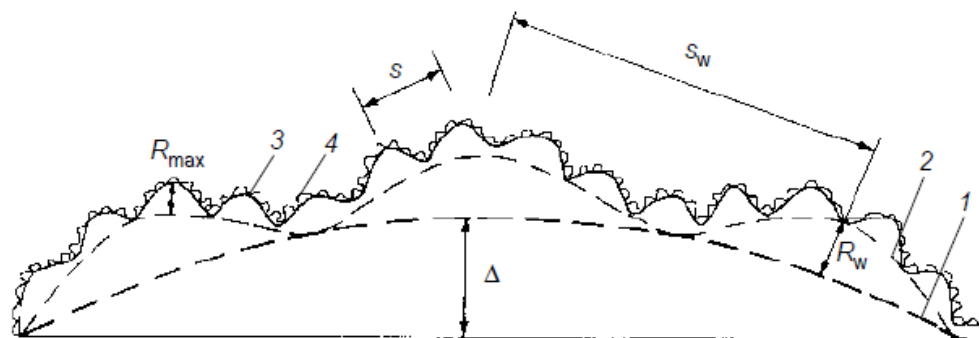


Figure 4-8. Component of surface profile. (1) error in form, (2) waviness, (3) roughness, (4) subroughness, S_w , R_w , waviness spacing and height; S , R_{max} , roughness spacing and height [52].

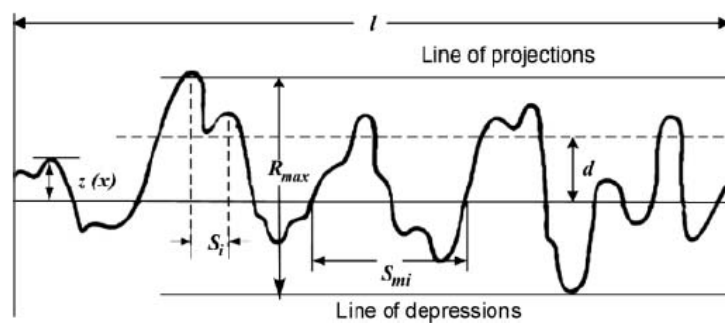


Figure 4-9. Rough surface profile [52].

In order to define the above surface parameters, there is a need to carry out specific measurements that are reported in Chapter 5.

4.2.5 Electrical equivalent of a grounding system under DC excitation

The electrical resistance of the grounding system for DC current excitation can be schematised by a series of several resistances, each of which is associated with a part of the system.

Figure 4-10 shows the parts that contribute to the analysis of the total resistance of the different grounding systems. Considering that R_1 is the resistance of the sample, Figure 4-10a represents the scenario of a fastener grounding system. The resistance is the series of the contact resistance between the sample and the grounding fastener, which can be identified as the shank of the fastener that is in contact with the sample, R_2 , and the resistance of the grounding fastener itself, R_3 . Figure 4-10b represents the scenario of the side grounding system with no highly conductive layer between the sample and the return electrode. R_2 represents the resistance due to the contact interface between the side of the sample and the electrode, whereas R_4 is the resistance of the metal electrode. Figure 4-10c shows the case of a side grounding arrangement where the side of the sample has been covered by a thin film of a high conductive layer with resistance R_5 . R_2 represents the contact resistance between the high conductive layer and the metal electrode, and again, R_4 is the resistance of the return electrode.

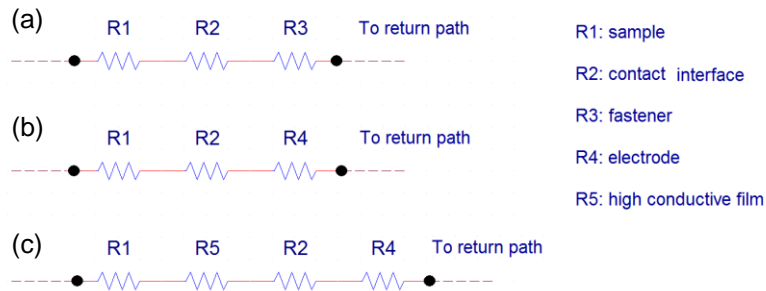


Figure 4-10. Electrical equivalent for DC current excitation of the grounding system: a) fastener grounding system, b) side grounding system, c) side grounding system with a high conductive film between the sample and the electrode.

4.3 The Grounding systems

Two categories of grounding arrangements have been studied: the fasteners grounding arrangement and the side grounding arrangement. Most of the test samples used for the lightning test require a connection with the grounding path of the circuit through metal fasteners distributed at the side of the sample (Figure 4-1). Although the fasteners ensure the flow of current from the panel to the return circuit, they influence the sample costs through the following factors, among others:

- number of fasteners and associated nuts and bolts, required to connect the sample with the grounding system.
- quality of the drilling; according to Liu [53], the anisotropic non homogenous, hard CFRP materials, are difficult to drill compared to conventional metals because the drilling process leads to undesirable damage, such as delamination and fibre pull out among others. At the moment, there are four main processes to drilling composite materials, each with specific characteristics and efficiency and with an associated cost.

- quality of the fastening; an interference fit requires a press to insert the fastener into the hole. The process is less cost effective and more time consuming compared to a classic clearance fit.

The *side grounding* arrangement was developed to simplify the manufacturing process of the sample and to reduce the manufacturing costs. The system allows the current to flow from the sides of the sample, thus avoiding drilling and relative fastening during the manufacture process, which is an advantage in terms of cost and time consumption.

4.3.1 Fastener grounding systems

- *fastener injection – 3-fasteners return*: one fastener is required to inject the current within the sample whereas three fasteners, at the opposite side of the injection, are required to collect the current (Figure 4-11a).

This configuration is used for experiments on the outgassing phenomenon at the interface between the injection fastener and the CFRP sample. The phenomenon under investigation occurs at the interface between the injection fastener and the sample, on the right hand side of the sample (Figure 4-11a), whereas the three fasteners on the left hand side are required for the collection of the current.

- *fastener injection – 1-fastener return* (Figure 4-11b): one fastener is required to inject the current within the sample and one fastener at the opposite side is required to drain the current, therefore, referred to as the grounding fastener. It can be considered a simpler version of the *3-fasteners* grounding arrangement.

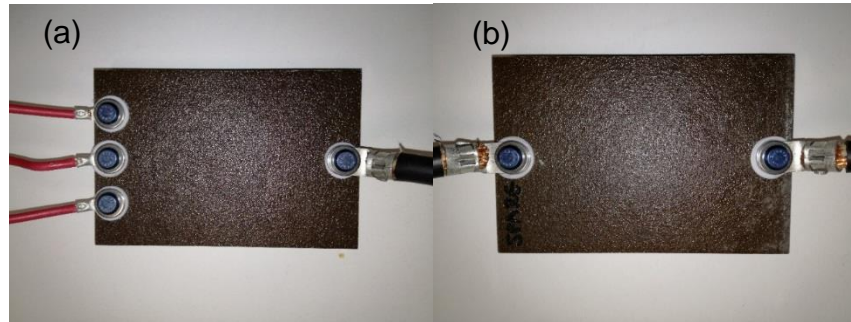


Figure 4-11. a) Return current path of the sample provided with three fasteners, b) return current path with one fastener.

4.3.2 Side grounding systems

- *fastener injection – no-layer return*: one fastener is required to inject the current into the sample. The current is collected through the opposite side of the injection, with no further layer of conducting material added between the sample and the test rig. This scenario considers the aluminium electrode to be directly in contact with the side surface of the CFRP sample. The mechanism of this type of contact has been explained in the previous paragraph. However, this scenario allows for the cutting of the sample, and no medium materials are required between the sample and the electrode. Henceforth, this scenario will be defined as the “*no-layer*” scenario (Figure 4-12a).
- *fastener injection – silver paint return*: one fastener is required to inject the current within the sample. The current is collected through the opposite edge of the injection, which has been covered by a layer of silver paint. In this case, the silver paint layer was manually painted. The silver paint layer is in contact with the metal electrode of the test rig. In this situation, the highly conductive layer creates a short circuit between all the fibres exposed on the sample surface, even the fibres that are not in real contact with the aluminium electrode. This enables a higher percentage of fibres to carry the

current. The benefit of this solution is a reduced contact resistance and an ease in applying the silver paint layer. The disadvantage of this solution is that the silver paint is not able to sustain a level of current density as high as the *metal sputter* solution before damage occurs (Figure 4-12b).

- *fastener injection – metal sputtering return*: one fastener is required to inject the current within the sample. The current flows out of the sample through the opposite side of the injection (the edge furthest from the injection point). In the third scenario, a layer of metal coats the sample side surface. In this work the coating of sample was done through the electric arc wire spray process by the Hexcel Company. The metals used for the metallisation are tin and zinc with a percentage of $70\% \text{ Zn} - 30\% \text{ Sn}$. The thickness of the layer is approximately $70 - 75 \mu\text{m}$. This solution has the same benefit as the silver paint in terms of decreasing the contact resistance, but with the advantage of carrying a higher current density, before damage occurs compared to the silver paint. The disadvantage of this design is that the coating process is more time consuming and more expensive to produce compared to the silver paint process (Figure 4-12c).



Figure 4-12. Contact sides of the samples: a) sample with no coating, b) sample with silver paint coating, c) sample with metal sputter coating.

Each fastener has a nylon nut between its head and the upper surface of the sample. This creates an electrical insulation between the two parts. Using this

solution, the injected current is equally injected within all the plies of the laminate.

4.4 Experimental set up and equipment

4.4.1 Test rig

To carry out the investigation of contact resistance dependence on surface pressure, a test rig was designed and built.

The test rig is divided into two sections:

- The electrical section is required to collect the current flowing within the sample. It includes the grounding electrode and the copper wires to connect the rig to the current generator return circuit.
- The mechanical section is required to control the load at the contact surface. It is a hand screw clamp made of steel and iron. In order to measure the applied force, a load sensor was placed between the clamp and the contact surface (Figure 4-13 shows the draft of the test rig with the sample and the load cell). To ensure that the applied load was uniformly distributed on the apparent contact area, a steel plate was placed between the load cell and the grounding plate. The mechanical section of the rig must be electrically insulated from the electrical section because all the current injected must flow through the sample and the grounding electrode. Thus, the application of two layers of GFRP (glass fibre reinforced polymer) was essential; one was between the sample and the clamp, and the other was between the electrode and the metal plate.

Parts of the test set (refer to Figure 4-13):

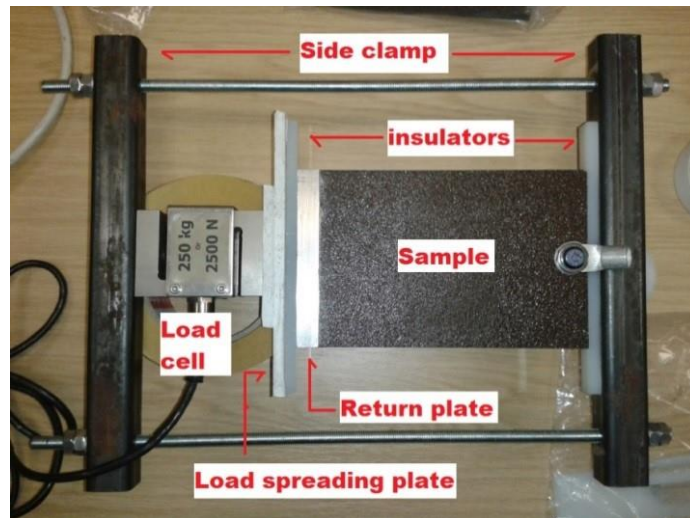


Figure 4-13: Test rig for side grounding arrangements.

- Test sample

The sample is a CFRP panel made of a stack of 36 unidirectional plies. The size of the sample is $150 \times 100 \times 9.7 \text{ mm}$, whereas the ply lay-up is

$$[-45/45/0/90/0_2/-45/45/0_2/90/45/-45/0_2/-45/45/0]_s$$

The 0° direction is along the longest side of the test sample, and the 90° direction is along the shortest side of the test sample.

- Injection point

The injection of the current takes place through a titanium fastener (Figure 4-14b) located 10 mm from the short side in a central position. The hole to host the fastener was drilled to achieve the interference fit allowing for better mechanical contact and lower contact resistance compared to the clearance fit. The diameter of the shank of the fastener is 7.93 mm , whereas the total height is 34.5 mm . This type of fastener is used in aerospace applications to join parts

of the aircraft, such as the T-joint in the fuel tank. Furthermore, one nut (Figure 4-14a) is required to tighten the fastener with a torque of $7N$; thus, a series of seven metal washers (Figure 4-14d) were placed as spacers between the nut and the lower surface of the sample, while two nylon washers (Figure 4-14c) were required between the head of the fastener and the upper surface of the sample to avoid the flow of current on the surface, and one crimp ring terminal (Figure 4-14e), which was used to establish a connection with the current generator, was located between the head of the fastener and the upper surface of the sample.

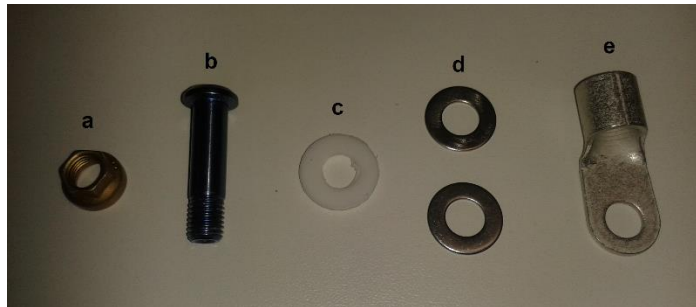


Figure 4-14. Injection fastener set: a) nut, b) fastener, c) nylon washer, d) metal washers, e) crimp ring terminal

- Clamp

The clamp ensures the contact between the return metal electrode of the test rig and the test sample. Moreover, it allows for the regulation of the pressure of the electrode against the sample edge through the two long screws at the edge of the rig. It is made by two longitudinal screws and two transversal bars. The load is controlled through two nuts located one on each screw.

- Insulating layers

The GFRP ensures a high level of insulation (typical breakdown voltage for the GFRP, which varies in the range of $20\text{-}50\text{ kV/mm}$). Furthermore, the metal rig is isolated from the rest of the circuit, as it stands over two thick nylon blocks.

- Load cell

It is important to measure the pressure of the clamp against the metal plate. In order for it to be electrically isolated from the circuit, it is positioned between the insulating layer and the clamp. It works in the range of $0 - 5000\text{ N}$, and it is connected to a load meter. According to the datasheet of the load cell, the *combined error* in measurement is defined as $\pm \% \text{ Full scale (max)} = 0.03$. The full scale of the transducer is 5000 N ; thus, the *combined error* is $\pm 1.5\text{ N}$ over the entire range of measurements. However, it is of interest to show the error in *% of reading* because for low values of the applied load, the *% error* in measurement increases substantially. Therefore, the percentage of error related to the load values applied in the experiment is shown in Figure 4-15b. It shows that at 600 N of load applied, the *% error* is 0.25% whereas at 3900 N , it is 0.03% .

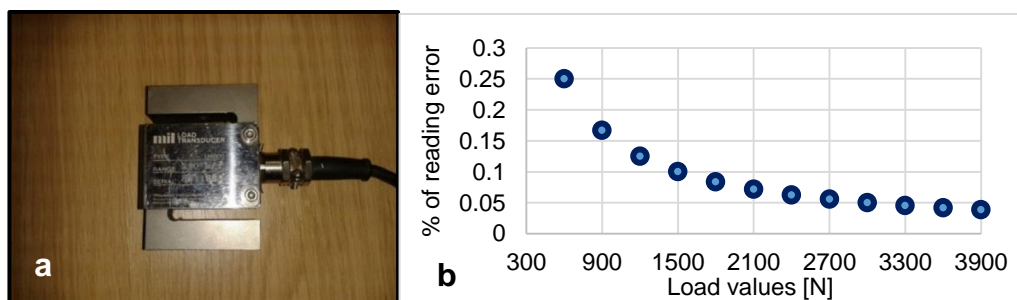


Figure 4-15. a) Load cell, b) % of reading error over the load levels applied during the test campaign.

- Return metal electrode

The return metal plate provides the electrical contact between the sample edge and the return path of the current. It allows contact over the entire sample edge. The dimensions of the electrode are *100X12X10 mm*. The metal plate is equipped with two fasteners on one of the faces in order to create the connection with the return wires.



Figure 4-16. Aluminium electrode: the two screws and nuts are required to connect the electrode with the circuit through copper wires.

- Load spreading plate

It is required to distribute uniformly the load along the entire side of the sample.



Figure 4-17. Load spreading plate with insulator and return metal plate.

4.4.2 Electric circuit and measurement equipment

The following equipment were used to perform the pressure and electrical measurements

- Power supply

The DC power supply GW Instek PSM 2004® is a programmable power supply that is able to deliver a DC current of up to 10 A with a voltage drop at the output of 20 V, thus giving a total power of up to 200 W.

- Multimeter (2 units)

Two Fluke 175 true RMS® multimeters, one connected in series with the circuit as an ammeter and the second connected over the sample, as shown in Figure 4-18, as a voltmeter to measure the voltage drop across the injection point and the return electrode. The datasheet reports the accuracy of the instrument as:

- DC mV: $\pm (0.15\% + 2 \text{ counts})$ in the range up to 600.0 mV
- DC Amps: $\pm (1.0\% + 3 \text{ counts})$ in the range up to 6.000 A

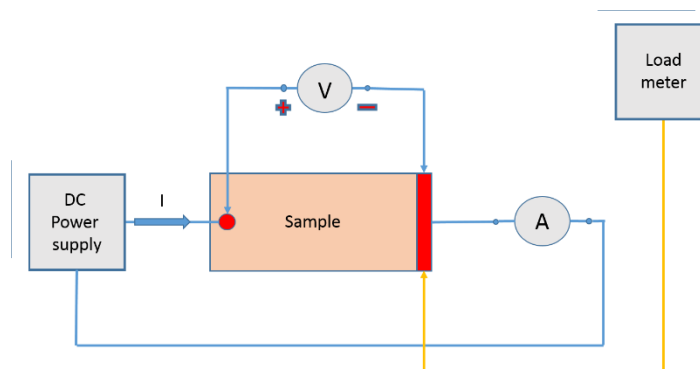


Figure 4-18. Schematic of the electric circuit and measurement system.

4.5 Measurement method

To measure the resistance variation due to different applied loads, an indirect method was used. The injected current and the relative voltage drop were measured, and the resistance was calculated using Ohm's law was calculated. A four probe method was used to improve the accuracy of the measurements. The voltage drop that was measured between the injection fastener and the return electrode can be considered as the sum of several voltage drops, as described below:

$$V = V_f + V_{c1} + V_s + V_l + V_{c2} + V_{re} \cong V_{c1} + V_{c2} + V_s \quad (4.9)$$

where,

V_f = voltage drop across the fastener (negligible).

V_{c1} = voltage drop across the contact between the fastener and the sample (negligible).

V_{c2} = voltage drop across the contact between the metal layer and the return plate (varies with load).

V_s = voltage drop across the sample.

V_l = voltage drop across the highly conductive layers (silver paint and metal sputter) (negligible).

V_{re} = voltage drop across the return electrode (negligible).

The resistance values were calculated for a range of applied load of $600 \div 3900$ N with steps of 300 N. Moreover, for each value of applied pressure, three values of current were injected, 100 , 500 , 1000 mA, to determine if variations of the applied current would lead to variations of the contact resistance due to the

variation of resistivity, or due to sparks between the two members of the contact. Table 4-3 shows the test matrix related to the campaign.

Table 4-3. Voltage drop for different load and current.

$\begin{array}{l} I \text{ (mA)} \\ L \text{ (N)} \end{array}$	I_1	I_2	I_3
	100	500	1000
300	$V_{1,1}$	$V_{1,2}$	$V_{1,3}$
600	$V_{2,1}$	$V_{2,2}$	$V_{2,3}$
900	$V_{3,1}$	$V_{3,2}$	$V_{3,3}$
1200	$V_{4,1}$	$V_{4,2}$	$V_{4,3}$
1500	$V_{5,1}$	$V_{5,2}$	$V_{5,3}$
1800	$V_{6,1}$	$V_{6,2}$	$V_{6,3}$
2100	$V_{7,1}$	$V_{7,2}$	$V_{7,3}$
2400	$V_{8,1}$	$V_{8,2}$	$V_{8,3}$
2700	$V_{9,1}$	$V_{9,2}$	$V_{9,3}$
3000	$V_{10,1}$	$V_{10,2}$	$V_{10,3}$
3300	$V_{11,1}$	$V_{11,2}$	$V_{11,3}$
3600	$V_{12,1}$	$V_{12,2}$	$V_{12,3}$
3900	$V_{13,1}$	$V_{13,2}$	$V_{13,3}$

$$R_{x,y} = V_{x,y} / I_y \quad (4.10)$$

4.6 Resistance measurement results

Using Eq. (4.10) the resistance values were calculated from the measurements of current and voltage drop, and a comparison was performed. The results refer

to the resistance between the injection point and the return electrode. It was assumed that the variation of resistance with load depends only on the variation of the contact resistance at the interface between the sample and the return electrode.

In fact, it can be considered that variation of the load does not lead to an appreciable variation of the resistance of both the CFRP sample and the return electrode because their resistances are related to the resistivity and the volume of the two components.

4.6.1 Metal sputter grounding system

Figure 4-19 shows the results for the *metal sputter* grounding system. Each set of points represents the resistance trend for each value of current injected. Immediately after, it is possible to note that, for the three sets, there is a reduction in resistance with the increase in load. Physically, the increase in load leads to an increase in the load bearing area, A_b , of the contact surfaces. This, in turn, corresponds to a reduction in contact resistance. However, in this case, Holm's law, which relates the resistance with the load, is no longer valid. In the graph of Figure 4-19, the line represents the trend of Holm's law in the load gap $600 - 3900 N$ normalised to the maximum value of the $1000 mA$ set, and it shows a discrepancy with the trend of the resistances calculated. Comparing the three sets, there is a general increase in the resistance with the increase in the current injected. According to Joule's law, an increase in current in a resistance leads to an increase in heating which, in turn, leads to a variation of resistance according to the following law:

$$\frac{dR}{R} = \alpha * dT \quad (4.11)$$

where dR/R is the relative variation of the resistance, α is the temperature coefficient of resistivity, and dT is the temperature variation. If the α coefficient does not vary with temperature, the equation can be approximated as a linear equation:

$$R(T) = R_0[1 + \alpha(T - T_0)] \quad (4.12)$$

Where $R(T)$ is the resistivity at the specified temperature, R_0 , is the resistivity at the temperature T_0 , and α is the *temperature coefficient of resistivity*, which can be either positive or negative. In the first case, an increase in temperature leads to an increase in resistivity. Conversely, for a negative α coefficient, the resistivity decreases with the increase in temperature. Holm [47] found that for a contact between two homogenous metal materials, the variation of the resistance with temperature follows the linearized Equation (4.12). Conversely, the graph shows that for a metal CFRP contact with a metal sputter layer, the linear equation is no longer valid. In fact, if the linear equation is valid, the three trends would be the same but vertically translated. Instead, in the plot, increasing the pressure leads the ΔR between the trends to decrease. Thus, it can be concluded in this case that the α coefficient is dependent on the temperature, which, in turn, is dependent on the applied pressure.

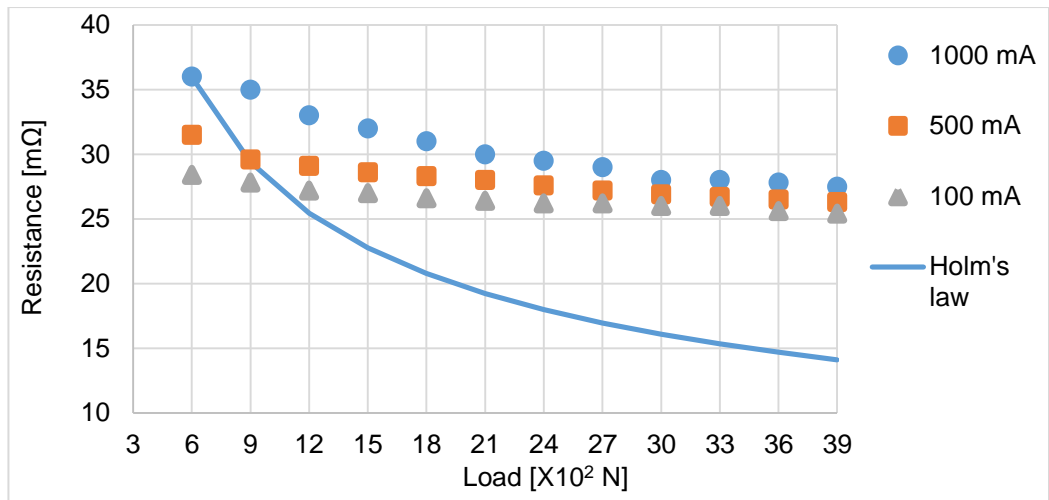


Figure 4-19. Resistance vs load for *metal sputter* grounding system for three values of current and Holm's law trend line normalised to the maximum value of 1000 mA.

4.6.2 Silver paint grounding system

The silver paint grounding system shows a resistance versus load behaviour similar to the metal sputter grounding system. In Figure 4-20, the resistance decreases with increasing pressure for all current levels, which means that the real contact surface area increases. Furthermore, there is a higher level of current to higher resistance, which means that the contact resistance is dependent on the temperature. The temperature rises because of the Joule effect at the constriction points of the contact surface. Moreover, the link between the resistance and the temperature is not linear.

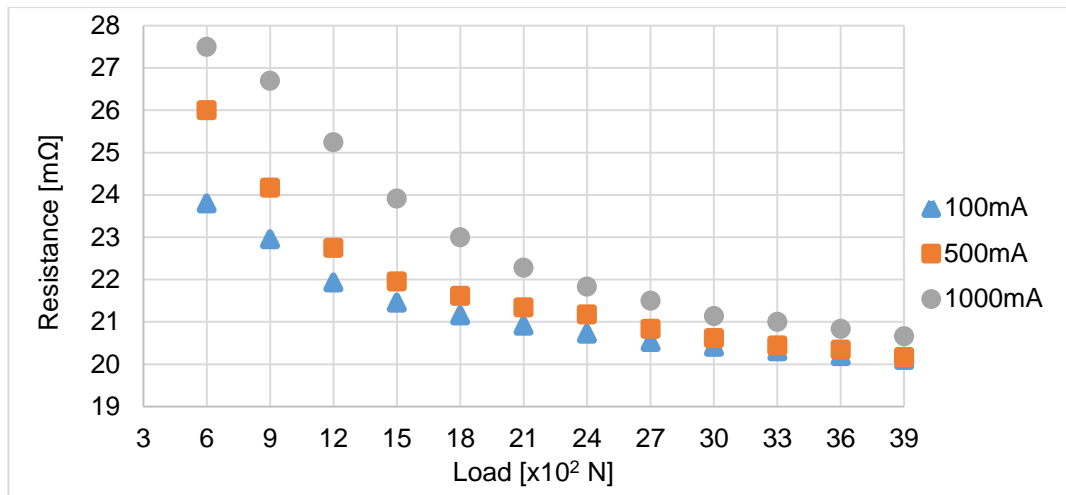


Figure 4-20. Resistance vs load for silver paint grounding system for three levels of current.

4.6.3 No-layer grounding system

The *no-layer* grounding system shows an exponential trend for three currents similar to the first two cases. However, at higher values of load, the resistances for the three currents can be overlapped, which means that the resistance is almost completely independent of the current and thus from the heating of the contact surface. Another aspect of Figure 4-21 to highlight is that at the lower load, the resistance at 500 mA is higher than the resistance at 1000 mA in contrast with the behaviour of the other two grounding systems. The experiment on this sample was carried out taking into account an additional factor: the flattening of the surface, due to the compression force. As explained previously, the load bearing area A_b is mostly created by plastic deformations of the two surfaces in contact. This means that, after the application of the load, the surfaces will remain deformed and, thus, will have a new load bearing area, which can be thought to be bigger than it was before the load application. This new load bearing area leads to a new resistance if the load is applied again. In this experiment, the resistance for the 100 mA and 500 mA from 600 N to 3900

N was calculated, after the clamp had been released and the test was carried out again for the 1000 mA to see the effects of the plastic deformation on the contact resistance. The result shows that the permanent deformation of the contact surfaces, due to plasticity, influences the contact resistance at lower pressure with a resulting lower resistance than was the case with the 500 mA . At higher pressure, the two tests can be overlapped, which indicates that the experiment is repeatable for load values above 3000 N .

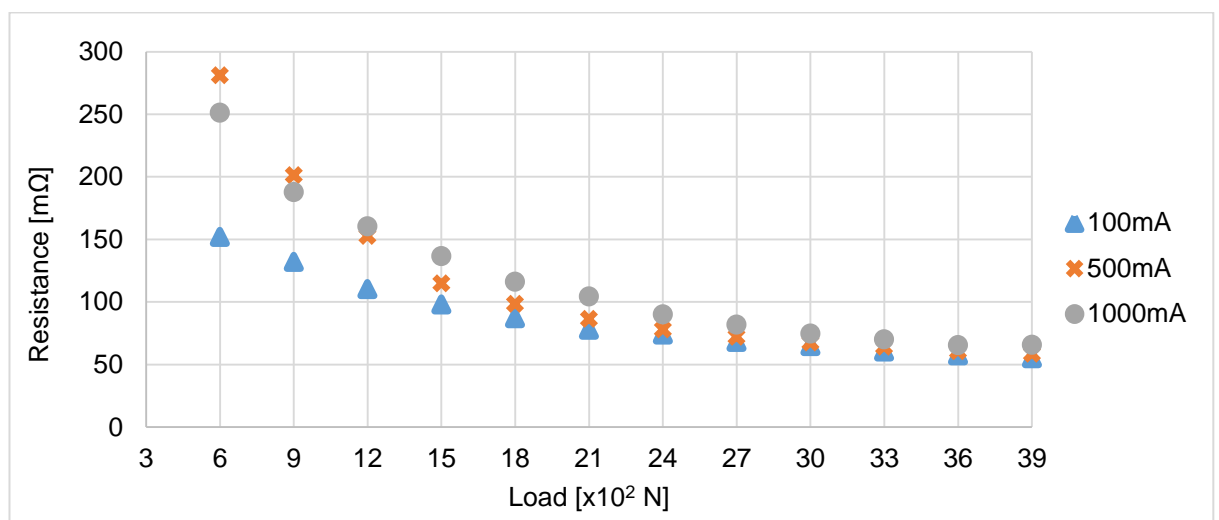


Figure 4-21. Resistance vs load for no-layer grounding system for three levels of current.

4.6.4 Fastener grounding systems

For the fastener grounding systems (*1-fastener* and *3-fasteners*), the load test rig is not required, as they are made by fasteners inserted in the sample with an interference fit. The connection of the return fasteners with the current generator occurs through the crimp ring terminals located underneath the head of the fasteners (Figure 4-11 a and b). In these two last cases, the three levels of current were injected, and the three respective values of resistances were calculated using the same method as for the other measurements. Moreover, the same electric circuit and the same measurement equipment were used (see

Figure 4-18 for details). The results for both grounding arrangements were included in one plot, and both show an increase in resistance with an increase in current in accordance with the other grounding systems.

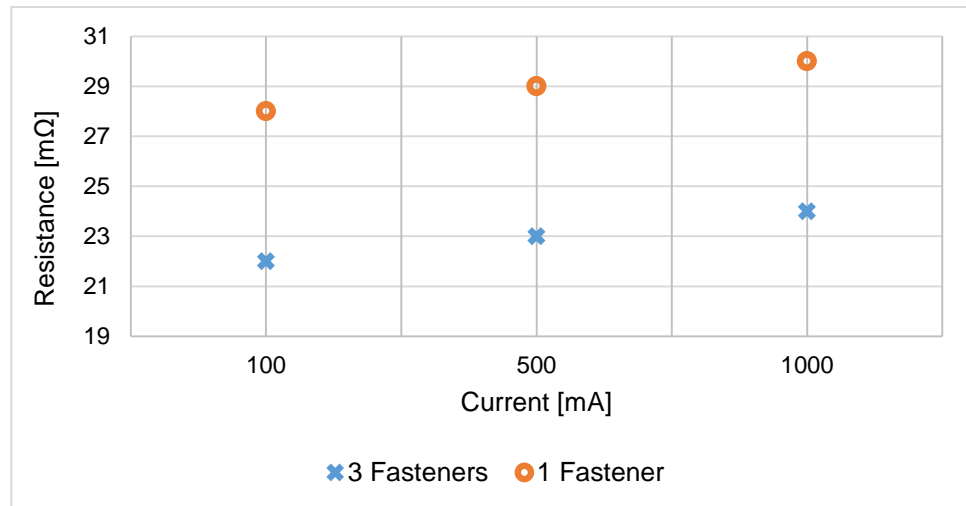


Figure 4-22. Fastener grounding systems. Cross for the three fasteners grounding system; circle for one fastener grounding system.

4.6.5 Comparison of grounding systems

The comparison between the different grounding systems was carried out using the resistance values calculated at 500 mA . The comparison at 100 mA gives the same results in terms of comparison, whereas at 1000 mA , the *no-layer* results were taken using a different method from the others. The plot in Figure 4-23 shows that the *no-layer* arrangement has the highest resistance for all pressure values. At 600 N , the *no-layer* system shows a resistance that is more than 10 times higher than that of the *silver paint* case. Instead, by increasing the pressure, the gap between the two cases decreases noticeably. In fact, at 3900 N , the *no-layer* resistance is less than three times higher than the *silver paint* resistance. The lowest value of resistance comes from the *silver paint* system at 3900 N . However, the *silver paint* values and the *metal sputter* values are

comparable. In addition, the results from the *3-fasteners* arrangement and *1-fastener* arrangement are aligned with the silver paint and metal sputter results.

The load factor is more crucial for the contact resistance in a *no-layer* system than in the others, especially at lower values of load.

The *silver paint* system shows a lower resistance compared to the *metal sputter*, and this can be explained by the silver paint layer producing a bigger *load bearing area* A_b , with the consequence of a reduced resistance when the load is applied.

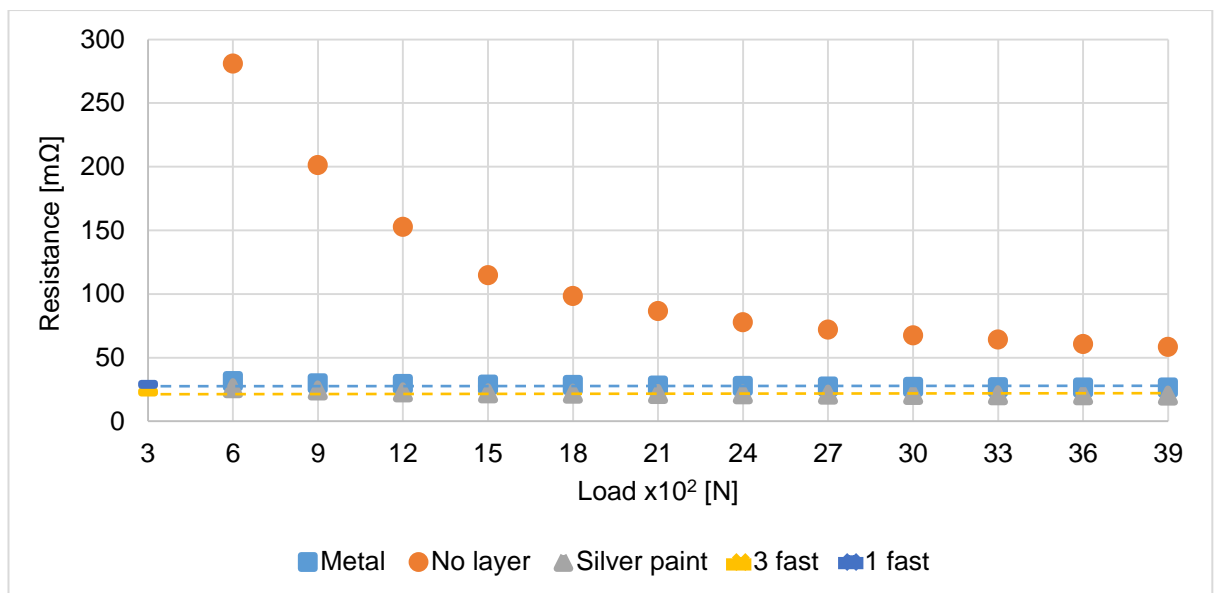


Figure 4-23. Comparison of the grounding systems resistances at 500 mA; it must be noted that the *3 fast* (blue dashed line) and *1 fast* (yellow dashed line) values are not related to any load values, but they have been added to the plot to aid comparison.

For the *side* grounding systems, the apparent contact area corresponds to the entire side of the sample, which means an area of 970 mm^2 whereas, for the *3-fasteners* arrangement, the apparent contact area is

$$\pi d * h * 3 = 24.9 * 9.7 * 3 = 724 \text{ mm}^2 \quad (4.13)$$

and for the *1-fastener* case

$$\pi d * h = 24.9 * 9.7 = 241.53 \text{ mm}^2 \quad (4.14)$$

where d is the diameter of the fastener, and h is the thickness of the sample. The calculation shows that the *1-fastener* grounding contact area is more than four times smaller than the *side grounding* contact area and around three times smaller than the *3-fasteners* grounding contact surface. However, there is no appreciable difference in resistance between the *1-fastener* and the *3-fasteners* case.

According to the accuracy of the measurement instruments, specifically the two multimeters, the current measurement is affected by an error of 1.6 % for the 500 mA injected current whereas, the voltage measurements are affected by an error between 1.6% for the lowest voltage drop measured (10.1 mV) and 2.4% for the highest (140.5 mV). The calculated resistance is affected by the propagated error which is in the range between 2.3% for the minimum value and 2.9 % for the maximum.

$$E_{R\%,min} = \sqrt{E_{C\%}^2 + E_{V\%,min}^2} = \sqrt{0.016^2 + 0.016^2} = 2.3\% \quad (4.15)$$

$$E_{R\%,max} = \sqrt{E_{C\%}^2 + E_{V\%,max}^2} = \sqrt{0.016^2 + 0.024^2} = 2.9\% \quad (4.16)$$

4.7 Numerical simulation and model validation

The parameters used for the numerical simulation in Chapter 3, specifically, the anisotropic electrical conductivity and the interlaminar conductivity, have been used to create a model of the real test samples used for the experimental test. The results of the low current measurements and of the numerical models have

been compared in order to provide a validation of the assumptions of the numerical model.

4.7.1 Geometry of the sample

The geometries of the real samples were replicated in the numerical models. Furthermore, the geometry of the injection fastener and the geometry of the grounding fasteners were also replicated. However, the nuts and metal washers of each fastener were not reported in the numerical model. This is because for the low current test, it was thought that they would not have produced relevant variations on the results, but would have the disadvantages of an increased computational cost during the drafting, the meshing, and the solving steps. Therefore, each numerical model represents a CFRP sample made of 36 plies quasi-isotropic with an injection fastener on one short side and one different grounding system for each model on the opposite side. The size of the sample is *150X100X9.7 mm*.

The triangular-prism meshing method described in Section 3.3.4 was replicated to mesh this model as well, and particular attention was paid to the meshing around the curvature of the fasteners. Figure 4-24 shows the geometry of the numerical models. Moreover, Figure 4-24d shows a zoom shot of the fastener area, which underlines the refinement of the meshing size in accordance with the curvature of the fastener compared to the rest of the panel. The meshing of the fastener was done automatically by the software in order to adapt it to the meshing of the plies.

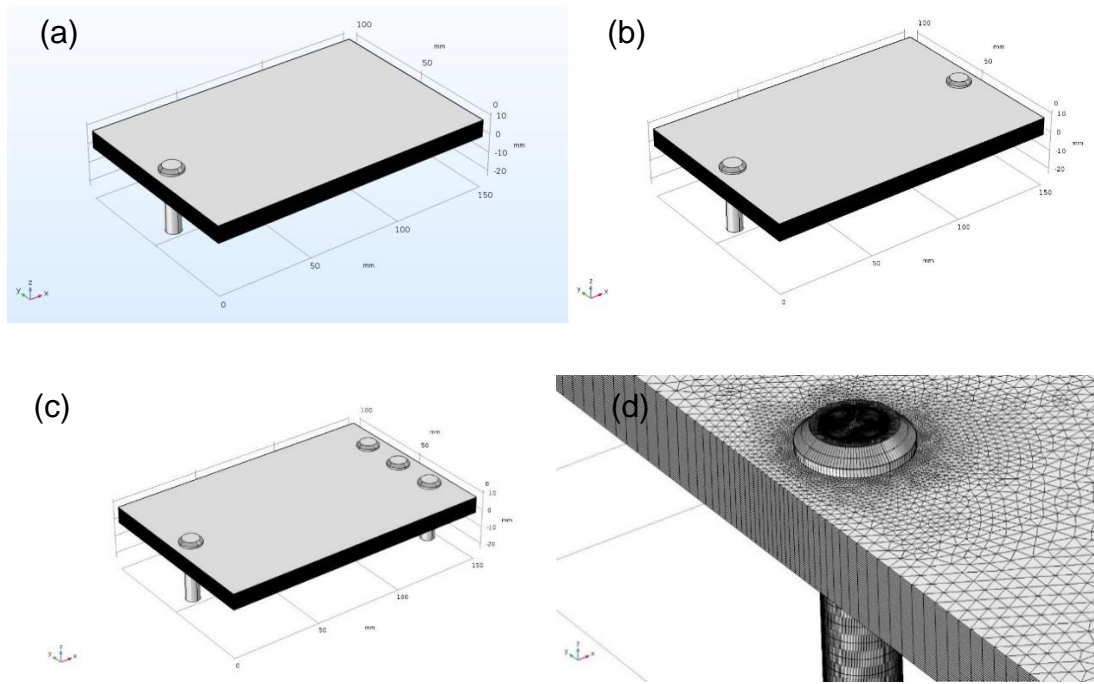


Figure 4-24. Geometry of the numerical models: a) geometry of the sample with the side grounding systems, b) geometry of the sample with 1-fastener grounding system, c) geometry of the sample with 3-fasteners grounding system, d) meshing refinement around the fastener region.

4.7.2 Electrical parameters

The electrical properties of the plies are the same as those used for the numerical model of Chapter 3; therefore, an orthotropic matrix of electrical conductivity was used:

$$\begin{bmatrix} \sigma_f & 0 & 0 \\ 0 & \sigma_t & 0 \\ 0 & 0 & \sigma_{tt} \end{bmatrix} = \begin{bmatrix} 16000 & 0 & 0 \\ 0 & 100 & 0 \\ 0 & 0 & 100 \end{bmatrix} S/m \quad (4.17)$$

Furthermore, the interlaminar conductivity was modelled as a homogenous resistive layer $35 \mu m$ thick with electrical conductivity of $2.4 S/m$.

The current injected at the head of the fastener and collected through the grounding system was $1 A$ DC for all the models to replicate the same current of the test.

4.7.3 Current distribution simulation results

The first column of Figure 4-25 shows the results of the current distribution, for the numerical simulation, within the first two bottom plies of the sample, which means 135° and $+45^\circ$. The enhancement of current density along the direction of the fibres in each ply is clear. The slices shown in the first column of Figure 4-25 are referred to a linear scale. This has the disadvantage of poor visualization of the current distribution far from the injection fastener but with the advantage of enhancing the visualization of the current distribution around the fastener. In this way, it is possible to produce a visual validation of this model by comparing testing with thermal acquisitions of high current tests carried out using impulse current with peak magnitude of 25 kA. The peak of the current waveform was considered as time reference ($t=0$ s) for the thermal acquisitions. Therefore, all the thermal images are associated to the time step at which have been acquired. The second column of Figure 4-25 shows the thermal evolution inside the same real sample during the high impulse current tests carried out in the Morgan Botti Lightning Laboratory (MBLL) of Cardiff University. The high current test was carried out in the same way as the low current test, which means the current was injected through the injection fastener and collected through the grounding system placed at the opposite side. The results of the physical test shown in this paragraph are extrapolated from the high current test campaign carried out on the test sample. Therefore, the test setup and procedure are described in the high current test campaign chapter (Chapter 6) using the lightning current generator described in Paragraph 6.2 and the thermal camera described in Paragraph 6.5. Each image corresponds to a specific time step during the injection of the current impulse. Specifically, the

image in Figure 4-25b was captured at the current peak time, $t=0$, and the image in Figure 4-25d was captured *44 ms* after the current peak. The increase in temperature recorded by the thermal camera is due to the Joule effect of the current path. Therefore, it can be assumed that specific locations of increased temperature are due to the enhancement of current density at the same location.

From this assumption, the temperature increase seen in Figure 4-25b can be interpreted as the current path of the current within the outermost ply of the sample, which is oriented in 135° . A comparison between the model result and the thermal camera acquisition shows a certain level of agreement, especially for the direction. In thermal acquisition, the area of enhanced temperature looks bigger than that in the numerical model, and this is because for the high current test, a current impulse of *25 kA* magnitude was used and also because the heat expands into the surrounding material. In Figure 4-25d, a new strip of enhanced temperature appears around the fastener; this corresponds to the ply underneath the first, which is oriented in $+45^\circ$. The delay is due to the fact that the heat generated in ply $+45^\circ$ must move into ply 135° before reaching the surface of the sample, and this process requires a certain duration of time. However, the thermal picture shows a good grade of agreement with the respective model, as seen in Figure 4-25c.

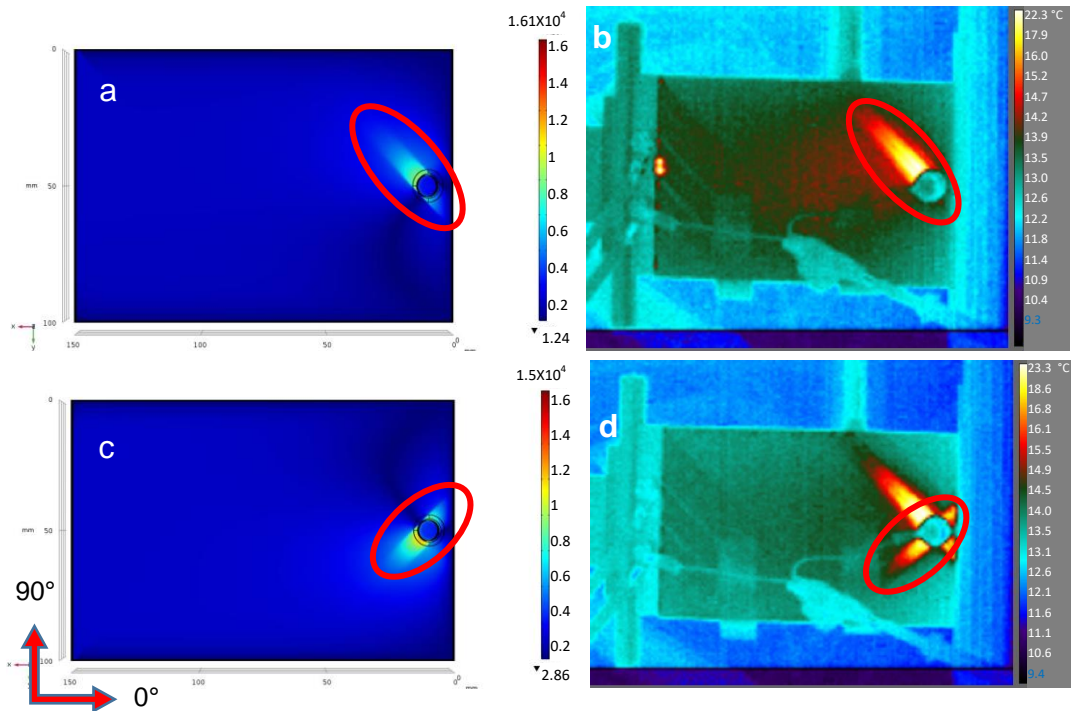


Figure 4-25. Comparison between numerical model and high current test: a) current distribution within ply -45° (135°). b) thermal capture at current peak. c) current distribution in ply 45° . d) thermal capture 44 ms after the current peak.

A further comparison of the resistance measured in the low current test and the numerical model was carried out, and they are shown in Table 4-4. The comparison reveals that for four of the five systems analysed, the resistances values are comparable with a maximum variation of 10.3% for the *1-fastener* case. The *no-layer* case, in contrast, shows no correlation between the numerical model and the real test. The numerical model does not consider the effect of the poor contact surface between the sample and the return electrode resulting in a poor correlation of the computational results compared to the real test.

Table 4-4. Comparison between resistances evaluated with the numerical model and the real measurements.

	Numerical model (mΩ)	Low current measurements (mΩ)	variation
Silver paint	22	20.16 @ 3900 N force	-4.9%
Metal sputter	27.5	26.3 @ 3900 N force	-4.5%
No-layer	20.5	58.44 @ 3900 N force	+184%
1 f grounding	26.3	29	+10.3%
3 f grounding	21.1	23	+8.7%

The comparison reveals that, for both the current distribution comparison and the electrical resistance comparison, there is a good level of agreement between the numerical model and the real test hence, it can be concluded that the designed model is a valid method to predict the current distribution within anisotropic laminate materials subjected to low DC current injection except for the *no-layer* case. In the latter case, the numerical model does not take into account the contact resistance between the sample and the grounding electrode.

4.8 Conclusion

The test campaign aimed to compare different grounding arrangements for a CFRP test sample in terms of electrical resistance performance. The value of resistance was calculated as an indicator of the performance, as it is related to the quantity of energy dissipated and the relative risk of damage to the system. For all the arrangements, a specified value of current was injected, and a

relative value of resistance was calculated through indirect measurements (four probe measurements). Two main groups of grounding systems were analysed: the *fastener grounding* system group and the *side grounding* system group. The *fastener grounding* system allows the current to flow out of the sample from one or more fasteners placed within the sample with an interference fit whereas the *side grounding* systems allow the current to flow out from the sample through one of the sides. The advantage of this second method compared to the first is that the sample does not require any drilling, fastening or accessories, hence being simpler to manufacture. On the other hand, a *side grounding* system requires a specific test rig, which allows for the control of the contact pressure between the side of the sample and the return electrode. Furthermore, for two of the three side grounding systems, the *silver paint* and the *metal sputter* system, a high conductive layer is required between the sample edge and the return electrode. The results show that the resistance of *silver paint*, *metal sputter*, *3-fasteners* and *1-fastener* systems are aligned. Instead, the *no-layer* case shows a higher resistance at all levels of pressure compared to the others. Furthermore, the resistance of the latter case is more dependent on the pressure compared to the others. The advantage of the *no-layer* case is its cost effectiveness because the sample does not require any grounding fastener or treatment of the side in touch with the return electrode. However, the contact resistance is related to the roughness of the side surface which, in turn, depends on the way the sample has been cut. Several technologies of cutting of CFRP are available, with each creating a surface with specific roughness characteristics. It might be thought that the sample surface of a *no-layer* arrangement can reach a level of polishing at which its contact resistance

becomes comparable with the other cases. If this polishing level exists, the cost of producing it must be taken into account and a comparison with the cost of creating the other scenario should be made. Between the *3-fasteners* case and the *1-fastener* case, no significant differences were seen; thus, the *1-fastener* case has the advantage that it requires only one grounding fastener. In general, for this test campaign, the *no-layer* arrangement at higher values of pressure can be considered the best choice in terms of cost effectiveness. Although its higher level of resistance does not create overheating or sparking at this current magnitude, it requires no further treatments on the side in contact with the return electrode.

The side grounding systems were developed in order to produce an outstanding advantage compare to the conventional fasteners grounding systems. It allows for a cost reduction of the sample because this method does not require the use of grounding fasteners. Indeed for each fastener used to make the grounding system, there are the following costs to be considered:

- Cost of the fastener which depends on the material on the design characteristics and any other finishing applied
- Cost of the accessories such as nuts, washers, insulators, etc.
- Cost to produce the hole where the fastener is located. This cost depends on the type of drill required but in general drilling of CFRP materials is more expensive compare to conventional metal
- Cost to insert the fastener in the relative hole. In the case of interference fit technique it is required a further manufacturing step to place the fastener in the relative hole and this has a cost.

All the above costs are related to one fastener. In the cases where several pairs of fasteners are required the costs raise according to the number of fasteners.

Clearly the side grounding system allows for avoiding all the above costs but it can have some disadvantages related to the costs required to produce the metallization, in the cases of metal sputtering system.

However, in a high current lightning test environment, where the current waveforms applied replicate the lightning current which means, impulse wave shapes with peak magnitude in the order of tens to hundreds of kA with a duration less than 500 μ s, the thermal effects of the current and the ability of each material to carry it without damage must be considered.

Chapter 5

CFRP surface roughness characterization using microscopic techniques

5.1 Introduction

This chapter provides the results of the microscopic characterization of the surfaces of different CFRP samples using an advanced technique based on optical microscopic acquisitions. An analysis is carried out to investigate the variation of roughness characteristics when a compression force is applied to the contact. Furthermore, some relations between the compression force, the roughness parameters, and the contact resistance have been discussed. At the early stage of the project, the surface characterization step had not been taken into account as part of the project. However, early in the development of the side grounding system and the relative test rig, the importance of the surface topography in the contact resistance was revealed. Thus, it was supposed that the compression force would modify the topography of the surfaces in contact, and consequently, the contact resistance. Therefore, it was decided to perform a surface characterization in order, firstly, to assess the main characteristics of the surface, from the topography point of view, and secondly, to eventually predict the variation of the contact resistance from the evaluation of those parameters.

The contact resistance depends on, among other things, the texture of the surfaces in contact with each other, and thus, on the topography of the surfaces. In recent years there has been wide investigations of how the contact

resistance depends on factors such as the load bearing area, metallic contact, quasi-metallic contact and apparent contact surface. Furthermore, a relationship has been found between the contact resistance and the force that acts on the contact surface [47]. However, most of those studies have been carried out using contact between homogenous metal materials. Conversely, only a small amount of literature is available for studies on metal-CFRP contact resistance (an investigation on the effects of the contact force on the contact resistance between CFRP and metal can be found in [46]). The need to study the electrical characteristics of a CFRP-metal contact stems from the fact that the aluminium electrode in touch with the sample edge creates a contact interface, specifically, a CFRP-metal contact (as described in Chapter 4). The CFRP member is a non-homogenous member and is made by two materials, namely, epoxy matrix and carbon fibres, which have electrical resistivities that is not comparable.

5.2 Surface characterization technique and equipment

Surface characterization refers to the study of the topography of a surface, specifically, surfaces that result from a manufacturing process, such as cutting, drilling or surface finishing. For each of those processes, several manufacturing technologies are available. This specific experiment analysed surfaces resulting from cutting processes. Although the cutting process of the samples under investigation is not known, it is possible to investigate the surface characteristics. In order to characterize a surface, the first step is to collect an amount of raw data using one or more techniques. The second step is to extrapolate from that data useful information through post processing

techniques. Currently, there is a wide range of parameters that can be extrapolated from raw data and which are analysable.

5.2.1 Images acquisition

There are several techniques to record data obtained from a surface; however, in this work, the optical microscope acquisition technique was used. Due to the dimension of the sample to be analysed, an inverted optical microscope was used. The inverted microscope works using the light source coming from the bottom, and the objectives are placed well below the sample. Because the optics are below the stage, and the sample is placed above the objectives, users can work with large and heavy samples. The Morgan Botti Lightning laboratory (MBLL) is equipped with an inverted optical microscope *Zeiss Axio Observer 7 materials*.



Figure 5-1. Zeiss Axiovision 7 materials optical inverted microscope.

The microscope itself is equipped with a CCD sensor, which is able to send a live view of the sample to a dedicated software program. Furthermore, the CCD sensor is able to capture still images, which can be saved or manipulated in post processing. The CCD sensor is able to capture images up to $1388 \times 1038 = 1.4 \text{ megapixel}$; each pixel has a size of $4.65 \times 4.65 \mu\text{m}$ whereas, each captured

image has a maximum size of approximately 4.3 MB [54]. With a magnification of 10X, the sensor is able to record a portion of the surface with a size of 988X739 μm . This means that each pixel is able to record a portion of the surface of 0.71X0.71 μm .

5.2.2 Data processing

After the acquisition of the images via the microscope and the CCD sensor, the second step is to analyse the images in order to extrapolate the relevant information. The microscope is managed by a dedicated software program, the Axiovision® software provided by Zeiss®. The software is able to pilot the microscope in order to record sequences of images of the surface in a specific location on the surface, using Cartesian coordinates. These sequences of images can be used to compose larger images, which take into account a larger portion of the surface. Moreover, the software is able to extrapolate 3D profiles of the surface under investigation. These two features of the software are defined as *mosaic* and *z-stack composition*. The *mosaic* feature is required because the image recorded by the sensor refers to a magnification of the surface of 10X, which means a rectangular portion of the surface measuring 988 μm wide and 739 μm high, which is equal to an area of 0.737 mm^2 . The total contact surface has an area of 970 mm^2 ; thus, the area recorded by a single image is roughly 0.08% of the entire surface, and so cannot be considered a valid representation of the entire surface. In fact, if the image is much smaller than the entire surface under investigation, it is possible that it shows only local characteristics and does not reflect the average characteristics. Therefore, it is necessary to consider a larger surface.

The ideal solution would be to analyse the entire surface, which means the analysis of a composition of 1320 images in mosaic. However, the maximum size of the image to be processed depends on the computational strength of the machine used for post processing. Therefore, a compromise must be found between the size of the captured image and the computational cost. Another factor that plays a role in the computational time is the *z-stack* function. The *z-stack* function is required for two main reasons: first, because the captured image must be entirely in focus in order to extrapolate the surface parameters, and second, because through this technique, it is possible to create 3D profiles of the surface topography using grey scale images. The issue of the focusing is related to the *depth of field* (DoF), which represents the portion of space on which a lens is able to focus (Figure 5-2).

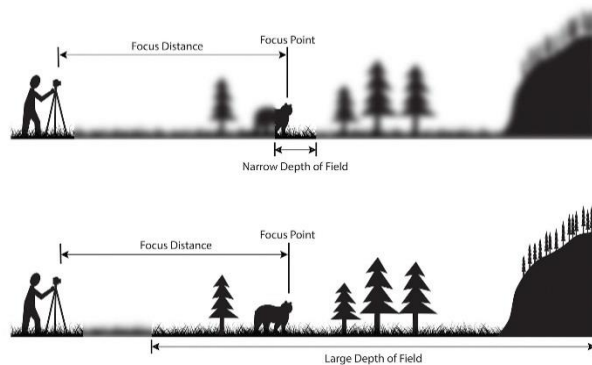


Figure 5-2. Schematic of different depths of field (DOF) [55].

The DoF depends on the lens aperture, the distance of the subject from the lens, and the focal length. Microscopy lenses have a wide focus aperture and wide magnification factors with the consequence that they have a very narrow DoF, in the range of a few μm . The surfaces under investigation have variations in height between the peaks and the valleys in the range of hundreds of μm . This means that the microscopy lens might be able to focus on some peaks of

the surface under investigation and keep the valley out of focus and vice versa (Figure 5-3).

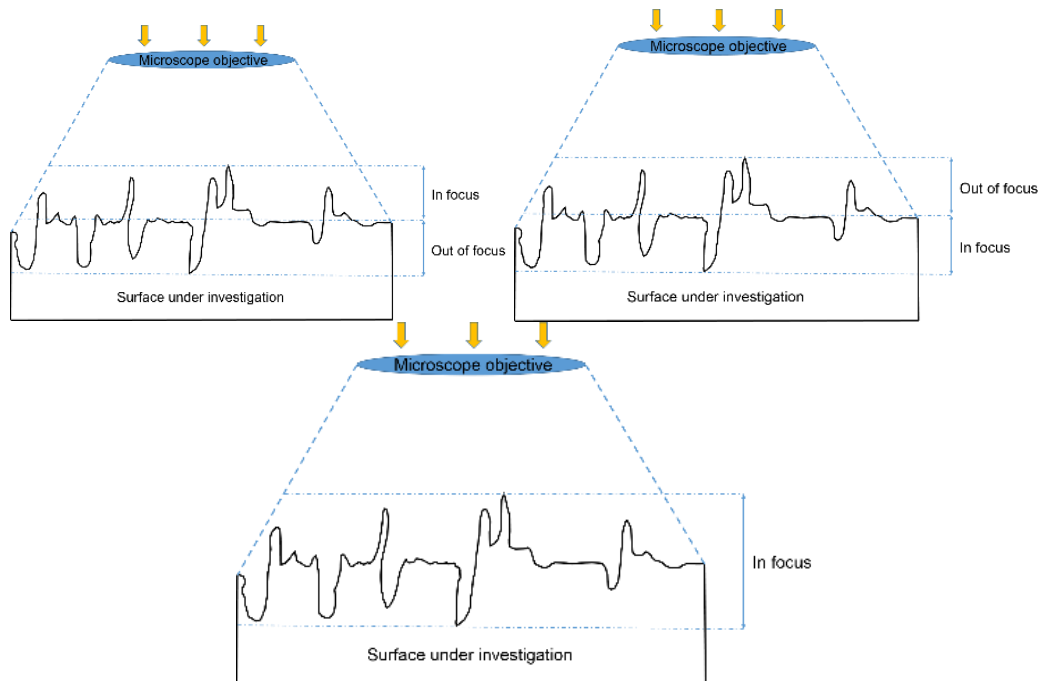


Figure 5-3. Schematic representation of the DOF of a microscope objective when used for surface analysis (Not to scale). The top left picture shows the upper part of the surface in focus whereas the top right picture shows the bottom part of the same surface is in focus. The bottom picture represents the processing of the two main pictures with the results of a new picture where all the surface is in focus.

To solve the problem of a narrow DoF, an advanced computational technique has been developed [56]; this is called *focus stacking*, and it allows for the creation of images that are completely in focus starting from images of the same subject but with only a small portion in focus (Figure 5-3). The same technique is used successfully in microscopy to create images of surfaces that are perfectly in focus and 3D profiles of the surfaces. The technique works, with the first step being the acquisition of a series of pictures of the same subject at different focal lengths. In this way, each picture shows a different portion of the subject in focus. The second step produces a single image that is entirely in

focus by using an algorithm that merges all the images taken during the first step (Figure 5-3).

Figure 5-3 shows a simplified scenario, where just two images of the same subject are required to compose an image that is completely in focus. In many cases, more than two pictures are required to produce a clear image that is in focus. In this analysis, for each portion of surface captured, a stack of between 18 and 30 pictures was captured. The number of pictures in the stack depends on the total height between the highest peak and the deepest valley of the surface investigated. In this investigation, the Axiovision® software automatically optimizes the number of layers by considering a distance between each layer of roughly $9.1 \mu\text{m}$. Therefore, for the evaluation of the computational cost to produce an image completely in focus, not only the size of the image, but also the number of layers needed to produce each image must be considered. Thus, returning to the case of the analysis of the entire surface, 1320 images will be required, each of which is made of a stack of 30 images (worst case); thus, there are 39,600 images to be processed. Each image has a size of 4.3 MB with the results of 170.3 GB of data to be processed for each surface. This amount of data cannot be processed by the machine, which runs the Axiovision® software linked with the microscope; thus, the solution was to investigate a section of the surface that would be large enough to be representative of the entire surface, but at the same time, could be easily processed by the software. The compromise was found in a section of the surface made by a mosaic of 6X13 tiles. The mosaic covers the entire height of the surface and has a length of roughly 5 mm (Figure 5-4).

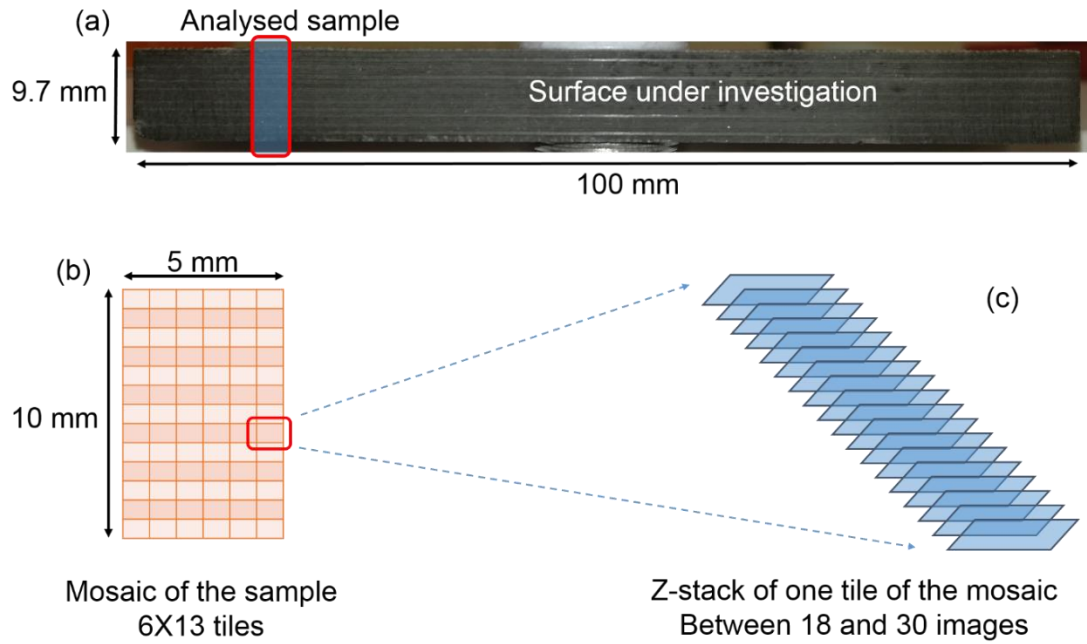


Figure 5-4. Mosaic and z-stack method: a) portion of surface under investigation, b) mosaic made by 6X13 tiles, c) z-stack composition for each tile of the mosaic.

For each surface, three different samples were recorded at three different random locations on the surface. Between the three samples, the variations in terms of roughness mean were found to be less than 5% and it has been considered not relevant with the consequence that the results of the investigation refer to one sample only.

5.2.3 Data acquisition

After the image acquisition step, the Axiovision® software produced the following results:

- the sequence of all the pictures captured by the microscope
- one image in colour TIFF format which shows the composition of the entire sample that is completely in focus, named a texture map

- one image in grey scale TIFF format, which shows the topography of the sample. The size of the image is 7634X14117 pixels and it generally occupies a memory space of 100 MB, named a topo map (Figure 5-5).

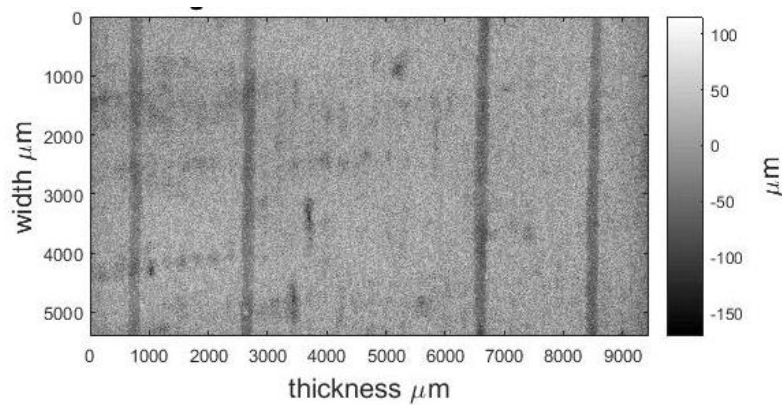


Figure 5-5. Typical raw TIFF image of the topography of the surface.

From this last grey scale picture, it is possible to extrapolate all the parameters regarding the roughness of the surface.

5.3 Profile and areal surface characterization

This section shows the parameters that can be extrapolated from the raw images acquired from the microscope; they can be divided into two main groups: profile parameters and areal (3D) parameters.

Although in this work, the areal parameters were considered, the description of the basics of the surface characterization was carried out referring to the profile parameters because the profile parameters have been standardized and described in the ISO standards, and they represent the reference for the surface measurements. The standardization for the areal characterization is still under development; thus, most of the definitions and standards refer to the profile standards.

5.3.1 Profile definition

The profile parameters are extrapolated when a profile of the surface texture is considered. The profile can be created using specific tools, such as the profilometer, or they can be extrapolated from areal data through post processing techniques such as the technique used in this work. Depending on the type of surface and type of measurement, there are several ways of developing a profile. It can be created using a plane normal to the surface (Figure 5-6a), a plane at an angle to the surface (Figure 5-6b), or a plane parallel to the surface (Figure 5-6c).

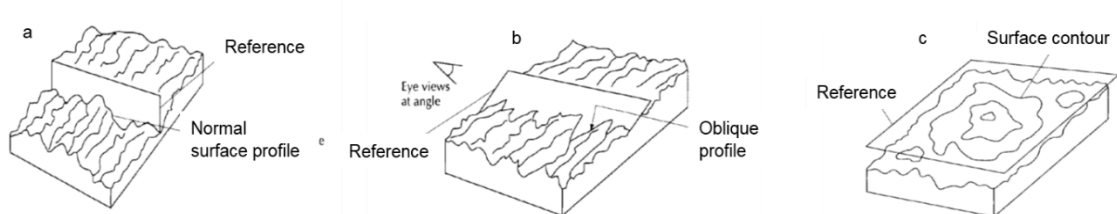


Figure 5-6. Planes for profiles acquisitions : a) Normal surface profile, b) oblique surface profile, c) parallel surface profile [57].

In this work, the profiles investigated were created using planes normal to the surfaces. However, for every normal profile, it is possible to extrapolate several characteristics which depend on filtering requirements.

5.3.2 Profile filtering

The filtering is required in order to focus the measurements on specific details, such as measurements of the roughness, of the waviness or of the form of a profile (Figure 5-7). These three parts form the primary profile, which is the profile without the filters, and this forms the basis for the evaluation of the parameters.

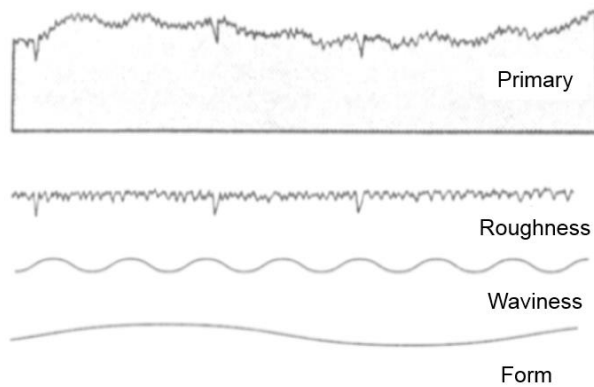


Figure 5-7. Primary profile and its composition as superimposition of roughness, waviness, and form [57].

In the literature, there are several definitions for the roughness. However, according to [58], it can be defined as “a *statistical representation of the high frequency (small wavelength) surface deviations (peaks and valleys) from the local mean surface height*”. Another definition of roughness can be found in [59], which defines the roughness as “*the deviations in the direction of the normal vector of a real surface from its ideal form*”. The waviness is defined as irregularities whose spacing is greater than the roughness sampling length whereas the form, in turn, is defined as the irregularities whose spacing is greater than the waviness sampling length. However, it must be considered that the roughness is produced by process marks during the machining, and it cannot be avoided. Conversely, the waviness and form result from problems during the machining process due to, for instance, poor accuracy of the tools, and they can be avoided.

In order to separate the three parts, as mentioned earlier, a filtering technique is required. In accordance with the ISO 115621, a Gaussian filter is applied to the profile to isolate either the roughness or the waviness from the primary profile.

Figure 5-8 shows the two Gaussian filters required to isolate the roughness and waviness. λ_s represents the smallest wavelength of the roughness range. Smaller wavelengths than λ_s are associated to sub-roughness. λ_c represents the intersection wavelength between the roughness and the waviness, whereas, λ_f is the intersection wavelength between the waviness and the form.

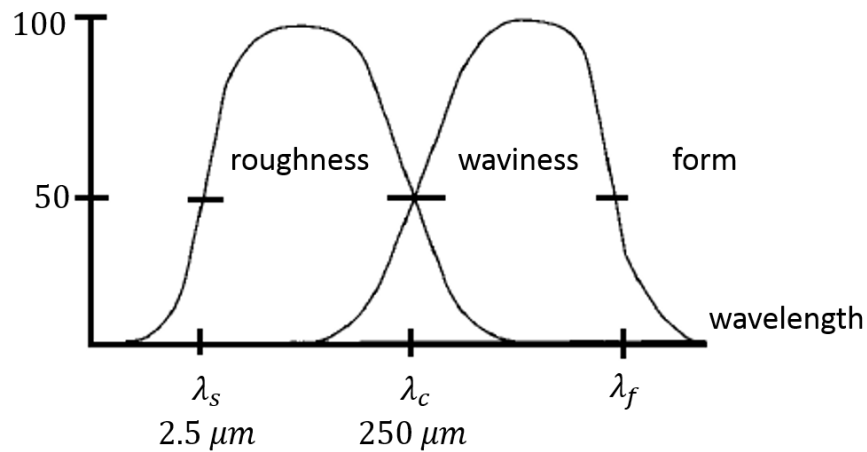


Figure 5-8. Gaussian filters used to isolate the roughness and the waviness from the primary profile [57].

Regarding the values of λ_s and λ_c the ISO 4287 establishes a set of values, as shown in Table 5-1.

Table 5-1 Roughness cut-off wavelength ratio (DIN EN ISO 4287).

λ_c (mm)	λ_s (μm)	$\lambda_c:\lambda_s$	Maximum probe radius (μm)	Maximum point space
0.08	2.5	30	2	0.5
0.25	2.5	100	2	0.5
0.8	2.5	300	2	0.5
2.5	8	300	5	1.5
8	25	300	10	5
Gauss-Filter: - Short Wave Cut-Off λ_s Long Wave Cut-Off λ_c				

The same description as was used for the profile characteristics can be applied to the areal characteristics. The areal characteristics usually come from optical acquisition, and the standardization processes are under investigation. Thus, for this specific work, the cut off wavelengths of the profile characterization included in the ISO 4287 were considered. Therefore, a cut-off wavelength for the roughness equal to $2.5 \mu\text{m}$ and a cut-off wavelength for the waviness equal to $250 \mu\text{m}$ were chosen.

5.3.3 Roughness parameters

In the literature, it is possible to find a series of parameters that can describe several aspects of a surface. These parameters can refer to the profile or to the areal acquisition. They can also refer to the primary, the waviness or the roughness acquisitions. In this work, the parameters that referred to the roughness of the areal acquisition were analysed, specifically the roughness parameters extrapolated from the optical microscope acquisitions (see Figure 5-4 for the details of the areal acquisition). The ISO 25178 describes the analysis of 3D areal surface texture. However, for the sake of simplicity, the descriptions in this section refer to the roughness parameters of the profile for a better understanding of the pictures.

The following parameters are calculated in reference to a mean line. The mean line is a line that bisects the profile so that an equal area lies above it as below it (Figure 5-9).

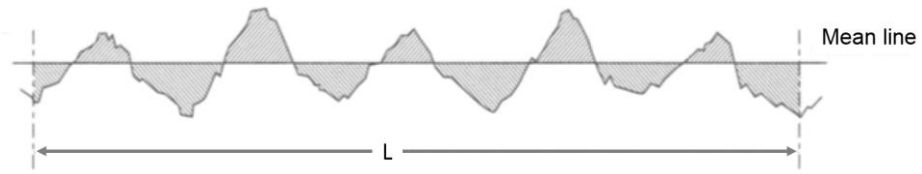


Figure 5-9. Mean line of the profile [57].

- R_a is the roughness arithmetic mean of the magnitude of the deviation of the profile from the mean line (Figure 5-10).

$$R_a = \frac{1}{l_r} \int_0^{l_r} |z(x)| dx \quad (5.1)$$

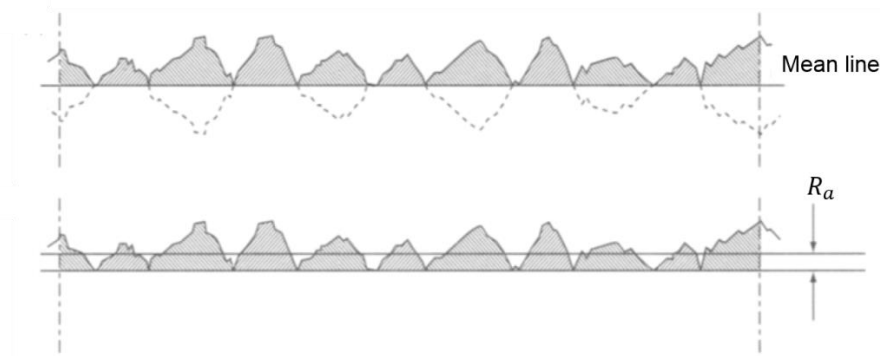


Figure 5-10. Arithmetic mean of a profile refers to the mean line [57].

- R_q is the root mean square associated to R_a (Figure 5-11).

$$R_q = \sqrt{\frac{1}{l_r} \int_0^{l_w} z(x)^2 dx} \quad (5.2)$$

- R_v is the maximum depth of the profile below the mean line (Figure 5-11).
- R_p is the maximum height of the profile above the mean line (Figure 5-11).

- R_t is the maximum peak to valley height (Figure 5-11).

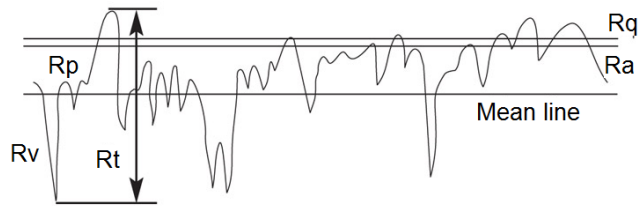


Figure 5-11. Illustration of the main amplitude parameters that referred to the profile.

- Amplitude density distribution. This curve shows the histogram of the height values of the profile.
- Material ratio curve (MR). This curve can be identified from a statistical point of view as the *cumulative distribution curve*, which is by definition the integral of the amplitude density distribution (Figure 5-12).

$$MR(h)\% = \left(\int_{-\infty}^h p(z) dz \right) * 100 \quad (5.3)$$

It is used to characterize surfaces used for bearing and, therefore, it is useful in this work because the surfaces under investigation create a bearing area with the return electrode surface.

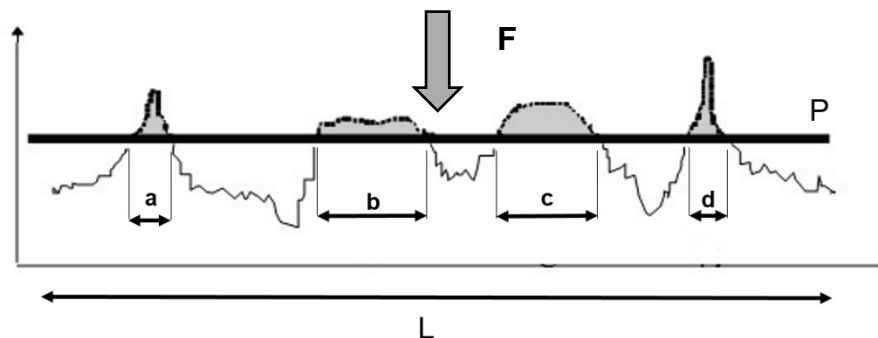


Figure 5-12. Load bearing area

$$MR(h)\% = \frac{a + b + c + d}{L} * 100 \quad (5.4)$$

5.4 Surfaces under investigation

Three different surfaces were analysed. They are the sides of three different CFRP test samples (Figure 5-13). The first surface (Figure 5-13a) was the naked side of the first sample, and henceforth, this will be identified as the “*no-layer*” surface. The second sample had the side painted with a layer of silver paint, and thus, the surface under investigation was a “*silver paint*” surface (Figure 5-13b). The third sample was treated with a metal sputtering process depositing a layer of metallization made by 70% Zn – 30% Sn and, thus, the surface under investigation was a “*metal sputter*” surface (Figure 5-13c).



Figure 5-13. Surface of the sample under investigation: a) No-layer surface, b) silver paint surface, c) metal sputtering surface.

5.5 Surface analysis method

The three surfaces were analysed after the contact with the return metal electrode and the compression force had been applied. Moreover, the other three surfaces with the same characteristics as the first three, but without any contact with the metal electrode, were analysed. A comparison between each pair of surfaces was carried out to highlight the eventual effects of the compression force on the surface topography.

The compression force applied was 3900 N , which corresponds to a pressure at the contact surface equal to 4.02 N/mm^2 .

The work flow for the calculation of the parameters is as follows:

- acquisition of the raw TIFF image, or primary TIFF image according to the definition in the previous section, using the method described in the data processing section (Figure 5-5 shows a typical image created by the processing technique).
- application of the filtering technique to the TIFF image in order to isolate roughness and waviness. The raw TIFF image created by the Axiovision® software was transferred in Matlab® and through this software, the filtering process was carried out.
- extrapolation of the roughness and waviness profiles from the roughness and waviness images.
- calculation of the roughness parameters and curves from the images.
- comparison of the parameters between the three pairs of surfaces

5.6 Surface visualization results

As explained previously, an inverted microscope was used, and thus the surface was above the objective of the microscope. This meant that any valley recorded by the microscope corresponded to a peak on the real surface and vice versa. Therefore, an inversion of the data of the picture was required. Furthermore, the surface plane had to be parallel with the focus plane, but, due to the dimensions and the weight of the sample, practically, the surface plane suffered an inclination in respect of the focus plane. Figure 5-14 shows a profile

along the 9.7 mm of height of the surface, and it is possible to see the inclination of the surface with respect of the horizontal plane. In order to correct this issue, a filter in Matlab was used.

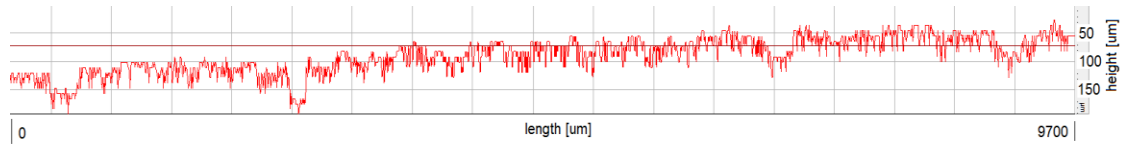


Figure 5-14. Profile inclined in respect of the horizontal line.

5.6.1 no-layer/no-pressure surface

The surface analysed is the *no-layer* surface without the application of the compression force (Figure 5-13a) and the image acquired by the microscope and elaborated by the Axiovision® software is shown in Figure 5-15a. The figure shows the primary areal, which includes the waviness, the roughness and the sub-roughness components.

Figure 5-15a shows the topography of the surface using a grey scale. The figure shows a pattern that follows the construction of the sample as a stack of plies in different directions. The darker bands correspond to the plies in the 0° direction, nine pairs in total, in accordance with the ply lay-up of the CFRP sample. The fibers in those plies run parallel to the surface under investigation.

In Figure 5-15b, the Gaussian filter has been applied with the cut-off wavelength of $2.5 \mu\text{m}$, which means that the noise and the sub-roughness components had been removed.

Figure 5-15c shows the longer wavelengths that define the waviness of the surface. To obtain this picture, a second Gaussian filter with a cut-off wavelength of $250 \mu\text{m}$ had been applied.

Figure 5-15d shows the roughness of the surface, which had been obtained from the subtraction of the waviness (Figure 5-15c) from the filtered image (Figure 5-15b).

Figure 5-15e shows a waviness profile, which had been extrapolated from the waviness picture. It corresponds to a profile traced at $3000\ \mu\text{m}$ of the width of the picture (the red line in Figure 5-15c). The same procedure was completed for the roughness profile (Figure 5-15f) extrapolated from the roughness picture (Figure 5-15d). The sampling length of the roughness was shorter than the sampling length of the waviness. Therefore, the roughness was plotted on the same trace of the waviness, but in a gap between 2800 and $3200\ \mu\text{m}$ (the red circle on the waviness profile shows the location where the roughness had been extrapolated). The image acquisitions show how the band pattern influences all the wavelengths of the surface from the primary to the roughness.

The parameters calculated from the surfaces are shown in Table 5-2. The left section shows the parameters that refer to the roughness amplitude (arithmetic mean R_a , root mean square R_q , deepest valley R_v , highest peak R_p and difference between highest peak and deepest valley R_t); the central section shows the arithmetic mean of the waviness (W_a), whereas the right section shows the variance (R_{var}) and the standard deviation (R_{std}) of the roughness.

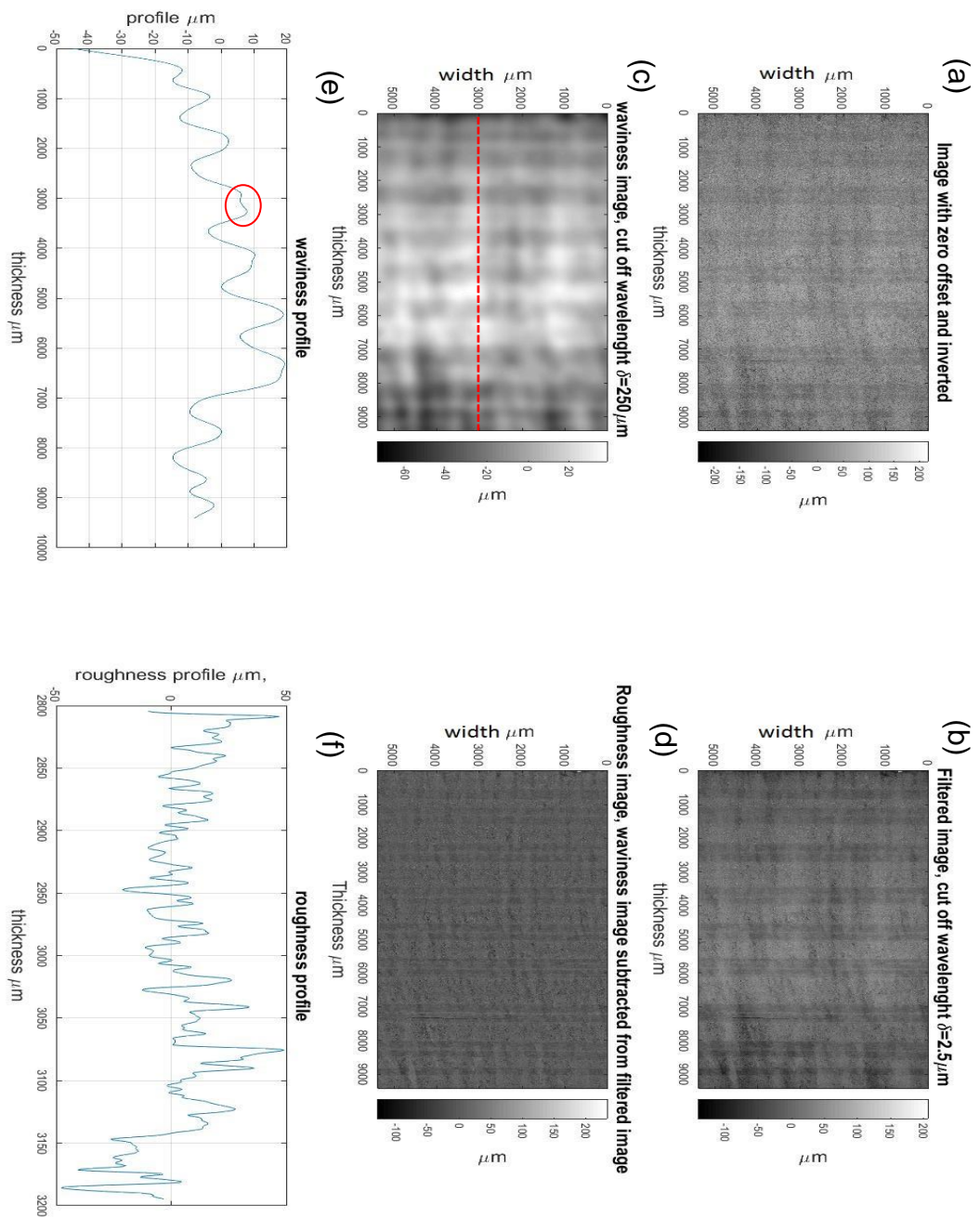


Figure 5-15. Areal and profiles acquisitions from no-layer/no-pressure surface: a) primary areal image, b) areal image filtered from noise and sub-roughness, c) waviness areal image. The red line shows the position of the normal plane where the waviness and roughness profiles have been traced, d) roughness areal image, e) waviness profile. The red circle shows the section where the roughness profile has been evaluated, and f) roughness profile.

Table 5-2. Left section, roughness amplitude parameters. Central section, waviness mean. Right section, statistical parameters of the roughness. All for the no-layer/no-pressure surface.

Roughness parameters		value	Waviness parameters		value	Statistical parameters		Value
R_a		10.66	W_a		13.37	R_{Var}		14.45
R_q		13.84				R_{Std}		3.8
R_v		142.89						
R_p		150.23						
R_t		293.12						

Figure 5-16 shows the material ratio curve (a) and the amplitude density distribution (b) for the primary acquisition (Figure 5-15a). The analysis carried out on the sample without applied force revealed that the height distribution is symmetric around the mean value. Furthermore, the symmetry of the distribution is reflected in the material ratio curve which shows that at the mean line of the surface, which is represented by the ordinate value of zero, the percentage of bearing area is 50%.

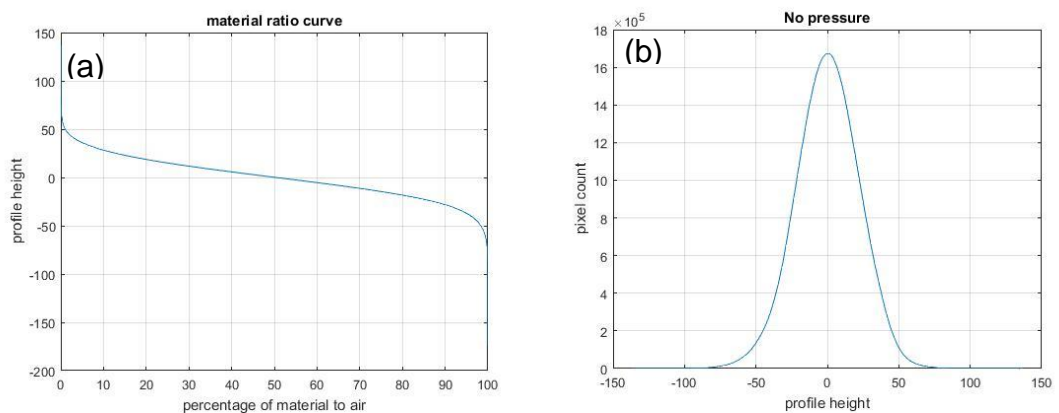


Figure 5-16. a) primary material ratio curve, b) primary magnitude density distribution.

5.6.2 no-layer/pressure surface

Figure 5-17 shows the sequence of acquisitions from the sample with *no-layer* after the application of the compression force of 3900 N. The surface acquisitions (Figure 5-17 a, b, c and d) show the band textures typical of the materials made by layers, and each band corresponds to a layer. The four darker bands refer to four plies where the fibres run parallel to the surface under investigation. The same behaviour was already seen in the no-layer/no-pressure case. However, in this case the darker stripes correspond to the four plies in 90° direction of the ply lay-up. This is due to the fact that this analysis was carried out on the lateral surface of the sample. Nevertheless there is no distinction between the plies in the other three directions. The waviness profile (Figure 5-17e) confirms the presence of the four valleys in correspondence to the plies in the 90° direction. The right side of the acquisition moves close to the border of the sample, and this can be seen through a darker band at the very right edge of the surface images. Furthermore, the waviness profile reveals a sharp drop in the waviness trend.

The parameters calculated from the acquisitions are shown in Table 5-3. As for the previous case, the left section of the table shows the amplitude parameters that refer to the roughness surface acquisition. The central section, on the other hand, refers to the mean of the waviness surface acquisition; whereas the right section shows the statistical parameters related to the height amplitude distribution of the roughness.

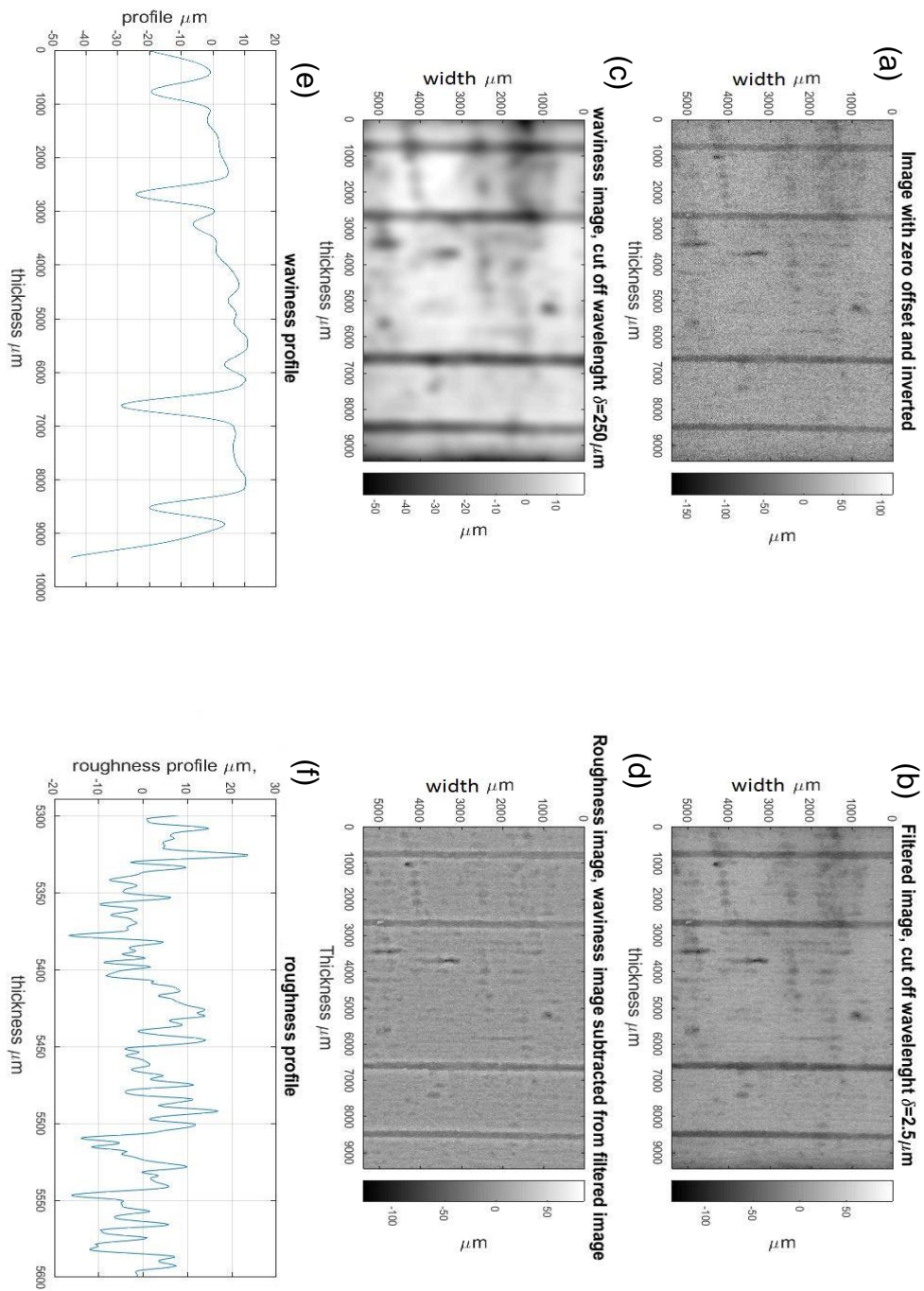


Figure 5-17. Areal and profiles acquisitions from no-layer/pressure surface: a) primary areal image, b) areal image filtered from noise and sub-roughness, c) waviness areal image, d) roughness areal image, e) waviness profile, f) roughness profile.

Table 5-3. Left section, roughness amplitude parameters. Central section, waviness mean. Right section, statistical parameters of the roughness. All for the no-layer/pressure surface.

Roughness parameters	value	Waviness parameters	value	Statistical parameters	value
R_a	8.61	W_a	10.15	R_{Var}	2.3
R_q	11.31			R_{Std}	1.51
R_v	129.06				
R_p	87.65				
R_t	216.71				

Figure 5-18 shows the material ratio curve (a) and the amplitude density distribution (b) for the *no-layer* sample after the application of the compression force.

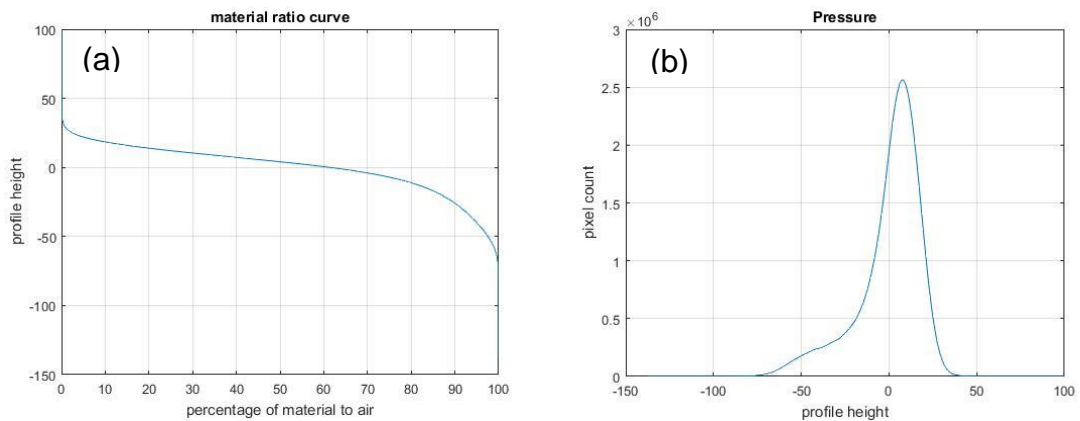


Figure 5-18. a) primary material ratio curve, b) primary magnitude density distribution.

5.6.3 Comparison pre- and post- compression

Table 5-4 shows a comparison of the main parameters regarding the roughness and the waviness, and the statistical values from the roughness amplitude

distribution. The columns (a) show the values from the sample without the compression force having been applied, whereas the columns (b) show the values for the sample after the application of the compression force. The table shows a decrease in the roughness mean of approximately 20% in line with the decrease in the root mean square. The compression force does not influence substantially the depth of the valley; indeed, the two samples show similar maximum depth lengths. Conversely, the compression force plays a role in the height of the peaks, as the height peak is decreased by approximately 40%. The waviness is subjected to a modification due to the compression with the result of a decrease in the waviness mean of 24%.

Table 5-4. Comparison between no-pressure and pressure of the *no-layer* surfaces: a) data referred to the no-pressure case, b) data referred to the pressure case.

Roughness parameters	Value (a)	Value (b)	Waviness parameters	Value (a)	Value (b)	Statistical parameters	Value (a)	Value (b)
R_a	10.66	8.61	W_a	13.37	10.15	R_{Var}	14.45	2.3
R_q	13.84	11.31				R_{Std}	3.8	1.51
R_v	142.89	129.06						
R_p	150.23	87.65						
R_t	293.12	216.71						

The comparison between Figure 5-15c and Figure 5-17c shows how the pressure modifies the waviness creating a flatter surface. The topography in the second picture tends to be more homogenous due to the flattening of the surface. However, as discussed previously, the compression force does not affect substantially the depressions of the surface. Indeed, the four valleys in correspondence with the four plies at the 90° direction are still present.

Figure 5-15e and Figure 5-17e show the waviness profile. In Figure 5-15e, the waviness shows a trend that is rather undulating, and it moves in the gap between $+20$ and $-20 \mu\text{m}$, that means a gap of $40 \mu\text{m}$ whereas, in Figure 5-17e, the gap is reduced to $30 \mu\text{m}$, from $+10$ to $-20 \mu\text{m}$, sign that the surface was compressed and deformed.

The roughness images (Figure 5-15f and Figure 5-17f) also show a restriction of the band of fluctuation of the roughness from $100 \mu\text{m}$ before the compression to $40 \mu\text{m}$ after compression.

Figure 5-16a and Figure 5-18a show the material ratio curves of the two surfaces. These curves have been used in this work to quantify the ideal bearing surface as a percentage of the total surface. Considering the zero profile height (the mean line) as a reference for both graphs, the *no-pressure* curve reveals how a hypothetical flat plane in contact with the surface at the height of the mean line would touch 50% of the entire surface. After the application of the compression force, the same plane would touch 60% of the entire surface confirming an increase in the contact surface after the application of the pressure.

Figure 5-16b and Figure 5-18b show the amplitude density distribution of the height of the profile, and for the *no-pressure* sample, the distribution is nearly symmetric around the mean value of zero. The sample with compression force shows a deformation of the distribution with the appearance of a negative tail. Furthermore, in Table 5-4, it is possible to note a decrease in the standard deviation and variance moving from a *no-pressure* sample to a *pressure* sample.

5.6.4 Metal sputter/no-pressure surface

Figure 5-19 shows the acquisitions from the surface covered by a layer of sputtered metal. The sputtering process does not create a completely flat surface; instead, the analysis reveals the presence of valleys, that is, dark bands which correspond to the plies in the 0° direction of which there are nine pairs in total, and peaks, that is, light bands. This pattern follows the same pattern of the CFRP surface underneath the metal sputtered layer. In comparison with the *no-layer case/no-pressure* (Figure 16), sometimes the pair is not completely discernible, and it looks like a single ply. The band texture is visible in images of all the four surfaces (Figure 5-19 a, b, c and d), which means that the texture affects the primary, the waviness and the roughness. Table 5-5 shows the parameters calculated from the data acquisition. In comparison with the *no-layer/no-pressure* surface, the parameters show a 14.6% decrease in the arithmetic mean of the roughness. A 5% decrease of the arithmetic mean of the waviness was recorded. Furthermore, the table shows a decrease in all the parameters compared to the *no-layer/no-pressure* case; that is because the surface under investigation follows the undulation of the underneath surface. An additional confirmation of these behaviours comes from the standard deviation of the amplitude distribution, which is 1.01 instead of the 3.8 for the other case.

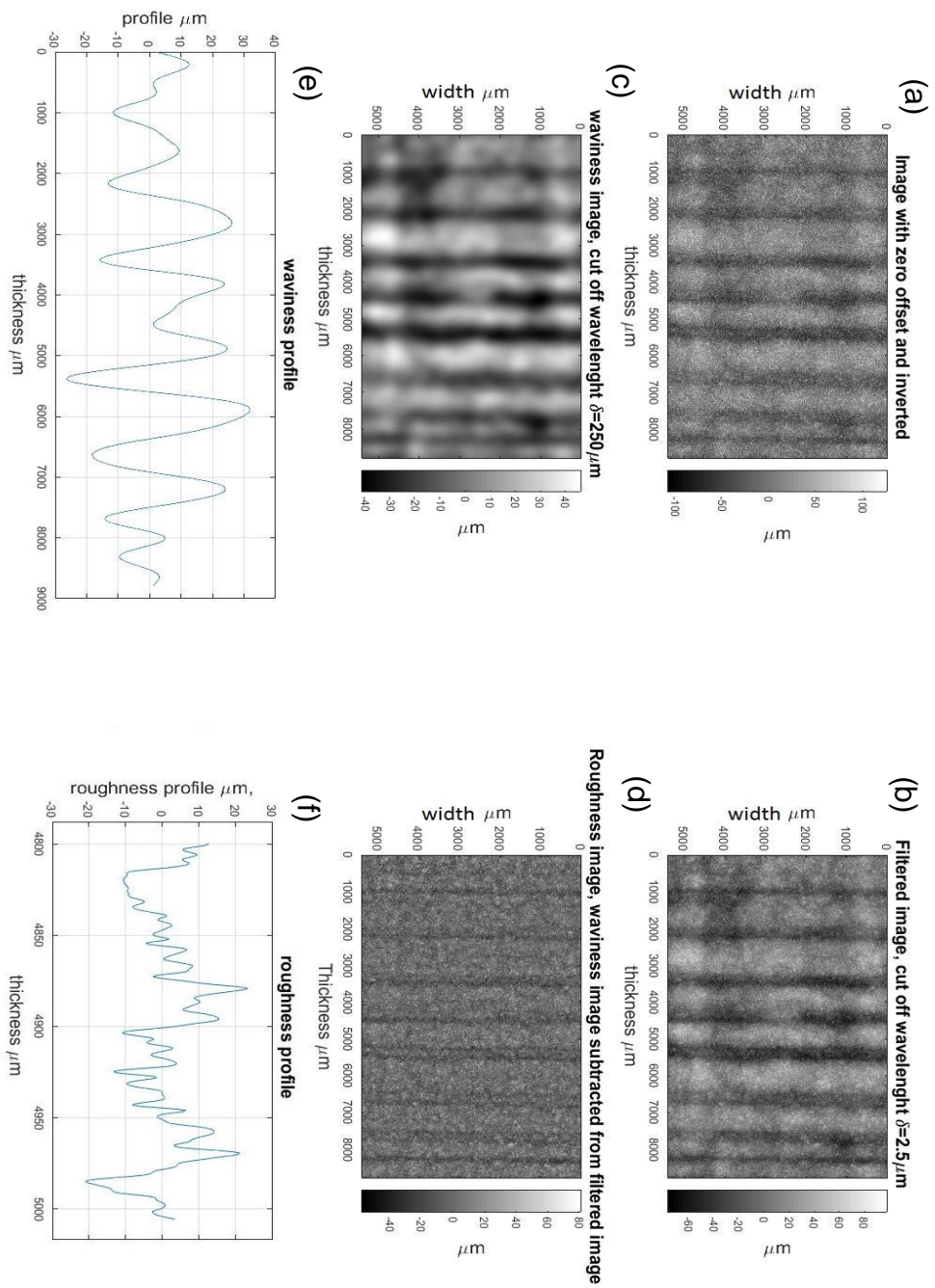


Figure 5-19. Areal and profiles acquisitions from metal sputter/no-pressure surface: a) primary areal image, b) areal image filtered from noise and sub-roughness, c) waviness areal image, d) roughness areal image, e) waviness profile, f) roughness profile.

Table 5-5. left section, roughness amplitude parameters; central section, waviness mean; right section, statistical parameters of the roughness. All for the metal sputter/no-pressure surface.

Roughness parameter	value	Waviness parameters	value	Statistical parameters	value
R_a	9.1	W_a	12.61	R_{Var}	1.02
R_q	11.45			R_{Std}	1.01
R_v	54.34				
R_p	81.28				
R_t	135.63				

Figure 5-20 shows the material ratio curve (a) and the height density distribution (b). The distribution appears to have a good level of symmetry around the mean line, whereas the material ratio curve shows the symmetry of the bearing surface around the mean line.

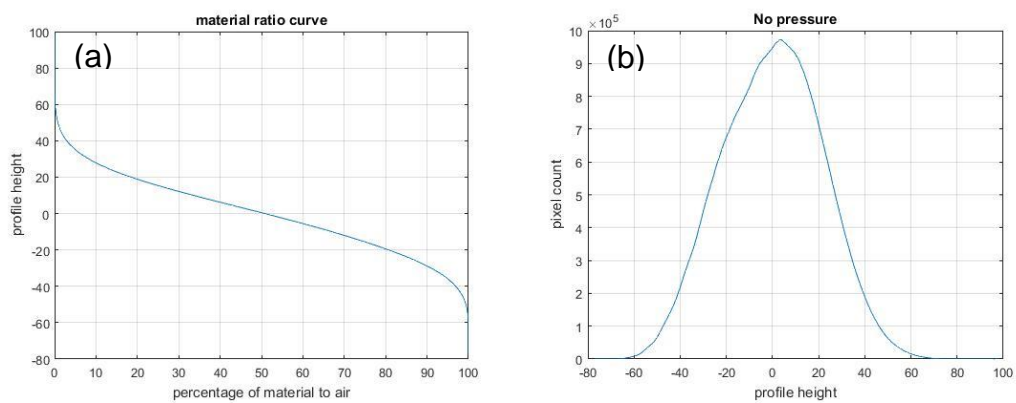


Figure 5-20. a) primary material ratio curve, b) primary magnitude density distribution.

5.6.5 Metal sputter/pressure surface

Figure 5-21 shows the acquisition from the metal sputter surface after the application of the compression force of 3900 N . Figure 5-21a and Figure 5-21b show a homogeneous surface, and the band pattern, which characterizes the rest of the surfaces, as seen previously, is less marked. Still present are the darker bands related to the four 90° direction plies, but they are softer and sometimes undistinguishable compared to the other cases. Focusing on the waviness image (Figure 5-21c), it is possible to notice a brighter part in the centre of the image, which means a higher zone. This brighter zone becomes darker closer to the edges of the sample. The waviness profile reveals a trend with a bell shape. The reason for this curvature is that the compression applied to the surface had a more pronounced effect on the edges of the surface with a consequence of a more pronounced plastic deformation. Table 5-6, left section, shows the parameters of the surface roughness. On the central section is the arithmetic mean of the waviness and the statistical parameters calculated from the amplitude density distribution of the roughness are shown in the right section. In comparison with the case of *no-layer/pressure*, the arithmetic mean is 15.4% lower; the highest peak and the deepest valley are reduced, too. Instead, the effects of the compression force on the edges of the sample helped to get the waviness mean higher than the *no-layer/pressure* case. The standard deviation of the roughness is substantially lower than the *no-layer/pressure* case, with 0.82 against 1.51 .

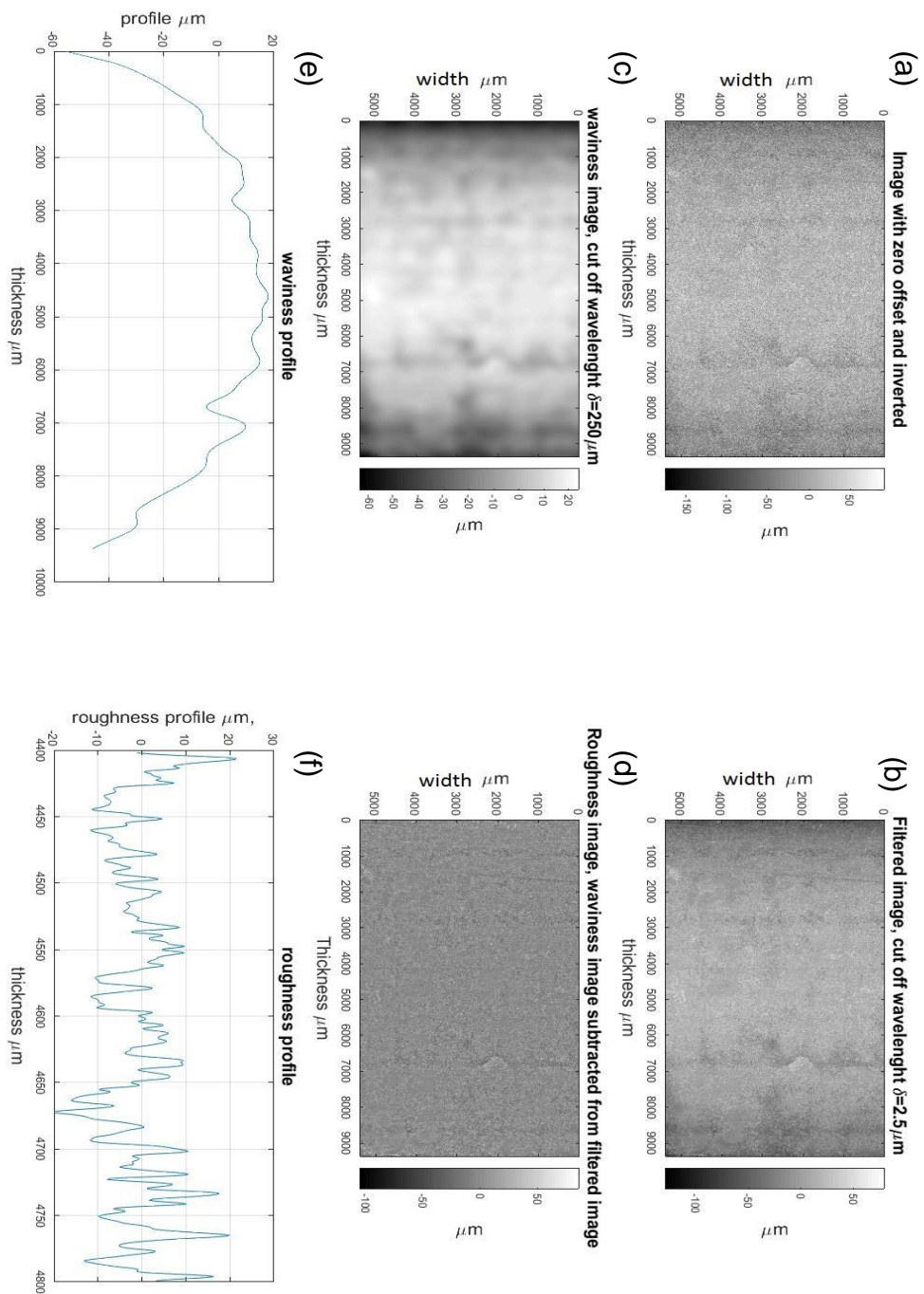


Figure 5-21. Areal and profile acquisitions from metal sputter/pressure surface: a) primary areal image, b) areal image filtered from noise and sub-roughness, c) waviness areal image, d) roughness areal image, e) waviness profile, f) roughness profile.

Table 5-6. Left section, roughness amplitude parameters; central section, waviness mean; right section, statistical parameters of the roughness. All for metal sputter/pressure surface.

Roughness parameter	value	Waviness parameters	value	Statistical parameters	value
R_a	7.28	W_a	12.99	R_{Var}	0.67
R_q	9.22			R_{Std}	0.82
R_v	105.68				
R_p	81.92				
R_t	187.61				

In Figure 5-22a, the material ratio curve shows the ideal bearing area of the surface, whereas Figure 5-22b shows the magnitude density distribution. The two graphs are comparable to that of the *no-layer/pressure*, and for magnitude distribution, it is possible to discern the presence of the negative tail, which has been already seen for the previous case. The negative tail of the magnitude distribution is the consequence of the fact that after the compression the peaks of the surface were plateaued whereas the valleys were unaffected.

Overall, the comparison between the *no-layer/pressure* surface and the *metal sputter/pressure* surface revealed the same behaviour in terms of amplitude density distribution; indeed, both cases showed that the negative tail and the material ratio curves can be superimposed. The metal *sputter/pressure* case showed a smoother surface in terms of roughness mean. However, the waviness had been affected negatively by the compression force at the edges of the sample, showing a higher value compare to the *no-layer* case.

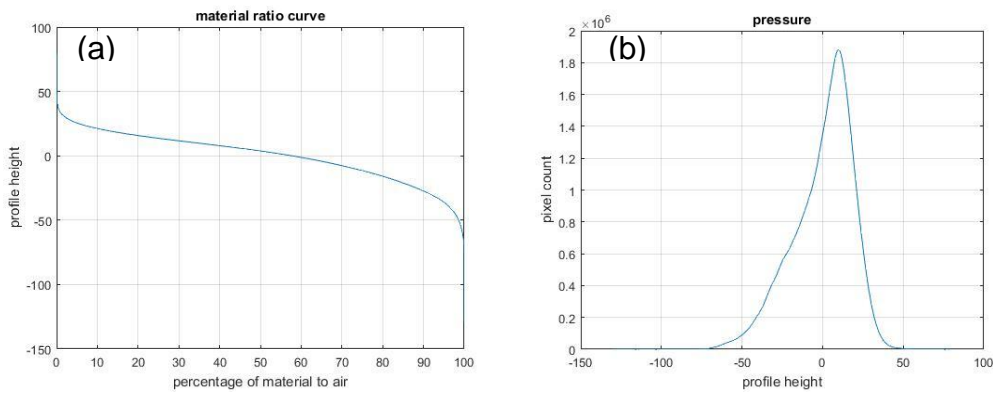


Figure 5-22. a) primary material ratio curve. b) primary magnitude density distribution.

5.6.6 Comparison no-pressure/pressure surfaces

Table 5-7 combines Table 5-5 and Table 5-6 to make a comparison between the two *metal sputter* surfaces. The roughness mean decreased by 20% after the application of the compression in line with the *no-layer* pair. The compression force does not affect the valleys. No substantial variation was noted for the height of the highest peak. The waviness mean was subjected to an increase after the compression force because the force deformed the edges of the sample creating a bell shape of the waviness profile. A decrease appeared for the standard deviation of the roughness amplitude distribution quantifiable with approximately 20%. The standard deviation represents an estimation of the variability of the heights of the surfaces. A decreasing in the standard deviation means that the height values are closer to the mean and this is, physically, the consequence of the compression of the surface peaks.

Table 5-7. Comparison between no-pressure and pressure of the metal sputter surfaces: a) data referred to the no-pressure case, b) data referred to the pressure case.

Roughness parameter	Value (a)	Value (b)	Waviness parameters	Value (a)	Value (b)	Statistical parameters	Value (a)	Value (b)
R_a	9.1	7.28	W_a	12.61	12.99	R_{Var}	1.02	0.67
R_q	11.45	9.22				R_{Std}	1.01	0.82
R_v	54.34	105.68						
R_p	81.28	81.92						
R_t	135.63	187.61						

A comparison between the series of acquisitions (Figure 5-19 and Figure 5-21) emphasises the effect of the compression force on the surface pattern. For the *no-pressure* sample, the topography follows the band pattern typical of the CFRP sample made by layers, and they are visible in the primary, waviness, and roughness areal acquisition. The application of the compression force flattens the surface at a point where the bands pattern is almost invisible, and just the valleys related to the four 0° plies are slightly distinguishable. This variation affected both the raw surface and the waviness. The roughness was less affected by the compression force compared to the waviness. A comparison between the two roughness profiles underlines how both profiles are confined in a band between -20 and $+20 \mu m$.

The evaluation of the differences between the two material ratio curves (Figure 5-20a and Figure 5-22a) shows how the application of the compression force has modified the ideal bearing area as well. The evaluation of the ideal bearing area at the mean line reveals an increment from 50% to 60% . Moreover, the

amplitude distribution was affected by the compression force. As a matter of fact, Figure 5-20b shows a distribution which is almost symmetric around the mean line, whereas, for the *pressure* sample, the distribution is asymmetric around the mean line and the negative tail that is typical of a surface which was deformed by a compression force.

5.6.7 Silver paint/pressure

The sample with the edge hand painted by silver paint was available only after the application of the compression force; thus, the surface was analysed and a comparison made with the two previous samples examined in this section.

Figure 5-23 shows the acquisition of the silver paint surface after the application of the compression force. Figure 5-23a, b and c show a brighter part on the right side, which is a consequence of the compression force that acted more on that specific part because that part formed a plateau higher than the rest of the surface, and thus, was more compressed. The roughness was affected as well by the compression on that region. Figure 5-23d shows a reduction in contrast in that area because of the flattening. The reason for the plateau can be explained by considering an accumulation of silver paint on that specific zone. All four areal images show again the band pattern, and each band refers to a ply of the sample. Again, four darker channels related to the four plies in the 0° direction are visible, and one of them is deeper than the others. This, in turn, depends on the depth of the channel underneath the silver paint, that is, the channel created by the ply. The waviness profile calculated on a horizontal line at $3000 \mu\text{m}$ reveals the increment of altitude of the surface after $2000 \mu\text{m}$. Furthermore, it shows the deep valley in correspondence with the 0° direction ply.

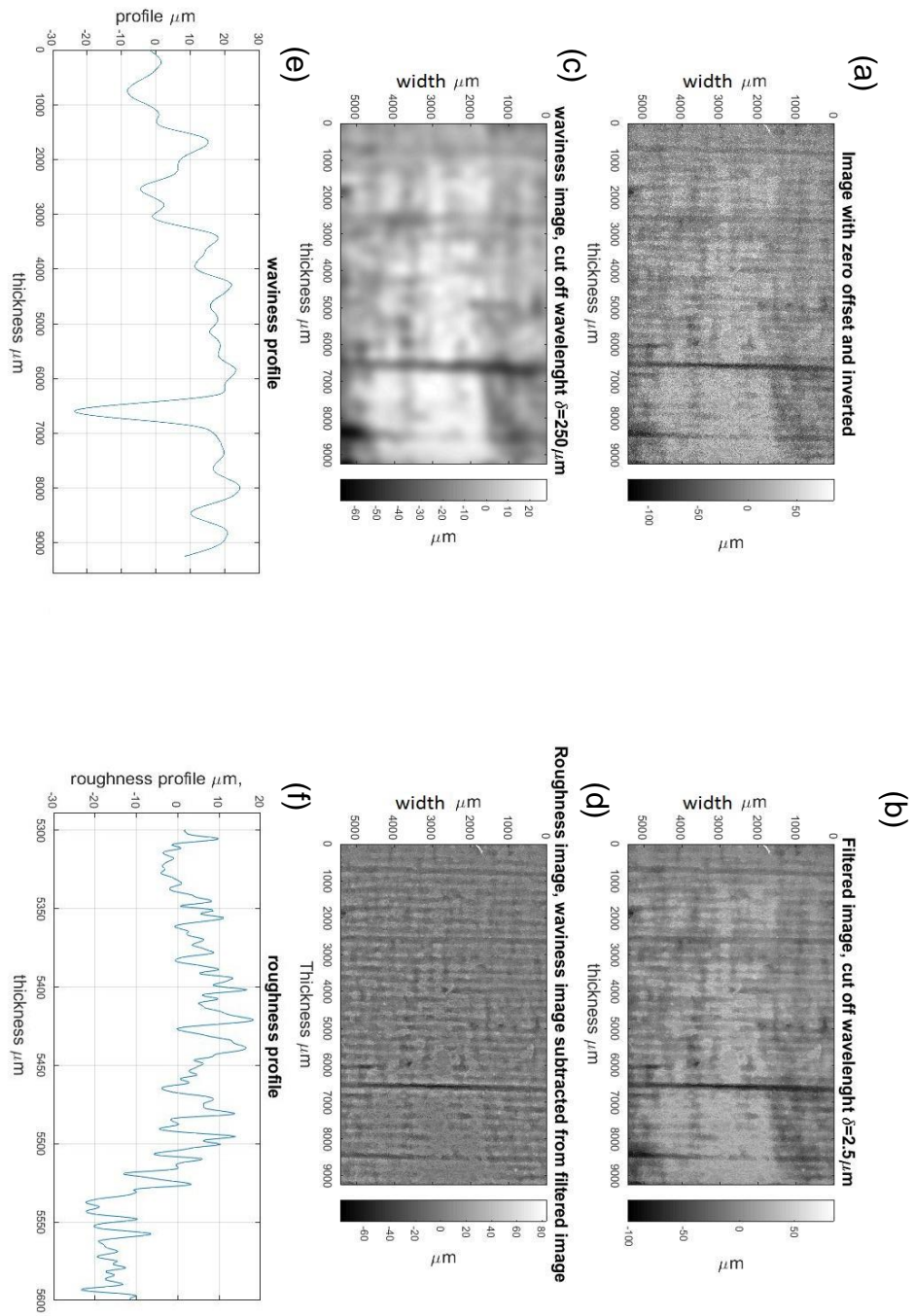


Figure 5-23. Areal and profiles acquisitions from silver paint/pressure surface: a) primary areal image, b) areal image filtered from noise and sub-roughness, c) waviness areal image, d) roughness areal image, e) waviness profile, f) roughness profile.

Table 5-8 shows the roughness parameters, on the left side, and a comparison with the other two samples analysed after the application of force (b for the *no-layer* sample and c for the *metal sputter* sample) reveals that this last roughness has the highest mean and the highest root mean square. The waviness mean is higher than the *no-layer* case but is lower than the *metal sputter* case. However, it must be emphasised that, for the *metal sputter* case, the deformation of the edges of the sample is due to the compression force. It might be feasible that without the smoothing of the edges, the waviness mean would be the lowest.

The statistical parameters of the roughness amplitude distribution show a decrement starting from the *silver paint* case to the *metal sputter* case.

Regarding the length of the highest peak and the deepest valley of the data acquired, they do not show a predictable trend.

Table 5-8. Comparison between silver paint (a), no-layer (b), metal sputter (c) cases after the application of the compression force.

Roughness parameters	Value (a)	Value (b)	Value (c)	Waviness parameters	Value (a)	Value (b)	Value (c)	Statistical parameters	Value (a)	Value (b)	Value (c)
R_a	8.8	8.6	7.3	W_a	10.6	10.1	13	R_{Var}	6.6	2.3	0.67
R_q	11.4	11.3	9.2					R_{Std}	2.5	1.5	0.82
R_v	79.8	129	105.7								
R_p	84.5	87.6	81.9								
R_t	164.3	216.7	187.6								

The material ratio curve shown in Figure 5-24a shows an ideal bearing area at the mean line equal to 50% of the entire area. For the other two cases, after the

application of the compression force, the bearing area was 60% of the entire area. Thus, it might be conceivable that before the compression, the bearing area of the silver paint surface at the mean line would be less than 50%.

Instead, the shape of the amplitude distribution is comparable with the other two cases, and the negative tail typical of the surfaces after the application of the compression force is visible.

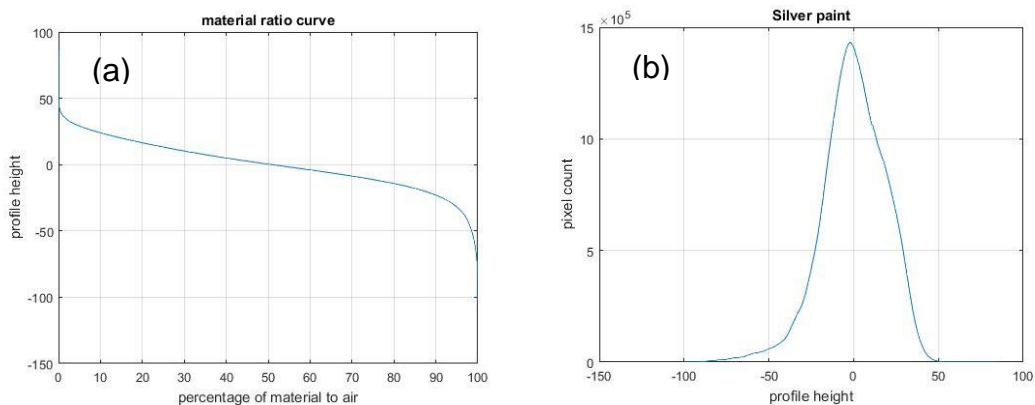


Figure 5-24. a) primary material ratio curve, b) primary magnitude density distribution.

5.7 Conclusion

This chapter has explored the roughness characterization of three surfaces. One of the three surfaces was covered by a metallized layer made by a sputtering process. Another one was covered by a hand painted layer of silver paint, whereas the third sample had its side without any coating. The characterization was carried out using an advanced technique based on the use of the optical microscope. The advantage of this technique is the ability to create areal images of the surface, using the focus stacking technique, instead of simple profiles; this makes it possible to take into account a superior quantity of data for a specific surface compared to a profile characterization. Furthermore, through the optical microscope technique, it is possible to

extrapolate from the areal acquisition any quantity of profiles, which can be used for characterization of the surfaces, such as for a simpler illustration of the topography of the surfaces using 2D graphs instead of 3D graphs.

The disadvantages of this technique are that the equipment is more complex and expensive compared to a profilometer. Furthermore, it is necessary to use one software programme to manage the microscope and to manage the focus stacking procedure, and another software programme to process the microscope acquisitions. Moreover, the technique is more time consuming compared to the profilometer technique. The computational cost is dependent on the size of the area under investigation.

Three pairs of surfaces, the first three surfaces without any compression force applied whereas, the second three after the application of a compression force of 3900 N , were analysed and characterized. The aim of the study was to understand how the deformation of the surfaces, due to the compression force, influences the roughness parameters that had been calculated previously. It has been seen that for the two coated surfaces, the compression force leads to a decrease in the roughness mean and root mean square. Furthermore, the standard deviation and variance are subjected to a decrease as well. The analysis of the amplitude distribution reveals that, before the distribution, its shape was symmetrical around the main value, but after the compression, a negative tail appeared in both samples, indicating that the negative tail could be associated with surfaces that have the peaks plateaued by the compression force and the valley unaffected.

The material ratio curve was used to quantify, in percentage, the ideal bearing area of the surface when in contact with another surface. It has been seen that

for the *no layer* and *metal sputter* surfaces, the ideal bearing area is subjected to an increment after the compression of 10%.

The comparison between the three surfaces after the compression revealed that the *metal sputter* surface shows the lowest values of roughness mean, root mean square and standard deviation. Thus, it can be considered as the less rough surface both before and after the compression. However, during the electrical test, the sample mounting in the test rig was not ideal, and this resulted in a deformation of the edges of the sample. This affected the waviness of the surface. After the electrical test, the waviness had increased instead of decreasing as occurred with the *no-layer* surface.

The *silver paint* case was analysed only after the compression; thus, there is no comparison available for before and after the electrical test. However, the hand painting of the silver paint layer created an accumulation of paint in a specific zone creating a plateau higher than the rest of the surface. Therefore, the compression force acted more on that plateau creating a flatter surface than the rest of the sample. The silver paint case showed the highest roughness mean, root mean square, and standard deviation positioning it as the roughest surface of the three.

Another aim of this investigation is to investigate whether it is possible to link the electrical resistance of the contact surface with the surface characteristics. It is possible to conclude that a decrease in the electrical resistance, due to an increase in the compression force, can be related to the decrease in the roughness mean and standard deviation of the roughness distribution.

These results can be applied in the development of new test arrangements and new test standards. It was seen that the surface roughness influences the contact resistances of the metalized samples with the results of a comparable contact resistance compare to the samples with fasteners grounding arrangement. These results can be considered the starting point for further investigations in order to find new methods and applications that have the capabilities of control some aspects of the grounding arrangement such as the surface characteristics and in turn the contact resistance.

The findings of this test campaign can be useful as well to predict the behaviour of the contact resistance and the surface parameters, at the contact interface between CFRP panels and fasteners structures which are very common in aircraft. The interference fit fastening acts as a compression force applied at the interface therefore, the same results of this test campaign can be valid as well for this structure. The tighter is the fit between the fastener and the panel and the lower is the contact resistance. Application of metal layers can be helpful, between CFRP surfaces in contact, when the current flow needs to be facilitated. Metallization through sputtering techniques can be more expensive and time consuming compare to the metallization through silver paint but it ensures the flow of higher level of current.

Chapter 6

High current test: experimental results on thermal and electrical variables measured under lightning current excitation

6.1 Introduction

The DC low current tests revealed the correlation between the contact resistance of the grounding system and the contact pressure for the side grounding arrangements. Furthermore, it could be seen that the coated side grounding arrangements, the metal sputter coating, and the silver paint coating showed comparable resistance with the fastener grounding systems for a range of contact force between *600 N* to *3900 N*. The *no-layer* case showed a similar performance in terms of contact resistance only for the highest values of compression force applied in comparison with all the other cases.

In this chapter, the performance of the grounding arrangements in a high current test environment is analysed. The high current tests are those for which the test samples are usually developed. Thus, the high current analysis represents the most important key objective of this work because the results of this analysis are proof of the quality of the grounding arrangement in a real high current test scenario.

This experiment measured the contact resistance of the grounding arrangements when the sample is subjected to an impulse current, which is a laboratory reproduction of a lightning current. Furthermore, a thermal analysis

was carried out to evaluate the performance of the grounding systems in terms of heating due to Joule effects. The results from all the samples were compared in order to evaluate the advantages and disadvantages of each.

6.2 Lightning current generator

The MBLL current generator reproduces the A, B, C, and D components. Each waveform is produced by a dedicated circuit, except for the D component, which is produced by a sub part of the circuit used to produce the A component. Therefore, the four components are produced by three circuits. This section describes in detail the A/D circuit, which is the circuit used to test the CFRP samples.

Figure 6-1 shows the schematic of the A/D components generator. The generator comprises a charging unit, a set of capacitance and a spark gap

The D capacitor bank is a single branch of the A bank. In addition, dumping and earthing switches are used for safety, specifically to keep the circuit grounded during the non-operation time and to discharge eventual charge still stored within the capacitances after the firing.

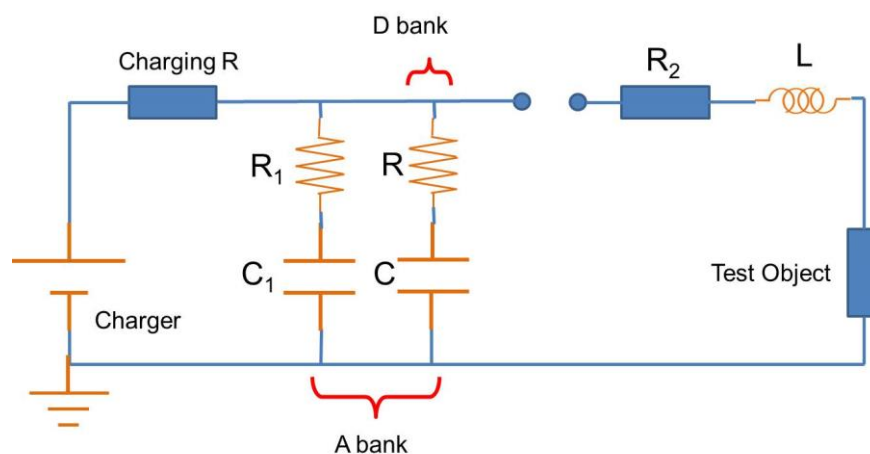


Figure 6-1. Schematic diagram of the A/D components generator.

6.3 Damage threshold assessment and outgassing phenomenon

Moving from low current test to high current test, usually the thermal effects become predominant. Most of the time, the limitations of a device to carry current are imposed by thermal conditions. The analysis focused on the performance of the grounding systems from the thermal point of view, specifically at the interface between the grounding system and the CFRP sample. Chemartin et al. [60] [61] suggested that thermal effects, due to current flow, at the interface region may originate in the two main mechanisms, namely, voltage sparks and thermal sparks. Although they considered the thermal and voltage sparks as a unique event, further studies have clarified that the two events have different mechanisms and physics. The voltage spark is a phenomenon related to the enhancement of the electric field between two materials separated by an insulator medium. If the electric field exceeds the dielectric strength of the medium, a voltage arc can appear between the two materials. The phenomenon can be present at the interface between two materials because the non-zero roughness of the members of the contact creates voids and gaps filled with air or other insulating materials. The thermal spark phenomenon is driven by the enhancement of the current density at the contact points between the two materials. The increase in current density leads to an increase in the temperature of the material through the Joule effect resulting in a thermal breakdown. Under particular conditions, both phenomena can lead the conductors of the contact interface to explode and eject molten debris due to a rapid increase in the pressure of the air trapped in the voids.

In the aerospace field, the phenomenon of ejection of molten debris from a contact interface is commonly known as outgassing. The mechanism and

physics of the thermal and voltage sparks, which lead to an overpressure at the contact interface with the consequence of the ejection of very hot particles, are carefully considered in the aerospace field. The studies carried out on the phenomenon are mostly concerned with the interface between the CFRP panels and the shank of metal fasteners that are usually used to join parts of the aircraft structure, such as fuel tank. Figure 6-2 shows the cross section of a typical joint structure where it is possible to identify a composite material, which is the skin of the aircraft at the level of the fuel tanks, and it is covered by a metallic protection and a paint layer, a rib or a spar made of either a composite or a metal, a fastener which joins the two parts and a nut to tighten the joint. Furthermore, an electrical insulating glass fibre layer can be present to limit the current flow from the outer skin to the inner part of the structure. The event of a lightning attachment on the head of the fastener creates a current path that runs from the fastener to the CFRP skin. However, a smaller part of the current can flow through the spar/rib. In both cases, the current must cross a contact interface with the possibility of the occurrence of the outgassing phenomenon. The ejection of hot particles usually appears at the nut interface.

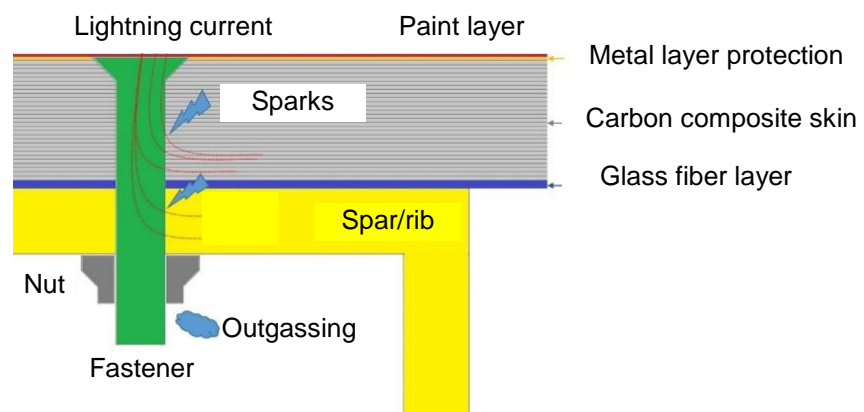


Figure 6-2. Simplified cross section of a T joint and the outgassing phenomenon at the interface between the fastener and the CFRP skin, spar/rib.

Under particular conditions, the hot particles produced by the outgassing can ignite the fuel if the event occurs within the fuel tank of the aircraft, with catastrophic consequences [62] [63]. Therefore, avoiding the outgassing event or nullifying its consequence is of primary importance for the aerospace industry.

Sparks and the related outgassing phenomenon can be present at the level of the grounding system of the sample as well. Both categories of grounding arrangement, that is, the *fasteners* and the *side* systems, can be affected by the phenomenon. Figure 6-3 shows a schematic of the phenomenon at the contact interface for the side grounding system.

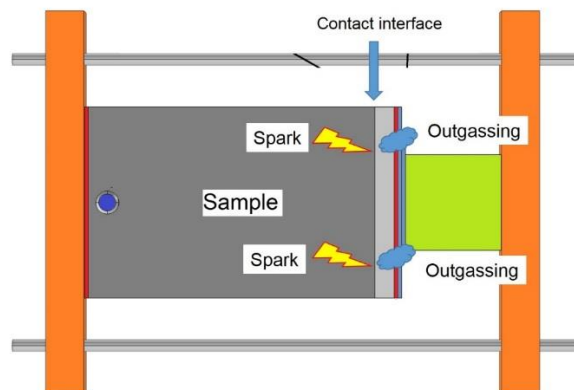


Figure 6-3. Outgassing phenomena at the interface between the CFRP sample and the grounding system.

Although the mechanism and physics related to the outgassing are not yet fully understood, the detection of the sparking phenomenon through the photography technique has been considered as the threshold for the reliability of the grounding arrangement. A similar method is suggested for the detection of the ignition source in fuel tanks in the EUROCAE ED-105 [36]. The test has been developed to answer the question of which level of impulse current each

grounding arrangement can withstand without suffering sparking/outgassing events.

6.4 Test procedure

The samples with the relative grounding systems were tested using an escalation strategy starting from a minimum peak level and ending at the peak level where the sparking phenomenon occurred. All of them were tested using a scaled version of the D component. The D component has been chosen considering the sample to be part of the 2A lightning zone of the aircraft [41]. Each sample was repeatedly tested using an increasing level of the D component magnitude. A still camera and a thermal camera were used to record any sign of sparking and/or outgassing. As said previously, the spark and/or outgassing phenomenon were considered as a threshold due to the ability of the specific grounding system to carry that specific amount of current. After the sparking event, the samples were not tested at higher current magnitude. Furthermore, a current sensor and a voltage sensor were used to measure the current injected and the voltage drop between the injection fastener and the grounding system. Through the current and voltage measurements, it was possible to evaluate the electrical resistance between the injection fastener and the grounding system (the same evaluation was carried out in the low current test campaign of Chapter 4). A comparison was carried out between the results of all the samples and the relative grounding systems.

6.5 Equipment

The equipment used to perform the test campaign included the following:

- D component current generator
- Still camera - used to record a still picture, which shows if a sparking event has occurred at the contact interface between the sample and the grounding system. Each test was carried out in a dark test chamber in order to capture even the smallest spark from the samples. Two red LEDs were placed within the framing of the still camera to verify the correct record of every test. Figure 6-4a shows the still image of the side grounding system before the test with the test chamber illuminated. Figure 9b shows the same framing during the test. The test did not produce any spark; thus, the frame remained completely black. Without the red dots, it is not possible to guarantee that the camera has recorded the image. Instead, the presence of the two red dots ensures that the framing has been correctly recorded.

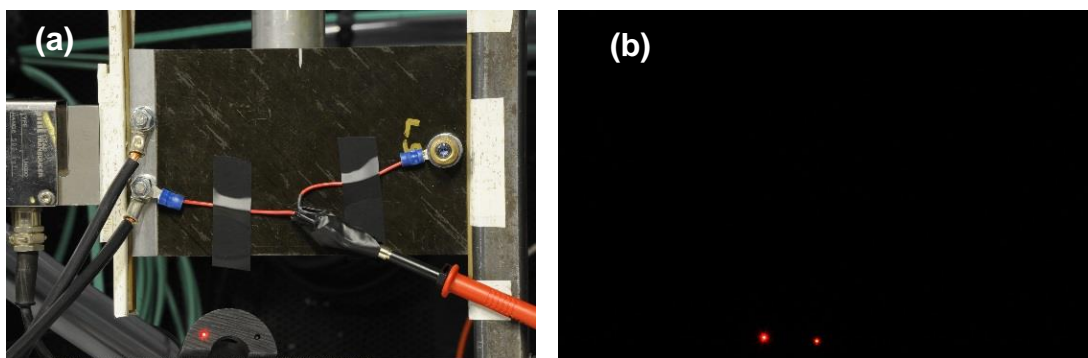


Figure 6-4. a) Still picture of the test sample before the test, b) still picture of the sample during the test. The red dots guarantee the correct record of the framing.

The camera used was a *Nikon D700*, a digital camera with a digital full frame sensor of *12.1 megapixel* coupled with an objective with a focal length of *180*

mm, a focal aperture of $f/22$ and an ISO of 500. The aperture time was 4 seconds for each test. The main advantage of this camera is the reduced level of noise recorded in the low light environments typical of the tests carried out.

- A thermal camera was required to record a sequence of thermal images during the firing events. They show the evolution of the temperature of the sample and the grounding system. Furthermore, it was used to record the ejection of hot particles in the form of outgassing from the contact interface, which do not emit light and, therefore, are not recordable using the still camera.
- The thermal camera used was the *Flir SC 7600*. Each image has an area of 160×128 pixels, and the frame rate was 850 Hz.
- For the current sensor (Figure 6-5), a Rogowski coil was placed around the wires that carried the current from the current generator to the sample. The Rogowski coil has the advantage that it does not disturb the main circuit because it is not electrically connected with any part of the main circuit. However, it requires an amplifier in order to amplify the voltage signal coming out.

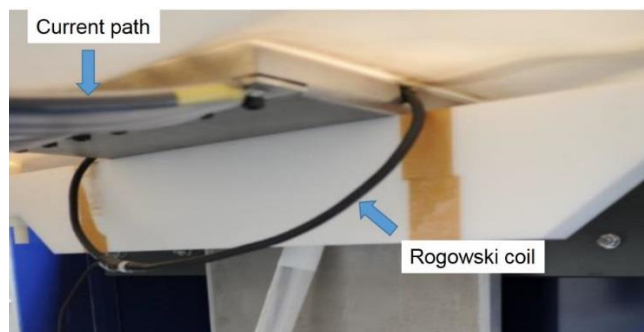


Figure 6-5. Rogowski coil placed around [64].

- Voltage sensor (Figure 6-6), a voltage probe was placed between the injection fastener nut and the grounding system. The two poles of the probe were placed under the nuts and tightened. It was necessary to place the wires very close to the sample in order to reduce the noise collected by the probe. Due to the very high impulse current, the electromagnetic field couples with the circuit of the probe and leads. In order to reduce the level of noise, it is crucial that any closed loop between the sensor and the sample must be as small as possible.

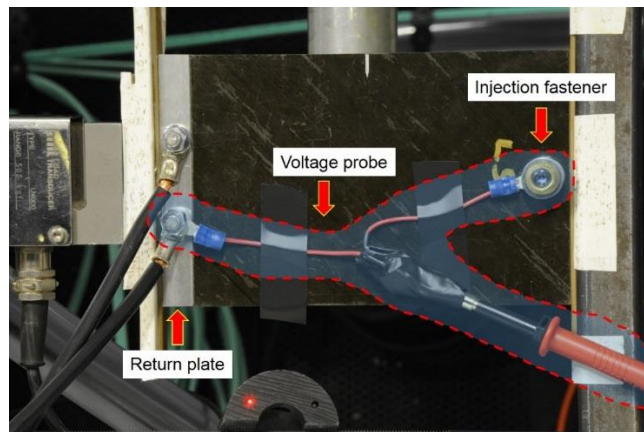


Figure 6-6. Voltage probe placed between the injection fastener and the return plate.

Both the Rogowski coil and the voltage probe were connected to a Tektronix oscilloscope in order to record the current and the voltage waveforms respectively.

6.6 Test samples and relative grounding systems

The grounding systems analysed in this test campaign are the same as those described in the Chapter 4. It was analysed the behaviour of three test sample with three different contact surfaces for the side grounding system, one sample with three fasteners grounding system and one sample with one fastener

grounding system. The three samples with side grounding system needed the special test rig able to control the force applied at the contact surface whereas the two fasteners grounding samples required only a wire connection between the grounding fasteners and the main circuit (for more detailed information on the test samples, the test rig and relative grounding systems please refer to section 4.3 and 4.4). All the samples including the test rig were carefully isolated from the ground plane of the main circuit using nylon blocks in order to avoid any current leaking from the test rig to the ground plane. For all the test samples the injection fastener was connected to the positive terminal of the main circuit through a copper wire of AWG 0 able to carry up to 195 A in DC steady state.

6.7 High current test results

Each sample was tested from a minimum current peak of 5 kA, which is the minimum available for the current generator. For each sample, the following data were recorded:

- current waveform
- voltage waveform
- still pictures before and during the test
- still picture of the side surface in contact with the metal electrode after the test
- pictures from the thermal camera acquisition before and during the test

Furthermore, the resistance value of each sample and grounding system was calculated using the voltage and current waveforms recorded through the

oscilloscope. The voltage drop measured by the voltage sensor can be defined mathematically as follows:

$$V_l(t) = Ri(t) + L \frac{di(t)}{dt} \quad (6.1)$$

where,

- $V_l(t)$ is the voltage drop measured across the sample and grounding system
- R is the resistance of the sample and grounding system
- $i(t)$ is the current injected
- L is the inductance of the sample and grounding system
- $\frac{di(t)}{dt}$ is the derivative of the current

The voltage drop comprises a resistive factor and an inductive factor. Figure 6-7, shows the superimposition of the normalized current and voltage waveforms measured from the metal sputter case at 50 kA peak. The figure shows that the two wave shapes are perfectly in phase. Thus, it can be concluded that, for these specific test samples, the inductance and relative reactive voltage drop are negligible and the sample can be considered as a pure resistor.

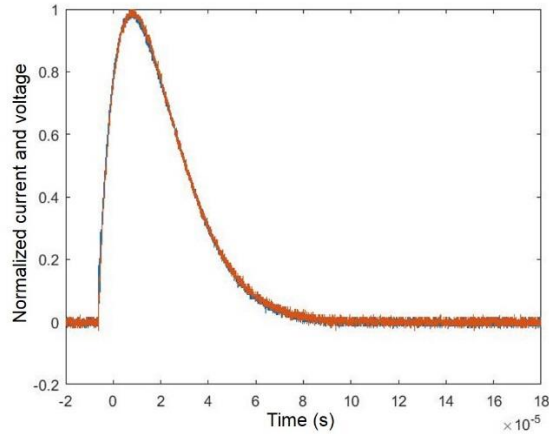


Figure 6-7. Normalized current and voltage superimposed.

Typical voltage and current acquisitions are shown in Figure 6-8. According to Equation (6.1), at the instant of peak current, the derivative of the current is zero. Therefore, Equation (6.1) can be reduced as

$$V_{l,p} = Ri_p \quad (6.2)$$

The resistance was calculated by evaluating the maximum values for the current and voltage from the respective waveforms.

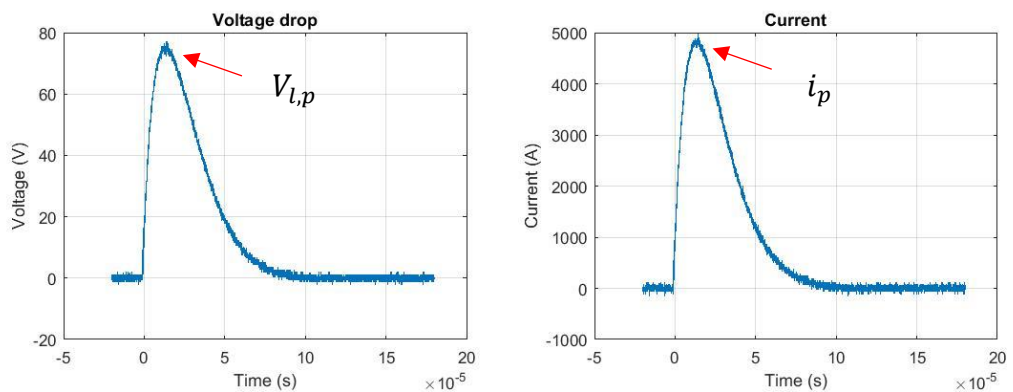


Figure 6-8. Typical voltage and current acquisitions.

The experiments for the three side grounding systems were carried out using the test rig designed for the low current measurements. In accordance with the results of the low current measurements, the lowest resistance appears at the

highest force applied by the clamp, that is, 3900 N . For this test, the same compression force of 3900 N was used to ensure the widest area of contact between the metal electrode and the sample, thus giving a better spreading of current and a lower probability of sparking.

Silver paint grounding system

Table 6-1 shows the measurements carried out on the *silver paint* grounding system for three consecutive current tests: 5, 6, and 7 kA peak. At 7 kA peak, the first sparking event at the contact interface between the sample and the return electrode was recorded. The table shows a decrease in the resistance related to the increase in the current peak. It was assumed that, at high current magnitude, the arc formation due to thermal and/or voltage sparks acts like short circuits between the two surfaces in contact. Section 2.3.1 describes the Voltage – Current characteristic of air gap and it is possible to notice that for voltage sparks in the “arc” region the electrical resistance of the gap is the lowest. The arcs can be considered, from the electrical point of view, as resistances whose values are much smaller than the contact spots resistance. This contributes to the decrease in the total contact resistance. The last column of the table shows the action integral associated with each current waveform. Each step of the current peak leads to an increase in the action integral of approximately 25%.

Table 6-1. Voltage, current, resistance and action integral at 5, 6 and 7 kA peak for *silver paint* sample.

	Voltage (V)	Current (kA)	R (mΩ)	Action integral (kJ/Ω)
sh001	77.1	4.97	15.5	0.598
sh002	89.8	5.87	15.3	0.844
sh003	99.4	7.1	14	1.16

Interestingly, the increase in the current peak from 5 kA to 6 kA led to a decrease in the resistance of 1.3%. A further increase in the peak of 1 kA led to a decrease in the resistance of 8.3%. This, experimentally, can in part prove the previous hypothesis; indeed, at 5 and 6 kA, the presence of sparking within the interface can be inferred because of the small decrease in the resistance. However, as these are not detectable by the still camera, they are not considered as the damage threshold. At 7 kA, the presence of sparking was clearly detected by the still camera and consequently, a faster reduction in the resistance was measured.

Figure 6-9 shows the still pictures before and during the test, while Figure 6-10 shows a zoom shot of the sparking location. No signs of sparking were observed at the injection fastener location.

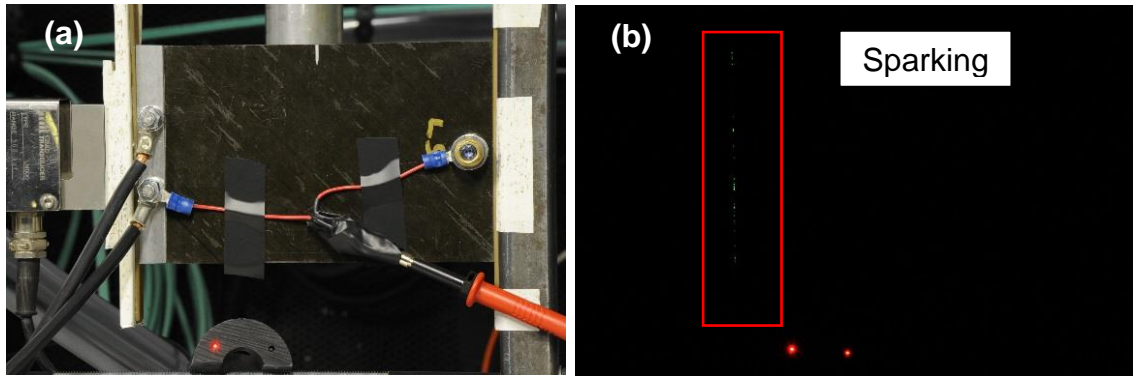


Figure 6-9. a) Still picture before the current injection, b) still picture during the current injection at 7 kA peak. Inside the red rectangle, sparking is visible located at the interface between the metal electrode and sample side.



Figure 6-10. Zooming of the sparking location at 7 kA peak (rotated).

Captures from the thermal camera reveal a sudden increase in temperature at the interface. In Figure 6-11, the temperature of the sample and relative grounding system was recorded before the current injection (a) and during the test (b). Figure 6-11b shows an increase in the temperature near the injection fastener, which follows the direction of the outermost ply of the sample, that is, 135° . Although the full scale of the thermal camera is 80°C , it is very likely that the temperature of the sparks is considerably higher.

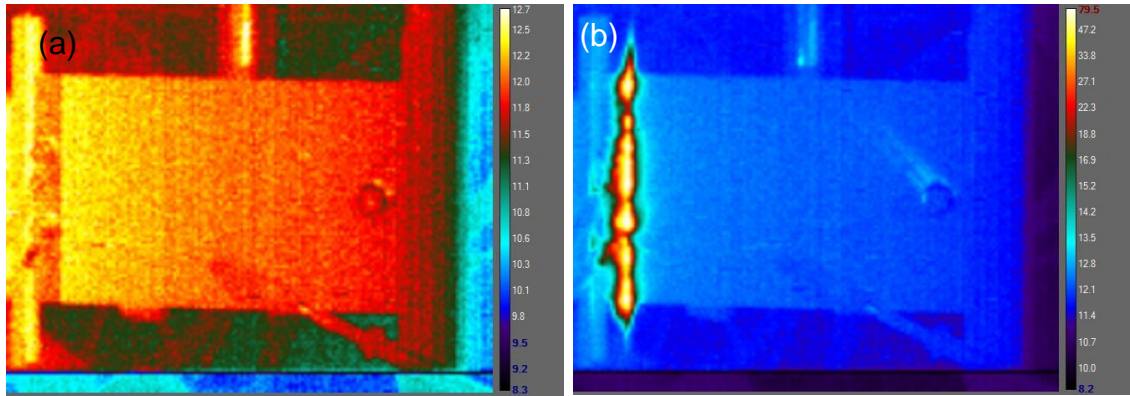


Figure 6-11. Acquisitions of thermal camera: a) before the current injection, b) during the current injection, 7 kA peak. An increase in temperature is noticeable in the correspondence to the interface between the sample and the return electrode.

The visual analysis of the surface after the test reveals the presence of dark zones, which are the signs of the silver paint layer burning or melting. It can be considered that the darker zone had a better contact with the return electrode and most of the current passed through. Therefore, this leads to increasing the temperature up to a thermal sparking.



Figure 6-12. Image of the sample side painted with silver paint after three consecutive high current tests at 5, 6 and 7 kA peak.

6.7.1 *No-layer* grounding system

Table 6-2 shows the measurements and relative resistance calculation for the tests on the *no-layer* grounding system. The *no-layer* grounding system was subjected to sparks across the contact surface during the first test using a peak current of 5 kA. As in the previous case, the sparks are due to arc formations between the surfaces in contact with a consequent reduction in the total resistance. It is assumed that at a level of current peak that did not create sparks, the resistance would be higher. A comparison with the *silver paint* case

shows a higher resistance analogous to the low current measurements where the *no-layer* case showed the highest resistance at 3900 N.

Table 6-2 Voltage, current, resistance and action integral at 5 kA peak for *no-layer* sample.

	Voltage (V)	Current peak (kA)	Resistance (mΩ)	Action integral (kJ/Ω)
sh001	107.01	4.8	22.16	0.590

Figure 6-13 shows the picture captured before and during the test; the right-hand picture clearly shows the sparking event at the contact interface, and Figure 6-14 shows further details of the area.

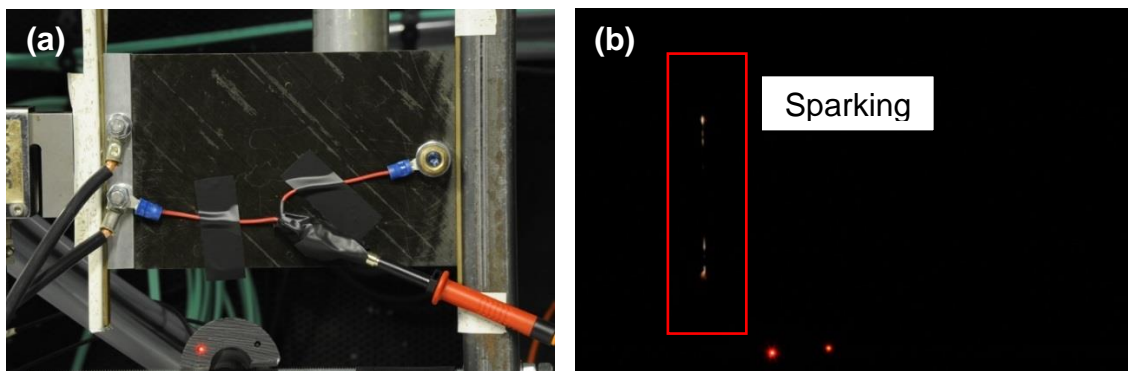


Figure 6-13. a) Still picture before the current injection, b) still picture during the current injection at 5 kA peak. Inside the red square visible sparking are located at the interface between the metal electrode and sample side.



Figure 6-14. Details shot of the sparking location at 5 kA peak (rotated).

The thermal camera recorded the increase in temperature due to sparking during the current injection. The visual analysis of the side surface of the sample after the test did not reveal relevant signs of damage.

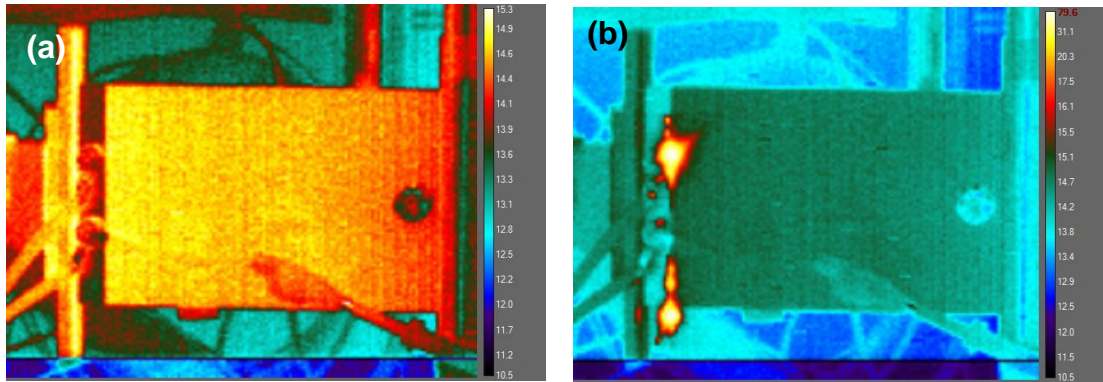


Figure 6-15. Acquisitions of thermal camera: a) before the current injection, b) during the current injection, 5 kA peak. An increase of temperature is noticeable in correspondence with the interface between the sample and the return electrode.

6.7.2 Metal sputter grounding system

The *metal sputter* case shows the best performances in comparison with the other two side grounding systems. Table 6-3 shows the results of the tests carried out; the grounding system did not show any sign of sparking at the still camera recording up to 60 kA.

Table 6-3. Voltage, current, resistance and action integral in the range 5-60 kA peak for metal sputter sample.

	Voltage (V)	Current (kA)	Resistance (mΩ)	Action integral (kJ/Ω)
sh001	64.91	5.3	12.22	0.612
sh002	75.18	6.2	12.15	0.861
sh003	85.68	7.1	12.11	1.17
sh004	99.14	8.3	11.98	1.6
sh005	109.78	9.2	11.97	1.99
sh006	121.79	10.2	11.95	2.5
sh007	144.65	12.1	11.93	3.6
sh008	167.55	14.2	11.76	4.96
sh009	188.55	16.3	11.53	6.5
sh010	229.84	20.4	11.28	10.1
sh011	283.23	25.3	11.2	15.8
sh012	336	30.4	11.03	23
sh013	385.68	35.3	10.9	31.3
sh014	438.56	40.6	10.79	41.3
sh015	513.94	48.9	10.52	58.3
sh016	556.33	52.9	10.5	69.4
sh017	610.23	59.4	10.27	88.7

Figure 6-16 shows the trend of the resistance as a function of the current peak and as for the *silver paint* case the decreasing of contact resistance can be associated to an increase of sparks at the contact interface.

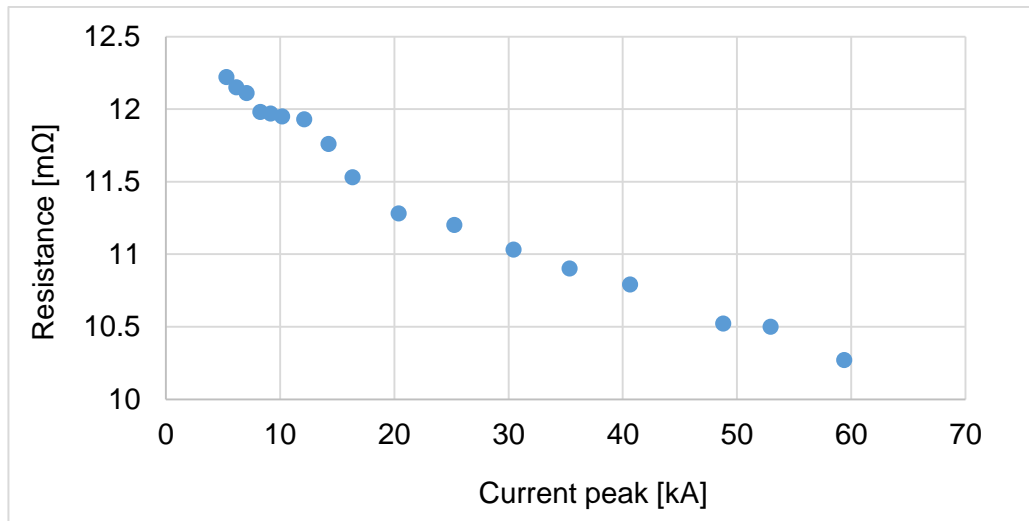


Figure 6-16. Resistance vs peak current.

The still camera detected the sparks at the interface as shown in Figure 6-17b and Figure 6-18. Moreover, Figure 6-17b reveals a spark located around the injection fastener, which is brighter compared to the sparks at the grounding interface. This spark is due to the connection of the voltage sensor, which was fitted between the metal washers underneath the nut. The spark did not occur at the interface between the injection fastener and the panel. Thus, it was not considered as a direct effect of the current along its natural path. Conversely, without the sensor, the spark would not have occurred. The thermal record, in Figure 6-19b, reveals the locations of the sparking and, as can be observed, some of the sparks are located at the corner of the sample. Due to the compression of the sample during the low current test, the corners of the surface were deformed with the consequence that at the corner locations, air gaps appeared, which led to the sparking.

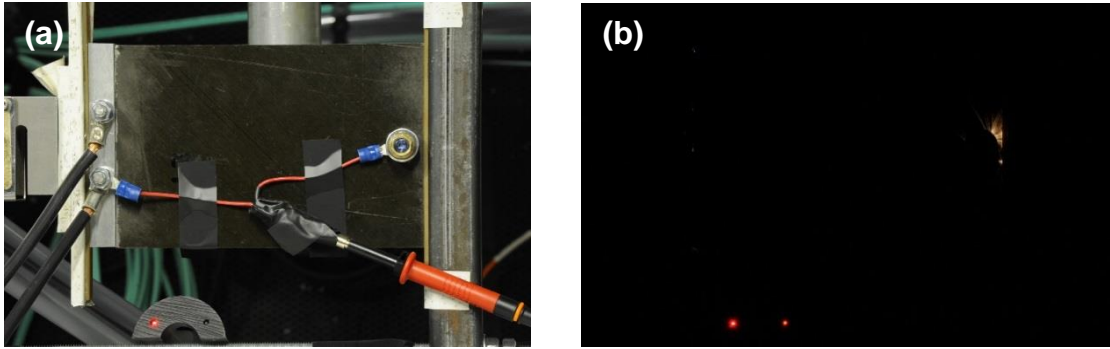


Figure 6-17. Still pictures of the metal sputter grounding arrangement: a) before the test, b) during the test.



Figure 6-18. Details of the sparks at the contact interface between the sample and the return electrode.

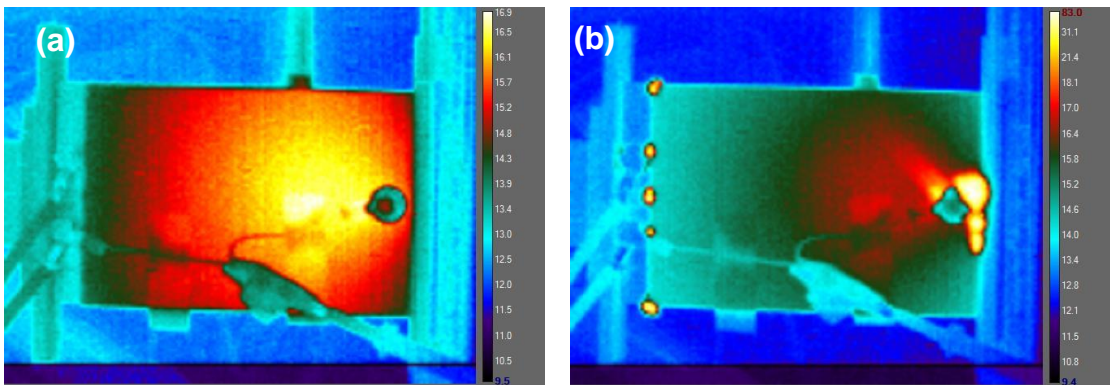


Figure 6-19. Acquisitions of thermal camera: a) before the current injection, b) during the current injection, 60 kA peak. An increase in temperature is noticeable at the interface between the sample and the return electrode.

Although the first spark was recorded at the peak current of 60 kA , the thermal camera recorded an increase in temperature at several locations along the contact interface at the current peak of 25 kA (Figure 6-20). However, the temperature scale shows that the maximum temperature is $22.3\text{ }^{\circ}\text{C}$; thus, it can

be concluded that at this current level, no relevant damage of the grounding system would appear.

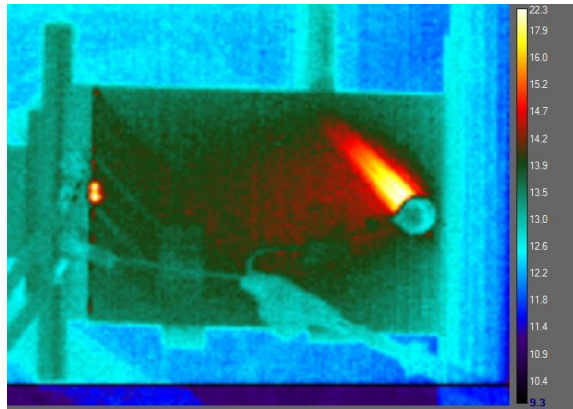


Figure 6-20. Thermal camera acquisition at 25 kA current peak. The frame shows some hot spots at the contact interface.

At 25 kA peak, the enhancement of temperature around the injection fastener is clear (right side of Figure 6-20). The enhancement follows the direction of the fibre in the outermost ply of the sample, 135°, and it reflects the direction of the current.

Furthermore, the thermal camera revealed the thermal effects of the current even for the internal plies of the sample. Figure 6-21a shows the thermal evolution of the test 44 ms after the current injection. A second, brighter strip is visible around the injection fastener related to the ply at 45°, which is the second ply of the sample. Moreover, Figure 6-21b shows another frame at 1119 ms after the current injection. The presence of a brighter strip can be clearly seen in the 0° direction associated with the third ply of the stack.

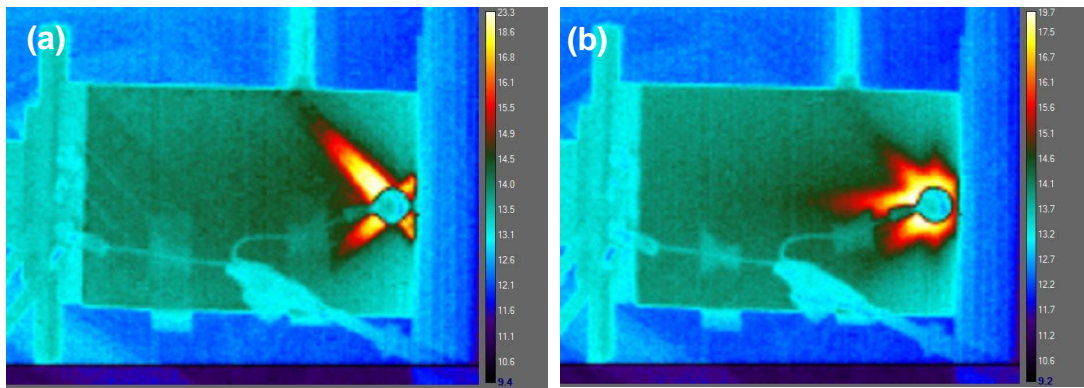


Figure 6-21. a) Thermal acquisition *44 ms* after the current injection, b) thermal acquisition *1119 ms* after the current injection.

In the analysis of the surface after the test, Figure 6-22 reveals that at the locations of the sparks recorded by the camera, there is likely to be a contact spots which have created thermal sparks (locations numbered 2, 3 and 4), whereas locations 1 and 5 are more likely to have triggered voltage sparks due to the air gap at the corner. At location 6, it can be seen that there was significant damage to the metal sputter coating which resulted in the total destruction of the layer. This may indicate that a large proportion of the current passed through this location causing thermal sparking.

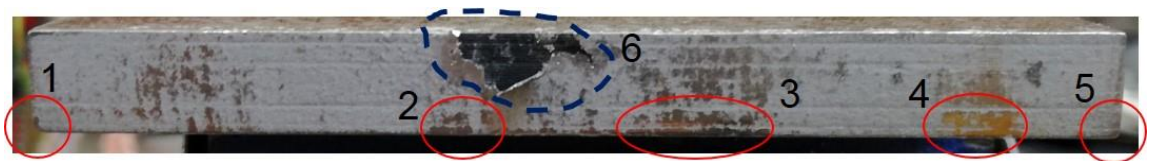


Figure 6-22. Still picture after the test. The picture shows the corners of the sample where sparks appeared (1 and 5). Furthermore, locations 2, 3 and 4 show potential contact areas where thermal sparking had occurred. The area at location 6 reveals deep damage of the metal sputter layer.

6.7.3 *3-fasteners* grounding system

The *3-fasteners* grounding system does not require the same test rig as the side grounding systems because no compression force is required. The benefit of this arrangement is the simplicity of fitting the sample into the current

generator circuit, but as discussed in Section 4.3, this arrangement requires three fasteners with associated drilling. For this arrangement, a current peak of 40 kA was reached (Table 6-4). The results show a decrease in the resistance with increase in the current peak compared with the other grounding systems described in the previous sections. Therefore, the mechanism of the thermal and voltage sparks at the contact interface is present in this grounding arrangement as well.

Table 6-4 Voltage, current, resistance and action integral in the range 5-40 kA peak for the 3-fasteners system.

	Voltage (V)	Current peak (kA)	Resistance (mΩ)	Action integral (kJ/Ω)
sh001	69.8	5	14.0	0.602
sh002	189.6	15.1	12.5	5.6
sh003	304.6	25.5	12	16
sh004	468.2	41	11.4	41

At maximum peak current, a bright spark was observed at the injection point, and Figure 6-23b indicates that the outgassing phenomenon occurred on the back side of the sample, where the head of the fastener is located.

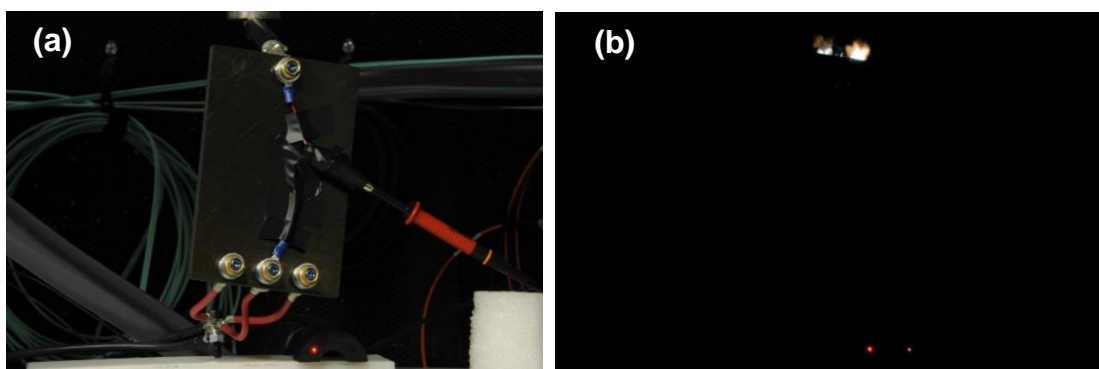


Figure 6-23. Still pictures of the 3-fasteners grounding arrangement: a) before the test, b) during the test.

The still picture does not show any relevant spark event around the three grounding fasteners. However, from the thermal camera acquisitions, Figure 6-24, it can be seen that, at the current peak (40 kA), some increase in temperature had occurred at the bottom side of the sample in correspondence of the grounding fasteners. Those hot spots can be associated to the sputtering of hot particles from the contact interface that have not been captured by the still camera and can be associated with relevant overpressures at the contact interface. The analysis of the sample after the experiment did not reveal any sign of damage.

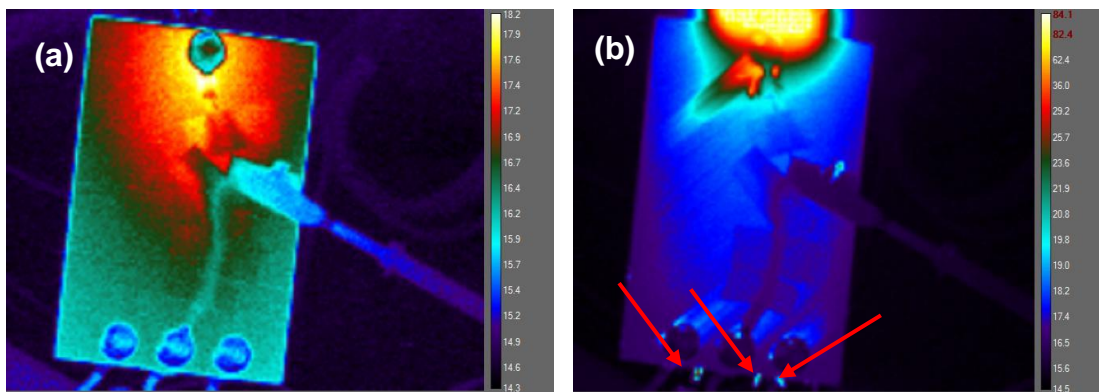


Figure 6-24. Acquisitions of thermal camera: a) before the current injection, b) at 40 kA peak. The red arrows highlight the sputtering of hot particles from the interface between the grounding fasteners and the sample.

6.7.4 1-fastener grounding system

The last grounding system analysed is the *1-fastener* grounding system. It can be considered as a simplified version of the *3-fasteners* arrangement. The presence of just one fastener as a return for the current reduces the current capability. Table 6-5 shows the measurement results up to a maximum current peak of 25 kA. Again, of interest is the reduction in the resistance with the increasing current peak which is sign of thermal and/or voltage sparks that are

present internally on the contact interfaces, but not visible externally up to 25 kA.

Table 6-5 Voltage, current, resistance and action integral in the range 5-25 kA peak.

	Voltage (V)	Current peak (kA)	Resistance (mΩ)	Action integral (kJ/Ω)
Sh001	88	4.9	18	0.588
Sh002	244.8	15	16.4	5.51
Sh003	388	25.1	15.5	15.7

Furthermore, this arrangement created a mirroring between the injection and the return fastener with the consequence of the same effects being expected on both sides of the sample. In addition, Figure 6-25b shows that both the injection and the collecting fasteners are affected by the sparking and/or outgassing phenomenon.

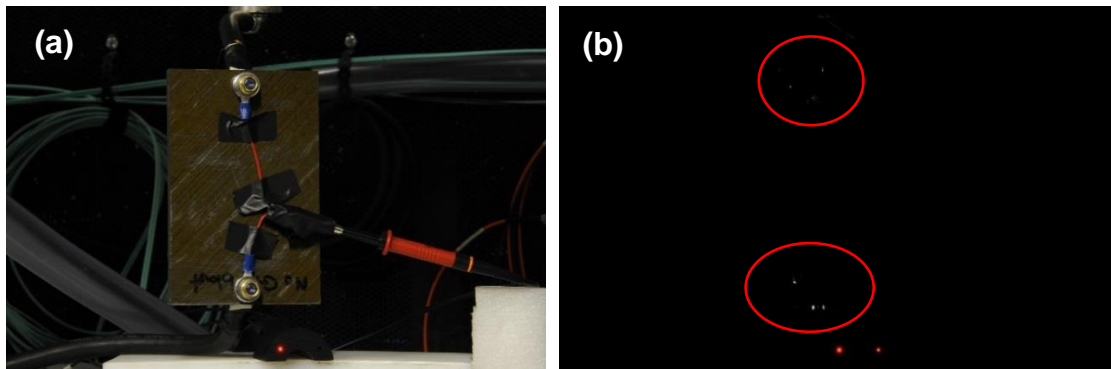


Figure 6-25. Still pictures of the 1-fastener grounding arrangement: a) before the test, b) during the test.

The thermal pictures of this experiment were recorded in a second experiment carried out under the same conditions as the first but without the voltage sensing circuit. Figure 6-26b shows hot spots around both the injection and grounding fastener in agreement with the still picture (Figure 6-25b).

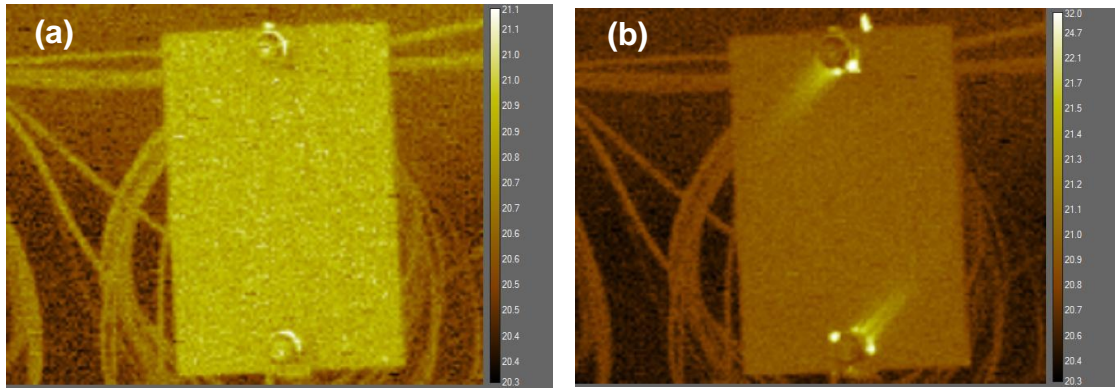


Figure 6-26. Acquisitions of thermal camera: a) before the current injection, b) during the current injection, 25 kA peak.

6.7.5 Resistance comparison for the various grounding systems

Following the analysis of the results of each grounding system separately, a comparison of the performances was undertaken. All the resistances calculated were traced in a single graph in Figure 6-27. In terms of absolute value of resistance, the *no-layer* system shows the highest resistance, whereas the *metal sputter* case shows the lowest. All the grounding arrangements are affected by a general reduction in resistance with the increase in current peak except for the *no-layer* case, which was tested only at 5 kA of current peak. However, a similar behaviour of the resistance can be expected as seen during other cases. The *silver paint* case showed a reduction in resistance during the third test at 7 kA, indicating that, for this specific case, the influence of the sparking at the contact interface was more relevant than for the other cases.

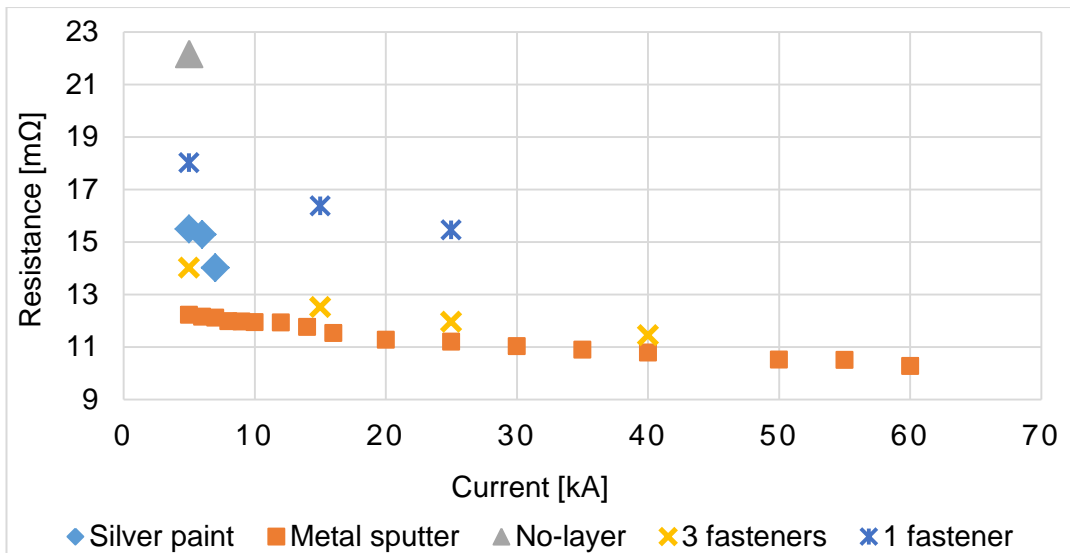


Figure 6-27. Comparison of the resistances calculated for the different grounding systems.

Of particular interest is the comparison of the high current test with the low current test. In the low current test, an opposite behaviour compared to this was seen, as the resistance increases with the increase of the DC current (refer to Figure 4-19 Figure 4-20 Figure 4-21). The phenomenon can be related to the resistivity of the contact resistance. The results of the low current DC test suggest that the resistivity has a positive temperature coefficient. In the high current test, it is expected that the resistivity behaves in a similar way as under low current test. Therefore, in the high current test the increase of the current has two consequences: an increasing of the resistivity due to its positive temperature coefficient and an increasing of the sparking phenomenon. These two phenomena have opposite effects on the resistance: the former contributes to its increase whereas the latter contributes to its decrease. From the results of the high current tests shown in Figure 6-27 it is possible to suppose that the effect of the sparking is predominant over the increasing of resistivity with the results of a general decreasing of the resistance. Table 6-6 shows the decrease

for the low current test at 500 mA and the high current test at 5 kA, with 3900 N compression force applied in the case of the side grounding system. The comparison shows how all grounding systems undergo a decrease in resistance in the range between 23.2% and 62%, which means that all the grounding systems are affected by the phenomenon of voltage/thermal sparks already at 5 kA. This indicates that, for each of the arrangements, there is a specific threshold, lower than 5 kA, above which the influence of the sparks becomes important in the reduction of the resistance.

Table 6-6 Resistances calculated from low and high current test. (*) The force is referred only to the grounding systems that require the compression test rig.

	Silver paint	Metal sputter	No-layer	3 fasteners	1 fastener
Resistance (mΩ) @ 500 mA 3900 N*	20.1	26.3	58.4	23	29
Resistance (mΩ) @ 5kA, 3900 N*	15.5	12.2	22.1	14.0	18.0
% of decreasing	23.2%	53.5%	62%	39%	38%

6.7.6 Assessment of the location of the grounding fasteners

When a fastener grounding system is used in the CFRP sample, the influence of the location of the grounding fasteners on the resistance between the

injection point and the grounding is of interest. The effects of the alignment of the grounding fasteners with the direction of the plies have been already discussed in Chapter 3 and the results have revealed that if the grounding and the injection fasteners are aligned with the ply direction, a highly conductive path allows the current to spread less within the ply. This, in turn, leads to a decrease in the resistance measured between the injection and the grounding point because the resistivity of the ply along the fibres is lower than the transverse and through-thickness directions. In order to verify this behaviour experimentally, a test was carried out on a square CFRP sample with a fastener located at its centre and four pairs of fasteners located around it in the directions 0° , 45° , 90° , and 135° . All the grounding fasteners are equally spaced at 40 mm from the injection fastener, as shown in Figure 6-28.

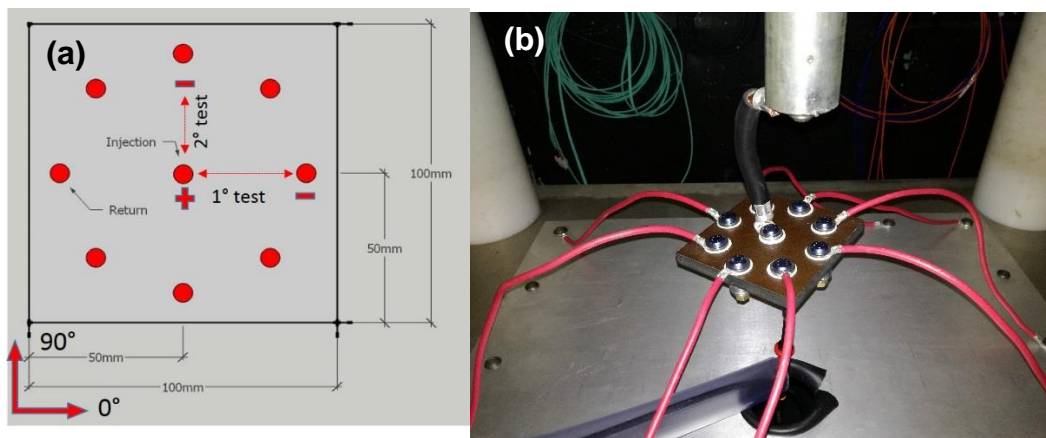


Figure 6-28. a) Square CFRP sample with one injection fastener at its centre and four pairs of grounding fasteners located at 0° , 45° , 90° and 135° . Voltage sensor location for test set 1 in 0° direction and test set 2 in 90° direction; b) picture of the sample connected to the rig of the MBL. The red wires connect the grounding fasteners to the ground of the circuit, whereas the black wire connects the central fastener to the injection point.

The sample is made by a stack of 36 plies with the following lay-up:

$$[-45\backslash 45\backslash 0\backslash 90\backslash 0_2\backslash -45\backslash 45\backslash 0_2\backslash 90\backslash 45\backslash -45\backslash 0_2\backslash -45\backslash 45\backslash 0]_s$$

According to the ply lay-up above, the number of plies in the 90° direction is 25% of the number of plies in the 0° direction (4 against 16). From an electrical point of view, plies in the same direction can be associated with resistances connected in parallel. Therefore, the equivalent resistance of 16 plies in parallel is four times lower than the equivalent resistance of 4 plies in parallel. With this hypothesis, and considering a balanced number of plies in $+45^\circ$ and $+135^\circ$, if the current is injected in the central fastener, and it is collected by the fastener pair located at the 90° direction, it should encounter a higher resistance than if it is collected by the fasteners pair placed in the 0° direction. The test aimed to verify the variation of the resistance with the position of the fastener pairs.

The test was carried out by injecting the D-component current shape with a peak of 5 kA in the central fastener of the sample. The current was collected through the grounding fasteners located at the side of the sample. The voltage drop was measured between the injection fastener and one grounding fastener. Two sets of experiments were conducted: in the first set of experiments, the voltage sensor was placed between the injection fastener and the fasteners placed at the 0° direction, whereas in the second, the sensor was placed between the injection fastener and the grounding fastener placed at the 90° direction (Figure 6-28).

Each set of experiments comprised four separate tests, with each of them varying the number of fastener pairs connected with the grounding circuit. Figure 6-29 shows the four different grounding configurations for each test set.

Furthermore, one current sensor was used in order to measure the amount of current flowing in the two main directions of the sample. In Figure 6-29 is shown the positions of the current sensors, the black circle, for each test carried out

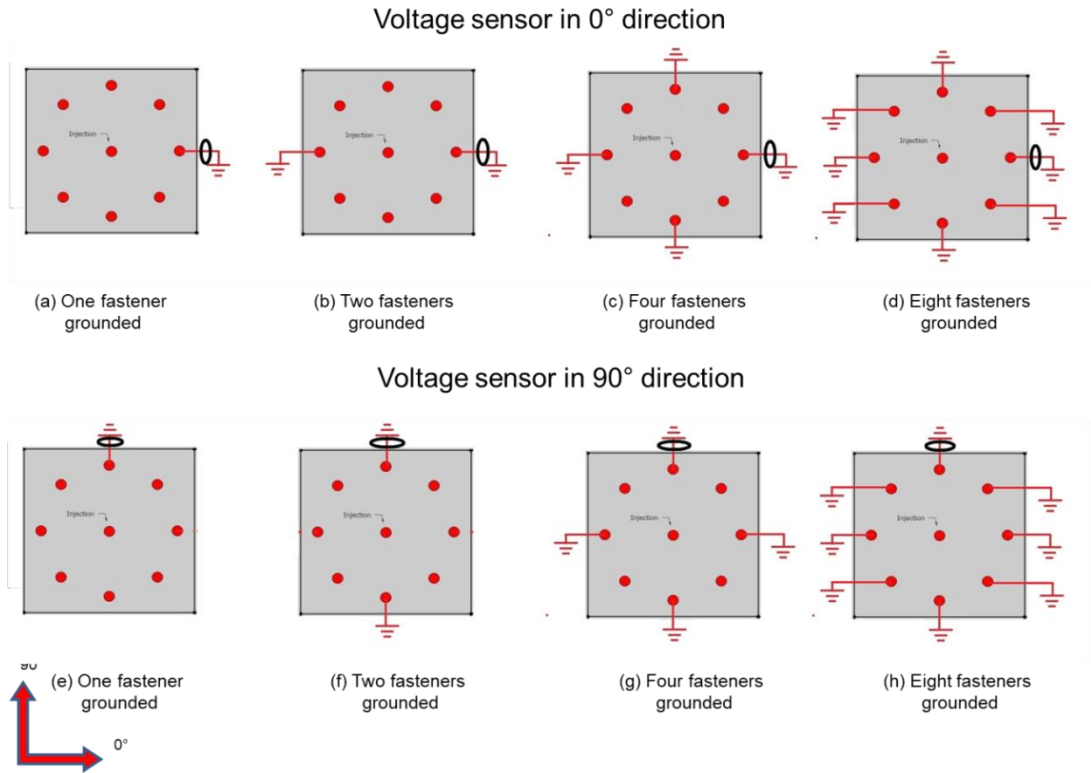


Figure 6-29. Grounding configurations of each test set and location of the current sensor (black circle).

The resistances were calculated from the measurements of the voltage and current using the same method as described in section 4.5 without consider the aspects related to pressure measurement. The results of the two test sets are shown in Table 6-7.

Table 6-7 Resistances in (Ω) calculated in the two test sets. Variation in percentage between the resistances calculated at the 0° and the 90° direction.

Grounding	1 fastener	2 fasteners	4 fasteners	8 fasteners
probe at 0°	1.03	0.67	0.53	0.46
probe at 90°	1.2	0.77	0.57	0.50
Var % 0°-90°	14.2%	13%	7%	8%

The analysis of the results reveals that for both tests, the increase in the number of grounding fasteners leads to a reduction in the resistance encountered by the current along its path inside the sample. This means that the current can spread over a wider section and flow through less resistive paths, and both factors contribute to a reduction in the resistance. Increasing the number of grounding fasteners from one to eight leads to a 55% reduction in the resistance in the first test and 58% in the second test.

However, the analysis of the location of the grounding fastener shows that in the case of the current collected by one fastener located on the 0° direction (in the same direction of 16 plies), the resistance is 14% lower than when the fastener is located at the 90° direction, (in the same direction of 4 plies). The difference in percentage decreases to 13% for the 2-fasteners grounding and falls to 7/8 % for the 4-fasteners and 8-fasteners grounding. Again, the different reductions between the resistances calculated for the 0° direction and the 90° directions can be explained by the fact that the current spreads within the sample more homogeneously and flows through less resistive paths when it flows in 0° direction.

6.8 Conclusion

This chapter provided the results of high current tests on five different grounding systems, three belonging to the family of the side grounding and two belonging to the fasteners grounding arrangements. The aim of the test was to investigate which of the grounding arrangements performs better under a high current environment. The objects under investigation were the electrical resistance of the grounding system calculated through indirect measurements of voltage and

current (four wires measurement). The thermal effects of current flow on the grounding systems were recorded using still and thermal cameras. The resistance value was used to assess the quality of the grounding system; lower resistance meant the system was better able to sustain a high level of current. Furthermore, the electro/thermal phenomenon defined as outgassing was taken into account as a threshold of the reliability of the system. The record of the outgassing phenomenon from the still/thermal camera meant the failure of the system to sustain the current. The tests were carried out using a laboratory reproduction of a part of the lightning current. Specifically, the D component of the EUROCAE ED-84 guide was used. Each sample was tested at several peak magnitudes of the current waveform up to the failure of the system.

The results have shown that the metal sputter grounding system is the most reliable of the five systems analysed. It was able to sustain an impulse current up to 60 kA peak. However, the post-test analysis revealed significant damage to the metal layer. The “3-fasteners” system reached a peak current threshold of 40 kA. Above this value, the sparking around the grounding fasteners was recorded. All grounding systems have shown a decrease of sample resistance with increasing current peak. This suggests that at the contact interface between the return electrode and the sample for the side systems or between the grounding fastener and the sample for the fastener systems, voltage and thermal sparks occur.

Indeed, the thermal camera was able to trace the presence of hot particles that are sputtered from the contact interface, something that the still camera did not record. Furthermore, through the thermal camera, it was possible to visualise the dynamic changes of the heat patterns within the sample. The heat flows

within each layer of the sample were recorded according to the direction of the fibres in that specific layer, and the heat flux was found to relate to the current flux.

This chapter includes the results of a test carried out in order to investigate the influence of the positioning and the number of the grounding fasteners on the current distribution in a square shaped CFRP sample. The number of plies in the 90° direction was 25% of the number of plies in the 0° direction (4 plies against 16). It was found that increasing the number of grounding fasteners from one to eight led to a decrease in the measured resistance of 55% and 58% for two different tests. Therefore, the number of fasteners contributes to the spreading of the current over a larger cross section and helps to the flow of the current through less resistive paths within the sample. Furthermore, it was proved that the positioning of the grounding fastener in the 0° direction led to a 14% reduction in the resistance compared to the positioning of the grounding fastener in the 90° direction. Again, the increase in the number of grounding fasteners around the injection point contributes to the 7% reduction in that discrepancy.

The results highlighted that the “metal sputter grounding system” can be a valid substituted to the conventional “fasteners grounding system”. The advantages of this new test setup are that the test sample is easier to produce because it does not require any drill, there is no need of grounding fasteners and relative washer and nuts. Furthermore, the metal sputter grounding systems allows for a better analysis of the sample contact surfaces before and after the test compare to the sample with fasteners system. A test rig built for metal sputter grounding systems allows for the control of the contact pressure and the use of different

test samples. The disadvantage of this method is a more complex and expensive test rig. Conversely, with this method the cost of the test sample is lower compare to the sample that requires grounding fasteners.

Chapter 7

Heat proposed analytical model for temperature rise in CFRP under lightning strikes and validation using numerical modelling

7.1 Introduction

In Chapter 6, the quality of five grounding systems was analysed under high impulse current magnitude. The thermal effects of the current are considered of primary importance especially at the interface between the sample and the grounding system (fasteners – sample interface and aluminium electrode – sample interface). Using the thermal camera allowed the detection of the increase in temperature in specific zones of the sample, and it was seen that the heat dissipates according to the direction of the fibres within the plies. The resistive heat is one of the factors responsible for damage to the CFRP materials under the direct effects of lightning strikes [65]. Thus, it was of interest to start an investigation to assess the dynamics and the limits of the current and the temperature, which would lead to damage of the CFRP materials. The study analyses the dynamics of the temperature of a tow of the carbon fibres normally used to produce CFRP materials for aerospace applications when it is subjected to a lightning current. An analytical solution and a numerical model were developed, and a comparison between the two was made with the aim to understand the detailed mechanism of interaction of current and heat in CFRP samples. At this stage, the experiment does not replicate a real scenario, but it is a starting point for a further development of models that are able to predict the effects

of the resistive heat in CFRP materials. The results show a correlation with the temperature variation calculated with both methods.

7.2 Energy associated with electric current

It is well known that the increase in temperature of a material caused by resistive heating is related to the energy associated, E , with the electric current passing through the material. Eq. 7.1 relates the temperature variation, ΔT , of a material having mass m , specific heat c , and electrical resistance R with the *action integral* of the current waveform delivered to the material ($\int_0^\infty i^2 dt$).

$$E = R * \int i^2(t) dt = m * c * \Delta T \quad (7.1)$$

$$\Delta T = k * \int i^2(t) dt \quad (7.2)$$

Where,

$$k = \frac{R}{m * c} \quad (7.3)$$

The equation can be used to describe an idealized scenario where the entire amount of energy delivered by the current to the object contributes to the increase in temperature, and no dissipation effects are present. Furthermore, the equation is independent of the geometry of the object. For a current waveform with an indefinite duration, the result of the equation causes the temperature of the object to rise indefinitely if no heat losses occur. Conversely, for a finite time and magnitude of the current, the object acquires a finite amount of energy that contributes to a finite increase in temperature. This can be the case of a lightning strike event where,

despite the very high magnitude of the current waveform, it is finite in time. In more realistic scenarios, it is very rare to find a system that does not exchange heat with its surrounding environment when a difference in temperature appears between them. If the object is hotter than the surrounding, in accordance with the second principle of thermodynamics, the heat transfers from the object to the external environment through the interface that separates the two parts, which is permeable to the heat. The heat dissipates in the surrounding environment through different physical processes, such as heat conduction, convection, and radiation.

When a CFRP panel is subjected to a lightning strike, the lightning current flows through the carbon fibres embedded in the epoxy matrix. Due to the non-zero electrical resistivity, the fibres transform electrical energy in to heat. The heat contributes to a temperature increase in the carbon fibres, which leads to a lack of equilibrium with the external environment, including, the plastic matrix and surrounding air. Therefore, some of the heat transfers from the fibres to the external environment. For a lightning strike event, the amount of energy delivered by the lightning current is finite. Therefore, the carbon fibres are exposed to a rapid increase in temperature followed by a decrease in order to return to a state of thermal equilibrium with the surrounding environment.

7.3 Temperature threshold

As mentioned in the introduction, the study was carried out to compare two approaches to solve an electro-thermal problem. The first step of the study was to assess a reliable temperature level at which it is possible to define damage to the carbon fibres. The threshold temperature was assessed using a previous experiment discussed in the literature. According to Storer and Fei [66] [67], the damage to fibres

can be defined as the loss of strength and stiffness from the mechanical point of view. The mechanical losses are due to the growth of surface flaws and/or mass loss. The articles refer to a minimum temperature of 300 °C as a threshold after which the fibres start to degrade. Moreover, Storer emphasised that when the fibres are embedded in an epoxy matrix forming a CFRP panel, it could be of interest to consider the glass transition temperature, T_g , of the polymer as a threshold of the degradation of the mechanical characteristics of the CFRP panel. The glass transition temperature is a threshold temperature at which the polymer starts to soften. However, at that temperature, the cooling down process is still reversible, and the polymer can recover its mechanical properties without any appreciable loss. T_g is usually lower than the degradation temperature of the fibres (for an epoxy matrix the T_g temperature is around the curing temperature, so is in the range 100-180 °C).

The study carried out shows that, for a specific current waveform injected within a tow of carbon fibres, there is a corresponding temperature increase to 300 °C.

7.4 Proposed analysis approach

The two methods take into account the same current waveform injected into the yarn of the fibres. It has the same shape as the D-component of the EUROCAE ED-84 guide, which has the following equation:

$$i(t) = I_0(e^{-\alpha t} - e^{-\beta t}) \quad (7.4)$$

where $\alpha = 22708 \text{ s}^{-1}$ and $\beta = 1294530 \text{ s}^{-1}$ are parameters linked with the rise time and the time to half peak. I_0 is the parameter linked with the magnitude of the current

impulse. In both methods, the α and β parameters were not varied whereas the I_0 parameter was varied.

7.4.1 Solution of proposed analytical model

The analytical method is based on the solution of Eq. 7.2.

One of the advantages of the analytical method was that, was not necessary to consider any specific aspect related with the design of the carbon fibre tow. Furthermore, it requires only three parameters to describe the object fully. Nevertheless, an analysis of the geometry of the carbon fibres tow is carried out using the numerical simulation section.

The solution of the equation using the double exponential current waveform is given below.

The current waveform is described by a double exponential equation; thus, the solution of the equation is

$$R * \int \left(I_0 (e^{-\alpha t} - e^{-\beta t}) \right)^2 dt = m * c * \Delta T(t) \quad (7.5)$$

$$\Delta T(t) = \frac{R * I_0^2}{m * c} \int [e^{-\alpha t} - e^{-\beta t}]^2 dt = \quad (7.6)$$

$$= \frac{R * I_0^2}{m * c} \int (e^{-2\alpha t} + e^{-2\beta t} - 2e^{-(\alpha+\beta)t}) dt \quad (7.7)$$

$$\Delta T(t) = \frac{R * I_0^2}{m * c} \left\{ \frac{e^{-2\alpha t}}{-2\alpha} + \frac{e^{-2\beta t}}{-2\beta} - 2 \frac{e^{-(\alpha+\beta)t}}{-(\alpha + \beta)} + p \right\} \quad (7.8)$$

The constant p can be found considering $\Delta T(t = 0) = 0$

$$p = \frac{1}{2\alpha} + \frac{1}{2\beta} - \frac{2}{\alpha + \beta} \quad (7.9)$$

The Eq. (7.8) can be expressed in a compact form,

$$\Delta T(t) = T(t) - T(0) = k_1 * k_2(t) * I_0^2 \quad (7.10)$$

$$T(t) = k_1 * k_2(t) * I_0^2 + T(0) \quad (7.11)$$

where

- $k_1 = \frac{R}{m*c}$ is a constant dependent on the filament characteristics.
- $k_2(t) = \frac{e^{-2\alpha t}}{-2\alpha} + \frac{e^{-2\beta t}}{-2\beta} - 2 \frac{e^{-(\alpha+\beta)t}}{-(\alpha+\beta)} + p$ is time dependent and depends on the rise time and duration of the current waveform.
- I_0^2 is a parameter linked with the maximum amplitude of the current waveform.

In this work, Eq. (7.12) was solved to find the value of I_0 to substitute in Eq. (7.5) to find an increment in temperature of the filament of 280 °K considering an ambient temperature of 293 °K,

$$I_0 = \sqrt{\frac{\Delta T}{K_1 K_2}} \quad (7.12)$$

In order to find the values of I_0 , knowledge of K_1 , K_2 is required.

For K_1 , the mass of the carbon yarn, m , the electrical resistance, R , and the specific heat, c , need to be known whereas, K_2 can be found considering,

$$K_2 = \lim_{t \rightarrow \infty} k_2(t) = p \quad (7.13)$$

ρ depends on the current waveform parameters α and β .

The exact values of K_1 and K_2 are shown in the Appendix B.

The equation has been solved in order to find a value of I_0 which leads an increase of temperature of the tow of $300\text{ }^\circ\text{C}$.

The value of I_0 is 295.78 A

7.4.2 Results

Figure 7-1 shows the trend of the temperature of the yarn (Eq. 7.11) together with the trend of the current impulse in a range of $250\text{ }\mu\text{s}$. After $250\text{ }\mu\text{s}$, the current can be considered to be almost zero, and the temperature can be considered constant.

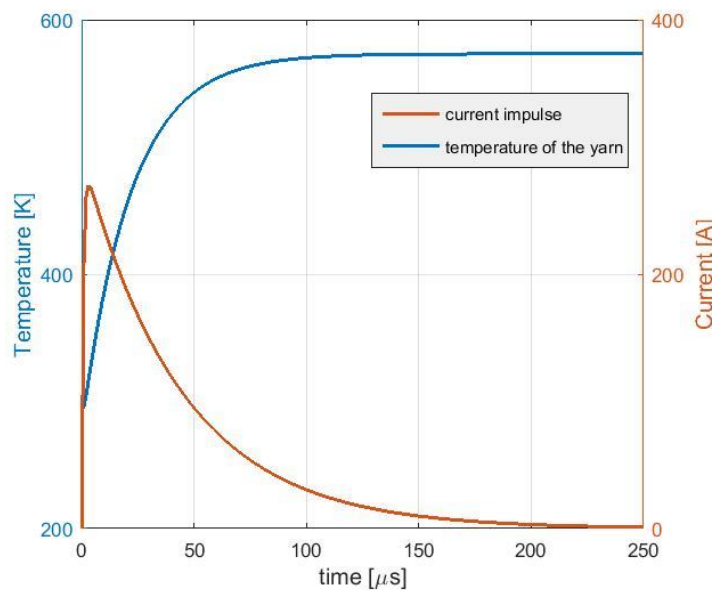


Figure 7-1. Trend of the temperature of the yarn and of the current impulse for $250\text{ }\mu\text{s}$ gap time.

The analysis of the temperature curve reveals that the temperature has a maximum $\frac{dT}{dt} = 11.16\text{ }^\circ\text{K}/\mu\text{s}$. The maximum temperature is $573.21\text{ }^\circ\text{K}$ at $250\text{ }\mu\text{s}$. However, the 95% of the maximum temperature, $544.55\text{ }^\circ\text{K}$, is reached at $t \approx 52\text{ }\mu\text{s}$. The delay between the current peak and the 95% of the maximum temperature depends on the

slope of the temperature trend during the transient. Therefore, it is dependent on the derivative of the temperature waveform.

$$\frac{d}{dt}T(t) = \frac{R * I_0^2}{m * c} * [e^{-\alpha t} - e^{-\beta t}]^2 = \frac{\rho * I_0^2}{d * S^2 * c} * [e^{-\alpha t} - e^{-\beta t}]^2 \quad (7.14)$$

Eq. (7.14) shows that, for a specific current waveform, and a specific carbon filament, the slope of the temperature increases proportionally with the square of I_0 , which implies that the delay decreases. In a similar manner, the slope decreases proportionally with the square of the section of carbon yarn S .

7.5 Numerical simulation of the heating process in CFRP materials

The numerical analysis was carried out to take into account the heat transfer between the carbon yarn and the surrounding environment. A comparison between the numerical and the analytical models was required to quantify the approximation of the analytical model compared with a more realistic scenario where the carbon yarn exchanges heat with the surrounding environment.

Two scenarios were taken into account: one with the yarn surrounded by air and one with the yarn surrounded by epoxy. For both simulations, the applied current waveform and the yarn have the same characteristics as in the analytical model (refer to the Appendix B). However, the heat exchange process is different for the two models. While for the fibres embedded in epoxy, the heat exchange is governed by conduction process, when the fibres were embedded in air, the heat exchange is driven mainly by convection.

The commercial software used for the simulation is COMSOL® Multiphysics. In this specific case, a coupling was used between an electrostatic simulation and a heat transfer simulation. The software, in the first step, solves the electrical problem of the

model; the output of the electric model, the current density, was used as the input for the heat transfer model, which was solved to compute the temperature throughout the geometry.

7.5.1 Geometry, input, equations and boundary conditions of the numerical model

Geometry

The model is made by the carbon yarn surrounded by a sphere of air for the first scenario and epoxy for the second one.

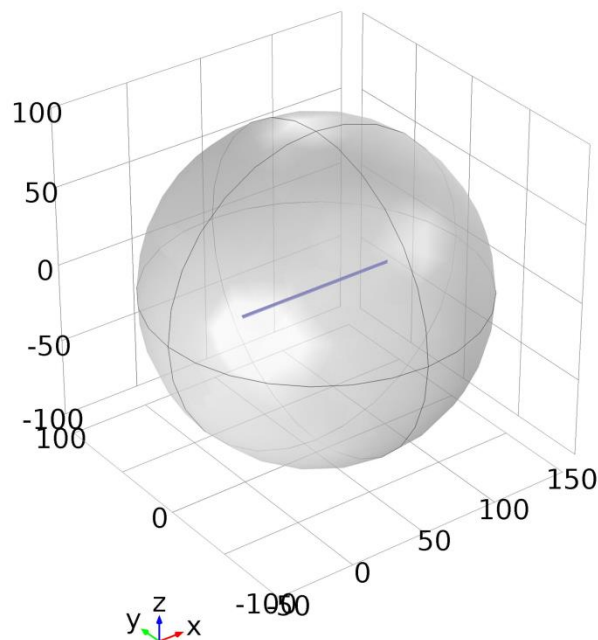


Figure 7-2. 3D rendering of the geometry of the numerical model. The sphere represents the air or the epoxy inside the sphere, the carbon yarn is visible. The scales are in millimetres.

In contrast to the analytical scenario, the numerical model considers the geometry of the carbon yarn. The yarn is made of several thousand of carbon filaments; in this case, 12,000 carbon filaments are put together to form the carbon yarn (Figure 7-3 shows a carbon fibre tow made from 12,000 filaments).

In this simulation, the tow was considered as a single conductor whose cross section is equal to the sum of the cross sections of the single fibres contained in the tow (the total cross section is reported in [18]) (see Figure 7-4). The simplification of the geometry of the object is chosen to match the computational strength available. It is not possible to solve a numerical problem that involves an electro-thermal coupled simulation in a time-dependent domain with 12,000 single carbon fibres with existing facilities.

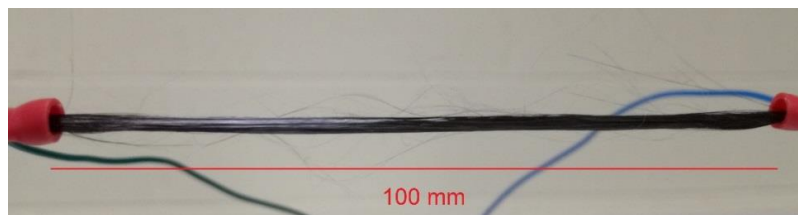


Figure 7-3. Carbon fibre in air. It is possible to note the yarn is composed of thousands of carbon filaments, some of which are broken.

Therefore, the approximation has the advantage of a smaller computational cost, but it has the disadvantage that the modelled yarn has a smaller exchange surface with the surrounding environment compared to a real yarn.



Figure 7-4 Rendering of the modelled carbon yarn.

Boundary conditions

The electrical boundary conditions applied were: the current was injected from the left end of the wire and collected through the right end. Whereas, the thermal boundary conditions applied were: the temperature of the surface of the sphere was constant and equal to 273.16 °K. Furthermore, for the case of the carbon yarn

embedded in air where the heat flux is governed mainly by the convection process it was modelled the effect of the convective flux using the following condition:

$$q = h \cdot (T_{ext} - T) \quad (7.15)$$

Where,

q is the heat flux in W/m^2

h is the heat transfer coefficient that in this study was set to $5 W/m^2K$

T_{ext} is the external temperature set to $273.16 \text{ }^\circ K$

T is the temperature in $^\circ K$

For the case of the carbon yarn embedded in the epoxy where the heat flux is governed mainly by the conduction process it was considered a perfect contact between the carbon yarn and the surrounding material. Perfect contact means that the real contact area is equal to the ideal contact area between the two materials.

Data required for the numerical model

In order to solve the equations of the numerical model, further data are required together with the data already presented.

Air sphere

- radius: 100 mm
- density: $1.2 - 0.6 \text{ Kg}/m^3$ [68]
- electrical conductivity: $0 \text{ S}/m$
- heat capacity at constant pressure: $1.01 \text{ KJ}/\text{Kg} * K$ [68]
- thermal conductivity: $0.02 - 0.04 \text{ W}/m * K$ [68]
- relative permittivity: 1

Epoxy sphere

- radius: 100 mm
- density: 1290 Kg/m³
- electrical conductivity: 10⁻⁶ S/m
- heat capacity at constant pressure: 1 KJ/Kg * K [69]
- thermal conductivity: 0.35 W/m * K [70]
- relative permittivity: 1

The length of the radius of the sphere was chosen equal to the length of the carbon yarn according to suggestion of the software support team. However, a further model, using a sphere with a radius of 50 mm was solved and not appreciable variations were found in terms of results and computational time. No further investigations were carried out on the sensitivity of the results in respect to the sphere radius.

Equations solved

The equation solved by the software is reported hereafter:

$$\rho C_p \frac{\partial T}{\partial t} - \nabla \cdot (k \nabla T) = Q \quad (7.16)$$

Where,

ρ is the density

C_p is the heat capacity

k is the thermal conductivity

Q is the heat source that comes from the electric section of the simulation.

The electrical equations coupled with the thermal are the same of that included in Section 3.3.2.

7.5.2 Numerical model simulation results

The computed results show that the temperature does not vary appreciably along the length of the filament. Therefore, for the discussion of the results, a cross section in the median section of the filament was considered. Figure 7-5a shows the 3D model; the lighter blue part is the air sphere, whereas the dark blue cross section represents the perpendicular plane to the filament, where the results have been evaluated. Figure 7-5b instead represents a zoom shot around the carbon filament extrapolated from the cut plane.

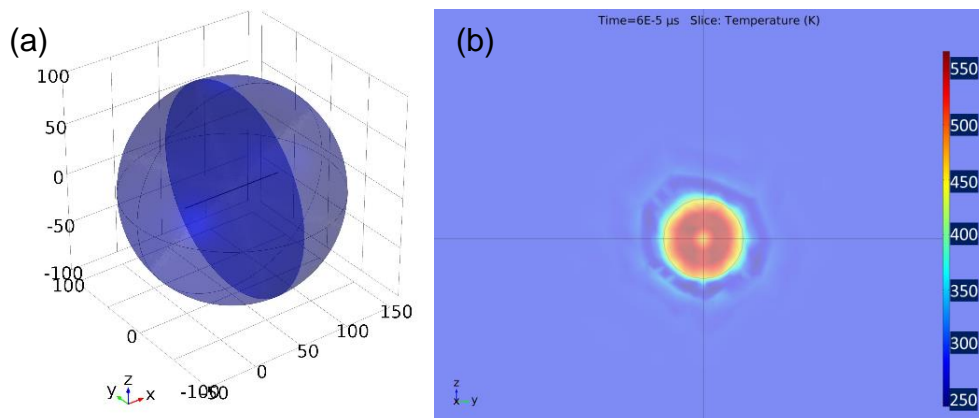


Figure 7-5. a) The light blue represents the sphere surrounding the carbon filament whereas the dark blue disk represents the cross section at which the maximum temperature has been calculated, b) zoom shot of the cross section around the carbon filament. The image shows the temperature at $60 \mu\text{s}$.

Table 7-1 shows the results of the maximum temperature reached by the filament for the two scenarios. The temperature was calculated over a time window of $300 \mu\text{s}$. The value of $300 \mu\text{s}$ was chosen because according to the results of the analytical model, the transient ends within $100 \mu\text{s}$. Therefore, a time window of $300 \mu\text{s}$ for the numerical simulation was considered sufficient to evaluate the transient. Moreover,

the numerical model required the specification of a number of points in time where the solution had to be calculated. Therefore, an array of time steps was included in the numerical model. The time steps were chosen to be closer during the transient in order to follow the rapid variation of the temperature.

Table 7-1. Temperature of the yarn with air sphere and epoxy sphere at specific time steps.

Time (μ s)	Temperature air sphere (K)	Temperature epoxy sphere (K)
1	293.1	293.1
2.2	304.6	305.8
3.2	316.0	318.4
5	336.2	340.8
10	383.9	393.5
20	447.0	463.1
30	488.3	508.4
60	548.7	573.6
90	564.6	589.4
120	568.7	592.1
150	569.7	591.3
200	570.1	588.8
300	570.1	583.6

The results show that, in the scenario with the filament surrounded by air, the temperature increases for the duration of the simulation, which means that the heat exchange process is not predominant for the first 300 μ s. Conversely, for the epoxy sphere case, the temperature reaches a maximum value of 592 $^{\circ}$ K at 120 μ s and,

after that, it starts to decrease. Thus, the dissipation process is visible. The maximum temperature for the epoxy sphere case is 22 °K higher than the maximum of the air sphere case. The fact that for both the surrounding materials no appreciable dissipation effects are visible for the first 300 μs can be related to the characteristic of both air and epoxy to be thermal insulators.

7.6 Comparison between analytical and numerical models

Figure 7-6 shows the trend of the current waveform and of the three models. The heat exchange process considered by the numerical model does not produce a noticeable deviation of the temperature trend compared to the analytical model within the first 300 μs for both numerical models. The heat exchange starts to be noticeable just in the epoxy sphere scenario after 120 μs. However, it must be noticed that the decrease in temperature is still negligible.

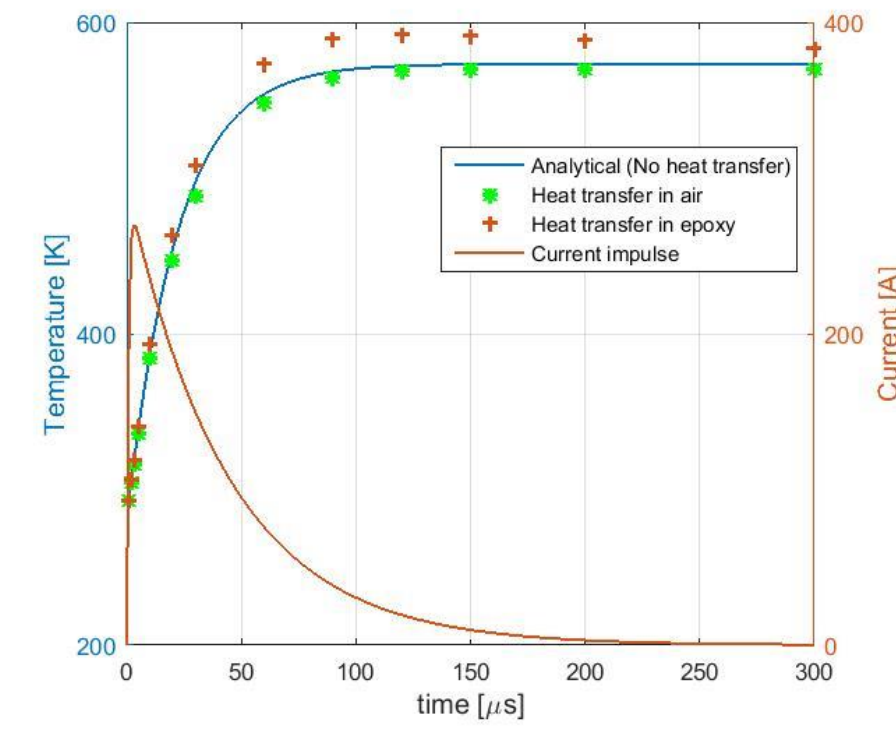


Figure 7-6. Comparison between the analytical model the air sphere numerical model and epoxy sphere numerical model.

7.7 Numerical simulation of an array of carbon fibres embedded in epoxy matrix

In order to consider a more realistic scenario of carbon filaments embedded in an epoxy matrix, a development of the geometry of the numerical model was carried out. In a real scenario, the carbon yarns are arranged in parallel, one next to the other, and embedded in epoxy in order to create unidirectional pre-preg plies. Thus, it would be more interesting to investigate the variation of the temperature in this more complex geometry where the exchange of heat can take place between the surrounding epoxy and eventually between the carbon filaments because of their vicinity. Again, a real scenario must take into account the interaction of millions of microscopic fibres embedded in the matrix as they might run in parallel or they might cross over each other. This developed model is used to consider a square array of filaments embedded in an epoxy matrix that replicates a very small part of a pre-preg unidirectional ply. Specifically, a carbon volume fraction of 40% was considered.

7.7.1 Geometry of the model

The square array of fibres (Figure 7-7) is composed of nine filaments arranged in a square shape. This configuration allows for the analysis of the temperature distribution for the central fibre, which exchanges heat with the eight surrounding fibres.

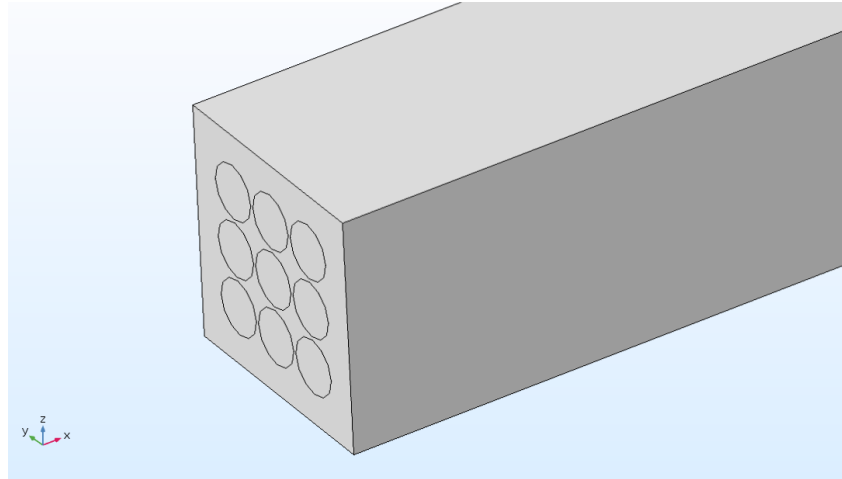


Figure 7-7. Geometry of the array of carbon filaments embedded in epoxy matrix.

In order to get the condition of a carbon volume fraction of 40%, the following geometric calculation was performed:

- Nine filaments occupy a cross section surface of $S_c = 0.25 \times 9 = 2.25 \text{ mm}^2$ which represents 40% of the total cross section.
- The remaining 60% of the matrix occupies a surface of $S_m = 3.375 \text{ mm}^2$.
- The total cross section is $S_t = S_c + S_m = 5.625 \text{ mm}^2$
- The side length of the square measures $l = \sqrt{S_t}$

The length of the array is 100 mm , and each filament has the same geometrical, electrical, and thermal characteristics as the previous model; the same is true for the epoxy.

Due to the more complex geometry, the model required a more complex meshing. The proximity between the filaments required a more refined mesh around the filament in order to have a good reproduction of the temperature within the small gaps between the fibres, which is considered as a critical point for the temperature. For this purpose, each filament perimeter was divided into 120 elements. From the

results of the meshing process, in Figure 7-8, it can be seen that, in the small gap between the filaments, there is an adequate number of meshing elements. The triangular elements were swept through the length of the filaments to create triangular prism meshing elements with a technique similar to that described in Chapter 3.

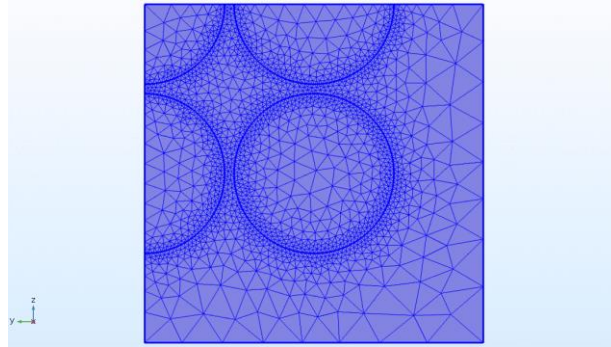


Figure 7-8. Refining of the mesh around the carbon filaments.

Considering the multiphysics nature of the model (electro-thermal coupling) and the time-dependent solution, it was necessary to resort to the division of the geometry into four sections. However, even with the help of the symmetrisation boundary conditions of the software, it was possible to solve only $\frac{1}{4}$ of the entire model. At the symmetry lines was defined the following boundary condition:

$$\bar{n} \cdot \mathbf{J} = 0 \quad (7.15)$$

Where

\bar{n} is the normal vector to the symmetry lines

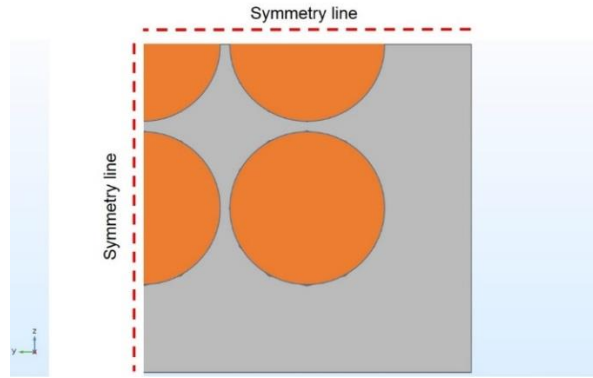


Figure 7-9. Section of the geometry used to solve the model. The top and left borders have been considered as symmetric surfaces.

7.7.2 Computation results for the refined numerical model of CFRP material

The excitation of the model is again a current waveform that replicates a scaled D-component. The peak of the impulse was chosen starting from the results of the analytical model (eq 7.1). However, considering the presence of 9 filaments, the I_0 value was multiplied by 9 and, considering that the geometry was reduced to $\frac{1}{4}$, a further division by 4 was carried out. Therefore,

$$I_{0,1} = \frac{9}{4} I_0 = 665.505 \text{ A} \quad (7.16)$$

The results show that the temperature does not change appreciably along the length of the filaments. Therefore, a cross section plane was considered at the middle of the geometry to evaluate the results. Furthermore, the analysis of the temperature changes in a specific position of the geometry was of interest. Figure 7-10 shows the four locations at which the temperature was evaluated. The central fibre and the corner fibre locations provided a comparison to explore if the temperature of the central fibre is influenced by the presence of eight fibres around it. Furthermore, the between fibres and external fibres locations were selected to compare the

temperature changes in a zone between two adjacent fibres with the temperature in a zone where only one fibre is adjacent.

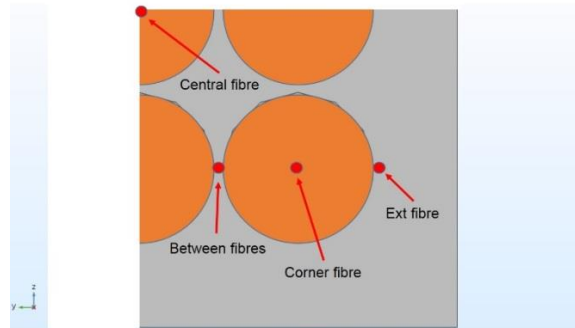


Figure 7-10. Position of the temperature evaluation points within the cross section of the geometry.

Table 7-2 shows the temperatures calculated at four locations for the time steps set in the simulation, while Figure 7-11 shows a graph with all the plotted values.

Table 7-2. Temperatures evaluated at the four positions shown in Figure 7-10.

Time (μs)	Corner ($^{\circ}\text{K}$)	Central ($^{\circ}\text{K}$)	Between ($^{\circ}\text{K}$)	Ext side ($^{\circ}\text{K}$)
1	293.1	293.1	293.1	293.1
2.2	304.5	304.5	292.8	293.7
3.2	315.7	315.7	292.5	294.2
5	335.9	335.9	292.2	295.2
10	382.8	382.8	292.2	297.2
20	447.8	447.8	293.6	298.3
30	492.1	492.1	294.8	297.8
60	551.8	551.8	295.2	294.3
90	567.2	567.2	296.9	294.4
120	571.2	571.2	303.5	298.2

150	572.2	572.2	313.6	303.8
200	572.5	572.5	333.2	314.1
300	572.5	572.5	370.9	333

The results reveal that in the first $300 \mu\text{s}$, the temperature inside both fibre cores does not decrease. However, after $90 \mu\text{s}$, it reaches a value of $300 \text{ }^\circ\text{C}$ and remains almost constant. It can be predicted that the temperature will not increase appreciably after $300 \mu\text{s}$. The temperature of the internal fibre is superimposed with the temperature of the corner fibre. Thus, it can be concluded that for this numerical model, the external fibres have no influence on the central fibre in the first $300 \mu\text{s}$. The heat generated within the fibres due to the Joule effect transfers to the external matrix and the consequence of this is the increase in temperature in the matrix near the fibres. At both the between and external side locations, an increase in temperature was recorded. However, there is no increase in temperature before $150 \mu\text{s}$. Although the temperature at the fibre cores remains nearly constant, the increased temperature of the matrix is due to the heat transfer from the most external part of the fibres. The rising trend of the temperature between the fibres is faster than that on the opposite side where there is only one adjacent fibre. This reflects the fact that in the narrow region between the fibres, there are two contributions to the heat transfer, specifically, one from each fibre; thus, the narrow region can be considered a weak region in terms of temperature increase. Furthermore, the results show that in the first $300 \mu\text{s}$, the temperature of the epoxy reaches a value of $70 \text{ }^\circ\text{C}$. Considering a glass transition temperature, T_g , of $150\text{-}180 \text{ }^\circ\text{C}$, which is typical for CFRP laminates for aerospace applications, the temperature of the epoxy is well below this level. It is predicted that the temperature at the epoxy locations will

continue to increase because of heat transfer until the temperature of the fibre is equal to the temperature of the matrix.

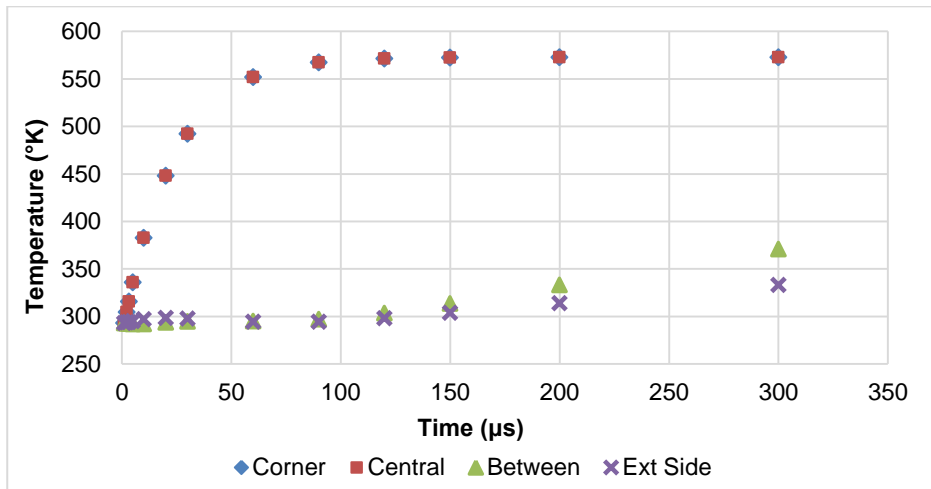


Figure 7-11. Temperature trend at the four locations specified in Figure 7-10.

7.8 Comparison with the analytical model

A comparison with the analytical model shown in section 7.4.1 is reported in Figure 7-12 where the current waveform, the variation of the temperature using the analytical model and the results of the numerical model are compared. As can be seen, a very close agreement is obtained between the temperature at the core of the fibres and the analytical method, following almost the same dynamic.

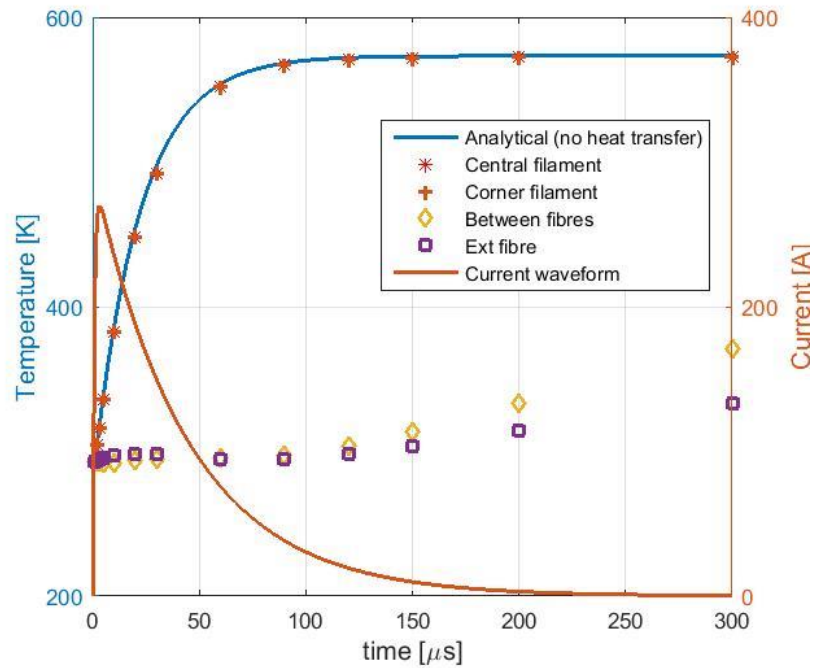


Figure 7-12. Comparison of temperature trend results from the analytical model and numerical models.

7.9 Conclusion

In this work, an analytical model was developed to investigate the temperature rise of carbon fibres following a lightning strike. Moreover, a comparison was carried out between this analytical and a numerical method. This shows the temperature trend due to the dissipation of energy through the Joule effect, in a time window of $300 \mu\text{s}$, for a carbon tow 100 mm long embedded in different materials. The two materials that surrounded the carbon filament were air and epoxy. A further, more complex numerical model was developed, and the comparison with the analytical and the simplified numerical model was carried out. All the models were excited through a scaled D-component lightning waveform.

The purpose of the comparison was to examine if a simple analytical model, which does not require both the geometry of the model and the heat dissipation process

can reproduce the temperature increase with a comparable level of accuracy compared to the numerical model.

The results show that the temperature rises within the fibres with a delay after the peak current has appeared. The delay depends on the peak magnitude of the current waveform and the cross section of the filament.

The analytical model produces similar results as the two numerical models in terms of temperature variation. Furthermore, no discernible differences were found between the output of the numerical model with air and the one with epoxy.

The developed finer numerical model, which considered an array of nine carbon filaments embedded in epoxy, required a refined mesh because of the narrow regions between the fibres. In order to reduce the computational cost, it was necessary to use symmetries in the geometry.

The results of this model are in agreement with the analytical method and with the two other numerical models. Although the central fibre was surrounded by eight filaments, it did not show a higher temperature compared to the outer fibres. Instead, the comparison between the temperature in the region between the fibres and the temperature on the external side of the fibres shows a difference in increase, with the temperature between the two fibres increasing faster than the other.

The analytical model can be reliable for the description of the temperature in the region very close to the current injection time. However, for a longer period of time, after $500 \mu\text{s}$, the analytical model is no longer reliable because it does not take into account any heat transfer process between materials. The numerical models have shown that the heat transfer process is not significant soon after the current injection due to the thermal insulating properties of the materials surrounding the filament, and

this is why the analytical method can be considered a reliable method of analysis. Conversely, the analytical method is not accurate if specific results are required in a more complex geometry, such as the one analysed in section 7.7. The numerical model can find potential applications in the study of the outgassing phenomenon at the interface between the metal fasteners and the CFRP panels due to its ability to show the changes in the temperature coinciding with time variation in the current impulse. However, for numerical simulations that consider the development of temperatures above 300 °C, it must be considered that the electro-thermal properties of the materials are not constant, but are a function of temperature.

Chapter 8

General conclusions and future work

In this thesis, extensive experiments were carried out on the grounding systems for CFRP test samples for lightning strike tests in aerospace applications. Numerical models were developed to simulate a number of scenarios and assess their performance for current distribution in CFRP material. Moreover, test samples were built and tested. Numerical computation enabled a basic knowledge of the electrical quantities inside laminated samples. The results can be considered both as the baseline and an extension of the knowledge acquired through the physical test. Through the physical tests instead, it was possible to carry out an extensive comparison of the performance of several grounding systems.

8.1 Research contribution

The research carried out by the author has contributed to expand the knowledge of the electrical interaction between CFRP laminates made by unidirectional plies and the respective grounding systems through numerical simulation and physical tests. The experiments were carried out after a comprehensive review of the most up-to-date investigation techniques and results. Previous works were reviewed, and their results were used as a baseline to design the experiments of this thesis. In some instances, a comparison was made between the results of previous studies and the results presented in this work.

A number of previous studies have been carried out on the current distribution within laminates made by unidirectional plies. However, there is a limited number of previous investigations on the electrical influence of the grounding system on the

CFRP sample. Therefore, the numerical simulations were designed to emphasize this aspect. The results show that the grounding system influences the distribution of the current within anisotropic unidirectional plies and can enhance phenomena that must be avoided or strictly controlled, such as the sparking or outgassing phenomena. Between all the scenarios investigated, which comprise one side system and four different fastener systems, the side grounding systems were shown to give the best overall performance. The side grounding allows for the best current distribution within quasi-isotropic laminates. However, the implementation of this grounding method, in a real-life scenario, introduces a new variable into the system, specifically, the contact pressure between the grounding electrode and the sample. This variable was not taken into account in the numerical simulation investigation. The consequence of this is that an eventual test rig for the sample requires a more complex design because of the control of the contact pressure. On the other hand, this grounding system has the advantage that the samples used are of a simple design because they do not require grounding fasteners and the respective holes to place them.

The fastener-grounding scenarios revealed that the current distribution within the CFRP sample is dependent on the quantity of fastener pairs used for the grounding and on their location within the sample. Fastener pairs aligned with the direction of the fibres prevent the current from spreading within the plies, with the consequence of enhancing the current density in specific paths within the sample.

Another relevant result associated with the numerical simulation was the influence of the interlaminar layer on the current distribution. The interlaminar layer is rich in resin and, therefore, has a lower conductivity compared to the core of the ply. This prevents the current from flowing in the through-thickness direction. It was found that

low values of interlaminar conductivity not only prevent the current from flowing in the through-thickness direction but also reduce the spread of the current in the plane direction.

The fastener grounding systems with eight fasteners demonstrated the closest performance compared to the side case in terms of current distribution.

The extensive numerical experiments on the current distribution were the baseline for the physical test campaign. Five different grounding systems were implemented in the same number of real test samples. Two grounding systems were designed to be used with grounding fasteners whereas the other three were designed to be used with a side grounding system. The difference between the three side grounding systems was at the interface between the side of the sample and the electrode used to collect the current. One side system had a layer of silver paint, the second system had a layer of sputtered metal and the third had no layer between the side of the sample and the return electrode. Therefore, the fibres and the matrix were in direct contact with the return electrode. The metal layers that coated two of the five samples acted as a short circuit between all the fibres at the side surface, resulting in an overall reduction in the contact resistance.

The low current DC test campaign was carried out to investigate the electrical resistance of the grounding system seen from the terminals. The results revealed how, for the three side grounding systems, the contact resistance is dependent on the pressure applied on the contact surface. Increasing the contact pressure leads to a decrease in the measured resistance. However, previous studies on metal-metal interfaces have established analytical relations between the contact resistance and the contact pressure. Therefore, the results of these measurements were compared with those analytical assumptions. The results did not show agreement with previous

studies mainly because, in other studies, the interface between two metal materials was considered. Previous to this research, the case of contact between metal materials and CFRP materials had not been strongly investigated from the electrical point of view. Thus, this study can be considered as one of the few to deal with this issue to date. The comparison between all five arrangements showed that the two fastener systems and the two coated side systems have similar contact resistance while, the *no-layer* system showed an appreciable increase in the contact resistance especially at low contact pressure compared to the other four cases. This is because only a few fibres of the sample are in touch with the return electrode.

The results of the resistance measurements were used to validate the numerical model. The comparison between the measured electrical resistances and those calculated numerically shows a good level of agreement except for the *no-layer side* grounding case, where the resistance measured was higher compared to the numerical model. A further comparison using 2D current distribution was carried out between the numerical simulation and the results of thermal recordings of the same samples taken during the high current test. It was assumed that the heat distribution recorded follows the current distribution. The visual comparison between the two results showed a good level of agreement because the current distribution of the numerical model had a similar shape and location as the heat distribution of the real samples.

The review of the interaction between the contact resistance and the contact pressure showed that the roughness characteristics of the surfaces in touch influence the contact resistance between them. In this thesis, a deeper investigation was carried out to determine the influence of the surface properties of samples in contact with the grounding electrode and this allowed improved understanding of

variations in the surface characteristics and the impact on the contact resistance. Although there is a wide range of parameters to characterize a surface in terms of roughness, only a few of them showed a reliable link with the contact resistance and the contact pressure. The analyses were carried out on surfaces without any pressure applied and on surfaces with an applied pressure of 3900 N. Comprehensive characterization technique, which required the use of optical microscope and post processing techniques of the images, such as the “focus stacking” technique, was used. It was demonstrated that a decrease in contact resistance can be related to a decrease in the mean and the root mean square of the surface roughness. The results revealed that surfaces subjected to a compression force show a wider load bearing area, which can be related to the real contact area and, thus, with the contact resistance. Furthermore, the height distribution graph gave an indication of the plastic deformation of the surface. For the non-compressed surfaces, the height distribution was symmetric around the mean value, and the heights of the surface were normally distributed whereas, for the compressed surfaces, the distributions showed a tail in the negative part because the compression force reduced the positive height of the distribution.

After the low current measurements, the samples were tested in a lightning current environment. An impulse current similar to a return stroke of natural lightning was used as the excitation for the samples and their respective grounding systems. The tests were carried out to investigate the thermal capability of the systems and the limits of electric current each grounding system can withstand. The results revealed that the presence of the metal sputter layer between the grounding electrode and the sample has benefits because it allows current peaks of up to 50 kA to be injected without any appreciable sign of sparking or outgassing phenomena recorded by the

still and thermal cameras. However, the visual analysis carried out after the test on the surface of the sample revealed signs of damage to the metal layer. The closer performance to the metal sputter grounding system was detected in the *3-fasteners* case and the *1-fastener* case. This is because of the interference fit of the grounding fasteners, which has benefits because it provides optimal contact between the fastener and the sample, thus reducing the risk of sparking at the interface. The silver paint case showed a poorer performance compared to the others because, at a 7 kA peak, sparking at the grounding interface was recorded/observed. Furthermore, the analysis of the surface after the test revealed signs of melting of the silver paint layer. The no-layer case showed the poorest performance, with sparking detected at a 5 kA peak. The low performance was attributed to the poor properties of the contact interface between the sample and the grounding electrode in terms of roughness characteristics.

The physical studies included an investigation into the effects of the location of grounding fasteners within CFRP laminates. The resistance between the injection fastener and several grounding fasteners located at different positions around the injection was measured. The sample under investigation had four times as many plies in the 0° direction as in the 90° direction. The results revealed that the resistance measured over the fasteners located at the 0° direction is considerably lower than that measured over the fasteners located at the 90° direction. This is thought to be a consequence of current flowing in lower conductivity paths. Therefore, for a grounding system made with fasteners, the position influences the current path within the laminates, especially for laminates with an unbalanced number of plies along the main directions.

From the high current test, it was concluded that the metal sputter grounding system is a valid alternative to the conventional fastener grounding system for a high current test up to 50 kA . For higher current it is required larger contact interface between the sample and the grounding electrode that implies the use of more than one side to ground the sample or to use larger test samples with larger sides. For a low current test instead, the no-layer grounding system at high contact pressure can be considered as the best choice rather than the other design. The no-layer sample can be considered as the most cost-effective design compared to the other four samples analysed.

In the last part of the thesis, it was considered of interest to investigate the comparison between a proposed analytical model and a numerical model to investigate the thermal effects of an impulse current injected into carbon fibres for aerospace applications. It was shown that a simple analytical model predicted, with a good level of agreement compared to the numerical model, the increase of temperature within carbon fibres surrounded by epoxy to a level at which the carbon fibres start to degrade. However, it could be seen that the analytical model is reliable only for the fast transient of a temperature increase after the current injection. The analytical model did not take into account the heat exchange with the surrounding environment.

8.2 Future work

The experiments carried out throughout this project have raised a number of questions which can be answered by further investigations. From the characterization of the roughness surface and from the results of the high current test, further investigation can be carried out to create contact surfaces which can

withstand higher current peaks, such as a full D-component. This would involve research on surface characteristics that can prevent sparking events. Methods of polishing the surfaces and reducing the roughness might be one answer. Another field which is worth investigating is the thermal properties of metal layers that can be used as a coating of the CFRP sample side. An ability to withstand higher temperatures means it has the ability to carry a higher level of current.

Further investigation must be carried out into the link between contact pressure and electrical resistance for contacts between metals and CFRP laminates. Those investigations can be useful not only to improve the performances of grounding systems, but also to improve the contact performance when the two materials are in contact in an aircraft structure. In that case, in the event of a lightning strike, the current might flow through the contact surface and create all the potential risks which that have been encountered during the high current test campaign of this thesis.

The fact that the current path within carbon laminates can be controlled by the position of the grounding fasteners can open up a new field of research where the material can be used as a medium for transporting electrical signals between several locations in a CFRP structure. Potential applications of this technology in addition to aircraft structures can be lightweight carbon bikes or car frames where a low weight of the structures is required. The use of the CFRP to transport electrical signals instead of a separate cabled network could advance in the direction of weight reduction.

Appendix A

Analytical calculation of the interlaminar conductivity.

The through-thickness resistance of each ply, (R_z), can be represented with three resistances connected in series, $R_z=2R_c+R_1$, as illustrated in Figure 0-1. The calculation of the interlaminar conductivity was carried out using the equation of the resistance of a conductor with length l and section S assuming that S is the area of the top/bottom surface of the sample and l is its thickness,

$$R = \frac{1}{\sigma} \frac{l}{S} \quad \text{A.1}$$

The above equation was adapted to this case considering,

$$S = L_x * L_y \text{ and } l = L_z \text{ (Refer to Figure 0-1)} \quad \text{A.2}$$

having,

$$R_z = \frac{1}{\sigma_{tt}} * \frac{L_z}{L_x L_y} \quad \text{A.3}$$

where,

σ_{tt} is the conductivity in through-thickness direction

$$L_z = L_1 + 2L_c \text{ and } R_z = 2R_c + R_1 \quad \text{A.4}$$

where,

L_1 is the thickness of the core of the ply

L_c is the thickness of the interlaminar layer

$$\sigma_{tt} = \frac{1}{R_z} * \frac{L_z}{L_y * L_x} = \frac{1}{R_1 + 2R_c} * \frac{L_z}{L_y * L_x} \quad \text{A.5}$$

$$R_1 = \frac{1}{\sigma_t} * \frac{L_1}{L_y * L_x} \text{ and } R_c = \frac{1}{\sigma_c} * \frac{L_c}{L_y * L_x} \quad \text{A.6}$$

where,

σ_c is the conductivity of the interlaminar layer

Substituting eq. A.6 in eq. A.5,

$$\sigma_{tt} = \frac{1}{1/\sigma_t * L_1 + 2 * 1/\sigma_c * L_c} * L_z \quad \text{A.7}$$

rearranging,

$$\sigma_c = \frac{2 * L_c}{L_z/\sigma_{tt} - L_1/\sigma_t} \quad \text{A.8}$$

Equation A.8 has been used to calculate the electrical conductivity of the interlaminar layer assuming that both the thickness of the core and the thickness of the interlaminar layer are constant. All the quantities present in the equation can be measured through electrical measurement and microscopic pictures.

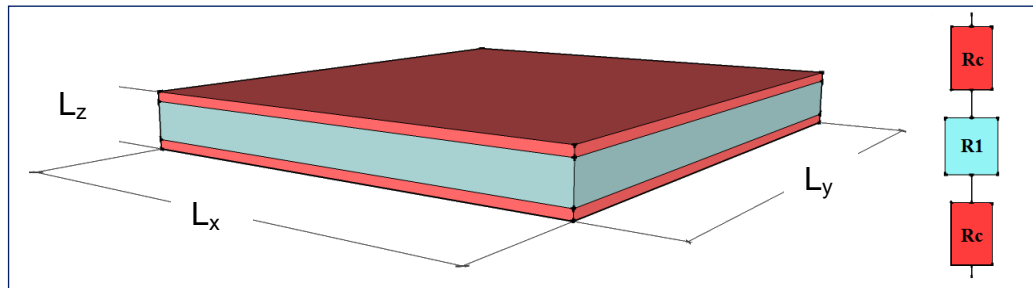


Figure 0-1: Representation of a single ply (not to scale) and its electric equivalent circuit.

Each ply has a thickness of 0.25 mm (L_z), the interlaminar layer has a thickness of 0.035 mm (L_1) and the panel is made of four plies with the lay-up [45/135/90/0]. Furthermore, the through-thickness and transverse conductivities values (σ_{tt} , σ_t) are

9 S/m and 100 S/m respectively. The conductivity along fibres (σ_f) is estimated to be 16000 S/m. The conductivity matrix is, therefore, given by

$$\begin{bmatrix} \sigma_f & 0 & 0 \\ 0 & \sigma_t & 0 \\ 0 & 0 & \sigma_t \end{bmatrix} = \begin{bmatrix} 16000 & 0 & 0 \\ 0 & 100 & 0 \\ 0 & 0 & 100 \end{bmatrix} \text{ S/m} \quad \text{A.9}$$

The value of the interlaminar impedance (σ_c) is 2.4 S/m.

Appendix B

Data required for the analytical model

The data required to solve the problem were extracted from the datasheet of a carbon tow used for aerospace applications, which is reported in [18]. The analytical problem requires the mass, the specific heat, and the electrical resistance. The datasheet reports the density of the carbon filament; thus, from the calculation of the volume, it is possible to find the mass. The specific heat is reported in the datasheet. For the electrical resistance value, the datasheet reports the electrical resistivity of the carbon filament. Therefore, from the length and cross section of the tow, it is possible to calculate the electrical resistance. Both the mass and the electrical resistance require knowledge of the length of the carbon tow to be calculated, and it is *100 mm*.

The relevant parameters used for the calculation, as extrapolated from the datasheet, are reported below.

Carbon tow data:

- density (d): $1.78 \text{ g/cm}^3 = 1780 \text{ kg/m}^3$
- tow cross sectional area (S): 0.25 mm^2
- filament diameter:
- specific heat (c): $0.21 \text{ cal/g} * ^\circ\text{C} = 879.22 \text{ J/Kg} * ^\circ\text{K}$
- electrical resistivity (ρ): $1.5 * 10^{-3} \Omega * \text{cm}$; electrical conductivity: $0.66 * 10^5 \text{ S/m}$

- thermal conductivity: $5.4 \text{ W/m} \cdot ^\circ\text{K}$

The current waveform data is taken from [41]

- $\alpha = 22708 \text{ s}^{-1}$
- $\beta = 1294530 \text{ s}^{-1}$

Characteristics of the yarn

- Length:

$$l = 100 \text{ mm}$$

- Resistance:

$$R = \rho \frac{l}{S} = 6 \Omega$$

- Mass:

$$m = d * (S * l) = 44.5 * 10^{-6} \text{ Kg}$$

In accordance with the data

$$k_1 = \frac{R}{m * c} = 1.533 * 10^2$$

$$k_2 = p = \frac{1}{2\alpha} + \frac{1}{2\beta} - \frac{2}{\alpha + \beta} = 2.0887 * 10^{-5}$$

The value of I_0 necessary to increase the temperature of the yarn to $280 \text{ }^\circ\text{K}$ starting from the ambient temperature of $293 \text{ }^\circ\text{K}$ can be found using Eq. 7.13

$$I_0 = 295.78 \text{ A}$$

References

- [1] "Wikipedia," [Online]. Available: <https://it.wikipedia.org/wiki/Aeroplano>.
- [2] "Aerospace engineering - A brief history of aircraft structures," [Online]. Available: <http://aerospaceengineeringblog.com/aircraft-structures/>.
- [3] "Composite in the aircraft industry," [Online]. Available: http://www.appropedia.org/Composites_in_the_Aircraft_Industry.
- [4] J. Pora, "Composite materials in the Airbus A380 - From History to Future," in *ICCM13*, Beijing, China, 2001.
- [5] K. Fabricius, "Airbus A350: Composites on Trial Part I," 2009. [Online]. Available: <http://scribol.com/technology/aviation/airbus-a350-composites-on-trial-part-i/>.
- [6] Wikipedia, "Fuel economy in aircraft," [Online]. Available: https://en.wikipedia.org/wiki/Fuel_economy_in_aircraft.
- [7] L. Nicolais, M. Meo and E. Milella, "Future Aircraft structures: From metal to composite structures," in *Composite Materials: A vision for the future*, Springer Science & Business Media, 2011, p. 218.
- [8] N. Stern, "Stern Review on the Economics of Climate Change," London, UK, 2006.
- [9] E. Rupke, *Lightning direct effects handbook*, Pittsfield, USA, 2002.
- [1] C. Rash, "Flight safety foundation - When lightning strikes," 9 July 2010.

- 0] [Online]. Available: <https://flightsafety.org/asw-article/when-lightning-strikes/>.
- [1 D. D. L. Chung, *Composite Materials - Science and Applications - Second*
1] *edition*, Springer, 2010.
- [1 L. E. Murr, "Examples of Natural Composites and composites Structures," in
2] *Handbook of Materials Structures, Properties, Processing and performance*,
Springer Reference, 2015, pp. 425-448.
- [1 "Ancient Egyptian architecture," [Online]. Available:
3] <http://graciousgrimoire.blogspot.co.uk/2015/09/ancient-egyptian-architecture.html>.
- [1 C. S. University, "What is chemical engineering - Advanced materials,"
4] [Online]. Available:
<http://navier.engr.colostate.edu/whatische/ChEL05Body.html>.
- [1 D. Chung, *Carbon Fibers Composites*, Butterworth-Heinemann, 1994.
5]
- [1 D. Hull, "Fibres and Matrices," in *An introduction to composite materials*,
6] *Cambridge Solid State Science Series*.
- [1 N. Iwashita, H. Imagawa and W. Nishiumi, "Variation of temperature
7] dependence of electrical resistivity with crystal structure of artificial graphite
products," *Carbon*, no. 61, pp. 602-608, 2013.
- [1 Hexcel, "IM7 HexTow DataSheet," [Online]. Available:
8] http://www.hexcel.com/user_area/content_media/raw/IM7_HexTow_DataSheet.pdf.

- [1 R. Chippendale, Modelling of Thermal Chemical Damage Caused to Carbon
9] Fibre Composite, Phd Thesis submitted to the University of Southampton,
2013.
- [2 C. Sonnenfeld , H. Medil-Jakani, R. Agogue', P. Nunez and P. Beauchene,
0] "Thermoplastic/thermoset multilayer composite: A way to improve the impact
damage tolerance of thermosetting resin matrix composites," *Composite
structures*, pp. 298-305, 2017.
- [2 E. Akca and A. Gursel, "A Review on the Matrix Toughness of Thermoplastic
1] Materials," *Periodicals of Engineering and Natural Science*, vol. 3, no. 2,
2015.
- [2 A. S. Bureau, "Advanced composite Materials," in *Aviation maintenance
2] technician - Airframe Handbook*.
- [2 Y. Okabe and N. Takeda, "Quantitative Evaluation of Interlaminar -
3] Toughened CFRP Composite by Ultrasonic Wave Propagation
Characteristics," *Journal of Composite Materials*, 1999.
- [2 A. M. Helmenstine, "Table of Electrical Resistivity and Conductivity,"
4] ThoughtCo., 15 March 2017. [Online]. Available:
<https://www.thoughtco.com/table-of-electrical-resistivity-conductivity-608499>.
- [2 Y. Hirano, T. Yamane and A. Todoroki, "Through-Thickness Electrical
5] Conductivity of Toughened CFRP Laminate," in *Thirty First Technical
Conference, American Society for Composites*, 2016.
- [2 R. Abid, "Variable Alternating current circuit," in *Electrical Characterization of*

- 6] *Aerospace Grade Carbon Fibre Reinforced Polymer*, PhD thesis submitted to Cardiff University, 2015, pp. 110-113.
- [2 T. Ogasawara, Y. Hirano and A. Yoshimura, "Coupled thermal-electrical
7] analysis for carbon/epoxy composites exposed to simulated lightning current," *Composites: Part A*, no. 41, pp. 973-981, 2010.
- [2 Y. Suzuki, A. Todoroki and Y. Mizutani, "Diagnosis for CFRP aircraft by
8] Joule heating using lightning protection system," *SRM*, vol. 2, no. 94.
- [2 A. Todoroki, M. Tanaka and Y. Shimamura, "Measurements of orthotropic
9] electric conductance of CFRP laminates and analysis of the effect on delamination monitoring with an electric resistance change method," *Composites Science and Technology*, vol. 62, pp. 619-628, 2002.
- [3 R. Abid, Electrical characterization of aerospace grade carbon-fibre-
0] reinforced polymer, Cardiff UK: PhD Thesis, 2015.
- [3 F. A. A. (FAA), "14 CFR Part 25 - Airworthiness Standards: Transport
1] category airplanes".
- [3 Y. Kostogorova-Beller, A. Soler and K. Cheng, "Lightning research at
2] National Institute for Aviation Research: Development of fastener sparking threshold database for metal fuel tanks: inception," in *2015 International Conference on Lightning and Static Electricity*, Toulouse, France, 2015.
- [3 B. M. Martin, "Part 25 Fuel Tank Structure Lightning Protection policy," in
3] *2015 International Conference on Lightning and Static Electricity (ICOLSE)*, Toulouse, France, 2015.

- [3 G. Serianni, *Applicazione Industriale dei Plasmi, Lessons Notes*, Padova, 4] 2010.
- [3 SAE/EUROCAE, "Policy Guidance for Lightning protection of Fuel Tank 5] Structure and Systems," 2014.
- [3 EUROCAE, "Aircraft Lightning test Methods ED-105," Paris, 2005. 6]
- [3 V. Martinez Garcia, "Weight saving in sandwich panels: is puncture a 7] showstopper?," in *2015 International Conference on Lightning and Static Electricity*, Toulouse, France, 2015.
- [3 T. Gibson, J. Chase Fielding and K. Kranjc, "Evaluation of Conductiv 8] nanomaterials for Lightning Strike protection of Polymeric Composites," in *2009 International Conference on Lightning and Static Electricity*, Oxford, UK, 2009.
- [3 EUROCAE, "ED-91 Aircraft Lightning Zoning," Paris, 1998. 9]
- [4 G. Sweers, B. Birch and J. Gokcen, "Lightning Strikes: Protection, Inspection 0] and Repair," *AERO*, vol. 4, no. 48, pp. 19-28, 2012.
- [4 EUROCAE, "ED-84 Aircraft Lightning Environment and Related Test 1] Waveforms," Paris, 1997.
- [4 S. Evans, S. Hellsten and M. Cole , "A review of computationl modelling 2] tools for lightning direct effects simulation," in *2011 International Conference on Lightning and Static Electricity*, Oxford, UK, 2011.

- [4 R. Greegor, Q. N. Le, B. A. Anway, B. A. Whiting and A. C. Day, “Finite
3] Element Simulation and experimental Analysis of Edge Glow for a generic
16-Ply Carbon Fiber Reinforced Plastic Composite Laminate,” in *2015
International Conference on Lightning and Static Electricity (ICOLSE)*,
Toulouse, France, 2015.
- [4 R. Chippendale, I. Golosnoy and p. Lewin, “Effects of different components
4] of a lightning strike waveform on the heating of different material: Alluminium
Alloy vs. Carbon Fibre Composites (CFCs),” in *2011 International
Conference on Lightning and Static Electricity* , Oxford, UK, 2011.
- [4 A. M. Robb, “Electroplated Copper Contacts for electrical Bonds and
5] Grounds to Carbon Fibre Reinforced Plastic Lightning Test Specimen,” in
ICOLSE 2007, 2007.
- [4 C. E. Anway, A. C. Day and J. T. Geis, “Contact Resistance in Carbon Fiber
6] Composite Materials as Function of Force,” in : *International SAMPE
Symposium and Exhibition*, 2010.
- [4 R. Holm, *Electric Contacts Theory and Application*, Springer- Verlag Berlin
7] Heidelberg GmbH, 1981.
- [4 G. Mastrolembo, M. Haddad, M. Cole and S. Evans, “Understanding Voltage
8] and Current Distribution of Cost Effective Carbon Composite Test Samples
for Aircraft Lightning Strike Tests,” in *ICCM20 20th International Conference
on Composite Materials*, Copenhagen, 2015.
- [4 R. Abid, A. M. Haddad, H. Griffiths, D. Clark, M. Cole and S. Evans,
9] “Electrical Characterization of Aerospace Graded Carbon Fiber Reinforced

Plastic Composites Under Low Current DC Impulse Energizations,” in *ICOLSE2013 International Conference on Lightning and Static Electricity*, Seattle USA, 2013.

[5 G. Mastrolemo, A. M. Haddad, D. Clark, M. Cole and S. Evans, “Modelling
0] the Effect of Ground Return Fasteners on Current Distribution and Power
Dissipation in Carbon Composite Test Samples Subjected to Lightning
Strikes,” in *UPEC2016*, Coimbra, Portugal, 2016.

[5 Airbus, Airbus internal documentation.

1]

[5 M. Braunovic, V. V. Konchits and N. K. Myshkin, *Fundamentals of Electrical
2] Contacts*, Taylor & Francis Group, LLC, 2006.

[5 D. Liu, Y. Tang and W. Cong, “A review of mechanical drilling for composite
3] laminates,” *Composite Structures*, vol. 94, no. 4, pp. 1265-1279, 2012.

[5 Zeiss, “AxioCam IC Compact performance,” [Online]. Available:
4] [https://applications.zeiss.com/C125792900358A3F/0/2CB8957203563235C
12579060047D23F/\\$FILE/48-0085_e.pdf](https://applications.zeiss.com/C125792900358A3F/0/2CB8957203563235C12579060047D23F/$FILE/48-0085_e.pdf).

[5 E. Gray, “Photography life,” [Online]. Available:
5] <https://photographylife.com/what-is-depth-of-field>.

[5 Wikipedia, “Focus stacking,” [Online]. Available:
6] https://en.wikipedia.org/wiki/Focus_stacking.

[5 D. Whitehouse, *Surfaces and their measurement*, Hermes Penton Science,
7] 2002.

- [5] Keyence, "What is Surface Roughness?," [Online]. Available:
8] <http://www.keyence.com/ss/products/microscope/roughness/line/index.jsp>.
- [5] Wikipedia, "Surface Roughness," [Online]. Available:
9] https://en.wikipedia.org/wiki/Surface_roughness.
- [6] L. Chemartin, P. Lalande and F. Tristant, "Modeling and simulation of
0] sparking in fastening assemblies.," in *ICOLSE 2013*, Seattle US, 2013.
- [6] L. Chemartin, P. Lalande, P. Elias, C. Delalondre, B. Cheron and F. Lago,
1] "Direct Effects of Lightning on Aircraft Structures: Analysis of Thermal,
Electrical and Mechanical Constraints," *Aerospace Lab Journal*, no. 5, 2012.
- [6] S. Evans, M. Jenkins, M. Cole, A. Fay and R. Mills, "An introduction to a new
2] aerospace lightning direct effects research programme and the significance
of Zone 2A waveform components on sparking joints," in *International
Conference on Lightning Protection (ICLP)*, Estoril, Portugal, 2016.
- [6] S. Evans, I. Revel, M. Cole and R. Mills, "Lightning Strike Protection of
3] Aircraft Structural Joints," in *International Conference on Lightning
Protection (ICLP)*, Shangay, China, 2014.
- [6] D. Adeuyi Oluwole, *Carbon Composite Materials For Aerospace Applications*,
4] Cardiff, 2010.
- [6] E. Rupke, *Lightning direct effects handbook*, Pittsfield: AGATE, 2002.
5]
- [6] A. Storer, "Quora," July 2015. [Online]. Available:
6] <https://www.quora.com/What-is-the-maximum-temperature-stability-of->

carbon-fiber-composite-and-glass-fiber-composite/answer/Alistair-Storer..

[6 S. Feih, E. Boiocchi, E. Kandare, Z. Mathys, A. Gibson and A. Mouritz,

7] “Strenght degradation of glass and carbon fibres at high temperature,” in *International Conference on Composite Materials (ICCM 17)*, Edinburgh, UK, 2009.

[6 “Engineering tool box,” [Online]. Available:

8] http://www.engineeringtoolbox.com/air-properties-d_156.html.

[6 “Engineering tool box,” [Online]. Available:

9] http://www.engineeringtoolbox.com/specific-heat-capacity-d_391.html.

[7 “Engineering tool box,” [Online]. Available:

0] http://www.engineeringtoolbox.com/thermal-conductivity-d_429.html.